Development of a bespoke sensory surface to combat biofouling in the maritime sector

A thesis submitted in partial fulfilment of the requirements of Liverpool John Moores University for the degree of Doctor of Philosophy

Karin Brenda Moejes

December 2019

Abstract

Biofouling is defined as the colonisation process of a solid surface (living or dead) by sessile organisms that poses a significant global industrial problem with increased drag, fuel consumption, greenhouse gas emissions and introduction of non-native species. Current biofouling management processes such as visual inspections, regulations, antifouling coatings, in-water cleaning, grooming, and dry-docking are included. Currently there is no *in situ* detection method available to recognise biofouling in real-time. One of the problem biofouling species is the blue mussel, *Mytilus edulis*, and was therefore chosen as the model organism in this study. The overall aim of the study was to develop a bespoke sensory surface to monitor *in situ* biofouling in real-time and demonstrating its use synergistically with a novel non-toxic antifouling technology, laser microtexturing. *M. edulis* were exposed to test surfaces and were compared to controls. Materials tested were PVC, Nylon 6, Silicone and PTFE with varying relative permittivities and surface energies. The sensor used was of the planar electromagnetic interdigitated electrode type. Frequency operating range on the VNA was from 10 MHz to 15 GHz, key frequencies were identified for *M. edulis* byssal plaque detection on the surface. Microtopographies were developed with a nanosecond pulsed fibre laser on stainless steel. Microtopographies were transferred to Silicone and antifouling and foul-release efficacy was assessed (byssal plaque area, total number of byssal plaques, adhesion strength). The presence of the microtopography demonstrated an increased plaque area with a reduced

adhesion strength. The combination of sensory surface with microtopography and silicone, as an antifouling mechanism, demonstrated the detection of *M. edulis in situ* and in real-time. The synergistic interaction of the sensor's EMW with the hydrophobic foul-release silicone surface and antifouling microtopography demonstrated detection of *M. edulis* byssal plaques as well as the specimen itself while reducing the incidence of mussel settlement overall.

Declaration

I, Karin Brenda Moejes, declare that the thesis presented has been composed by myself and has not been submitted for any other degree or professional qualification. The work contained herein is my own, except where explicitly stated otherwise, and was carried out at Liverpool John Moores University Faculty of Science and Faculty of Engineering, under the supervision of Dr Simone Dürr.

Karin Brenda Moejes

19th December 2019

Acknowledgements

I would like to express my deepest gratitude to my Director of Studies, Dr Simone Dürr for giving me this opportunity, and for her tireless support, guidance and expertise. I am forever grateful. Your determination, patience, kindness and infectious laugh has allowed me to develop and grow as a researcher and a person. Thank you.

My greatest thank you to Dr Martin Sharp whose kindness and direction have been indispensable throughout the project. I would like to thank Dr Olga Korostynska for the opportunity and for believing in me to author my first paper under her guidance.

I would like to extend my thankfulness to Dr Alex Mason for his crucial wealth of knowledge in his advisory role in the project. My deepest thank you to Dr Sheelagh Conlan whose advisory role was essential to the project, and whose kindness, positivity, expertise and unwavering support are deeply appreciated.

Dr Stephen Wylie, I would like to thank you for joining my supervisory team at such a late stage, and for believing in the research and in me. Your patience and depth of knowledge are truly appreciated. I would like to thank Dr Andy Shaw for his advisory role on the project, for taking the time to explore the development of a sensory surface and for his crucial expertise.

A special thank you to the technical staff in both the Faculty of Engineering and the Faculty of Science at Liverpool John Moores University, your support and knowledge has been indispensable.

Acknowledgements

To my family and friends across the globe, your unconditional love and support have been a constant source of strength and positivity. I thank you all for the patience and understanding over the course of the research, I will forever be indebted to you. This is for you.

Lastly, I would like to thank Liverpool John Moores University for my PhD studentship which was awarded as FET - SCS Joint PhD Studentship Project 2016/17 to Dr Simone Dürr, Dr Olga Korostynska and Dr Martin Sharp.

Table of Contents

Chapter 4

List of Figures

List of Tables

List of Equations

Chapter 1

General Introduction

“I hate a Barnacle as no man ever did before,

not even a Sailor in a slow-sailing ship.”

- *Charles Darwin*

1.1. Introduction

As maritime navigation developed from the ancient Greeks and Phoenicians through to modern war fleets and trading ships, the problem of biofouling has only grown alongside it (Hellio and Yebra, 2009). Biofouling is defined as the colonisation process of a solid surface (living or dead) by sessile organisms (Wahl, 1989; Dürr and Wahl, 2004; Dürr and Watson, 2010), this essentially makes these organisms hitchhikers as they adhere to the hulls of ships (Wrange *et al.*, 2016). In order to adhere to the hull, the biofouling process may be generally divided into five main stages which may occur one after the other, overlap or even concurrently (Dobretsov *et al.*, 2009). Biofouling is defined to begin in the first few moments with (1) the adsorption of a 'conditioning film' (dissolved organic molecules), (2) colonisation by prokaryotes, (3) dispersion of some cells, (4) colonisation by unicellular eukaryotes (e.g. diatoms, ciliates and flagellates), and finally, (5) colonisation by multicellular eukaryotes (Railkin, 2003; Dobretsov *et al.*, 2006) (*figure 1.1*). These molecules and organisms are further split into two larger groups of microfoulers (1-4) and macrofoulers (5), the prior of which creates a biofilm (or slime) that in turn usually facilitates the attachment of the larger macrofoulers (e.g. tubeworms, barnacles, macroalgae and mussels) to initiate a highly dynamic process (Zobell and Allen, 1935; Callow and Callow, 2002). However, a biofilm is not necessarily needed for the formation of macrofouling and some invertebrate larvae are able to settle permanently on clean surfaces within an hour, quicker than the colonisation by some prokaryotic bacteria

(Fletcher, 1977; Roberts *et al.*, 1991; Lehaitre and Compère, 2008; Ralston and Swain, 2009).

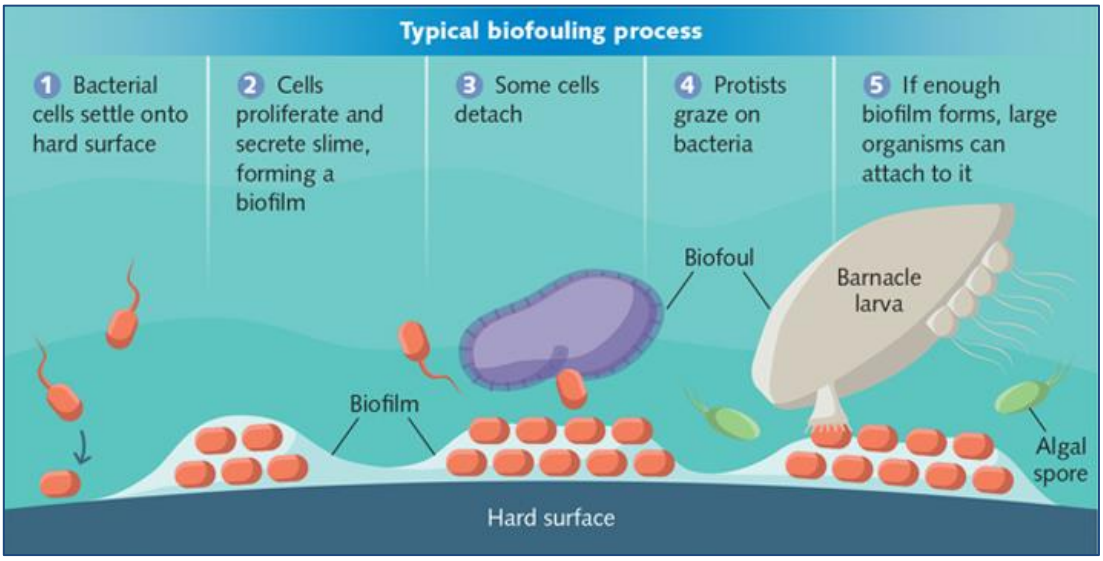

Figure 1.1 – Stages of Biofouling Development *begin with the settlement and formation of the 'conditioning film' and microfouling (**1 – 4**). This is then usually followed by the attachment of large macrofoulers such as barnacles and mussels (**5**) (source: Fischer et al., 2012; Venugopalan, 2016).*

1.1.1. Maritime biofouling: ecology, economy and emissions

Microfoulers help create a 'slime' that exists within an extracellular polymeric substance (EPS) and although a complete biochemical profile is not easily achieved, it is made of biopolymers that contain polysaccharides, glycoproteins, glycolipids and even extracellular DNA to create a matrix (Flemming *et al.*, 2007). Although the biofilm may be created by microscopic fouling constituents, as a whole, the biofilm is capable of imparting a powering penalty on ships of between 11% to 21% (Schultz, 2007). On the other hand, the heavy calcareous fouling organisms (macrofoulers) are capable of imparting an 86% powering penalty and consequently, an economic and environmental penalty as well (Schultz, 2007). In

both cases, the weight and surface roughness is increased by the build-up of biofouling organisms on the hull of ships, which in turn increases frictional drag and thus decreases speed (Abbott *et al.*, 2000). In order for ships to compensate for added weight and increased drag, they increase power. Consequently, fuel consumption is increased in order to maintain speed, and therefore also adding to engine stress (Bixler and Bhushan, 2012). To put this into context, a biofilm of only 1 mm may result in an 80% increase in friction and therefore, a 15% loss in speed (Lewthwaite *et al.*, 1985; Hellio and Yebra, 2009). An added 5% more biofouling may result in a 17% increase in fuel consumption and inevitably a 14% increase in greenhouse gas emissions. According to Hellio and Yebra (2009), with the added hundreds of millions of tonnes of carbon dioxide (CO_2) emissions, there is an expected fuel consumption of 486 million tonnes by 2020. Economically, for the US navy alone, biofouling amounts to an estimated US$56 million for the DDG-51 class destroyer per annum (Schultz *et al.*, 2011). Were the shipping industry a country, it would be the sixth largest greenhouse gas emitter with 932 tonnes produced in 2015 (Olmer *et al.*, 2017) compared to the 729.8 tonnes Germany released in the same year (International Energy Agency, 2017) (*figure 1.2*).

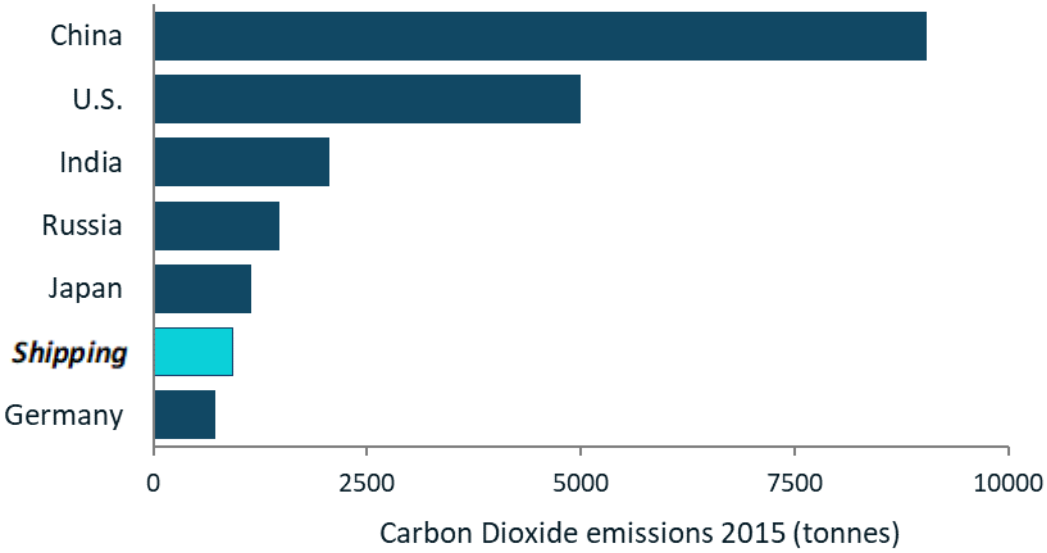

Figure 1.2 – Carbon Dioxide Emissions of the Shipping Industry *in relative to the countries with the highest emission in 2016 (data from: Olmer et al., 2017; IEA, 2017).*

In April of 2018 a strategy to reduce greenhouse gas emissions from ships by 50% by 2050 in relation to 2008 levels, 1,135 million tonnes of CO_2, was initiated by the International Maritime Organisation (International Maritime Organistaion, 2018).

The damage done by biofouling on ships is not limited to the increase in drag, but physical damage may be caused as well. Biofouling may often cause corrosion, particularly localised, severe corrosion as a result of non-uniform biofouling (Edyvean, 2010). Large macrofoulers may cause the formation of these localised corroded areas as they create oxygen concentration cells. The presence of dissolved oxygen allows for the production of corrosion-promoting metabolites such as sulphide from macrofoulers, which react with iron to form a corrosive product (Little *et al.*, 2008). In fact, the corrosion may be accelerated by a factor of 1000 to 100,000 (Edyvean, 2010).

1.1.1.1. Introduction of Non-Native Species

The diverse and dynamic biofouling community may in turn impact other environments to which they may be alien; the anthropogenic activities of shipping may introduce new, non-native and sometimes invasive species, which would not have been introduced to a new environment otherwise due to physical barriers (Lewis and Coutts, 2010). This may happen not only via fouling on the hull of ships, but also via ballast water, which has been a well-known vector for the introduction of invasive species for decades (Davidson *et al.*, 2009) (*figure 1.3*).

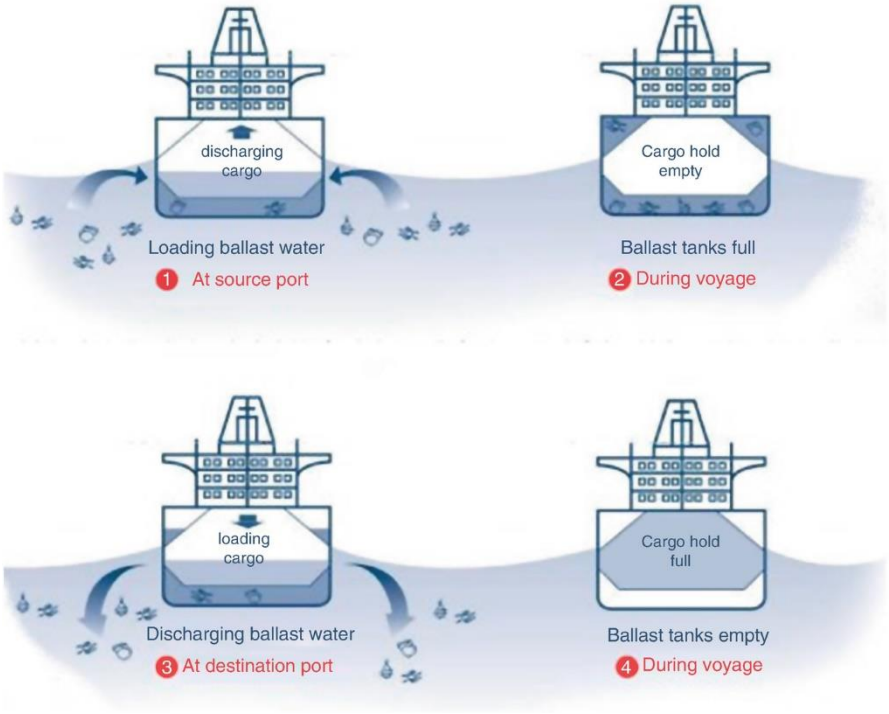

Figure 1.3 – Ballast Water Exchange *whereby ballast water is loaded during cargo discharge (**1**). The vessel then travels with a full ballast tank (**2**) to the destination port where the ballast water is discharged, as cargo is loaded (**3**). The vessel then leaves the port with a full cargo hold (**4**) (source: International Maritime Organistaion, 2019).*

The high-surface area to volume ratio of the ballast tank facilitates the development of 'interior hull biofouling' and enables the accumulation of

organisms that may survive the harsh environment of the ballast tank (Drake *et al.*, 2005). Major biofouling organisms such as the freshwater Zebra mussel *Dreissena polymorpha* were transported in the ballast tanks of ships and into the Great Lakes of America (Mills *et al.*, 1993). The likely mechanism for the spread of *D. polymorpha* was described as the uptake of larvae settling on the walls of the ballast tank where metamorphosis and growth may be continued to occur until the adults spawn and produce more larvae that are released at the recipient port (Johnson and Padilla, 1996). One of the main concerns of the introduction of a non-native species is its ability to possibly overwhelm native species and reduce the biodiversity of the habitat (Bax *et al.*, 2003). The benthic North Pacific Seastar *Asterias amurensis* was transported via ballast water from its native China, Japan, Korea and Russia, to the oceans surrounding southern Australia and Tasmania (Byrne *et al.*, 1997; Ross *et al.*, 2002; Hwang *et al.*, 2011). This predatory seastar is described as one of the world's 100 most invasive species (Lowe *et al.*, 2000) and was likely taken up in the ballast water during the planktonic larval stage in a native port. Once discharged back into the water column at a destination such as Melbourne, Australia, the metamorphosed non-native invasive North Pacific seastar was found to consume the eggs of the endemic endangered handfish (*Brachionichthys hirsutus*) (Edgar *et al.*, 2017).

Invasive species are proven to be dangerous, even deadly at times. Marine dinoflagellates are able to produce toxins that are consumed by shellfish and fish alike, and then consumed by humans leading to paralytic shellfish poisoning (PSP) resulting in numbness of the tongue, lips and finger tips, and in severe cases,

death (Mee *et al.*, 1986). One of the first recorded fatalities caused by this type of poisoning may be dated as far back as 1793 (Hallegraeff, 2010) and although the spread of these toxins via ever increasing harmful algal blooms events is understood, it has been shown to occur via anthropogenic activities as well (Ribeiro *et al.*, 2012). These same anthropogenic activities may even lead to outbreaks of cholera whereby ship ballast water had been contaminated with the bacterium *Vibrio cholerae* (McCarthy and Khambaty, 1994). Ruiz *et al.*, (2000) found both serotypes of the bacteria O1 and O139, which cause human epidemic cholera, in the plankton of 93% of all the ships sampled. With dividing cells obtained in these samples, these viable bacteria could be a source of another ballast water assisted cholera outbreak.

1.1.2. Antifouling: A Balancing Act

Since antiquity and the occurrence of biofouling, the need to develop an effective antifouling coating encompassed strategies from wax and tar to metals and poison (Bressy and Lejars, 2014). It is estimated that an effective antifoulant coating or husbandry technique may save over an estimated US$150 billion per annum by 2020 (Hellio and Yebra, 2009), not to mention it would also reduce the anthropogenic impact of international shipping and its capacity of introducing new, invasive and harmful species (Lewis and Coutts, 2010). Additionally, it is estimated that marine antifouling coatings reduce carbon dioxide and sulphur dioxide emissions of 384 million and 3.6 million tonnes annually, respectively (Bressy and Lejars, 2014).

The most efficient antifoulant to date was tributyltin (TBT), an organotin biocide that first came around in the early 1960's as a 'free association' paint with a self-polishing copolymer (TBT-SPC) in the 1970's (Omae, 2003). By the 1980's, TBT was utilised by over 80% of commercial ships (Abbott *et al.*, 2000) with its capacity to remain effective for up to five years allowing for a modest cost of production (Bressy and Lejars, 2014). Nevertheless, in the 1980's reports from Plymouth Sound, UK showed imposex of dog-whelk, whereby females would develop male genitalia due to exposure to TBT and thus affecting their reproduction. Around the same time, it was shown to cause shell thickening in oysters, devastating the particular industry (Gibbs and Bryan, 1986). Finally, TBT was revealed to impact large mammals, including sea otters which were found dead containing organotin compounds at 34 to 4100 ng/g on a wet weight basis (Murata *et al*., 2008). As a result of the environmental impacts of TBT, restrictions were imposed and eventually a complete ban on organotin based compounds was implemented in 2008 (International Maritime Organization, 2016).

It could be argued that despite TBTs immediate impact on marine life, the ability of TBT-SPC to create a smooth hull (reducing drag and fuel consumption) could save an estimated 7.3 million tonnes of fuel and 23 million tonnes of carbon dioxide that it would otherwise produce (Abbott *et al.*, 2000; Evans *et al.*, 2000). This means that TBT remains the most efficient, though illegal antifouling method; however, the devastation on marine life outweighs these perceived benefits. It is therefore necessary to find a balance between the efficiency, ecology and economy of an antifoulant to provide effective husbandry in tackling biofouling.

In the last 10 years, the so-called nanotechnology coatings were developed as a non-toxic option (Khanna, 2008; AMBIO, 2010). However, new EU legislation places nanomaterials under the EU Biocidal Products Regulation (528/2012) (European Union, 2012) and ECHA Workplan on Nanomaterials for 2016-2018 (European chemicals agency, 2015) requiring costly and long-term tests making this new technology only relevant to a very limited number of applications as well.

The maritime industry is continuously finding and using other biocides such as copper, in antifouling coatings (Thomas and Brooks, 2010). Copper's use as a biocide increased since the ban on TBT due to its toxicity and relatively low environmental risk (Brooks and Waldock, 2009). Nonetheless, this increased use since resulted in high concentrations of the metal occurring due to leaching from antifouling coatings, particularly within enclosed waters such as estuaries and harbours as well as in the sediment. Moreover, some algae and diatoms are resistant to inorganic copper and so the use of booster biocides was introduced, such as Igarol 1051 (Turner, 2010). Acting as an effective photoinhibitor, Igarol 1051 demonstrated an effect on non-target species such as coral and mangroves, even at low concentrations (Dafforn *et al*., 2011). Continued research on the use of various biocides recently began to move from metals such as copper and zinc, to non-metal biocides or natural and natural-derived biocidal products (Rittschof, 2000). Biocides operate within a polymer matrix that acts either in a self-polishing manner or by leaching. Self-polishing polymers are so-called due to their release of the surface layers of the polymer and therefore release of the antifouling biocides (Kiil *et al.*, 2001; Howell and Behrends, 2006; Bressy *et al.*, 2009). These

self-polishing paints with a sustained release rate may allow ships to go up to 60 months without the need for repainting (Bressy and Lejars, 2014). The alternative method is often referred to as free association paints whereby the antifouling biocides are slowly released from the polymer matrix in an uncontrolled manner resulting in their effect lasting between 18 to 24 months (*figure 1.4*).

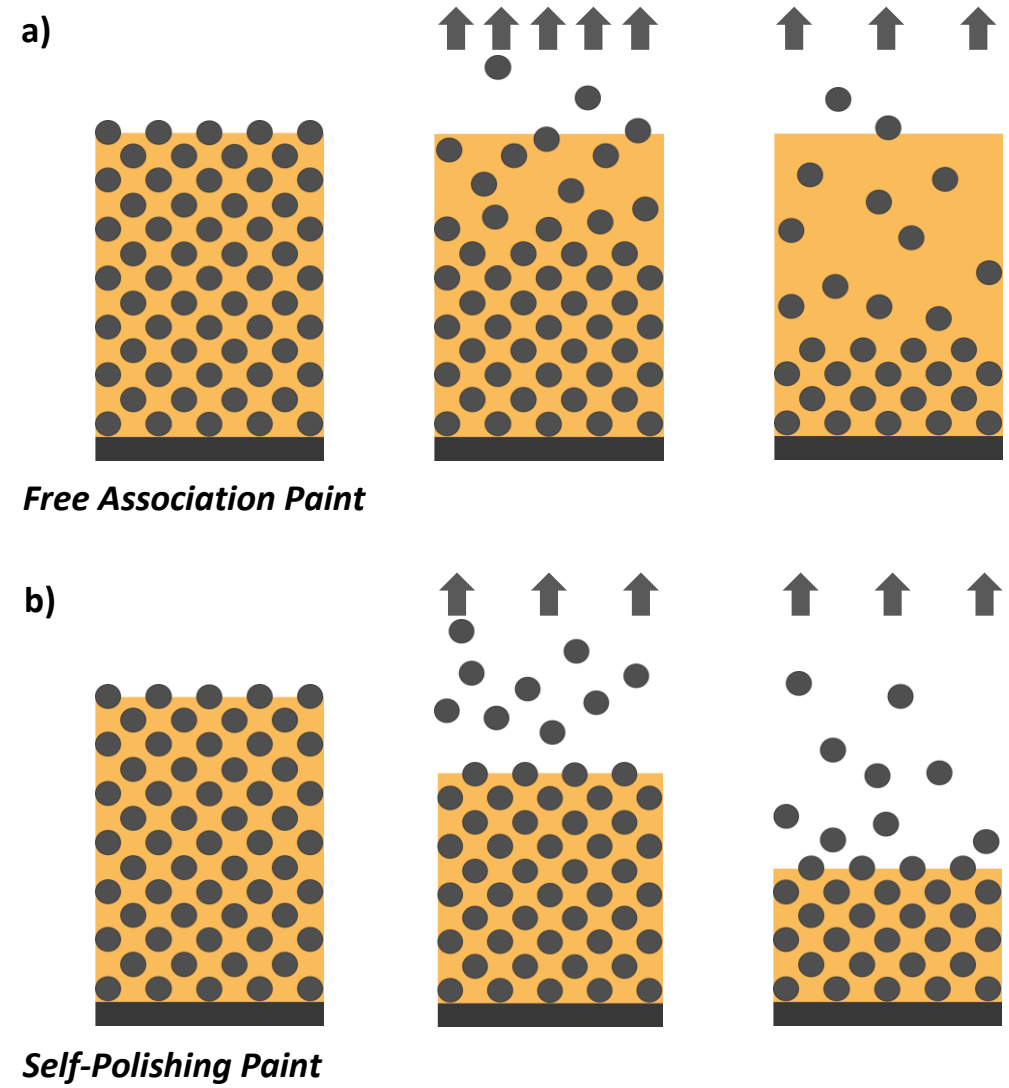

Figure 1.4 – Free Association and Self-Polishing Biocide Antifouling System*. Free Association paint whereby the biocide is released from the matrix initially rapidly, and then begins to decrease with time (**a**). Self-polishing paints allow for a slow controlled release of biocide over time (**b**) (adapted from: Bressy et al., 2009).*

However, these biocides remain subject to restrictive legislation such as the European Biocidal Products Regulation (BPR, 528/2012) (European Union, 2012) and so research moved to focus on non-toxic alternatives.

1.1.2.1. Non-Toxic Antifouling Technology

More recently, foul-release coatings (FRC) mainly based on silicone elastomers are coming into use (Dürr and Watson, 2010). These coatings are described to not contain any biocides and so, are advantageous as they are non-toxic. This antifouling technology is defined to rely on the reduced ability of the fouling organism to adhere to the surface and thus allowing it to be removed by the hydrodynamic stress of the moving vessel or a gentle clean of the surface (Schultz *et al.*, 1999; Holm *et al.*, 2004). Fast-moving ships are advantaged by these systems that enable the release of fouling organisms over 20 knots (Salta *et al.*, 2010), however, commercially available FRCs were developed to be efficient from over 8 knots for 5 to 10 years (Bressy and Lejars, 2014).

Traditionally FRCs are founded on their surface hydrophobicity and low surface energy to reduce adhesion force. The silicone elastomer is based on a poly(dimethyl)siloxane (PDMS) chain that allows for a flexible backbone with low surface energy side groups (*figure 1.5*) (Meyer *et al.*, 2006).

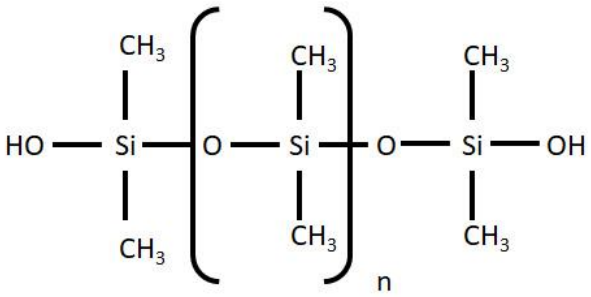

Figure 1.5 – Molecular Structure of Poly(dimethyl)siloxane. *The siloxane bonds allow for a low elastic modulus and the methyl non-polar functional group lends to the hydrophobic properties of PDMS (source: Henniker Plasma, 2017).*

Adhesion is reduced by FRCs and the energy for removal is lowered, therefore drag is decreased with a reduction in biofouling (Candries and Anderson, 2001; Townsin and Anderson, 2009; Corbett and Winebrake, 2010). In turn, costs, fuel consumption and greenhouse gas emissions are decreased.

However, susceptibility to biofouling, particularly the development of biofilms that may withstand speeds of up to 30 knots is sustained with FRCs (Bressy and Lejars, 2014). In order to improve the release efficacy of the paint, additive oils (1-10 wt.%) are introduced including silicone-based, fluorinated or amphiphilic oils. The addition of hydrophilic polyethylene glycol (PEG) has been shown to reduce adhesion strength likely due to PEG migration to the surface when in contact with water (Li *et al.*, 2017). The PEG chains extend from the surface to create a flexible brush-like surface that reduces the ability for adhesion and self-cleaning with hydrodynamic stress.

Nevertheless, the leaching of these oils into the marine environment and their possible toxicity is needed to be further investigated (Nendza, 2007). Furthermore, vessels that are slow moving or spend considerable time in port, such as navy vessels, are left highly susceptible to biofouling when using FRCs.

1.1.3. Shipshape: Locating and Limiting Biofouling

In order to enable effective biosecurity and husbandry, maritime industries need to be able to determine the amount of biofouling and the time of removal. Current regulations include voluntary guidelines from the International Maritime Organisation (IMO) (International maritime organistaion, 2011), while in specific

countries mandatory regulations for removal of biofouling from hulls were introduced, with New Zealand having specific thresholds for broad taxonomic groups (Zabin *et al.*, 2018). These regulations are generally enforced in the form of underwater inspections and cleaning by divers and/or scheduled (or even unscheduled) dry docking for removal and re-application of the antifouling coating (Townsin, 2003). One major reason for inspecting biofouling on ships is that they pose a biosecurity threat with the possible introduction of non-native marine species and although the best precaution would be avoidance by refusing entry of a biofouled ship, this is rarely implemented (Hopkins and Forrest, 2008). Teams of commercial divers are supervised by qualified marine biologists to carry out a visual inspection of the hull, resulting in high costs and occupational health and safety hazards for the divers involved (Floerl and Coutts, 2013) (*figure 1.6*). Remote Operated Vehicles (ROVs) or Autonomous Underwater Vehicles (AUVs) may accompany the divers or operate alone and are equipped with a variety of technologies such as lights, cameras, acoustic systems, transmission of data, status updates, conductivity-temperature-depth sensors and sonar systems (Valavanis *et al.*, 1997; Wemli, 2002; Negahdaripour and Firoozfam, 2006; Vaganay *et al.*, 2006; Wang *et al.*, 2008)

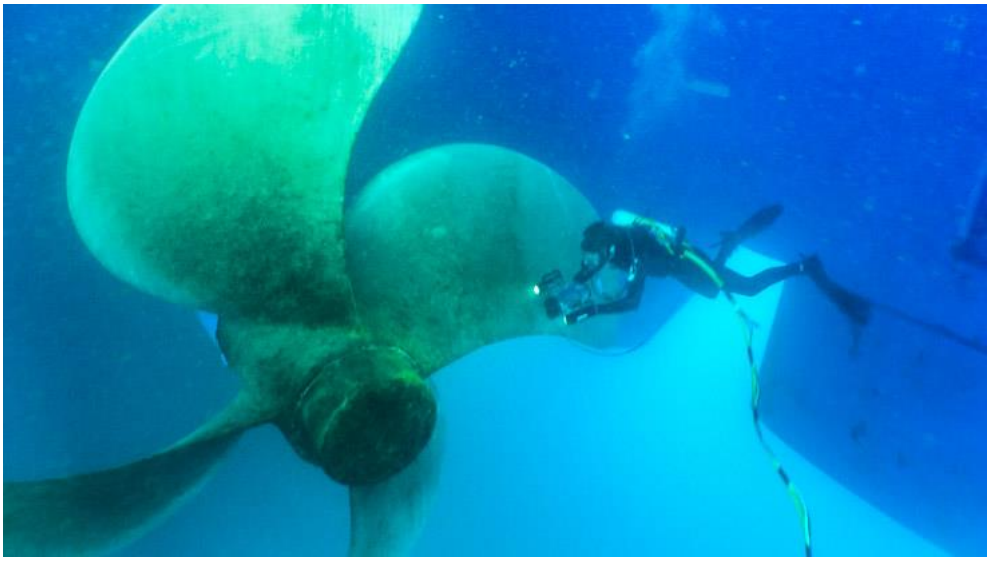

Figure 1.6 – Diver Inspects Biofouling on the propeller of a vessel *(source: Commercial Diving, 2013).*

1.1.3.1. Hull Cleaning: A Dirty Job

Hull inspections are conducted in the dry dock as a scheduled event to allow for visual inspection of the entire hull as well as removal of the unwanted biofoulers with water blasters and scrapers, and reapplication of an antifouling coating (Hopkins and Forrest, 2008; Adland *et al.*, 2018). However, between dry docking events biofouling is managed with in-water cleaning (Zabin *et al.*, 2018). Scrapping, brushing or blasting of the hull allows for simple mechanical removal by ROVs and/or divers and are the most common methods used (Hopkins and Forrest, 2008). Despite the necessity of hull cleaning, this may sometimes lead to a reduction in the antifouling coating lifetime as it may erode and damage the coatings (Holm *et al.*, 2003; Oliveira and Granhag, 2016).

Recent advances are inspired from the daily human activity of routinely brushing teeth in order to prevent the build-up of plaque. 'Hull grooming' is based on the

same principle in that an autonomous underwater vehicle (AUV) equipped with brushes is deployed to clean any biofouling on the hull (Hearin *et al.*, 2015). This method is described as a proactive, regular and gentle mechanical maintenance of the ship's hull and may reduce costs by increasing the time between dry docking events and reducing drag, fuel consumption and greenhouse gas emissions. Even with this proactive approach, it is not compatible with all coating types and the high frequency of hull grooming may not be suitable (Tribou and Swain, 2010). Furthermore, if the fouling pressure is too great or frequency too low, hull grooming no longer is accepted as a viable option to tackle biofouling (Tribou and Swain, 2015).

In-water cleaning may result in the release of live marine organisms into the water column (up to 70%) and may even lead to the release of biocides, such as copper, from the antifouling coating (Morrisey and Woods, 2015; Scianni and Georgiades, 2019). Capture and subsequent treatment or removal of the biofouling organisms by heat or ultrasonic treatment may still leave areas with biofouling hotspots due to biocide removal and lead to a low efficacy for macrofouling antifouling (Davidson *et al.*, 2008; Scianni and Georgiades, 2019).

1.1.3.2. Other Methods to Locate and Limit Biofouling

Biofouling accumulation may be defined by the effect on the ship's performance based on propeller shaft torque measurements (Foteinos *et al.*, 2017). A torque meter, based on strain gauges, is used to measure the engine power. The propeller shaft torque is calculated using engine simulation software based on an

increase in power demand (Foteinos *et al.*, 2017). Noise from wave resistance, air resistance and calm water resistance are all calculated and filtered in order to isolate the increase in resistance from biofouling. Nevertheless, with changing ship and environmental conditions small performance losses may be missed and therefore fuel penalties are being incurred (Schultz *et al.*, 2011; Logan, 2012).

Ultraviolet (UV) wavelength light is described as a possible alternative method to detect biofouling based on fluorescence properties of microorganisms that contain natural intracellular fluorophores (Pathak *et al.*, 2017). Under UV light these fluorophores radiate when excited due to three aromatic amino acids - tyrosine, phenylalanine, and tryptophan. UVC (250-280 nm) wavelengths implemented in an antifouling capacity may be able to consistently prevent biofouling (Salters and Piola, 2017). Similarly, chlorophyll may be excited in a similar manner to allow for its detection (Senger, 1995; Dring *et al.*, 1996). This method is used in remote sensing of harmful algal blooms, but possibly also in the detection of biofouling by algae and other chlorophyll containing organisms (Fischer *et al.*, 2012).

Nevertheless, there are currently no sensors available in the maritime industry to monitor *in situ* biofouling accumulation. The need for effective husbandry is immense. It may allow for a streamlined and efficient antifouling strategy, reduce the risk of transporting non-native species, reduce costs associated with increased biofouling and reduce greenhouse gas emissions from shipping.

1.2. Sensors for the Detection of Biofouling

Sensors are made in a vast array of geometries, sizes, materials and mechanisms of detection depending on their various applications (McQuade *et al.*, 2000; Beigl *et al.*, 2004; Leung *et al.*, 2006; Yang *et al.*, 2011; Gong *et al.*, 2014; Homola *et al.*, 2014). Sensors are designed to detect or measure an outcome or change and relay that information back. In the case of a sensor detecting the presence of biofouling on a surface, the sensor may be able to measure changes in flow, microwave chemistry, capacitance, ultrasonic thickness, force, optical fibre, biochemistry, electrochemical film or sonar (Lowe and Rezkallah, 1999; Nomura *et al.*, 2001; Kuoni *et al.*, 2003; Lekakou *et al.*, 2006; Sumetsky *et al.*, 2007; Feng *et al.*, 2009).

Electromagnetic planar sensors with interdigitated electrodes (IDE) are developed as a sensor with a multitude of applications from detecting lactate (Mason *et al.*, 2013) and protein binding (Salazar-Alvarez *et al.*, 2014) to glucose levels (Mason, Korostynska, *et al.*, 2013) and milk quality (Joshi *et al.*, 2017). With the wealth of applications of a planar IDE sensor using microwave frequencies, their application in the field of biofouling, particularly in the maritime industry, may be advantageous but is not yet transferred to the field. A sensor to detect the marine biofouling *in situ* may be key to streamlining and reducing the economic cost of untimely or unscheduled inspections via dry docking, limiting the risks involved for divers, allowing for efficient husbandry and curtailing the risk of the introduction of invasive species.

1.2.1. Electromagnetic Wave Planar Sensor

The interaction of propagating electromagnetic waves (EMW) is used to detect the material under test (MUT) (Frau *et al.*, 2018) (such as a biofouling organism) by measuring the reflection coefficient (R). The electromagnetic waves consist of an electric field (**E**) and a magnetic field (**B**) that oscillate in phase from one another (*figure 1.7*).

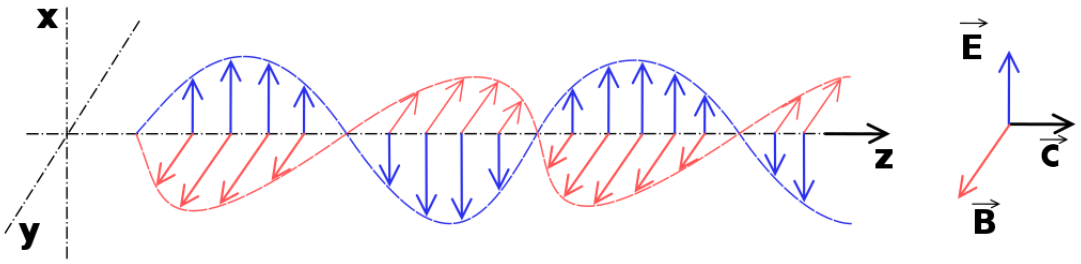

Figure 1.7 – Electromagnetic Waves *show the electric field (**E**) in blue oscillating in the **±x** direction and the magnetic field (**B**) in red oscillating in the **±y** direction as the wave propagates through **+z** in a vacuum and therefore travelling at the speed of light (**C**) (edited source: Geophysics, 2015).*

Based on the wavelength (λ), different electromagnetic waves are categorised from low frequency (f) microwaves and radio waves, to high frequency x-rays and gamma rays. Microwave and radio waves may be used to characterise materials as they are able to propagate through low-loss dielectrics and the speed of the wave (c) is impacted by the dielectric/relative permittivity (ε_r) of the material (*equation 1.1*) (Korostynska *et al.*, 2013).

$$\lambda = \frac{c}{f} = \frac{c_0}{\sqrt{\varepsilon_r}} = \frac{\lambda_0}{\sqrt{\varepsilon_r}}$$

Equation 1.1

Whereby c_0 is defined as the speed of the wave in free space and λ_0 as the wavelength in free space. *Equation 1.1* is used to highlight the effect of the relative permittivity on the wavelength. When an electromagnetic wave passes between regions with different permittivities, a reflection will occur. So seen with the reflection coefficient (*equation 1.2*) (Korostynska *et al.*, 2013).

$$R = \frac{\sqrt{\varepsilon_{r1}} - \sqrt{\varepsilon_{r2}}}{\sqrt{\varepsilon_{r1}} + \sqrt{\varepsilon_{r2}}}$$

Equation 1.2

In a parallel plate capacitor, there is an electric field between the positive and negative electrodes, and the electric field passing through the MUT is dependent on its relative permittivity; the same principle is applied to IDEs (*figure 1.8*).

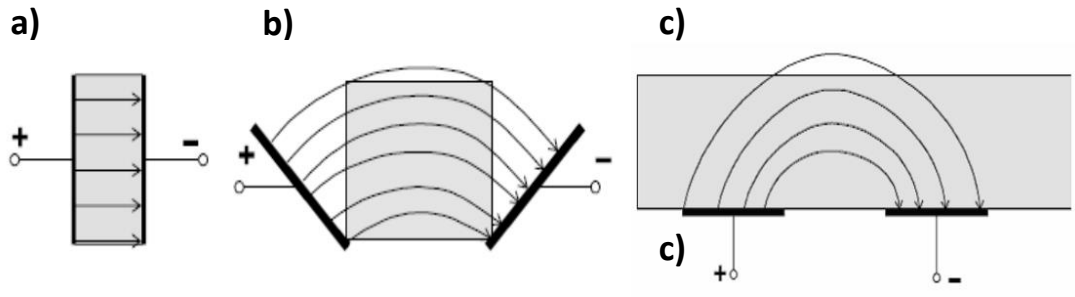

Figure 1.8 – From Parallel Plates to Coplanar IDE*. The parallel plate capacitor (**a**) development (**b**) into the final planar IDE (**c**) (source: Mukhopadhyay, 2005).*

However, a localised electric field with higher sensitivity is generated by manipulating the size of the electrodes, the space between the electrodes, the number of electrodes and the overall surface area (IDE geometry) (Mukhopadhyay, 2005). Using smaller electrodes the electric field is confined closer to the surface with 80% of the electric field and current flow between two electrodes in a layer less than L/2 (L = sum of electrode width) (*figure 1.9).*

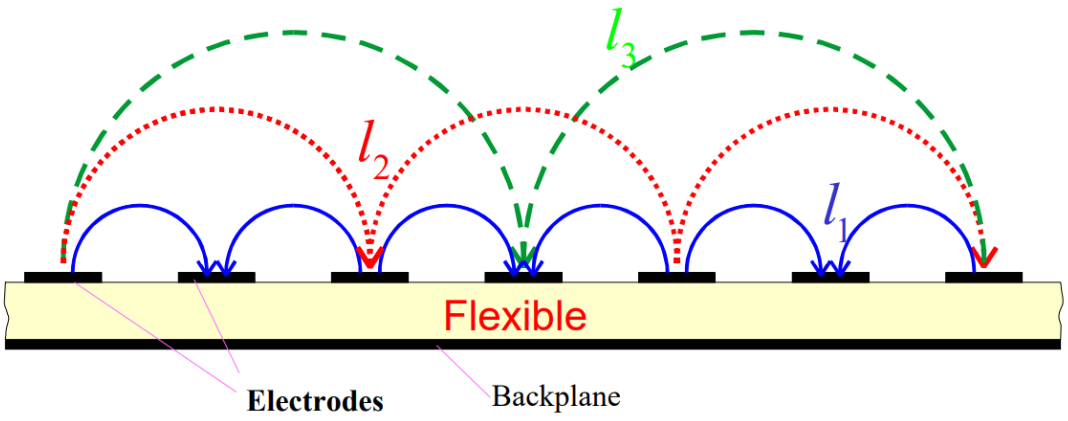

Figure 1.9 – Varying Field Heights Based on Wavelength *are shown here with three different lengths (l_1, l_2 and l_3) (source: Mukhopadhyay, 2005).*

These planar sensors are often coupled with a specific surface that interacts with the target, such as protein binding sites or chemical coatings for a detectable change (McQuade *et al.*, 2000; Homola *et al.*, 2014; Frau *et al.*, 2017). These antennas may also act as an acoustic wave sensor whereby a physical change is detected when the electric field is disturbed causing a measurable change in the signal amplitude and/or phase, as seen in the detectable changes in algae concentrations in solution (Moejes *et al.*, 2018). Furthermore, smaller dimensions of electrodes and interdigitated gaps are found to result in increased redox cycling efficiency, and an increase in the number and width of electrode fingers results

in an increased signal (Grover, 1999). A vector network analyser (VNA) is used to generate a signal and then measures the reflection coefficient expressed as scattering parameters, S-parameters, by measuring both the amplitude and phase (Mason *et al.*, 2013).

The vast applications of sensors based on low frequency microwave and radio waves is in part due to their ability to travel in guided wave structures, propagate through materials and demonstrate measurable amplitude and phase upon interaction with the MUT (Baker-Jarvis and Kim, 2012). Coupled with an IDE pattern that allows for localised and sensitive detection, a non-species-specific sensor may show the benefit of detecting the presence of any biofilm, biofoulant and non-organic material. Application of these novel sensors in the maritime industry may allow for biofouling to be specifically located without the risks and costs associated with divers, ROVS or dry docking for the identification and removal of biofouling (Townsin, 2003; Hopkins and Forrest, 2008; Floerl and Coutts, 2013). By detecting where biofouling has occurred, ships can have targeted, regular, and more gentle cleaning, likely reducing the need for toxic antifouling paints and better preserving the longevity of foul-release coatings (Holm *et al.*, 2003). Potentially, by obtaining *in situ* and up-to-date biofouling information of the hull, ships will be able to do a cost—benefit analysis in order to determine when the cost of excess fuel consumption outweighs the cost of getting the ship cleaned. Moreover, it is likely that by implementing better biofouling management strategies (targeted, regular cleaning), the increase in surface roughness associated with biofouling will be reduced and therefore, so

will the excess fuel consumption, engine stress, cost and greenhouse gas emissions (Abbott *et al.*, 2000; Hellio and Yebra, 2009; Bixler and Bhushan, 2012). Furthermore, sensors on the vessels hull, ballast tank or niche areas may allow for better biofouling management that in turn reduces the danger of introducing non-native and/or invasive species as well reduce corrosive damage to the vessel by biofouling organisms (Davidson *et al.*, 2009; Edyvean, 2010; Lewis and Coutts, 2010). In order for research to begin on such a sensor to detect biofouling in the maritime industry, a single model organism must be selected for initial sensor development.

1.3. *Mytilus edulis*: A Model Species

The model biofouling organism *M. edulis* is one of the most dominant and problem biofouling species in temperate regions worldwide (Dürr and Wahl, 2004). The species is able to dominate and monopolise new substrata, thus reducing species diversity (Dürr and Wahl, 2004). Some reasons thought to be behind their biofouling success include their rapid growth rate, high fecundity and wide ecological tolerance (Wilkens *et al.*, 2012). Known also as the common blue mussel, their roughly triangular outline shell may come in several colours from blues and purples to browns, and they are usually between 5 to 10 centimetres in length (Tyler-Walters, 2008). The depth ranges for these equivalve bivalves from the intertidal to up to 5 metres depth, where they adhere to the surface with their thread-like byssus in densely packed fouling communities (*figure 1.10*).

Figure 1.10 – Mytilus edulis *fouling on an intertidal rock face (**a**) and an individual common blue mussel (**b**) (source: Marine Stewardship Council, 2019; Trepte, 2019).*

M. edulis is able to live in exposed and sheltered regions as densely packed beds with an associated biofouling community (Seed and Suchanek, 1992). During succession a dynamic microhabitat for a diverse community showing an associated increase in species richness diversity. Some species such as barnacles are shown to exhibit an increased growth rate due to improved filter-feeding and decrease of predation when settled on live *M. edulis* with no impact on the mussel growth rate (Laihonen and Furman, 1986). Conversely, other studies demonstrated that the presence of epibiotic barnacles on mussels resulted in increased predation from the shore crab *Carcinus maenas,* which may in turn interfere with mussel filtering (Wahl *et al.*, 1997; Enderlein, 2000; Enderlein *et al.*, 2003).

In some regions *M. edulis* is known to spawn in the spring and again in the late summer (Chipperfield, 1953; Dare and Edwards, 1975). Larval development under optimal conditions is set to occur in under 20 days with metamorphosis setting in from 20 to 40 days usually (Pechenik *et al.*, 1990; Widdows, 1991). The free-swimming pediveliger stage is able to use its foot to find and settle on a filamentous substrate and avoid large, filter-feeding adults. This initial settlement of the pediveliger stage, known as a spatfall, allows for growth and metamorphosis before moving to the secondary adult substrata (Davies, 1974; Wang and Widdows, 1991; Filgueira *et al.*, 2014). Recruitment onto these adult substrata is known to be usually sporadic and difficult to predict, however, their importance in the development of these dense mussel beds are a vital ecosystem in itself.

M. edulis is able to adhere to a wide range of surface types with the secretion of adhesive byssi to anchor to substrata allowing for their biofouling persistence and semi-mobility (Waite and Tanzer, 1981; Silverman and Roberto, 2007) (*figure 1.11*). As a well-studied organism, and its important role in biofouling communities, *M. edulis* is pre-selected as a necessary and ideal model organism for research.

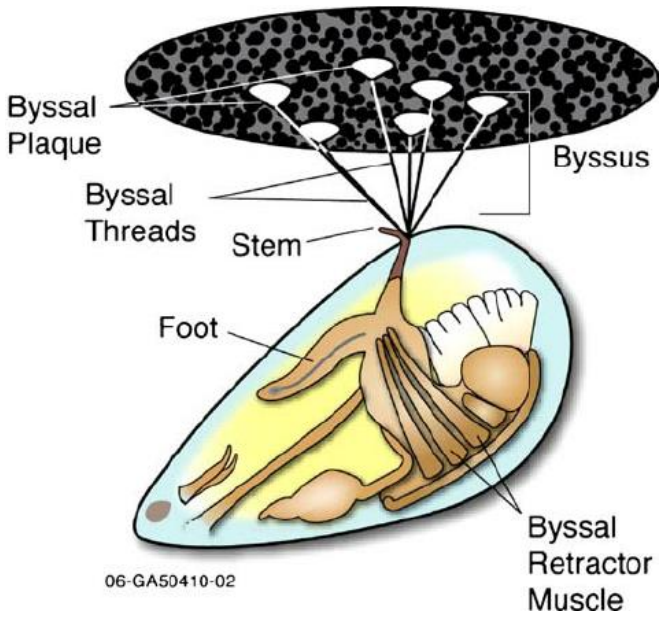

Figure 1.11 – Mytilus edulis Anatomy *(source: Silverman and Roberto, 2007)**.***

1.3.1. Structure and Formation of *M. edulis* Byssus Thread and Plaque

From the exocrine glands in the foot of *M. edulis*, a series of byssal threads are produced, which contain up to 10 specialised adhesive protein types, collagen, polyphenol oxidase and proximal thread matrix protein (Silverman and Roberto, 2007) (*figure 1.12*).

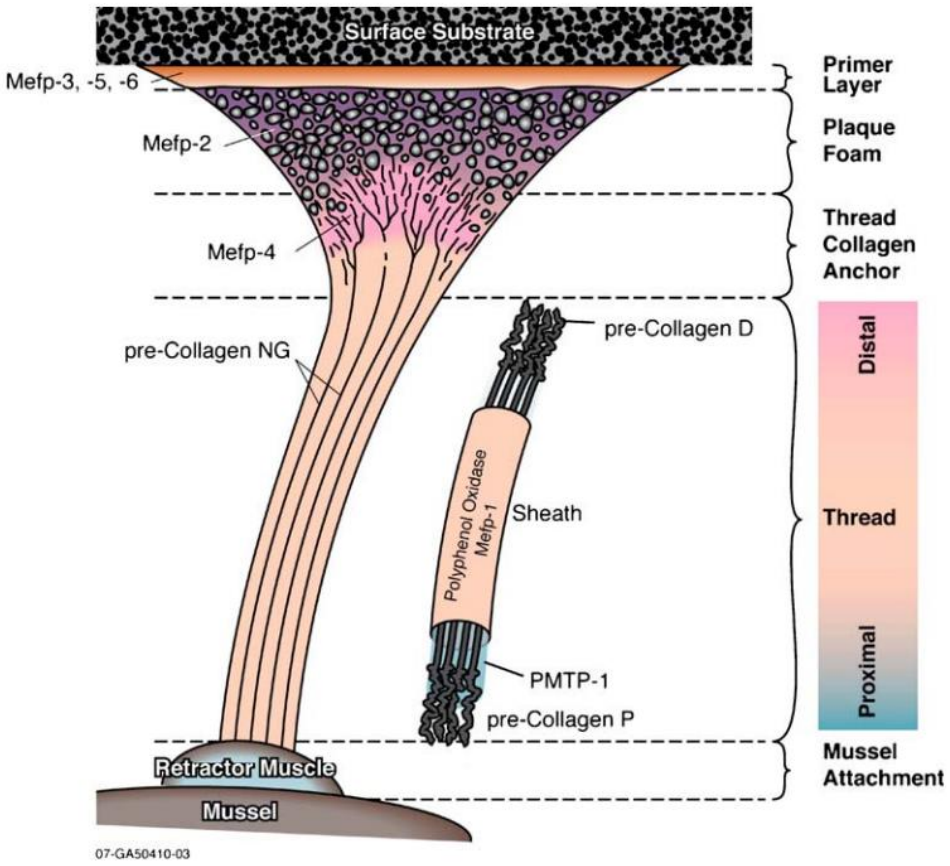

Figure 1.12 – Mytilus edulis Byssus *highlighting the protein composition and structure of the byssus thread and plaque (source: Silverman and Roberto, 2007).*

These proteins are deposited along the ventral groove by the mussel foot whereby it presses against the substrata creating a secure perimeter before cavitation occurs, generating a negative pressure suction for temporary adhesion and the release of adhesive proteins (Tamarin and Keller, 1972). In this cavitation, *M. edulis* is able to prepare the surface for adhesion whereby the pH and ionic state are altered from marine conditions, pH 8 and 0.7 mol l^{-1} ionic strength, and lowered to an average pH 5.5 and 0.15 mol l^{-1} ionic strength (Yu *et al.*, 2012). The reason for acidification in the cavitation is not fully understood, but it is hypothesised to essentially clean the surface, activate biochemical groups, regulate the redox environment and for protein control. At this stage the proteins

are secreted by the mussel foot from the distal to the proximal, starting with proteins such as *Mytilus edulis* foot protein - 3 (Mefp-3) and Mefp-5 that undergo condensation to form coacervates (mixing of two polyelectrolytes at a pH whereby they neutralize each other) (Zhao *et al.*, 2016). Cross-linking of proteins in order to solidify the byssal plaque is proposed as one mechanism; however, another is phase inversion where discontinuous water becomes dispersed within continuous coacervates. The secrete is solidified into a load-bearing porous substance (*figure 1.13*).

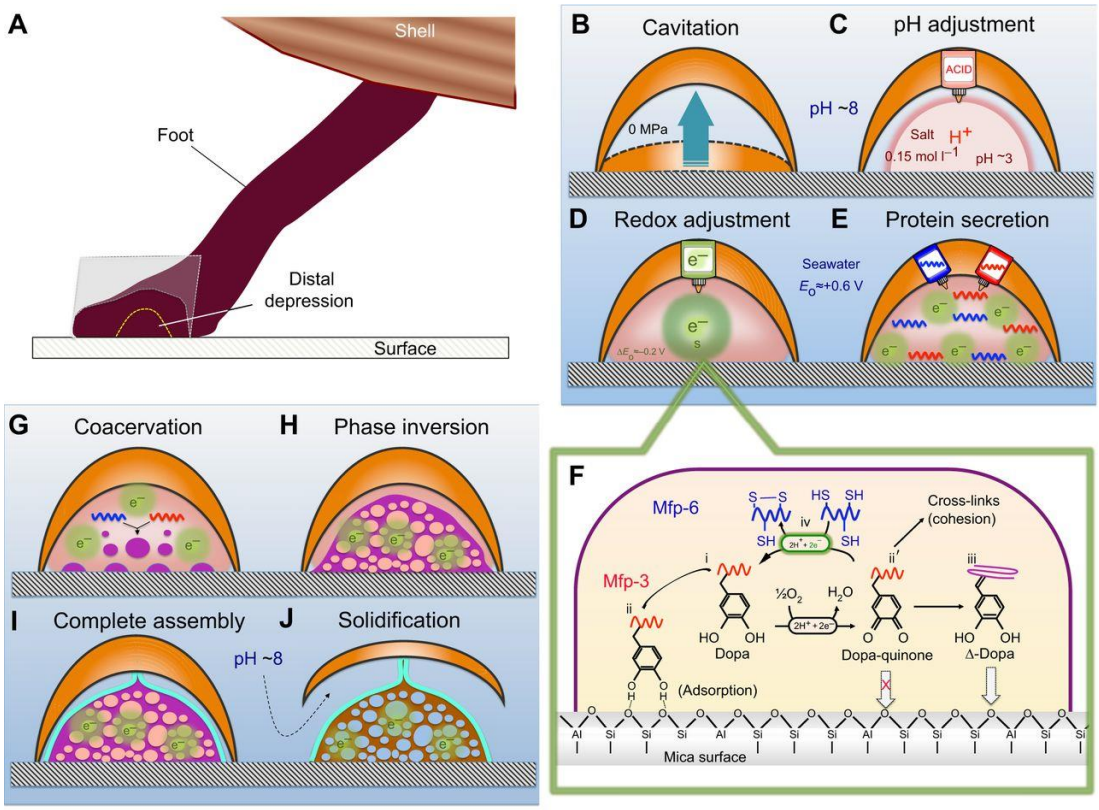

Figure 1.13 – Mussel Plaque Protein Deposition. *The foot first pushes against the surface creating a secure perimeter where cavitation occurs (**a**). At this point changes in pH and ionic strength allow for protein secretion (**B-E**) of DOPA rich proteins (**F**). Condensation of these proteins forms coacervates that undergo phase inversion and solidification into a load-bearing porous material (**G-J**) (source: Waite, 2017).*

The *M. edulis* foot proteins (Mefp 1-5) are known to contain varying concentrations of 3,4-dihydroxyl-L-phenylalanine (L-DOPA) with distal Mefp-3 and Mefp-5 containing the highest concentrations at 21 mol % and 27 mol %, respectively (Papov *et al.*, 1995; Waite and Qin, 2001; Silverman and Roberto, 2007). Further stabilisation of the byssus plaque is explained with cross-linking between adhesive scleroproteins. Oxidation of DOPA to DOPA-quinone by a catechol oxidase is preceded by posttranslational modification of tyrosine to DOPA by hydroxylation with a polyphenoloxidase (tyrosinase) (*figure 1.14*).

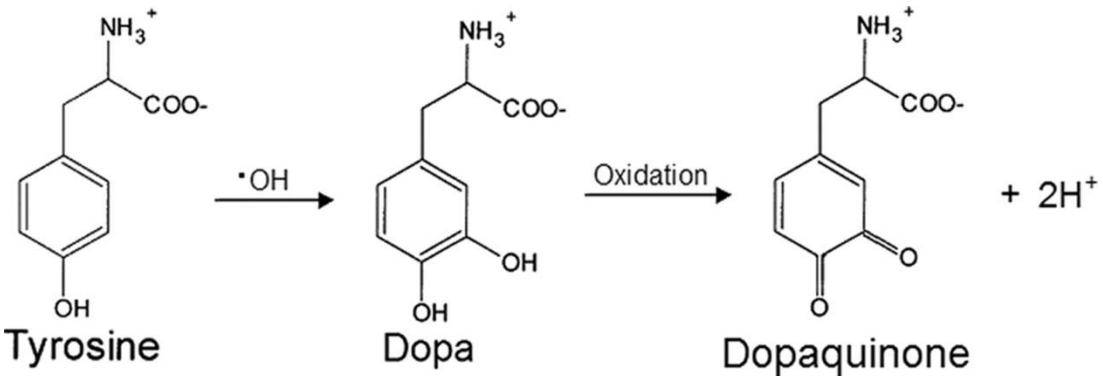

Figure 1.14 – Hydroxylation of Tyrosine to DOPA and Oxidation of DOPA to DOPA-quinone *(source: Zhang et al., 2010)**.***

Further strengthening via cross-linking of the adhesive proteins form an intermolecular bridge of aryl-aryl coupling of aryloxy radicals (di-DOPA formation) or via tyrosinase-induced Michael-type addition reactions (Aldred *et al.*, 2006; Horsch *et al.*, 2018). Furthermore, these cross-links are shown to increase under higher seawater flow around the byssus threads highlighting their importance in the ability for *M. edulis* to thrive within the hydrodynamic stress of their environment (McDowell *et al.*, 1999; Sun *et al.*, 2001). These cross-linking reactions are thought to be vital for solidification of the mussel adhesive glue and

may explain the gradient nature of the byssal thread from the more flexible proximal region towards the stiffer distal region (Brazee and Carrington, 2006). The stiffer distal region with a high number of crosslinks is explained with the repetitive nature of these proteins, particularly Mefp-1. As the first identified and most studied of the *M. edulis* byssi polyphenolic proteins, Mefp-1 is a large hydrophilic protein with 897 amino acids, a molecular mass of 115 kDa and a poorly defined secondary structure, likely resembling a random coil with a self-avoiding random conformation with helix-like decapeptide segments (Haemers *et al.*, 2005; Silverman and Roberto, 2007). The numerous repeating hexapeptide and decapeptide repeat domains, with 60-70% posttranslational hydroxylation modification, were found to contain an amino acid sequence of AKPTYK and AKPSYP'P"TYK, respectively (Y denotes DOPA, P' denotes trans-2,3- cis-3,4-dihydroxyproline and P" represents trans-4- hydroxy-L-proline) (Silverman and Roberto, 2007). The lack of a defined secondary structure may allow for the functional groups to be available for cross-linking to increase cohesion and for adherence to a multitude of the surfaces including Teflon™. Furthermore, DOPA complexes with both metal ions and oxides, such as iron (Fe^{3+}) and semimetals, such as silicon, are utilised to adhere to rocks and glass (*figure 1.15*) (Silverman and Roberto, 2007).

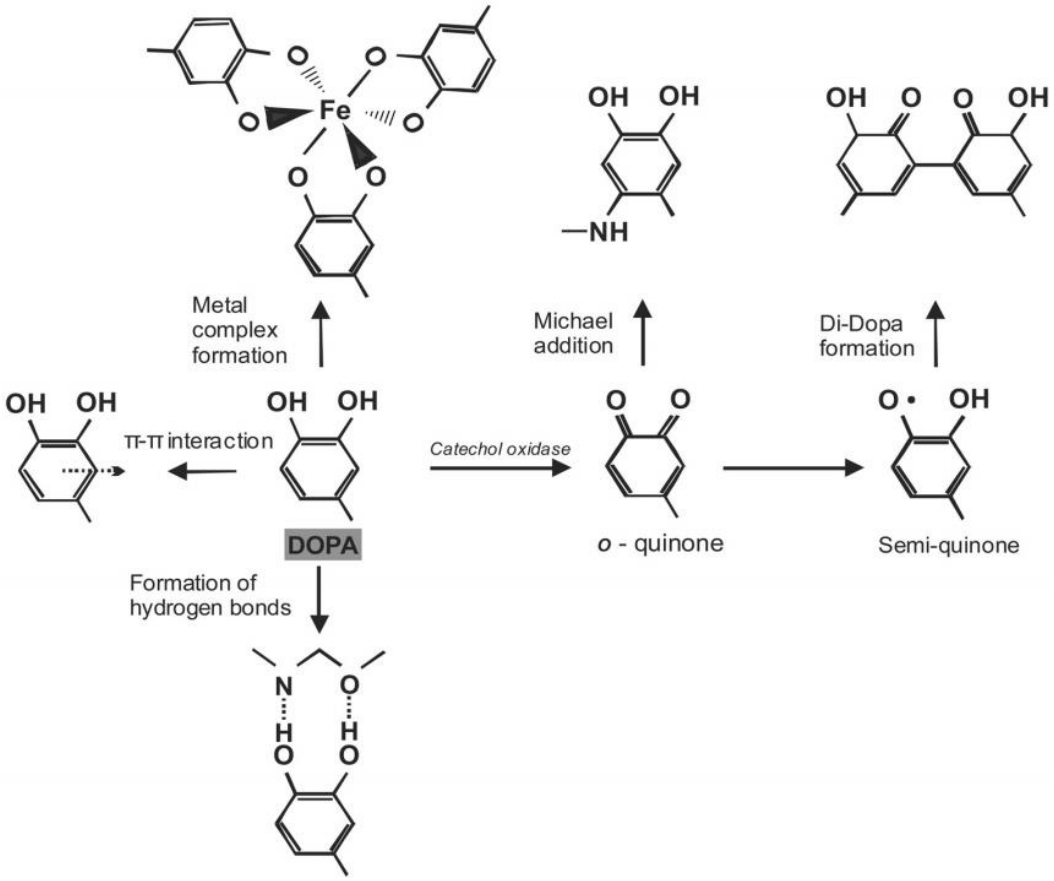

Figure 1.15 – DOPA Mussel Adhesion and Cross-linking*. DOPA is able to form complexes with metals, the catechol side chains may form hydrogen bonds with hydrophilic polymers and form a non-covalent bond with an aromatic group (source: Wiegemann, 2005).*

Depending on the properties of the attachment surface, adhesive protein expression may be determined and matched to the properties of the surface (Vreeland *et al.*, 1998; Warner and Waite, 1999). Young and Crisp (1981) showed that byssal plaque is spread further and with lower tenacity on low-energy, hydrophobic surfaces. The surface energy is deemed by some to be the most important physical and chemical characteristic of the surface on mussel adhesion (Callow and Fletcher, 1994). The contacts between the substrate surface and the water allows for non-covalent interactions such as Van der Waals forces,

hydrogen bonds and electrostatic interactions. Therefore, the mussel is thought to overcome these forces in order to adhere to the surface (*equation 1.3*) (Callow and Fletcher, 1994).

$$W_{sl} = \gamma_s + \gamma_l - \gamma_{sl}$$

Equation 1.3

Whereby the work of adhesion (W_{sl}) is based on the work necessary to disrupt these interactions and is therefore equivalent to the sum of the surface free energy of the solid (γ_s) and the surface tension of the liquid (γ_l) minus the interfacial tension between the two (γ_{sl}) (Callow and Fletcher, 1994). The equation highlights that a lower surface energy will result in a weaker adhesion. This preference was shown in paired preference assays demonstrating an affinity for slate over glass and an affinity for glass over paraffin wax (Crisp *et al.*, 1985). Not only was there a difference in the number of byssi put down, but also in their appearance; plaques on polar, high-energy surfaces had a reduced contact angle θ compared to those with low energy surfaces as explained with the *equation 1.3*. However, the work by Crisp *et al.,* (1985) did not consider other material variabilities such as modulus or polarity (Aldred *et al.*, 2006). More recently, Aldred *et al.,* (2006) showed a positive correlation between the plaque spreading and an increased wettability as well as a faster attachment to a hydrophilic surface. Similarly, topography was shown to be a key factor in the settlement of various sessile organisms depending on the topographic features of width, spacing, height, geometry, roughness and distinct surface features (Berntsson *et*

al., 2000a; Chung *et al.*, 2007; Cooper *et al.*, 2011). These changes in topography may either increase or decrease their settlement and adhesion on a surface (Carl *et al.*, 2012). Investigating the effect of topography may allow for further understanding of settlement and adhesion mechanisms of biofouling organisms as well as possible development of a non-toxic antifouling surface.

1.4. Microtopography Antifouling Surface

Despite biofouling being known to commence within minutes on a submerged solid surface (living or dead) by sessile organisms (Wahl, 1989; Callow and Callow, 2002; Dürr and Wahl, 2004; Dürr and Watson, 2010), there are naturally occurring microtopographies that face similar biofouling pressure yet remain unfouled (Scardino *et al.*, 2003; Bers and Wahl, 2004). This naturally low fouling ability is seen particularly in crabs (e.g. *Cancer pagurus*), mussels (e.g. *M. edulis*, *M. galloprovinvialis*) and sharks (e.g. *Carcharhinus brevipinna, C. galapagensis*) (Scardino and De Nys, 2004; Scardino and de Nys, 2011). The micro- and macroscale topography of the *C. pagurus* carapace consists of smaller spicules/microtrichia (MT) that surround larger endocuticular bulges (EB) (Sullivan *et al.*, 2014) (*figure 1.16*).

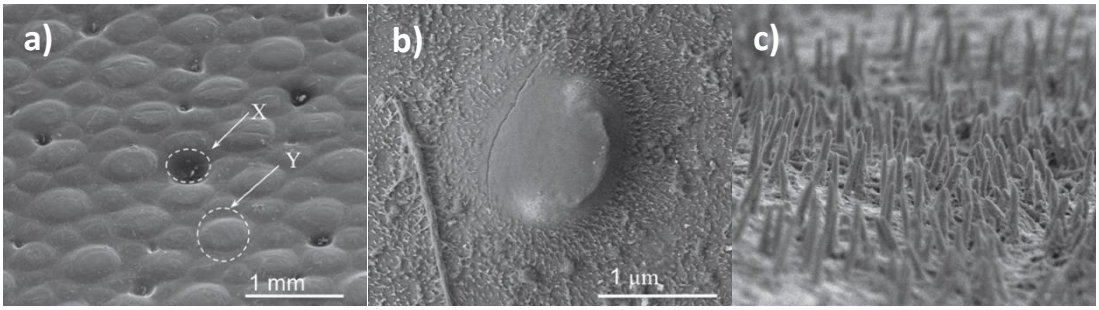

Figure 1.16 – Scanning Electron Microscopy (SEM) of C. pagurus Carapace Microtopography *whereby the raised endocuticular bulges (EB) are shown (Y, arrowed) as well as occasional pits with sensory setae (X, arrowed) (**a**). The EB is shown surrounded by microtrichia (MT) (**b**), whose distribution is shown in more detail on the dorsal surface of the carapace (**c**) (source: Sullivan et al., 2014).*

When exposed to a marine environment, the EB topographic features of the *C. pagurus* carapace facilitate in the reduction of diatom settlement and even

though they may be commonly found on the MT, the diatom settlement occurs between the topographic features or bridged across them (Sullivan *et al.*, 2014). It is therefore thought that a reduced contact area between the diatoms and the surface topography of the carapace may allow for increased removal rate with hydrodynamic forces. Resin replicates of the *C. pagurus* carapace microtopography immersed in a marine environment show a significant reduction in the recruitment of *Balanus improvisus* barnacle cyprids, however, it does not show an effect on *M. edulis* larvae or the ciliate *Zoothamnium commune* (Bers and Wahl, 2004).

Similarly, the natural ripple microtopography of the *M. edulis* shell, together with an intact periostracum, demonstrates antifouling efficacy (Wahl *et al.*, 1998) (*figure 1.17*).

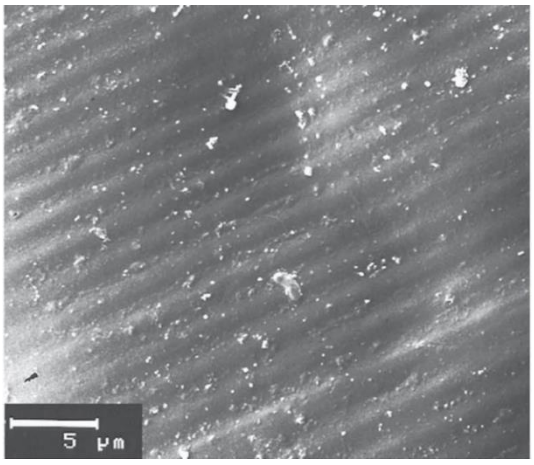

Figure 1.17 – SEM of Mytilus edulis Periostracum Microtopography *showing ripples (source: Bers and Wahl, 2004).*

The presence of a chemical defence system of the periostracum alone shows a reduction in attachment of marine bacteria (*Cobetia marina* and *Marinobacter hydrocarbonoclasticus*), diatoms (*Amphora coffeaeformis)* and barnacle cyprids

(*Balanus amphitrite)* (Bers *et al.*, 2006). Nevertheless, resin replicates of the *M. edulis* surface microtopography immersed in a marine environment demonstrate a significant reduction in the initial recruitment of *B. improvisus* cyprids, however this effect was not sustained, and in week 4 of the study there was a significant attractive effect (Bers and Wahl, 2004).

Replication of these naturally occurring antifouling microtopographies does not always follow the natural antifouling success (Salta *et al.*, 2010), however, research into microtopographies as an antifoulant is developing with inspiration being taken from nature (bioinspiration or biomimicry). Most notably is the recently patented Sharklet™ (Brennan *et al*., 2010; patent: US 20100126404), a microtopography that may prevent bacterial colonisation and therefore infection in the medical field (Mann *et al*., 2014) as well as having been evaluated as an antifoulant (Salta *et al.*, 2010) (*figure 1.18*).

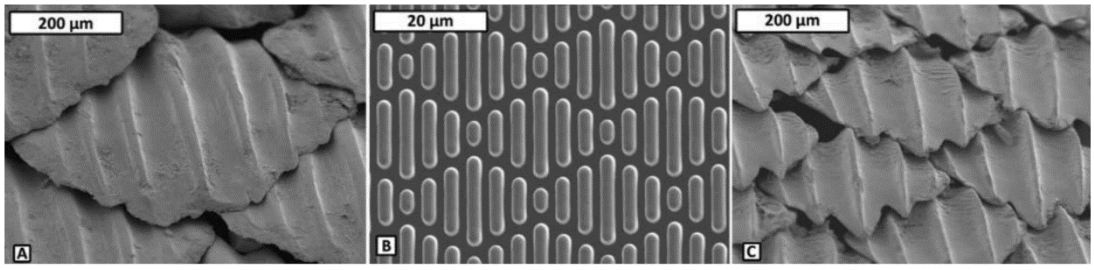

Figure 1.18 – Biomimicry of Sharkskin *showing the spinner shark (C. brevipinna) (**a**) and the Galapagos shark (C. galapagensis) (**c**) in reference to the fabricated Sharklet™ film (**b**) (source: Scardino and de Nys, 2011).*

Sharklet™ is shown to reduce settlement of *Ulva* zoospores (Schumacher *et al.*, 2007; Magin *et al.*, 2010), barnacle cyprids (*B. amphitrite*) (Schumacher *et al.*, 2007), and bacteria *C. marina* (Magin *et al.*, 2010) and *Staphylococcus aureus*

(Chung *et al.*, 2007; Cooper *et al.*, 2011). Furthermore, this shark inspired microtopography exhibits a reduction in drag of 5 to 10% which may further be beneficially for a future antifouling microtopography within the maritime industry (Bechert and Bartenwerfer, 1989; Bechert *et al.*, 1997; Salta *et al.*, 2010; Pu *et al.*, 2016; Chen *et al.*, 2018; Lee *et al.*, 2020).

1.4.1. Microtopography Antifouling Mechanisms of Action

The reduced ability for settlement is related to the size scale of the topography being slightly smaller than the size of the spore/larvae reducing the available contact area and making it so that the single topographic feature cannot support the entire mass (Salta *et al.*, 2010; Carl *et al.*, 2012). Conversely, a topography slightly larger is known to increase settlement as it provides more points of contact and refuge from hydrodynamic stress (Callow *et al.*, 2002). Therefore this antifouling approach is based on the behaviour of marine sessile organisms towards their place of final settlement as they show species-specific surface preferences towards factors such as the chemistry and physical properties (Prendergast, 2010) and is likely based on the number of attachment points on the topography (Attachment Point Theory; Scardino *et al.*, 2008). This is further supported by the increased attachment seen on smooth surfaces when compared to a topography with a slightly smaller scale (*figure 1.19*).

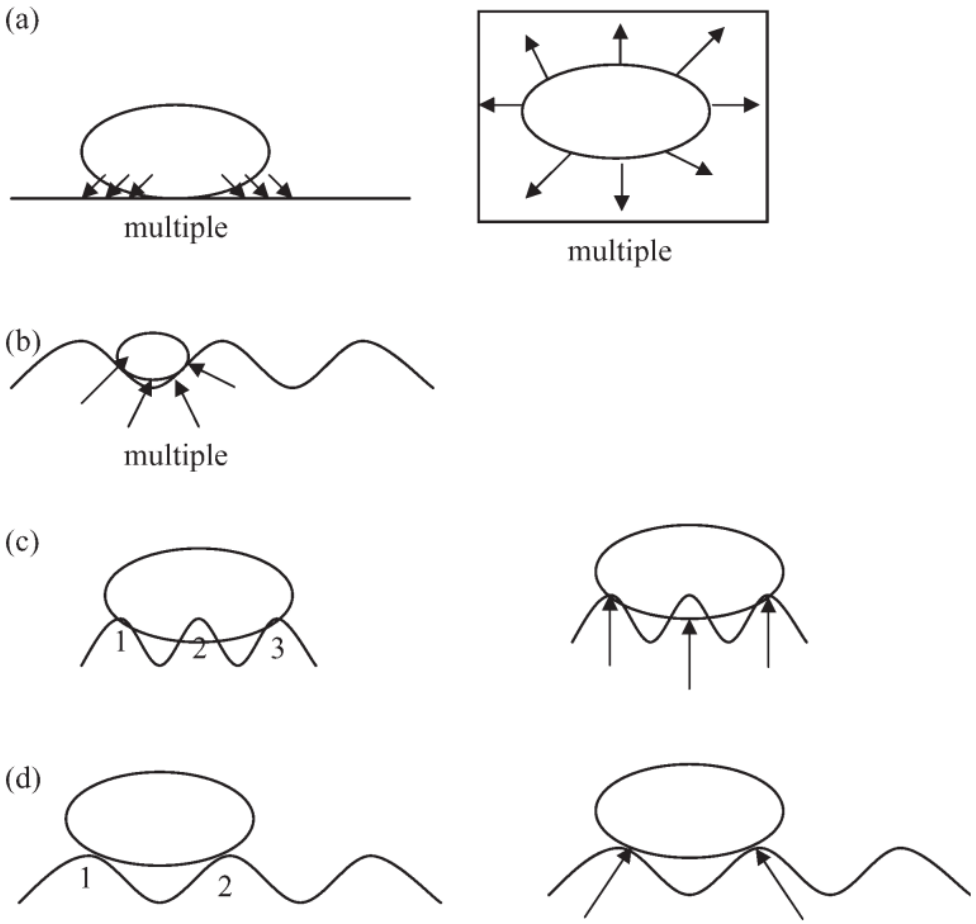

Figure 1.19 – Attachment Point Theory. *On a smooth surface, there are multiple attachment point available for any diatom (**a**). Species-specific example show F. carpentariae on 2 µm ripples with multiple attachment points (**b**), N. jeffreyi on 2 µm ripples with 3 attachment points (**c**) and Amphora sp. on 4 µm ripples with 2 attachment points (**d**) (source: Scardino et al., 2006).*

The Attachment Point Theory is demonstrated *in situ* in a study with greatly reduced settlement of fouling organisms such as the cyprids of the barnacle *Balanus improvisus* of 92% with microtopographic features of 30 to 45 µm height and 150 to 200 µm in width when compared to a smooth control (Berntsson *et al.*, 2000b). This was further reduced by 98% with PVC riblets of 350 µm height and 134 µm width (Berntsson *et al.*, 2000a).

Microtopography may lead to a change in the wettability of the surface that also may be responsible for the reduction in settlement and attachment (Carman *et al.*, 2006). Wettability is based on a balance of adhesive and cohesive forces and is generally described in terms of the contact angle θ (Choi *et al.*, 2002). A low contact angle (below 90°) signifies a favourable wetting surface as the droplet spreads and is termed a hydrophilic surface (Tylkowski and Tsibranska, 2015; Hebbar *et al.*, 2017). Conversely a contact angle greater than 90° indicates a hydrophobic surface (*figure 1.20*).

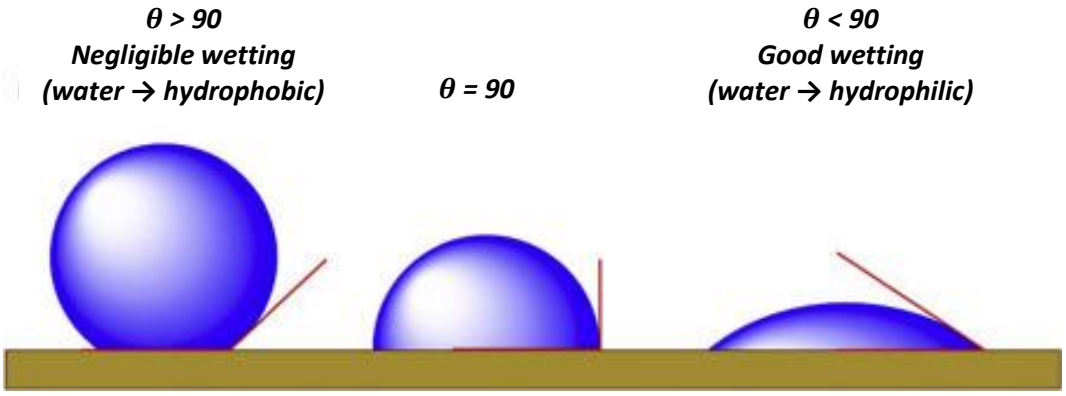

Figure 1.20 – Schematic Demonstrating Contact Angles on Solid Surfaces *whereby a hydrophobic, low energy surface exhibits a contact angle above 90° with little wetting, and a hydrophilic, high energy surface displays a contact angle below 90° with good wetting (source: Hebbar et al., 2017).*

Young's equation describes the three-phase contact angle of the solid, liquid and vapour/gas for an ideal surface that is flat, inert, nonporous, smooth, homogenous, insoluble and rigid (Carman *et al.*, 2006; Tylkowski and Tsibranska, 2015; Hebbar *et al.*, 2017) (*equation 1.4*).

$$\gamma_{SG} = \gamma_{SL} + \gamma_{LG} \cos \theta$$

Equation 1.4

Whereby γ_{SG} is the solid-gas surface energy, γ_{SL} is the solid-liquid surface energy and γ_{LG} is the liquid-gas surface energy. However, this ideal situation is not widely applicable as solid surfaces tend to be rough which can in turn impact the wettability and therefore the equation was modified (Tylkowski and Tsibranska, 2015). Wenzel (1936) assumed that the resultant contact angle $(\cos \theta_W^*)$ changed with topography or roughness (r) due to the increased surface area where the water followed the contours for homogenous wetting (*equation 1.5*) (Carman *et al.*, 2006).

$$\cos \theta_W^* = r \cos \theta$$

Equation 1.5

Further to this, Cassie and Baxter (1944) proposed that wetting on porous waxy surfaces is shown to change the behaviour of water as it does not follow the contours, but rather sits upon a structure of wax and air (*equation 1.6*) (Carman *et al.*, 2006).

$$\cos\theta_C^* = f_1 \cos \theta - f_2$$

Equation 1.6

Whereby f_1 and f_2 denote the ratio of the area of liquid beneath the drop that is in contact with the solid surface and the air, respectively, and the resultant contact angle is $\cos\theta_C^*$ (Carman *et al.*, 2006). These may be impacted by the surface tensions resulting in air entrapment for high-energy surfaces, fully wetted for moderate surface energy and wicking in surfaces with a low energy (*figure 1.21*).

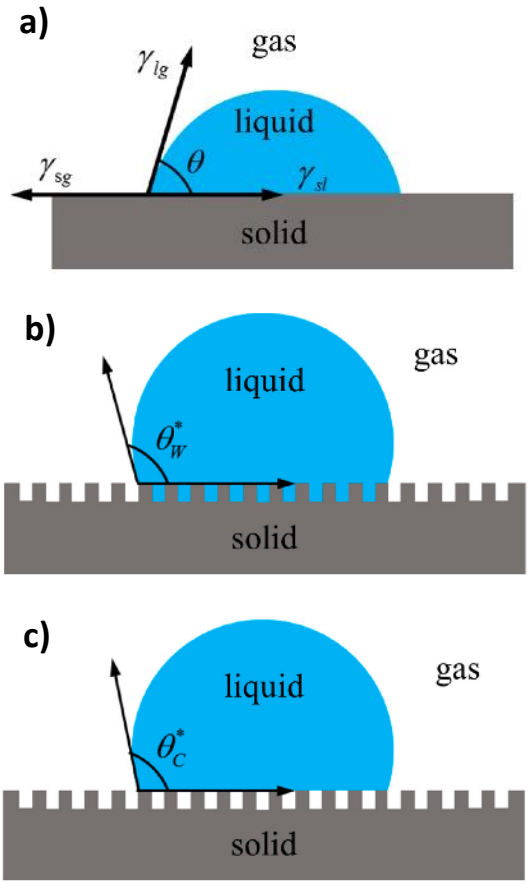

Figure 1.21 – Wetting Models *demonstrating Young's theory (**a**), Wenzel's theory (**b**) and the Cassie-Baxter theory on contact angles (**c**) (source: Han et al., 2019).*

Wetting transition from Cassie-Baxter to Wenzel state on a rough hydrophobic surface can occur due to stability of the wetting state based on the free energy or external stimuli (e.g. vibrations), however, it is the presence and maintenance of the Cassie-Baxter state that is important for superhydrophobic surfaces (contact

angle greater than 150°) which are dependent on the intrinsic hydrophobicity and the surface roughness (Hao and Wang, 2016; Nosonovsky and Bhushan, 2016; Zhang *et al.*, 2019).

Biofouling attachment on a microtopography may occur between the topographic features, not unlike Wenzel's theory, or across them, resembling Cassie-Baxter theory on wetting. This may in turn impact the number of attachment points and therefore may result in less biofouling settlement as well as a reduced adhesion strength for an effective antifouling surface (Berntsson *et al.*, 2000*a*; Berntsson *et al.*, 2000*b*; Callow *et al.*, 2002; Scardino *et al.*, 2006).

Research into the impact of surface properties including wettability, surface energy and topography has remained focused on microfouling algae and bacteria, and macrofouling spores and larvae (Chung *et al.*, 2007; Schumacher *et al.*, 2007; Magin *et al.*, 2010; Cooper *et al.*, 2011; Carl *et al.*, 2012). There is a gap in the literature on the possible use of topography as a non-toxic antifouling solution for adult semi-sessile macrofoulers such as *M. edulis* despite their immense economic and environmental impact.

1.5. Thesis Aims

The maritime industry is in need of an efficient biofouling monitoring system and antifouling solution that lies within the constraints set out by the International Maritime Organisation (IMO). Application of bioinspired microtopographies, as well as other engineered microtopographies, as an antifouling technology may offer an alternative to toxic TBT, copper, biocides, or the additive oils (e.g. silicone oils) found in some FRCs (Abbott *et al.*, 2000; Rittschof, 2000; Nendza, 2007; Brooks and Waldock, 2009; European Union, 2012; Bressy and Lejars, 2014; International maritime organistaion, 2016). As the shipping industry continues to be an integral part of the global supply chain, responsible for over 90% of trade (Kosowska-Stamirowska *et al.*, 2016), the IMO estimates that there could be an increase in greenhouse gas emissions of 50% to 250% in 2050, from 796 million tonnes of CO_2 in 2012 (International Maritime Organistaion, 2015). An appropriate antifouling technology could help save millions of tonnes of these potential greenhouse gas emissions and over an estimated US$150 billion per annum by 2020 (Hellio and Yebra, 2009). The possibility of considerable environmental and economic savings from an effective antifouling technology, both as an antifoulant as well as a hydrodynamically effective surface (Howell and Behrends, 2006) may be possible with the development of antifouling microtopographies. These benefits can be expanded with the development of a novel and bespoke sensor to detect biofouling which may allow for it to be specifically located and removed, particularly in niche areas which pose the risk of introducing non-native and/or invasive species (Davidson *et al.*, 2009; Lewis

and Coutts, 2010). Furthermore, regular, and targeted cleaning may reduce the surface roughness of the hull associated with biofouling build-up which in turn may decrease drag and therefore decrease excess fuel consumption and greenhouse gas emissions (Abbott *et al.*, 2000; Hellio and Yebra, 2009; Bixler and Bhushan, 2012).

This study aims to address the significant global industrial problem of biofouling in the maritime sector, by developing a bespoke sensory surface to monitor *in situ* biofouling in real-time and demonstrating its use synergistically with a novel non-toxic antifouling technology developed with laser microtexturing. The first step towards addressing this was with the development of a sensor to detect *M. edulis* plaque on a surface (Chapter 2). This was then followed by the development of an antifouling and foul-release microtopography (Chapter 3) and the finally, integrating these two research aspects to generate a prototype sensory surface for *in situ* testing (Chapter 4). The implications of this research is then considered in a general discussion (Chapter 5).

1.5.1. Chapter 2 – Detection of *M. edulis* on a Surface

In order to develop a sensor to detect *M. edulis* biofouling on a surface, varying EMW sensor geometries were to be investigated and therefore, the **first aim of the study was to determine the efficacy of *M. edulis* detection depending on the geometry and number of IDEs of the planar EMW sensor, *in vitro***. Once an appropriate sensor was determined, further testing was necessary to address the **second aim of the study to determine if the efficacy of the sensor was impacted**

by the orientation, *in vitro*. Once the efficacy of the sensor was determined, the **final aim was to determine the efficacy of the sensor when detecting *M. edulis* plaque on differing materials based on wettability and relative permittivity, *in vitro*.** The EMW are impacted not only by the properties of *M. edulis* byssal plaque, but also by the properties of the surface material, which may enhance or diminish the sensing efficacy of the sensor.

1.5.2. Chapter 3 – Development of a Non-Toxic Antifouling and Foul-Release Surface

The second part of the project addresses the need for a non-toxic antifouling solution for the maritime industry that **aims to develop a microtopography pattern on stainless steel dependant on the hatch spacing and speed of an SPI nanosecond pulsed fibre laser and transfer of the microtopography to a silicone surface, *in vitro***. Once the textured panels were successfully developed, the **second aim was to determine the efficacy of the microtopography on silicone as an antifouling, foul-release surface towards *M. edulis* attachment, *in vitro*.**

1.5.3. Chapter 4 – Efficacy Testing of the Antifouling and Foul-Release Sensory Surface *in situ*

By bringing the sensor and the microtopography aspect of the research together, the **final aim of the study was to determine the efficacy of the sensory antifouling surface towards *M. edulis* attachment and detection under real-time conditions, *in situ*.** This final aim closes the loop to the overall aim of the study

(see 1.5) and will be the final measure for the success of the developed sensory surface with antifouling properties.

Chapter 2

Detection of the Blue Mussel, Mytilus edulis, on a Surface

“He who loves practice without theory is like the sailor who boards ship without a rudder and compass and never knows where he may cast.”

- *Leonardo da Vinci*

2.1. Introduction

The economic and environmental impacts of biofouling are well understood and research into antifouling strategies are vast (Schultz, 2007; Schultz *et al.*, 2011). This pertains to the research in fouling benthic communities, adhesion, removal strategies and grooming strategies to name a few (Seed and Suchanek, 1992; Callow and Fletcher, 1994; Silverman and Roberto, 2007; Tribou and Swain, 2010, 2015; Oliveira and Granhag, 2016). However, there is a gap in the knowledge of a method for the detection of biofouling in the maritime industry. *In situ* detection, particularly of macrofouling, may streamline and optimise fouling management, saving time, money and reducing the environmental impact. Moreover, as regulations are shown to restrict the acceptable level of biofouling on ships, clear and quantifiable biofouling regulations are enforced in some countries that must be upheld (Zabin *et al.*, 2018). The use of regulation is one of the few strategies in place to reduce the risks associated with biofouled ships from the complete ban of TBT in 2008, to the Craft Risk Management Standard (CRMS) requirement by New Zealand's government for international vessels (International maritime organistaion, 2016; Irving and McCarthy, 2018). In the latter, vessels need only provide evidence that their hull is continuously maintained, that the vessel is cleaned no less than 30 days prior or that it is to undergo a dry-docking clean of the hull within 24 hours of arrival. Evidence for this is based on the ship's Biofouling Management Plan and record book, the vessels history and certificates, as well as dates and reports of dry-docking and inspections/maintenance. Only with this monitoring system are the levels of

biofouling detected and the associated risks reduced. Biofouling is defined to begin moments after a vessel enters a body of water and therefore even with these regulations in place, the risk of introducing a non-native species or even forcing ships to unnecessarily dry-dock is assessed to remain high (*figure 2.1*) (Railkin, 2003; Dobretsov *et al.*, 2006; Lewis and Coutts, 2010).

Figure 2.1 – Dry-docked Ship with Heavy Biofouling on the Hull *(source: Mace, 2016).*

2.1.1. Sensors for the Detection of Biofouling

The advancement of sensors in this age of technology is seen to be a vital element in the development of the Industrial Internet of Things (IIoT) which refers to an interconnected network of machinery with sensors to provide accurate and real-time data (Potyrailo, 2016). Traditional and linear manufacturing was developed by the inclusion of sensors towards a more dynamic and interconnected system making the manufacturing process much safer, efficient and cheaper (Chen *et al.*,

2016; Civerchia *et al.*, 2017). This is particularly down to the ability to pinpoint issues and predict when and where they may occur. This so-called "predictive maintenance" allows for a proactive and safer approach; pressure sensors that are able to detect dangerous pressure conditions in an oil well and therefore avoiding an incident is such an example (Khan *et al.*, 2017; Aalsalem *et al.*, 2018). Such sensors are able to generate vast amounts of data for records and regulation compliance, monitoring and control, prediction of failures and trigger maintenance, and increase information flow and responsiveness (Lee and Lee, 2015; Hossain and Muhammad, 2016; Zhang *et al.*, 2017). A similar network of sensors could potentially be applied to the maritime industry for real-time and *in situ* monitoring of biofouling which may help propel the shipping industry into the Fourth Industrial Revolution or Industry 4.0 (Wan *et al.*, 2016). Currently the maritime industry appears to lag behind with no sensors presently available to detect biofouling *in situ*. Utilisation of such a sensor may allow for monitoring of biofouling development without the risks and costs associated with divers, ROVs or dry-docking as well as to assist regulatory authorities in monitoring compliance and maintenance of vessel records (Townsin, 2003; Hopkins and Forrest, 2008; Floerl and Coutts, 2013; Irving and McCarthy, 2018; Zabin *et al.*, 2018). With the ability to monitor biofouling, there may be an improvement in biofouling control with targeted, regular, and gentle hull cleaning. In turn, this will reduce biofouling accumulation, particularly in niche areas, which may decrease the risk of introducing an invasive species and facilitate in maintaining the durability of antifouling coatings to allow for a long-lasting antifouling capacity (Holm *et al.*,

2003; Davidson *et al.*, 2009; Lewis and Coutts, 2010). Furthermore, a reduction in biofouling on the hull surface will reduce the associated drag penalties and therefore decrease engine stress, costs, fuel consumption and greenhouse gas emissions (Abbott *et al.*, 2000; Hellio and Yebra, 2009; Bixler and Bhushan, 2012).

2.1.1.1. Electromagnetic Wave Sensor

One sensor that may be of great benefit to the industry is the electromagnetic wave (EMW) planar sensor with an interdigitated electrode (IDE) array. This type of EMW sensor showed application in a variety of fields from the detection of heavy metals such as lead (Frau *et al.*, 2018), to biomedical applications such as in the detection of lactate (Mason *et al.*, 2013), to the detection of phytoplankton concentration (Moejes *et al.*, 2018). Microwave based detection may help to analyse multiple parameters and therefore give a unique signal spectrum dependant on the material under test (MUT). With the vast diversity of the biofouling community, a contactless sensor based on the interaction of the propagation of the EMW and the MUT is reported here in terms of scattering parameters (S-parameters) as the Reflection Coefficient of S_{11} (the scattering parameter for a one-port network) is dependent on the relative permittivity of the MUT (Mason *et al.*, 2013). Permittivity is measured based on the ability for the MUT to polarise due to the applied electromagnetic field (relative permittivity) (*equation 2.1*).

$$\varepsilon_r = \varepsilon' - j\varepsilon''$$

Equation 2.1

Whereby the permittivity (ε_r) is defined based on the materials ability to transmit an electric field, accounting for the energy stored (ε') and any losses (ε'') (j is a complex or imaginary number) (Mason *et al.*, 2013; Moejes *et al.*, 2018). This complex value is varied with a changing frequency as well as with changes in the material (e.g. concentration) impacting on its permittivity. A vector network analyser (VNA) is used to measure these changes allowing for the detection or characterisation of a MUT. By measuring a full spectrum of frequencies from 10 MHz to 15 GHz with 60,000 measurements between, the likelihood of finding an appropriate frequency where a change is measurable is increased.

2.1.1.2. Interdigitated Electrode Geometry

The signal strength of an IDE is dependent on its geometry: area, width and gaps between electrodes. The efficiency of an IDE ($\mathrm{IDE_{eff}}$) is defined as the ratio of the sensing area (A) to the total area of the sensor (A') (*equation 2.2*) (Grover, 1999).

$$\mathrm{IDE_{eff}} = \frac{A}{A'}$$

Equation 2.2

Based on this equation, efficiency for a simple IDE senor is deduced based on the geometry of the finger electrodes based on the width (X), height (Y), electrode width (E) and the gap width (G) (*equation 2.3*) (Grover, 1999).

$$\mathrm{IDE}_{\mathrm{eff}} = \frac{\frac{GY}{G+E}\left(X - \underline{2}\,G - E\right) + G^2 + GE}{XY}$$

Equation 2.3

The efficiency of a generic sensor is denoted in the equation that may be optimised by rounding the corners of the electrodes and therefore ensuring the width remains constant across the entire sensor (Grover, 1999). Therefore, the G- term ($\underline{2}$) in *equation 2.3* is then defined as equal to $(2 - \frac{\pi}{2})$ and the increase in efficiency is determined with the reduced gap width from 2 to 0.429 (arbitrary units; Grover, 1999). However, the optimisation of the sensor efficiency is additionally improved by changing the dimensions in either the X or Y element by increasing the length of the electrode fingers or by adding additional fingers, respectively (*figure 2.2*).

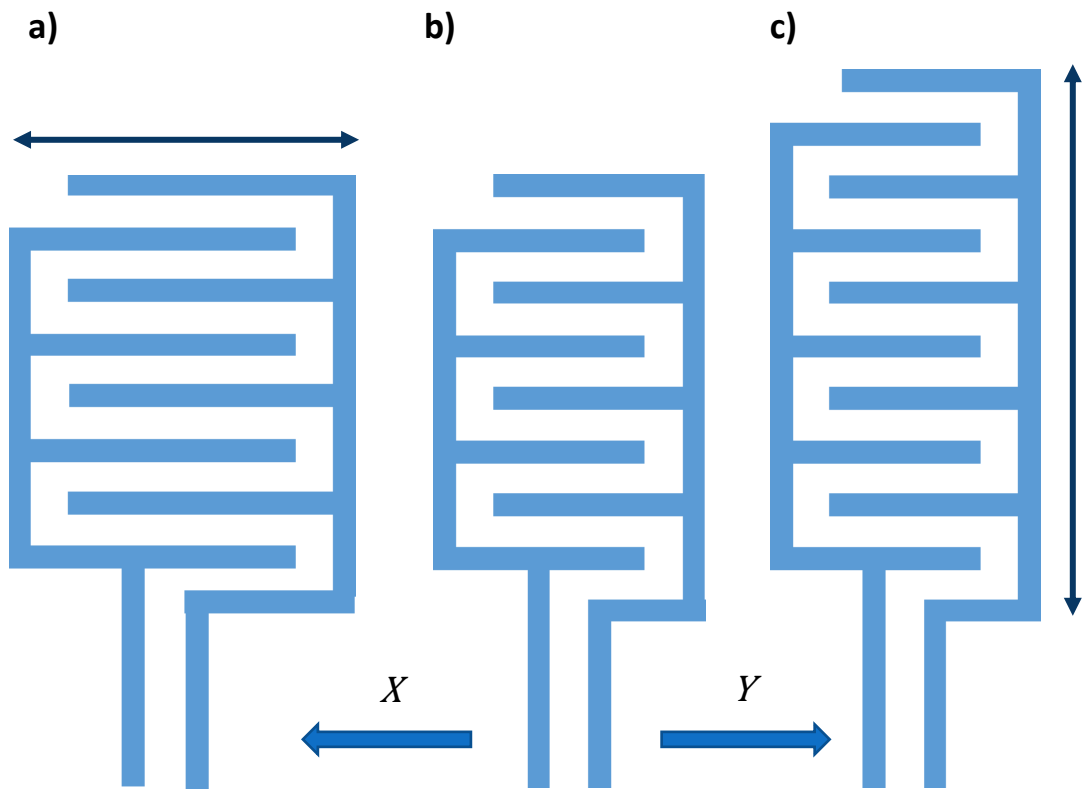

Figure 2.2 – IDE Geometry Modification *where there can be an increase in the length of the electrode fingers (direction X) (from **b** to **a**) and an increase in direction Y with additional electrodes (from **b** to **c**) (adapted from: Grover, 1999).*

Studies showed that when the size of the gap between electrodes (G) is constant at 1 (arbitrary units) and the thickness of each electrode (E) is constant at 0.1 (arbitrary units), in the first instance, the length of the electrode fingers (X) remains constant and the number of electrode fingers (Y) increases by the power of ten, the sensing area (A) linearly increases by the power of ten (Grover, 1999). However, there is also a proportional increase in the total area of the sensor (A'), consequently the efficiency of the sensor (IDE_{eff}) is unchanged. In the second instance, the number of electrode fingers (Y) remains constant and the length of the electrode fingers (X) increases by the power of ten, the sensing area (A)

actually increases at a faster rate than would be expected from a linear increase by the power of ten and approaches a maximum efficiency ($\frac{G}{G+E}$). (Grover, 1999). This maximum efficiency does not approach the theoretical maximum, but rather is the result of the gap width divided by the gap width and the electrode width (*Table 2.1*).

Table 2.1 – Changes in IDE Sensor Efficiency Based on Changes in Geometry *whereby, in the first instance, the length of the electrodes (**X**) is constant and the number of electrodes (**Y**) is increased by the power of ten resulting in a linear increase of the sensing area (**A**), however, a proportional increase in the total senor area (**A'**) leaves the efficiency (IDE_{eff}) unchanged. In the second instance, the constant number of electrodes (**Y**), but increase in the length of the electrode fingers (**X**) by the power of ten results in a faster increase in the sensing area (**A**) and thus efficiency approaches the maximum efficiency ($\frac{G}{G+E}$) of 0.9091 (adapted from: Grover, 1999).*

X	Y	A	A'	IDE_{eff}	$\frac{G}{G+E}$
10	10	72.92	100	0.7292	0.9091
10	100	719.3	1000	0.7193	0.9091
10	1000	7183	10000	0.7183	0.9091
10	10000	71820	100000	0.7182	0.9091
10	100000	718200	1000000	0.7182	0.9091
10	10	72.92	100	0.7292	0.9091
100	10	891.1	1000	0.8911	0.9091
1000	10	9073	10000	0.9073	0.9091
10000	10	90890	100000	0.9089	0.9091
100000	10	909100	1000000	0.9091	0.9091

Increase in the width and number of the electrode fingers may result in a proportional increase in the signal (Grover, 1999). This is further corroborated with simulations that showed changes in geometry resulted in changes in the penetration height of the electromagnetic field, which may therefore be designed to detect in the near-field (*figure 2.3*). The IDE array type sensor showed to have many benefits including the high sensitivity to nearby changes that rapidly decays with distance.

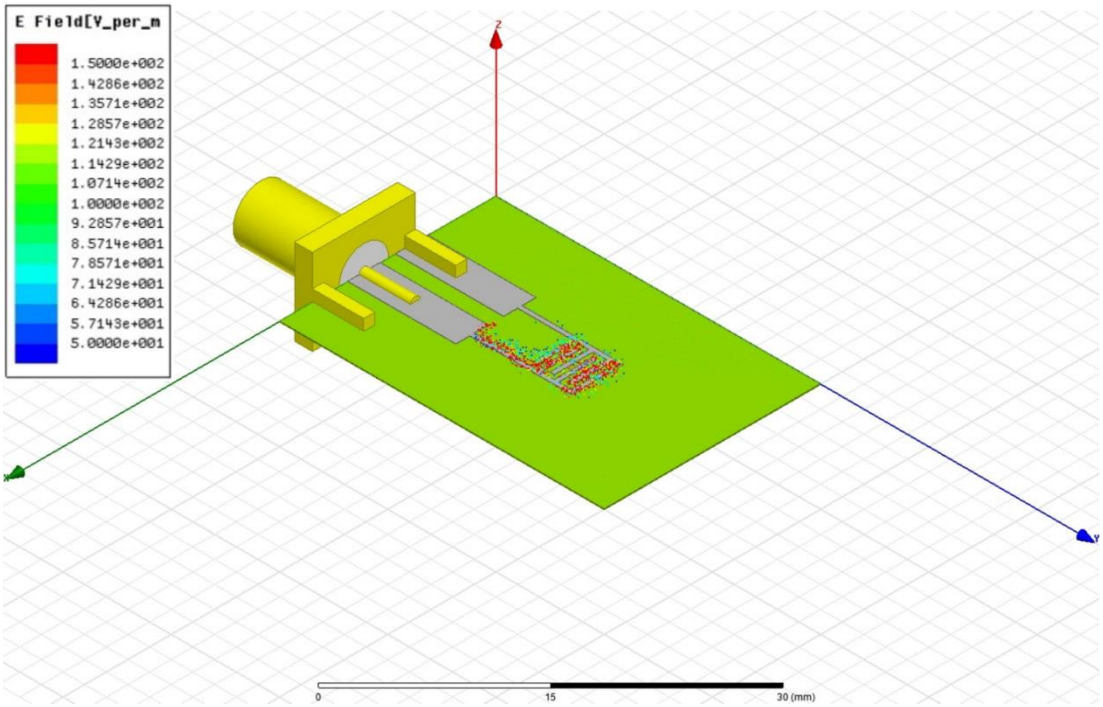

Figure 2.3 – Simulated 3D IDE Sensor *using Ansoft HFSS finite element modelling software (edited source: Korostynska et al., 2013).*

2.1.1.3. The Sensing Material

IDE based sensors are thought of as being mechanical or chemical sensors, with the latter being subdivided into capacitive, resistive and surface acoustic wave (SAW) (Grover, 1999). Mechanical IDE sensors may be used as pressure sensors because as the force on the sensor is increased, the area of contact between the

IDE and a semiconductor layer is increased, resulting in a reduction in resistance and completion of the circuit between the two IDEs (Grover, 1999; Teng *et al.*, 2007). Chemical IDE sensors are also dependant on the large surface area of the IDE to interact with the sensing material, which dictates the capacitive or resistive nature of the sensor. Capacitive sensors are seen to rely on the sensing layer acting as a dielectric to measure changes in resistance and the resistive sensors rely on the sensing layer being a resistor to measure changes in capacitance (Grover, 1999). Finally, SAW sensors are seen to operate on the propagation of the wave through the sensing material and the MUT whose properties may affect the wave. The impact of the analyte is generally shown as a decrease in the velocity of the wave as the analytes concentration increases (Frau *et al.*, 2017; Moejes *et al.*, 2018). Moreover, specificity of the sensing material is found to allow for optimisation of the sensor (*figure 2.4*) (Frau *et al.*, 2018).

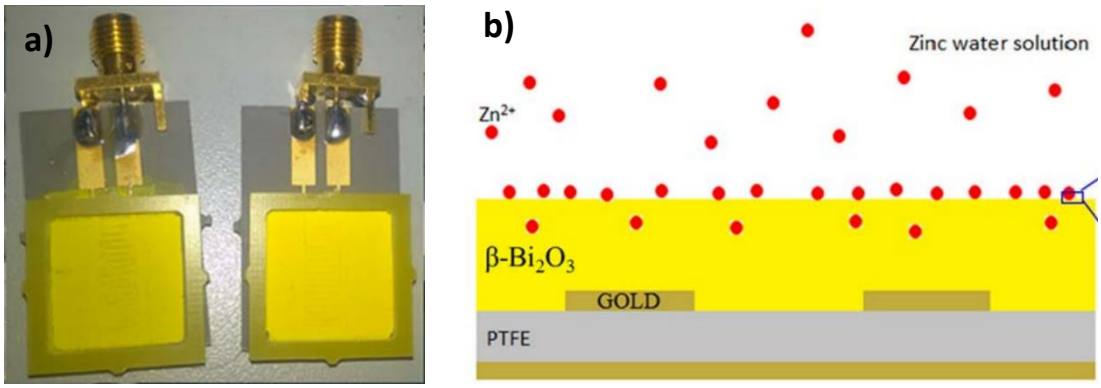

Figure 2.4 – A Functionalised Sensor *with a bismuth oxide sensing material for the detection of Zinc (**a**) and a partial cross-section of the sensor (**b**) (source: Frau et al., 2017).*

Changes in the Reflection Coefficient due to the impact of the wave by the analyte is measurable (Korostynska *et al.*, 2013; K. B. Moejes *et al.*, 2018). This may be further impacted on by the properties of the surface material on the reflected EMW in the same manner. The velocity of the wave as it enters the dielectric is affected by the relative permittivity of different materials, reducing them by a factor $\sqrt{\varepsilon}$ (*figure 2.5*) (Sebastian, 2008).

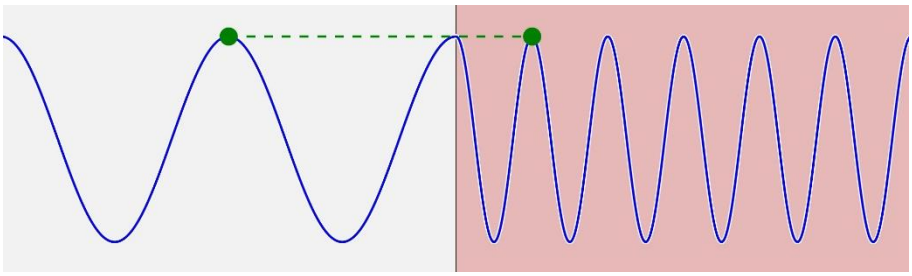

Figure 2.5 – A Wave Entering A Material with a Higher Relative Permittivity *reducing its speed and therefore its wavelength (source: Rumpf, 2017).*

Some reflection of the incident wave is evident at the boundary between the two different materials (Sebastian, 2008). This is necessary to achieve continuity of the electric field. The measurable changes of the EMW entering a different material due to their respective relative permittivities may be predictable with their increasing relative permittivity as applied to *equation 1.1*, however the relative permittivity of the model organism the blue mussel, *Mytilus edulis* plaque is unknown and may be changeable depending on the mixture of adhesives (see Chapter 1, Section 3.1.).

2.1.2. Surface Material Properties

For this study, four materials were evaluated: 1) Nylon 6; 2) Silicone; 3) PVC; 4) polytetrafluoroethylene (PTFE; Teflon™). Nylon 6 is widely used in the marine environment, particularly in ropes, threads, tie cords and netting (Klust, 1982; Timmers *et al.*, 2005; Andrady, 2011), while silicone is used in antifouling foul-release coatings (Meyer *et al.*, 2006), PVC shows widespread use in biofouling research (Dürr and Wahl, 2004; Bullard *et al.*, 2010) and PTFEs use as a non-stick coating extends to the medical field to prevent bacterial fouling leading to infections (Lawrence and Turner, 2005). Furthermore, their relative permittivity was also considered, as a higher permittivity may reduce the input frequency necessary to detect the presence of *M. edulis* byssal plaque on the surface (Korostynska *et al.*, 2013). Finally, as the selected material was to be developed into an antifouling and foul-release surface, it was necessary to consider the surface properties.

The surface properties of each material may have an impact on the adhesion of the mussel plaque itself; different surfaces may result in different protein expression levels as adhesives may be matched to the surface properties to maximise adhesion (Vreeland *et al.*, 1998; Warner and Waite, 1999). The byssal plaque may spread further and tenacity is lowered on low-energy surfaces as they are shown to have a preference for hydrophilic, high-energy surfaces (Aldred *et al.*, 2006). The selected materials are known to be a hydrophobic, and therefore are low wettability surfaces.

2.1.3. Aim

In order to be able to design a sensory surface for biofouling detection, basic factors were considered. The **first aim of the study was to determine the efficacy of the model species, the blue mussel *M. edulis,* detection depending on the geometry and number of IDEs of the planar EMW sensor, *in vitro*** (*Pilot Experiment: Initial Detection of M. edulis Plaques with Four EMW Sensors with Varying IDE Geometries*). Further, detection efficacy on a surface may not only be impacted by the factors geometry and number of the IDE's, but by Orientation of the material relative to the sensor array. Therefore, the **second aim of the study was to determine if the efficacy of detection was impacted by the Orientation, *in vitro*** (*Pilot Experiment: The Impact of Orientation on the Detection of M. edulis Plaques with Four EMW Sensors with Varying IDE Geometries*). Finally, this led to the consideration of the type of surface to be used for biofouling detection. In the maritime industry, various types of materials from metals to polymers are in use with multiple types associated with each other. All surfaces in the marine environment may show the potential to be biofouled and so exhibit the need to be included in the development of a sensory surface for detection of biofouling. In the present study, materials were selected to obtain a wide range of the factors wettability and permittivity leading to the **final aim of the study to determine the efficacy of *M. edulis* detection on differing materials based on wettability and relative permittivity, *in vitro*** (*Efficacy of Varying Sensing Materials for Detecting M. edulis plaque on a Surface with the Selected EMW Sensor*).

2.2. Methods

2.2.1. *M. edulis* Collection and Culture

Specimens of *M. edulis* were collected from the Liverpool Royal Albert Dock (53°24'02.9"N 2°59'30.6"W) and Liverpool Watersports Centre (53°23'33.9"N 2°59'07.6"W) in Liverpool, UK. Biofouling present on shells was removed using a sponge scourer. A monoculture of *M. edulis*, between 3 to 6 cm in length, were then kept in Exo Terra standard Faunariums (30 × 19.3 × 20.6 cm) in 28 psu artificial seawater (Aquarium Systems Instant Ocean Sea Salt) (measured with a refractometer) in the LJMU NSP cold room at 8°C with aeration and regularly fed with the planktonic diatom *Tetraselmis suecica*. *T. suecica* was obtained from cultures maintained by Dr S. Conlan (BES; Faculty of Science at Liverpool John Moores University). The artificial seawater of the mussel cultures was changed twice a week and the tanks regularly cleaned. Mussels were only exposed to a Treatment once.

2.2.2. Interdigitated Electrode Sensors

Four planar electromagnetic wave sensors were employed whereby each sensor consisted of a PTFE substrate, a gold (Au) back plate and with varying gold electrode numbers or geometry; 1 line electrode, 3 pair (3pr) interdigitated electrodes (IDE), 9 pair IDE (9pr) and 2 × 3 pair IDE (2 × 3pr). Each sensor had a radio frequency (RF) coaxial, SubMiniture version A (SMA), straight jack (50 ohm) connector soldered on for attachment to the VNA (*figure 2.6*).

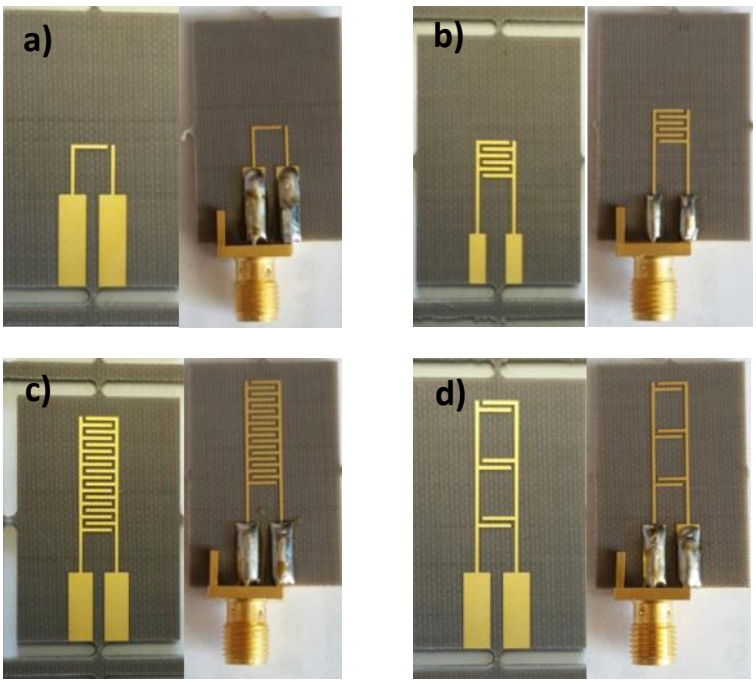

Figure 2.6 – Four sensors with differing IDE numbers and geometries examined for possible detection of Mytilus edulis on a surface*. Each sensor is presented here before (left) and after soldering of the RF coaxial SMA connector (right). The single electrode of the 1 line sensor (**a**), the 3pr sensor (**b**) and the 9pr sensor (**c**) show an increasing number of IDEs covering an increasing surface area. The 2 × 3pr (**d**) differs in that it contains 3 pairs of 2 electrodes covering a distant equal to that of the 9pr sensor, but with a reduced number of IDEs.*

2.2.3. Surface Material Selection

The novel methodology was designed to investigate the ability of the manufactured planar EMW sensors to detect *M. edulis* byssi plaque on a surface. The localised electric field of the IDE sensors allowed for an estimated penetration height of 1.8 mm (O. Korostynska 2017, personal communication). It was therefore concluded that a surface thickness of 1 mm should allow for near-field surface detection only.

In total, four materials were selected due to their interaction with both the sensor and the mussel: relative permittivity and hydrophobicity, respectively (*table 2.2*).

Table 2.2 – Surface Hydrophobicity and Electrical Properties *(data from: Polymer Properties Database, 2015; Goodfellow, 2019).*

		Nylon 6	Silicone	PVC	PTFE
Dielectric Constant		3.6	2.9 – 4	2.7 – 3.1	2.0 – 2.1
Surface Tension	Calc. γ_s(mN/m)	48.3	22.8	40	23.9
	Exper. γ_s(mN/m)	45.2	21.7	41.1	21.1

Polyvinyl chloride (PVC) (SIMONA via Ensinger Ltd.) panels of 50 x 50 x 1 mm, in battleship grey is a widely used synthetic amorphous polymer and is utilised in scientific research to help study mussel settlement and biofouling. This hydrophobic plastic has a dielectric constant of 2.7 to 3.1 at 1 MHz.

50 x 50 x 1 mm white panels of PTFE, commonly known under the brand name Teflon™ (Direct Plastics), was one of the materials investigated. The hydrophobic fluoropolymer is used in cookware as a non-stick coating on pans and more relevantly, as a coating in catheters to prevent microfouling of bacteria that could lead infections and as a foul-release coating in shipping (e.g. Intersleek 900). PTFE has a dielectric constant of 2.0 to 2.1 with a low energy surface.

Nylon 6 or polycaprolactam (Direct Plastics) is a semi crystalline polyamide, and unlike other nylons, it is not a condensation polymer, instead it is formed by ring opening polymerisation. Similarly, Nylon 6 also has a wide range of applications,

pertinently in a large variety of threads, ropes, filaments, nets, and tie cords. Nylon rope is partial to biofouling with its uses in towing, surge lines, boat falls and as netting in aquaculture. As with the other polymers, this translucent Nylon 6 50 x 50 x 1 mm panels were also hydrophobic and have a dielectric constant of 3.6.

Silicone, with a dielectric constant range between 2.9 and 4, is used in cookware, dry cleaning, electronics, medicine and in foul-release antifouling coatings due its hydrophobic and non-toxic properties. Thomtastic 30 (T30) Silicone mix (Thomson Brothers Ltd.) was specifically developed for a more rigid panel to be used in the experiment (the manufacturer did not provide the dielectric constant for Silicone T30). The Silicone was mixed per instructions with a 10:1 (w/w) base to curing agent ratio with the resultant mixture comprising of a hardness of 30 Shore A, viscosity of 140 mega Pascal (mPa), a linear shrinkage of less than 0.1% and 24 hours to achieve a full cure at 23 °C. In order to obtain panels of Silicone, a PVC mould was devised with a 1 mm depth and an area of 40 x 40 mm; 1 mm thickness of the Silicone to correspond to the other materials (*figure 2.7*).

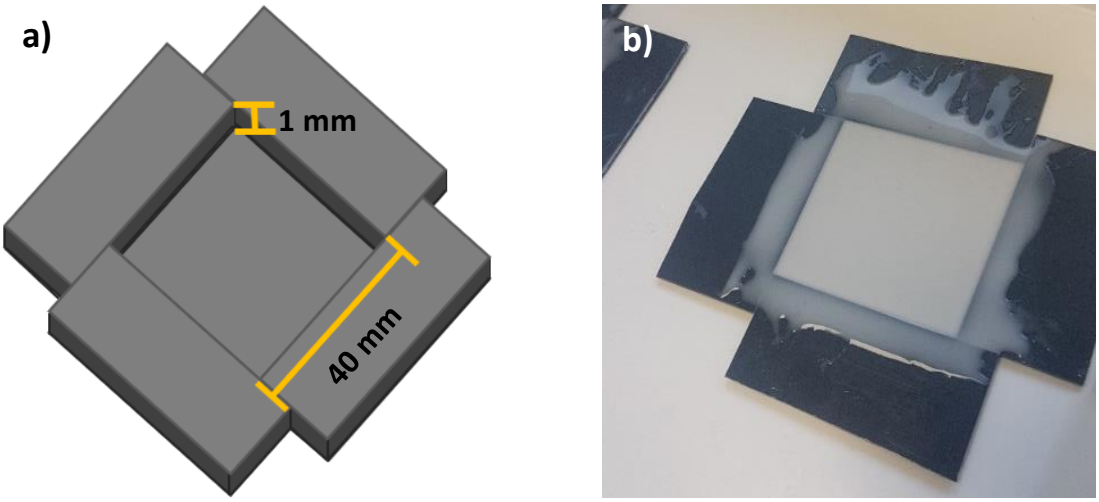

***Figure 2.7 – PVC mould used for Silicone panels**, which is shown both schematically (**a**) and photographed with Silicone poured into the mould (**b**).*

The Silicone mixture was weighed to obtain approximately 3 g per mould and then poured with any excess Silicone scraped off. Once the Silicone cured for at least 24 hours, a scalpel was used to cut around the edges of the mould and the Silicone panel peeled out.

2.2.4. Experimental Design

2.2.4.1. Pilot Experiment:

Initial Detection of M. edulis Plaques with Four EMW Sensors with Varying IDE Geometries

PVC panels (SIMONA via Ensinger Ltd.) of 50 × 50 × 1 mm were setup either with a mussel (Treatment) or without a mussel (Control) as the material to function as a surface in these experiments. Individual *M. edulis* specimens were secured to the Treatment panels with a rubber band whereby the dorsal edge of the shell was perpendicular to the PVC panel. This initial experimental procedure included individual Treatment (n = 8) tanks and a Control (n = 1) tank of

8.5 × 15.5 × 10.5 cm setup with 28 psu artificial seawater and an aerator in an 8°C cold room for 24 hours.

Following exposure to the Treatment and Control condition, panels were prepared for data collection. From the Treatment panels, the rubber band was carefully cut with scissors and removed, and the mussel byssi threads were cut close to the ventral section of the shell. Sheets of FR4 were laser cut to create 20 × 20 × 1 mm wells and double-sided tape was attached to one side of the well. A disposable scalpel was then used to trim the excess double-sided tape. The Control and Treatment PVC panels with byssal plaque present on the surface were selected, the FR4 well secured, the PVC sheet trimmed to size and placed back in 28 psu seawater ready for data collection (*figure 2.8*).

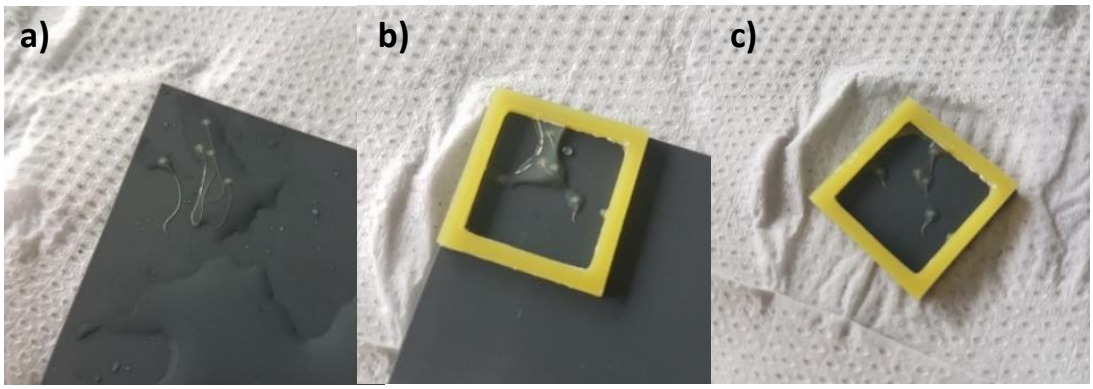

Figure 2.8 – Preparation of Treatment Panels *where a 50 × 50 × 1 mm PVC panel after exposure to a mussel in 28 psu artificial seawater is shown (**a**). Byssi were trimmed and FR4 with double-sided tape placed around the deposited plaques to create a well (**b**) and finally the excess PVC removed (**c**) and then placed back in 28 psu seawater.*

The Impact of Orientation on the Detection of M. edulis Plaques with Four EMW Sensors with Varying IDE Geometries

Three tanks were set up, Tank I (8.5 × 15.5 × 10.5 cm), Tank II (11 × 17 × 11.5 cm) and Tank III (11 × 17 × 11.5 cm) with 28 psu artificial seawater in an 8 °C cold room. A single PVC panel placed in Tank I and Tank II, with an individual mussel was secured to the Treatment panel with a rubber band for 24 to 96 hours, after which it was replaced with a new mussel secured to the same PVC panel in order to maximise the number of byssi put down. This was done over a 3-week period totalling 14 mussels and 9 mussels for Tank I and Tank II, respectively. 6 PVC panels placed in Tank III with a freely placed individual *M. edulis* specimen in the tank for 24 to 96 hours, after which it was replaced with a new mussel with the same 6 PVC panels. This was also carried out over a 3-week period totalling 9 mussels for Tank III. An additional Control tank with a single PVC panel in 28 psu artificial seawater was also set up in an 8 °C cold room for a 3-week period (*figure 2.9*).

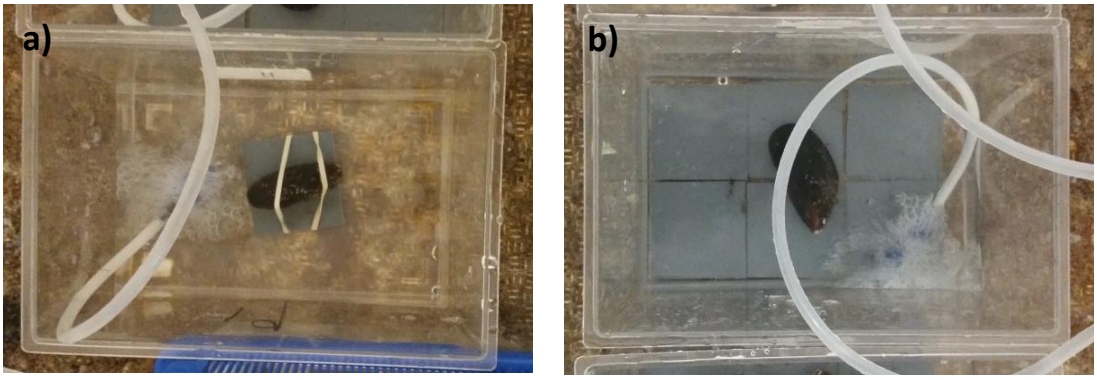

Figure 2.9 – Tank II (a) and Tank III (b) with a mussel *secured to the PVC panel and a freely place mussel with 6 PVC panels, respectively.*

Following exposure to the Treatment or Control condition, the panels were prepared for data collection (as previously described in the Pilot Experiment: Initial Detection of *M. edulis* Plaques with Four EMW Sensors with Varying IDE Geometries) whereby the rubber band was carefully removed, the mussel byssi threads cut and the FR4 well secured, and the PVC sheet trimmed to size as shown in *figure 2.8*.

2.2.4.2. Efficacy of Varying Sensing Materials for Detecting *M. edulis* Plaque on a Surface with the Selected EMW Sensor:

Four materials were investigated (PVC, PTFE, Nylon 6 and Silicone) whereby for each material surface, 30 x 19.3 x 20.6 cm tanks were setup with a single Treatment panel (with a mussel secured to the panel with a rubber band) (n = 40) and a Control panel (no mussel) (n = 40) in a single tank with 28 psu artificial seawater in an 8 °C cold room for each of the four materials for 24 hours. With the lower rigidity of the Silicone, a 50 x 50 x 1 mm PVC panel was used for support when securing the mussel to the panel and then removed before data collection (*figure 2.10*).

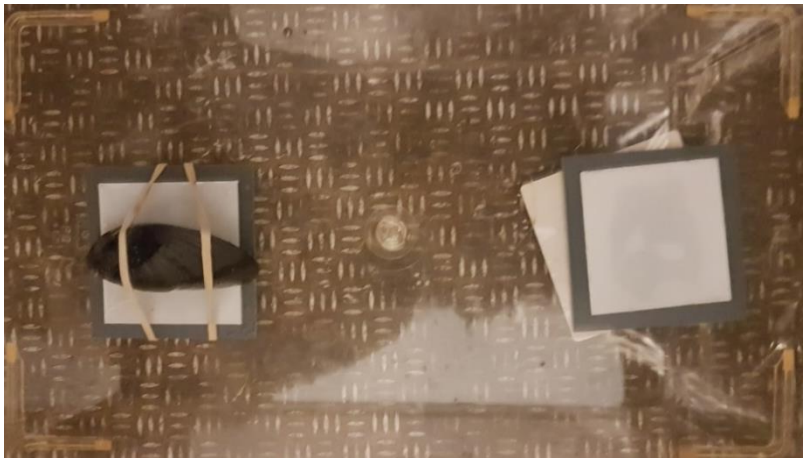

Figure 2.10 – The Silicone Treatment (left) and Control (right) with a PVC support panel *in a 30 x 19.3 x 20.6 cm tank before the addition of the artificial seawater.*

After 24 hours, the panels were prepared with a FR4 well as shown in *figure 2.8*.

2.2.5. Data Collection

A VNA (Rohde & Schwarz ZVA24) was used to determine the S_{11} scattering parameter (S parameter) by measuring both the amplitude and phase of the signal reflected by the sensor over a frequency range of 10 MHz to 15 GHz with 60,000 data points measured per sweep (for each measurement taken), in a temperature controlled (21°C) sensor laboratory (*figure 2.11*). A calibration was performed to remove the effect of the coaxial line connecting the VNA to the sensor.

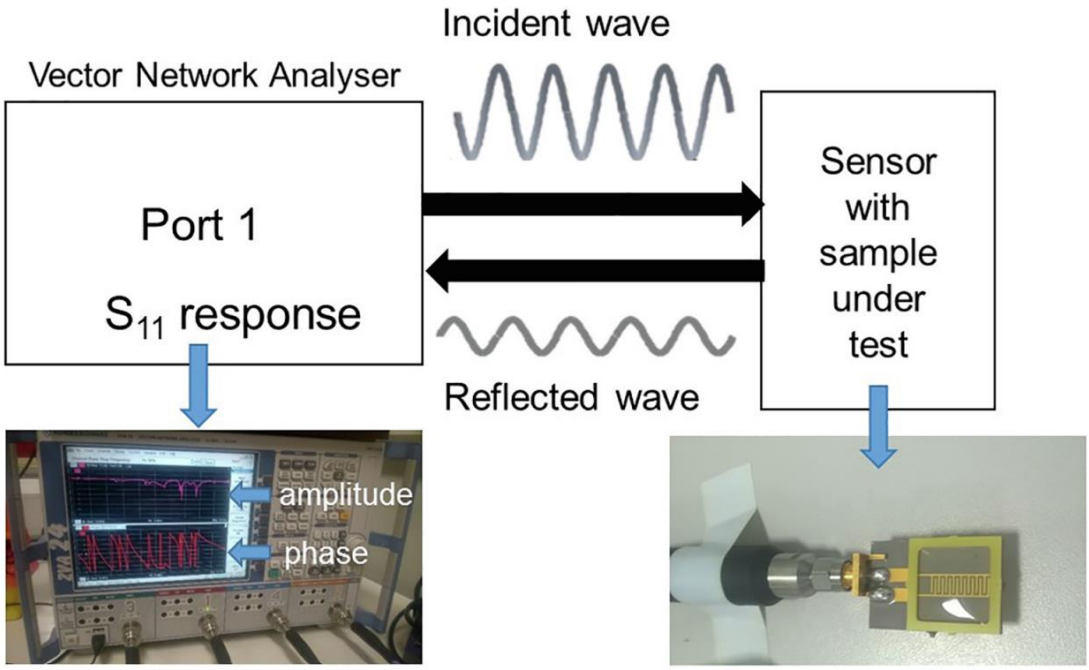

Figure 2.11 – Schematic Setup of a VNA *and a liquid sample under test with a planar IDE EMW sensor (source: Frau et al., 2019).*

The panels were dried on the bottom and excess liquid was removed from the surface using capillary action with a paper towel to ensure that no damage occurred to any plaques on the panel. The panels were then placed over the IDE of the sensor and 400 µl of 28 psu artificial seawater was added to the well (*figure 2.12*).

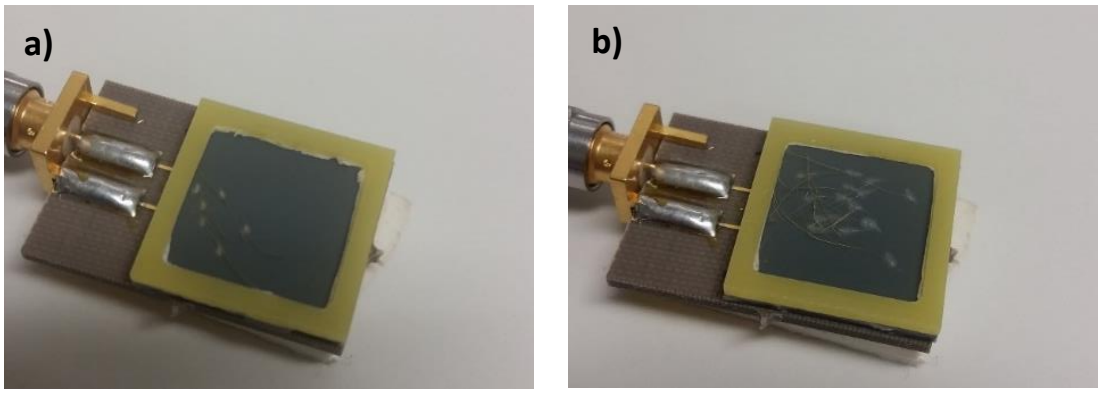

Figure 2.12 – Detecting the presence of M. edulis plaque on PVC panels *with 6 plaques (**a**) and 14 plaques (**b**) on a sensor connected to the VNA.*

2.2.5.1. Pilot Experiment:

Initial Detection of M. edulis Plaques with Four EMW Sensors with Varying IDE Geometries

With each of the four sensors (1 line, 3pr, 9pr and 2 × 3pr Au PTFE sensors) 5 full sweep measurements (60,000 frequency points from 10 MHz to 15 GHz) were taken for each Treatment panel (n = 5) and the Control panel (n = 1) with 400 µl of 28 psu artificial seawater (**Wet Measurement**). The panel was lifted and placed back between each measurement to account for air entrapment, random error of the placement of the panel, and fluctuations of the instrument and of the environment. After the Wet measurements, excess water was removed from the well and the panels left to air dry on the bench, and 5 full sweep measurements (60,000 frequency points from 10 MHz to 15 GHz) were taken for each Treatment panel (n = 5) and the Control panel (n = 1) with no seawater (**Dry Measurement**).

The Impact of Orientation on the Detection of M. edulis Plaques with Four EMW Sensors with Varying IDE Geometries

Each treatment PVC panel (n = 4) from Tanks I, II and III, as well as the Control (n = 1), had 10 full sweep measurements (60,000 frequency points from 10 MHz to 15 GHz) taken with 400 µl of 28 psu artificial seawater with each of the four sensors and the Orientation noted as Orientation A. The panels were then rotated 90° anti-clockwise to Orientation B where an additional 10 full sweep measurements were taken. Each panel was rotated three times to give four Orientations marked as A, B, C and D, with 10 full sweep measurements per Orientation (*figure 2.13*). Designation of Orientation A was random.

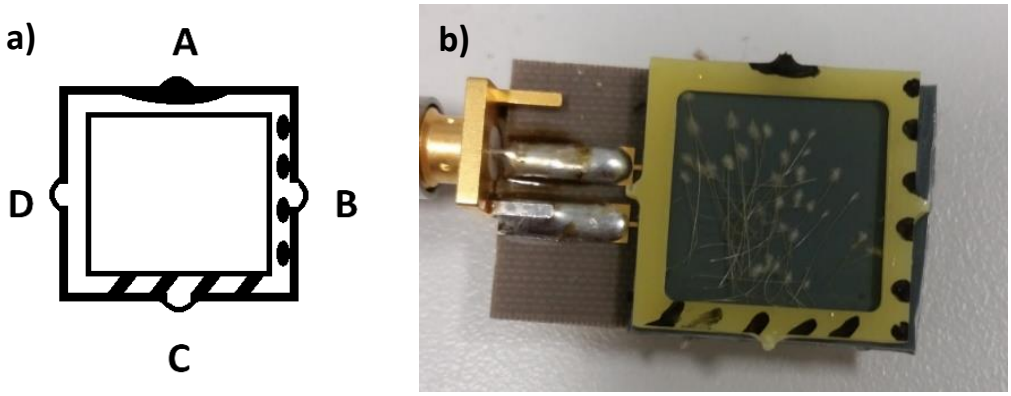

Figure 2.13 – Investigating the Possible Effect of Orientation *where each side denotes an Orientation of which the Orientation A is randomly assigned (**a**). The Treatment panel with 32 plaques is shown in Orientation D on the sensor (**b**).*

2.2.5.2. Efficacy of Varying Sensing Materials for Detecting *M. edulis* Plaque on a Surface with an EMW Sensor

Using the selected sensor, for each of the Treatment panels (n = 40) and Control panels (n = 40) of the four material surfaces, three full sweep measurements (60,000 frequency points from 10 MHz to 15 GHz) were taken per Orientation, resulting in 12 full sweep measurements per panel. The Orientations were no longer marked due to possible interference of the marker properties with the sensor.

2.2.6. Analysis

The panels were visually examined and the number of byssal plaques on the surface recorded. The VNA was used to measure the Reflection Coefficient as S_{11} dB and the mean was calculated per Treatment and per Orientation (where applicable), per panel, at each of the 60,000 measured frequencies between 10 MHz to 15 GHz.

2.2.6.1. Pilot Experiment:

Initial Detection of M. edulis Plaques with Four EMW Sensors with Varying IDE Geometries

Analysis of the mean Reflection Coefficient S_{11} dB as a binary (plaque and no plaque or Treatment and Control) in order to identify individual frequencies where the sensors are able to best detect the presence of *M. edulis* plaque on the PVC panel. The mean Reflection Coefficient at each frequency (60,000 frequency points from 10 MHz to 15 GHz) of the Control panel (5 measurements) and the mean Reflection Coefficient at each frequency for each Treatment panel (5 measurements each) was plotted for both the **Wet** and **Dry Measurements** for each of the four sensors. The largest difference in the mean Reflection Coefficient of the Treatment (n = 5) and the Control (n = 1) across the 60,000 frequency points from 10 MHz to 15 GHz allowed for a single frequency to be deduced where detection is occurring. This was done for each of the four sensors.

No statistical analysis was carried out due to there being only one Control, which would act as a pseudoreplication.

The Impact of Orientation on the Detection of M. edulis Plaques with Four EMW Sensors with Varying IDE Geometries

The mean Reflection Coefficient of each of the 60,000 frequency points from 10 MHz to 15 GHz, of each Orientation (10 measurements per Orientation) for the Treatment (n = 4) and Control (n = 1) was deduced. The biggest difference between the mean Reflection Coefficient of the Treatment and the Control for

each Orientation was then deduced and the corresponding frequency recorded e.g. difference between mean Reflection Coefficient of the Treatment with three plaques in Orientation A and the Control in Orientation A. This was done with all four sensors. The mean frequency at which the biggest difference per Orientation, per sensor occurred was then graphically presented and compared with the results of the **Wet experiment.**

No statistical analysis was carried out due to the presence of a single Control, which would act as a pseudoreplication.

2.2.6.2. Efficacy of Varying Sensing Materials for Detecting *M. edulis* Plaque on a Surface with the Selected EMW Sensor

The panels were visually examined and the number of plaques on the surface recorded. Data for the number of plaques were tested for the assumptions of normality (Kolmogorov-Smirnov; (Quinn and Keough, 2002)) and homogeneity of variances (Levene's test; (Quinn and Keough, 2002). If assumptions were met a one-way ANOVA (factor 1: 4 materials; variable: number of byssal plaques) was used, followed by a Tukey HSD posthoc test to determine differences between materials. Level of significance was 5%. Statistical analysis was conducted using SPSS (Version 26; IBM).

The mean Reflection Coefficient for the Treatment (n = 40) and Control (n = 40) (3 full sweep measurements of 60,000 frequency points from 10 MHz to 15 GHz per Orientation, per panel) for each of the four materials was plotted using MATLAB (version 9.2; R2018b; Mathworks®). Their respective standard error (SE)

values were also plotted as a line, which may indicate frequencies at which the Reflection Coefficient peaks may be unreliable and may therefore be discarded. A previous assumption for detection was that the Control Reflection Coefficient be more negative than the Treatment Reflection Coefficient as affected by the relative permittivity or dielectric constant (A. Mason 2018, personal communication; Moejes *et al.*, 2018). The assumption was that the dielectric constant of the Treatment, with the presence of the *M. edulis* byssal plaque, allows it to store electrical energy in an electric field resulting in a less negative Reflection Coefficient than the Control, as shown in the *equation 1.2*. Coupled with the largest difference between the mean Reflection Coefficient for the Treatment and Control, this was used to determine the frequency at which the sensor was able to detect plaque on the surface of each material.

Data from each panel (consisting of 12 measurements per panel) measured as Reflection Coefficient were tested for the assumptions of normality (Kolmogorov-Smirnov; (Quinn and Keough, 2002)) and homogeneity of variances (Levene's test; (Quinn and Keough, 2002)). If assumptions were met a two-way nested ANOVA (factor 1: 4 materials, factor 2: Treatment and Control; variable: Reflection Coefficient) was used and to determine differences between materials and a one-way nested ANOVA was used for Treatment differences per material. If assumptions were not met, ANOVA was still used (Underwood, 1996) and the level of significance was always 5%. Statistical analysis was conducted using SPSS (Version 26; IBM).

Reliability and Replicability of Sensing Materials for Detection of M. edulis plaques on a Surface with the Selected EMW Sensor

The data were analysed for replicability and repeatability by considering the difference between the mean Reflection Coefficient for the Treatment panel (n = 40) and Control panel (n = 40) for each tank, without regarding the previous assumption of the Treatment being less negative than the Control as the electrical properties of the *M. edulis* byssal plaque are unknown and may demonstrate electrical elastance or capacitance at any given frequency. These data were plotted as a scatter graph along with a line graph of the overall mean Reflection Coefficient of the Treatment and Control.

The largest difference between the mean Reflection Coefficient of the Treatment and Control was used to determine the frequency at which the sensor was able to detect plaque on the surface of each material without regarding the previous assumption of the Treatment being less negative than the Control. Data from each panel (consisting of 12 measurements per panel) measured as Reflection Coefficient were tested for the assumptions of normality (Kolmogorov-Smirnov; (Quinn and Keough, 2002)) and homogeneity of variances (Levene's test; (Quinn and Keough, 2002)). If assumptions were met a one-way nested ANOVA (factor 1: Treatment and Control; variable: Reflection Coefficient) was used to determine differences between materials. If assumptions were not met, ANOVA was still used (Underwood, 1996) and the level of significance was always 5%. Statistical analysis was conducted using SPSS (Version 26; IBM).

2.3. Results

2.3.1. Pilot Experiment:

Initial Detection of M. edulis Plaques with Four EMW Sensors with Varying IDE Geometries

5 Treatment panels with 2 plaques, 3 plaques, 6 plaques, 9 plaques and 12 plaques were obtained (*figure 2.14*).

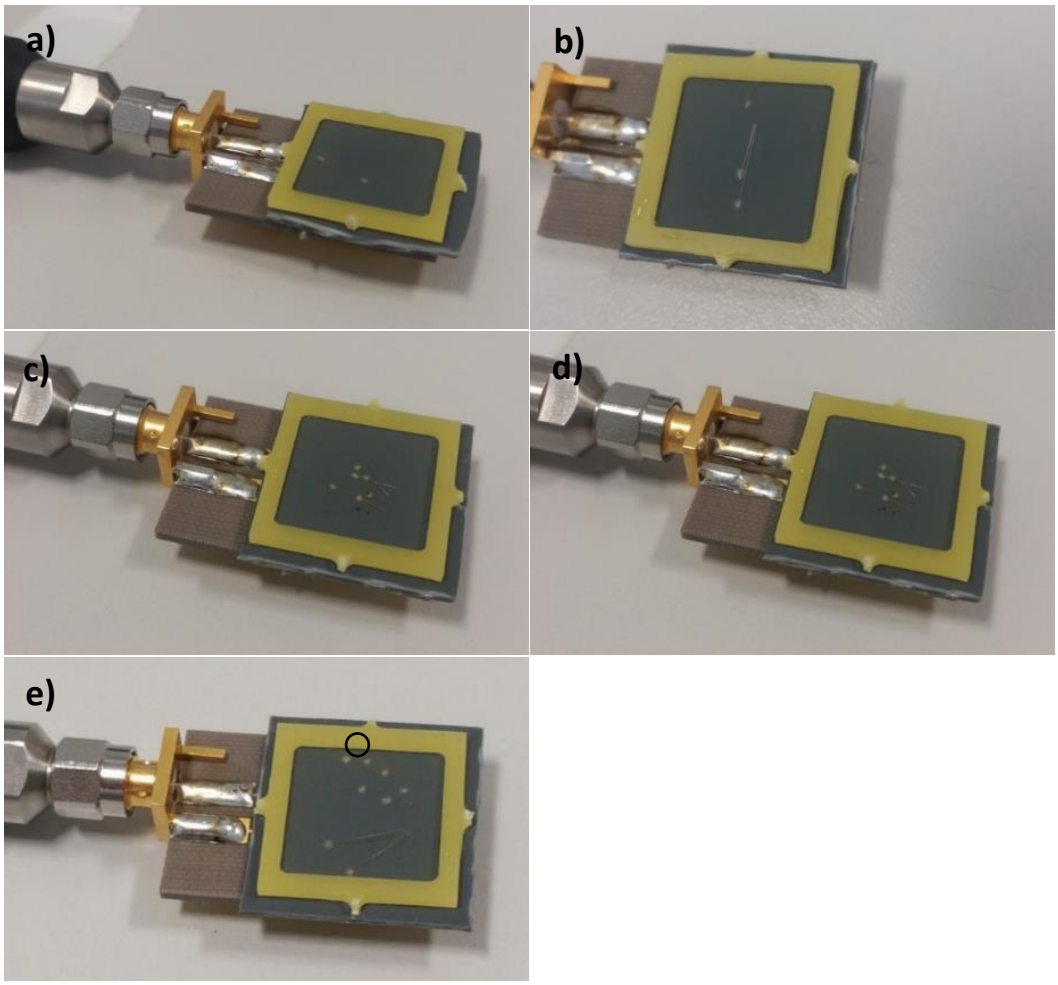

Figure 2.14 – Treatment PVC Panels with Plaques being Measured on a Sensor. *The five treatment panels had 2 plaques (**a**), 3 plaques (**b**), 6 plaques (**c**), 12 plaques (**d**) and 9 plaques of which one is just underneath the FR4 well shown in the black circle (**e**).*

Measurements with artificial seawater (**Wet**) as well as **Dry** from 10 MHz to 15 GHz were plotted as the mean Reflection Coefficient of the 5 repeat measurements for the four sensors 1 line Au PTFE (*figure 2.15;* **Wet** (**a**) **Dry** (**b**)), 3pr Au PTFE (*figure 2.16;* **Wet** (**a**) **Dry** (**b**)), 9pr Au PTFE (*figure 2.17;* **Wet** (**a**) **Dry** (**b**)) and 2 x 3pr Au PTFE (*figure 2.18;* **Wet** (**a**) **Dry** (**b**)).

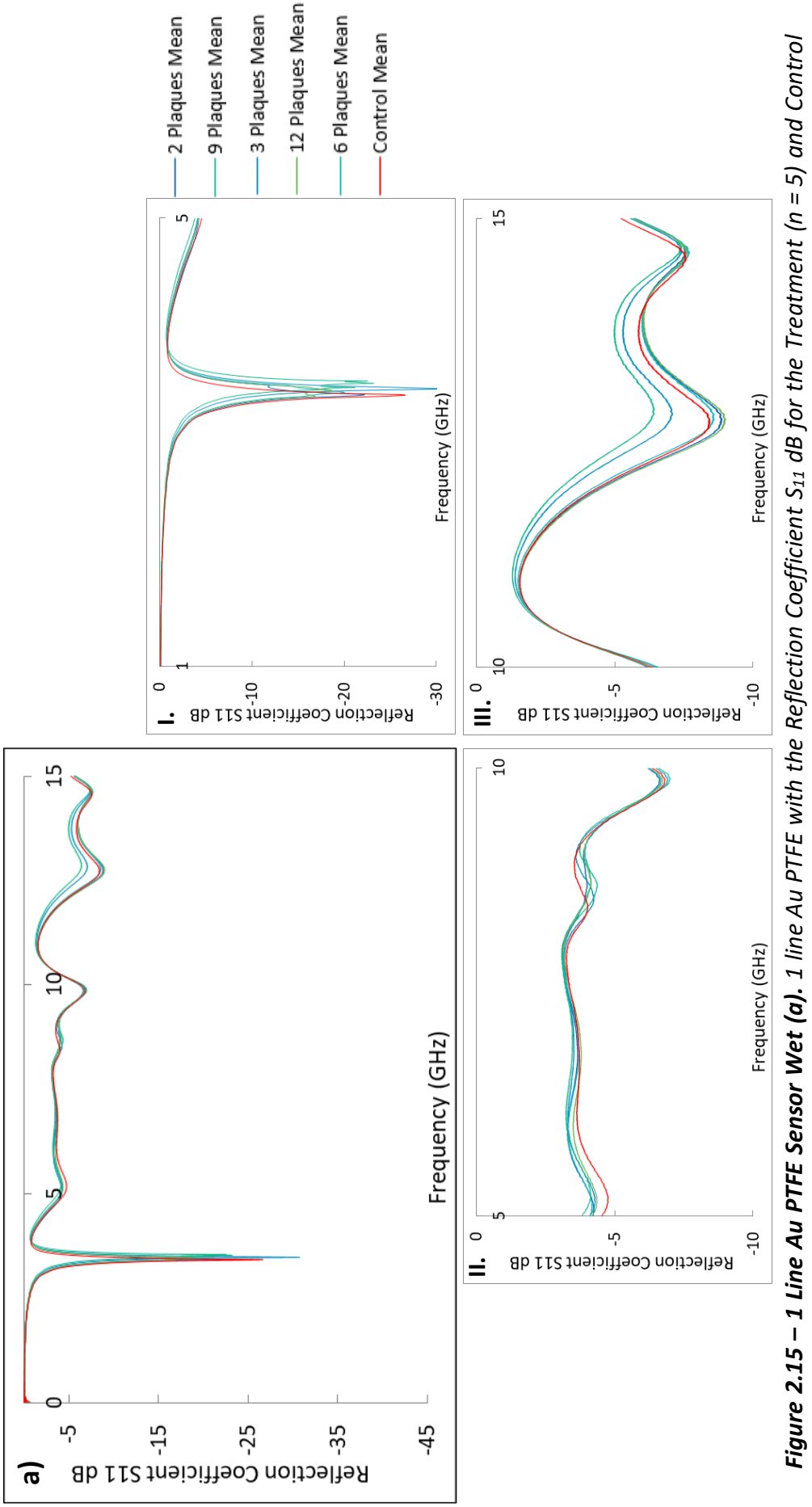

Figure 2.15 – 1 Line Au PTFE Sensor Wet (a). *1 line Au PTFE with the Reflection Coefficient S_{11} dB for the Treatment (n = 5) and Control (n=1) panels from* ***10 MHz to 15 GHz. Figures I., II. and III.*** *show the output at* ***1 to 5 GHz, 5 to 10 GHz*** *and* ***10 to 15 GHz****, respectively.*

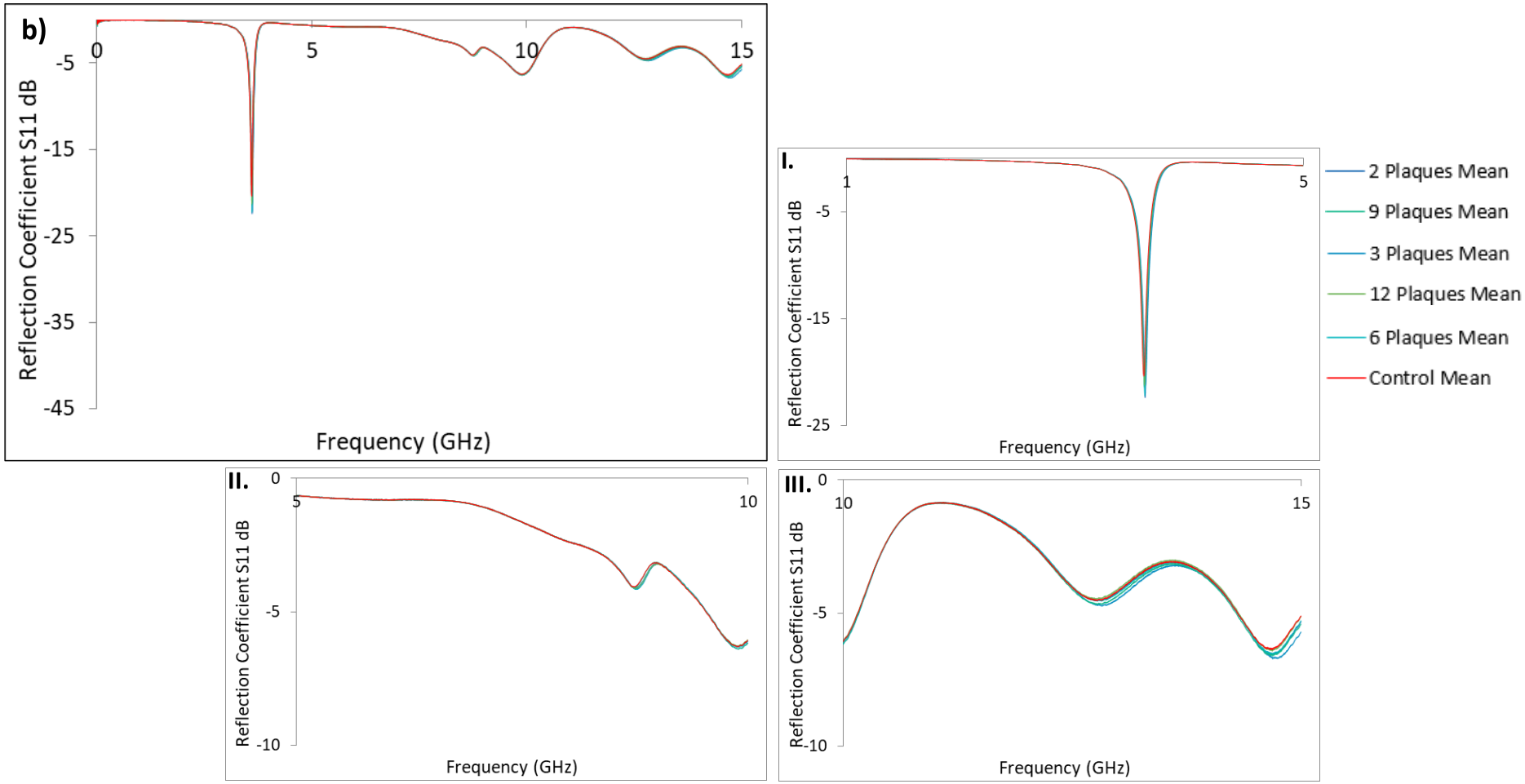

Figure 2.15 – 1 Line Au PTFE Sensor Dry (b). *1 line Au PTFE with the Reflection Coefficient S_{11} dB for the Treatment (n = 5) and Control (n=1) panels from* ***10 MHz to 15 GHz****.* ***Figures I., II. and III.*** *show the output at* ***1 to 5 GHz****,* ***5 to 10 GHz*** *and* ***10 to 15 GHz****, respectively.*

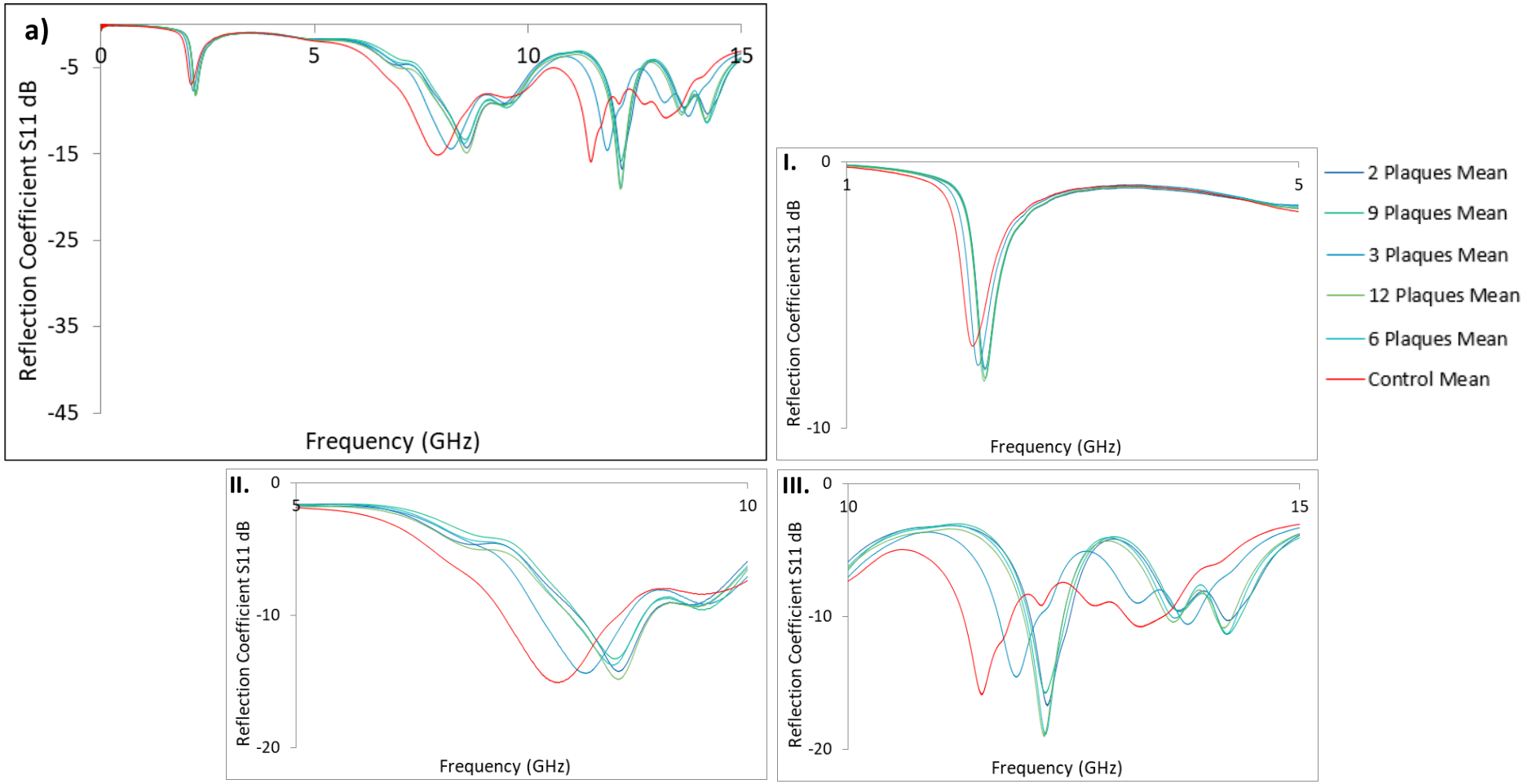

Figure 2.16 – 3pr Au PTFE Sensor Wet (a). *3pr Au PTFE with the Reflection Coefficient S_{11} dB for the Treatment (n = 5) and Control (n=1) panels from* ***10 MHz to 15 GHz****.* ***Figures I., II. and III.*** *show the output at* ***1 to 5 GHz, 5 to 10 GHz*** *and* ***10 to 15 GHz****, respectively.*

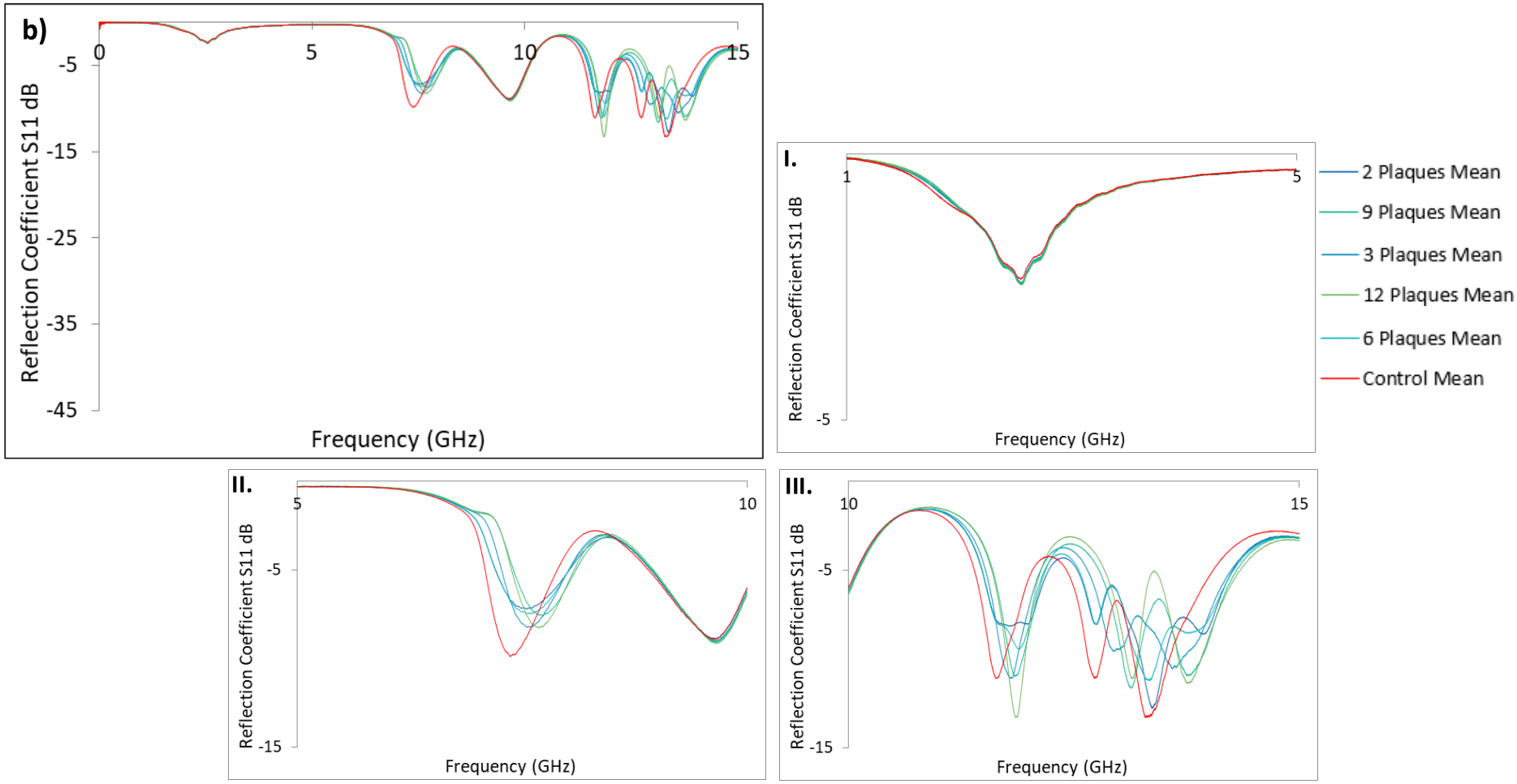

Figure 2.16 – 3pr Au PTFE Sensor Dry (b). *3pr Au PTFE with the Reflection Coefficient S_{11} dB for the Treatment (n = 5) and Control (n=1) panels from* ***10 MHz to 15 GHz****.* ***Figures I., II. and III.*** *show the output at* ***1 to 5 GHz, 5 to 10 GHz*** *and* ***10 to 15 GHz****, respectively.*

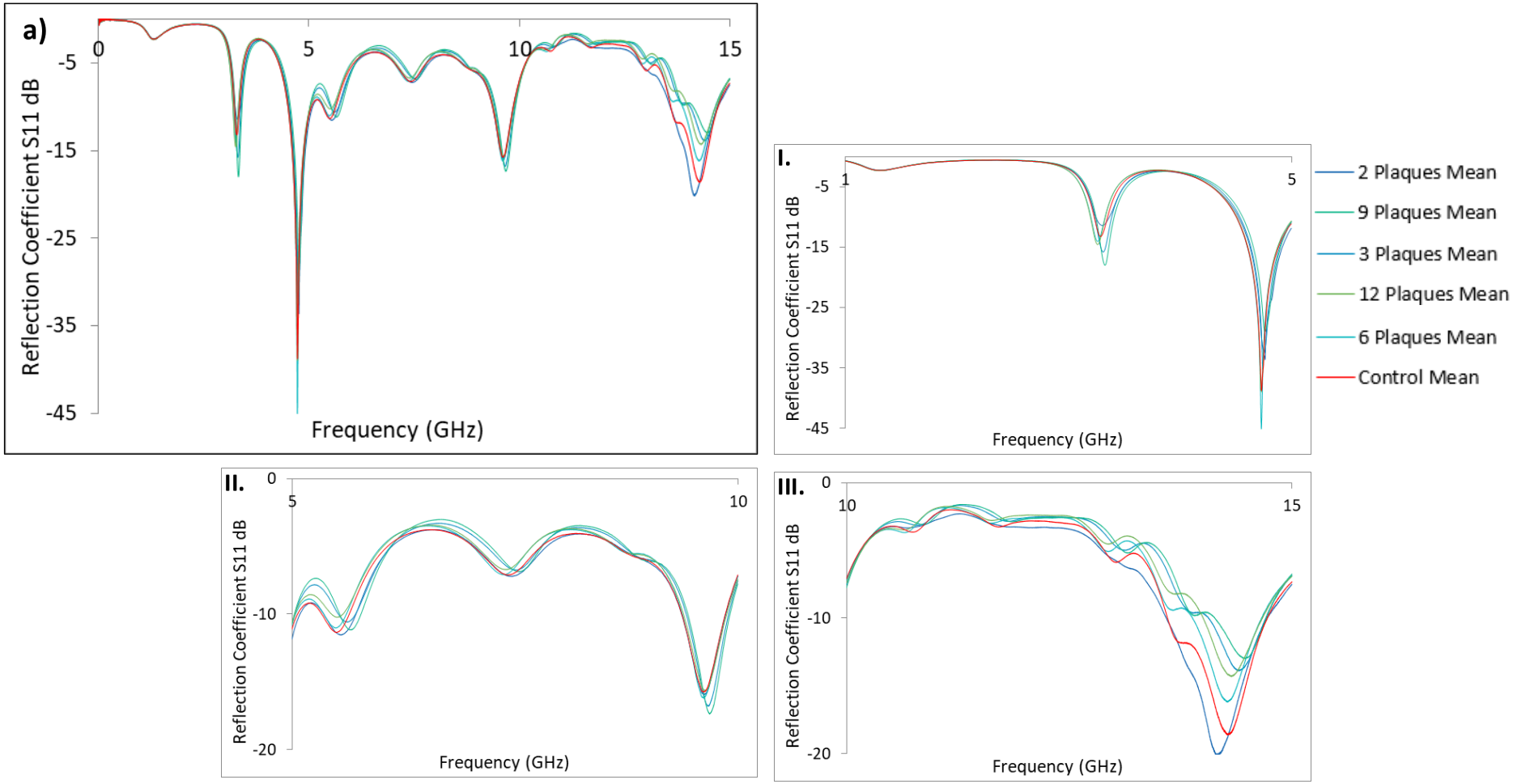

Figure 2.17 – 9pr Au PTFE Sensor Wet (a). *9pr Au PTFE with the Reflection Coefficient S_{11} dB for the Treatment (n = 5) and Control (n=1) panels from* ***10 MHz to 15 GHz****.* ***Figures I., II. and III.*** *show the output at* ***1 to 5 GHz, 5 to 10 GHz*** *and* ***10 to 15 GHz****, respectively.*

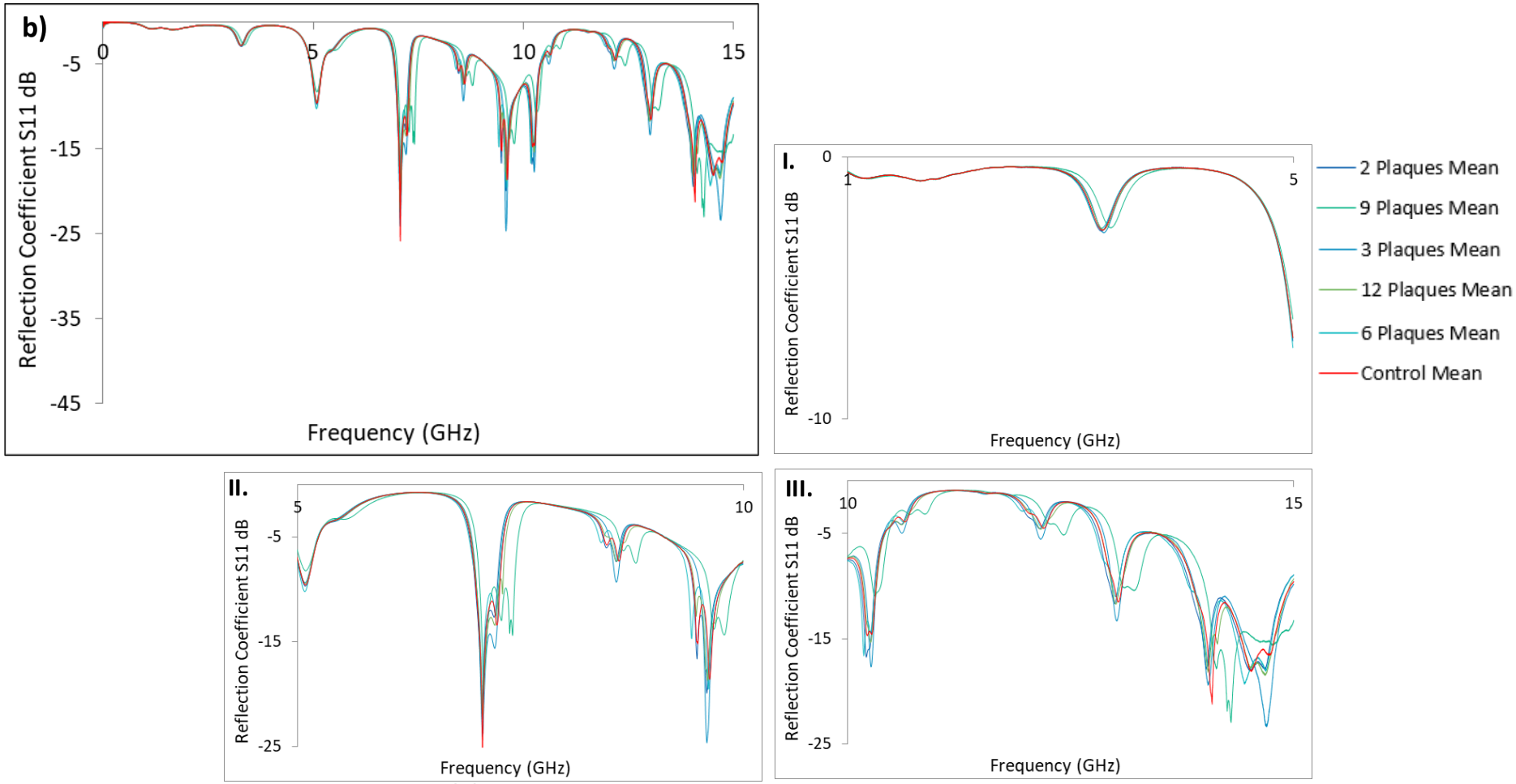

Figure 2.17 – 9pr Au PTFE Sensor Dry (b). *9pr Au PTFE with the Reflection Coefficient S_{11} dB for the Treatment (n = 5) and Control (n=1) panels from* ***10 MHz to 15 GHz****.* ***Figures I., II. and III.*** *show the output at* ***1 to 5 GHz****,* ***5 to 10 GHz*** *and* ***10 to 15 GHz****, respectively.*

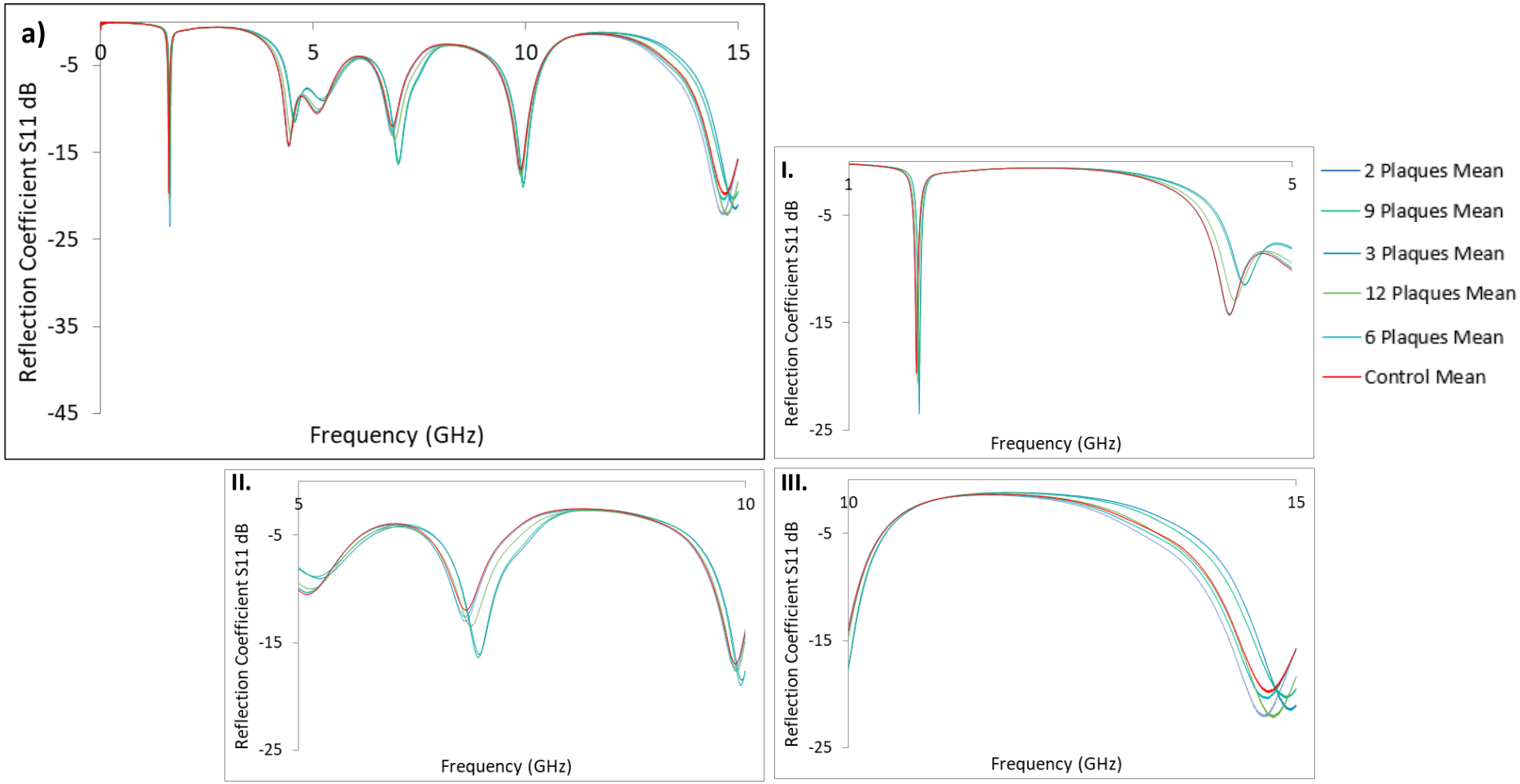

Figure 2.18 – 2 × 3pr Au PTFE Sensor Wet (a). *2 × 3pr Au PTFE with the Reflection Coefficient S_{11} dB for the Treatment (n = 5) and Control (n=1) panels from* ***10 MHz to 15 GHz***. ***Figures I., II. and III.*** *show the output at* ***1 to 5 GHz***, ***5 to 10 GHz*** *and* ***10 to 15 GHz****, respectively.*

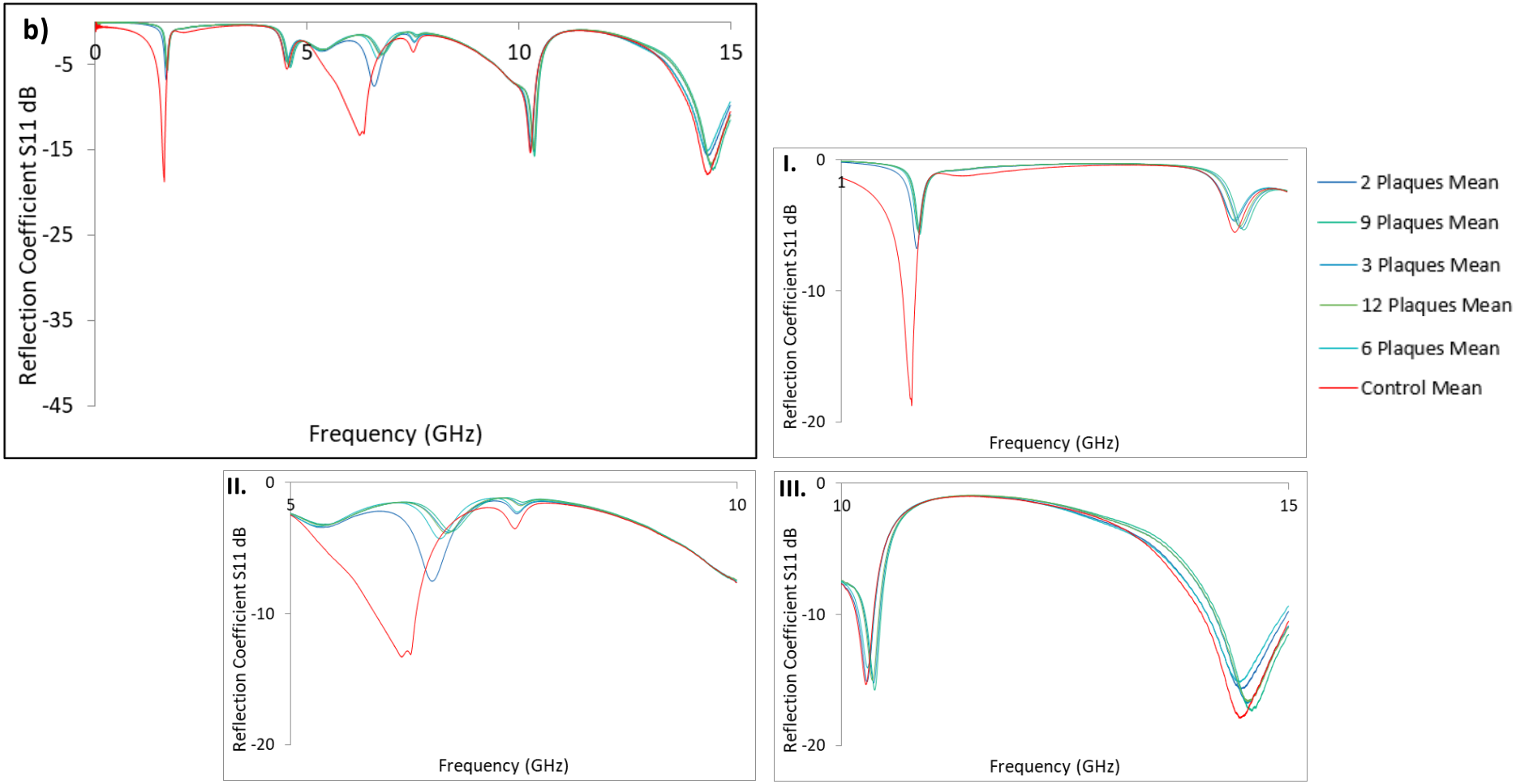

Figure 2.18 – 2 × 3pr Au PTFE Sensor Dry (b). *2 × 3pr Au PTFE with the Reflection Coefficient S_{11} dB for the Treatment (n = 5) and Control (n=1) panels from* ***10 MHz to 15 GHz***. ***Figures I., II. and III.*** *show the output at* ***1 to 5 GHz***, ***5 to 10 GHz*** *and* ***10 to 15 GHz***, *respectively.*

Differences are shown between the **Wet** and **Dry** Reflection Coefficient S_{11} dB outputs with both the Treatments and the Control. In the **Wet** condition, the 1 Line Au PTFE had the biggest difference between the Treatment and Control at 3.42 GHz for all except the 2 plaques panel, which was at 3.41 GHz; the 3pr Au PTFE sensor had the largest difference at 11.5 GHz for all the panels; the 9pr Au PTFE sensor detected the biggest difference at 4.73 GHz for all except the 12 plaques panel; and the 2 × 3pr sensor had the biggest difference between the Treatment and Control at 1.61 GHz (*table 2.3*).

The Impact of Orientation on the Detection of M. edulis Plaques with Four EMW Sensors with Varying IDE Geometries

The Treatment panel from Tank I had 32 plaques, Tank II had a Treatment panel with 18 plaques and Tank III had two panels with 6 plaques and 5 plaques. The largest difference was then deduced between the mean Reflection Coefficient of the Treatment and the Control for each Orientation and the corresponding frequency recorded (*table 2.3*).

Table 2.3 – The Frequency identified where the largest difference between each Reflection Coefficient of the Treatment and the Control occurred for all the sensors in the Initial detection Wet condition and at each Orientation.

Sensor	*Treatment*	*Frequency with the largest difference compared to the Control (GHz)*				
	Number of plaques	**Initial Detection; Wet**	**Orientation A**	**Orientation B**	**Orientation C**	**Orientation D**
1 Line	*2*	3.41	-	-	-	-
	3	3.42	-	-	-	-
	5	-	3.38	3.40	3.43	3.38
	6	3.42	3.37	3.40	3.43	3.37
	9	3.42	-	-	-	-
	12	3.42	-	-	-	-
	18	-	3.38	3.40	3.45	3.38
	32	-	3.38	3.40	3.49	3.38
Average frequency		***3.42***	***3.38***	***3.40***	***3.45***	***3.38***
3pr	*2*	11.47	-	-	-	-
	3	11.46	-	-	-	-
	5	-	11.18	13.71	13.72	7.68
	6	11.48	13.86	13.73	13.72	7.85
	9	11.48	-	-	-	-
	12	11.47	-	-	-	-
	18	-	11.13	13.73	13.72	14.02
	32	-	7.51	13.73	13.72	7.68
Average frequency		***11.47***	***10.92***	***13.73***	***13.72***	***9.31***
9pr	*2*	4.73	-	-	-	-
	3	4.73	-	-	-	-
	5	-	4.64	4.66	4.67	4.68
	6	4.75	4.64	4.67	4.69	4.70
	9	4.73	-	-	-	-
	12	14.2	-	-	-	-
	18	-	4.64	4.67	4.67	3.22
	32	-	4.64	4.67	4.68	4.69
Average frequency		***6.64***	***4.64***	***4.67***	***4.68***	***4.32***
2 × 3pr	*2*	1.61	-	-	-	-
	3	1.61	-	-	-	-
	5	-	1.58	14.88	1.58	1.59
	6	1.61	1.58	1.60	1.59	1.59
	9	1.61	-	-	-	-
	12	1.61	-	-	-	-
	18	-	1.59	1.60	1.59	4.34
	32	-	1.58	4.34	1.59	1.59
Average frequency		***1.61***	***1.58***	***5.61***	***1.59***	***2.28***

The initial detection of *M. edulis* plaques with the 1 line Au PTFE sensor showed the biggest difference between the Reflection Coefficient of the Treatment and Control for the **Wet** experiment at 3.42 GHz ± 0.002 GHz. The impact of Orientation showed the biggest difference between the Treatment and Control for Orientation A at 3.38 GHz ± 0.003 GHz; Orientation B at 3.40 GHz ± 0.000 GHz; Orientation C at 3.45 GHz ± 0.014 GHz; and Orientation D at 3.38 GHz ± 0.003 GHz (*figure 2.19*).

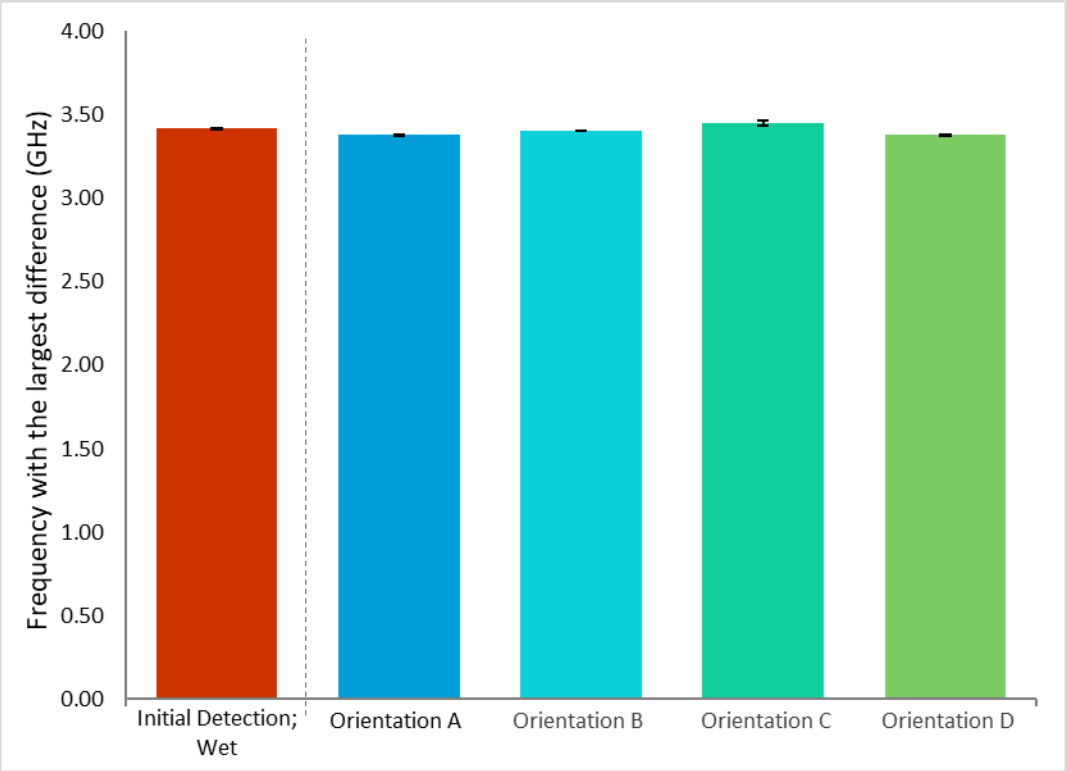

Figure 2.19 – 1 Line Au PTFE Sensor; Frequency with the Largest Difference Between the Reflection Coefficient of the Treatment and Control *for the initial detection of M. edulis in the* ***Wet*** *condition and the frequency with the largest difference between the Treatment and Control for the four Orientations when investigating the impact of Orientation showing a* ***detection frequency range for 1 Line Au PTFE Sensor from 3.38 GHz to 3.45 GHz for M. edulis byssal plaque.***

The initial detection of *M. edulis* plaques with the 3pr Au PTFE sensor showed the biggest difference between the Reflection Coefficient of the Treatment and Control for the **Wet** experiment at 11.47 GHz ± 0.004 GHz. The impact of Orientation showed the biggest difference between the Treatment and Control for Orientation A at 10.92 GHz ± 1.303 GHz; Orientation B at 13.73 GHz ± 0.005 GHz; Orientation C at 13.72 GHz ± 0.000 GHz; and Orientation D at 9.31 GHz ± 1.571 GHz (*figure 2.20*).

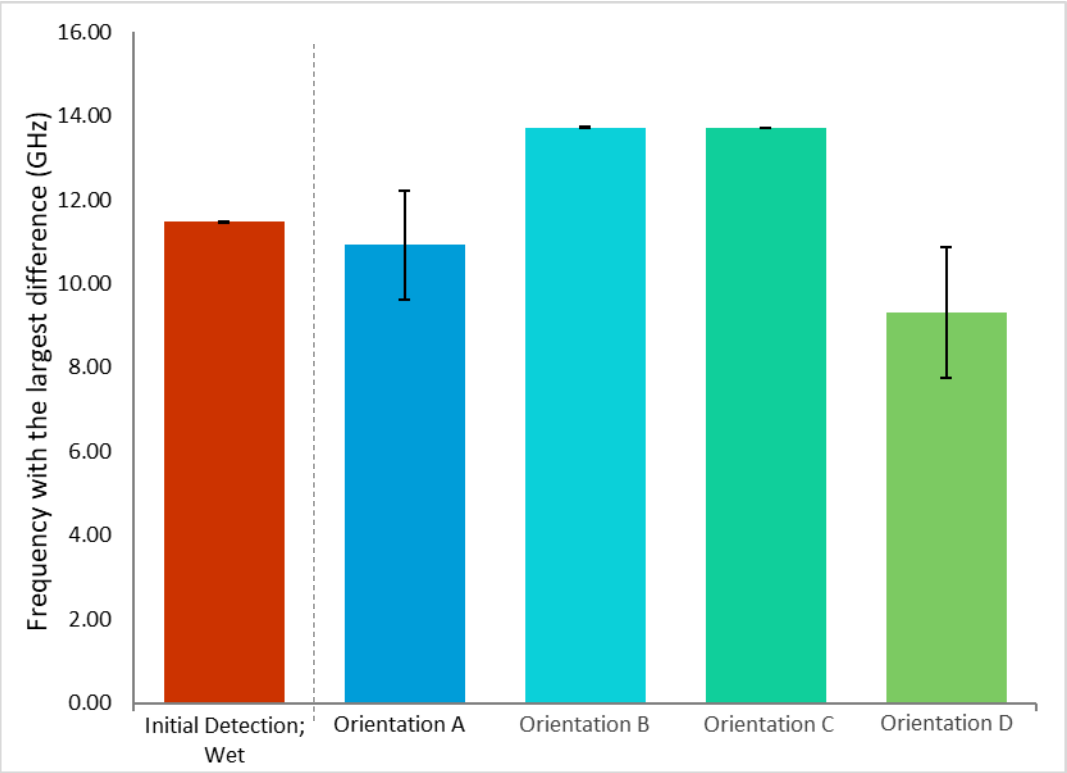

Figure 2.20 – 3pr Au PTFE Sensor; Frequency with the Largest Difference Between the Reflection Coefficient of the Treatment and Control *for the initial detection of M. edulis in the* ***Wet*** *condition and the frequency with the largest difference between the Treatment and Control for the four Orientations when investigating the impact of Orientation showing a* ***detection frequency range for 3pr Au PTFE Sensor from 9.31 GHz to 13.73 GHz for M. edulis byssal plaque.***

The initial detection of *M. edulis* plaques with the 9pr Au PTFE sensor showed the biggest difference between the Reflection Coefficient of the Treatment and Control for the **Wet** experiment at 6.64 GHz ± 1.901 GHz. The impact of Orientation showed the biggest difference between the Treatment and Control for Orientation A at 4.64 GHz ± 0.000 GHz; Orientation B at 4.67 GHz ± 0.003 GHz; Orientation C at 4.68 GHz ± 0.005 GHz; and Orientation D at 4.32 GHz ± 0.368 GHz (*figure 2.21*).

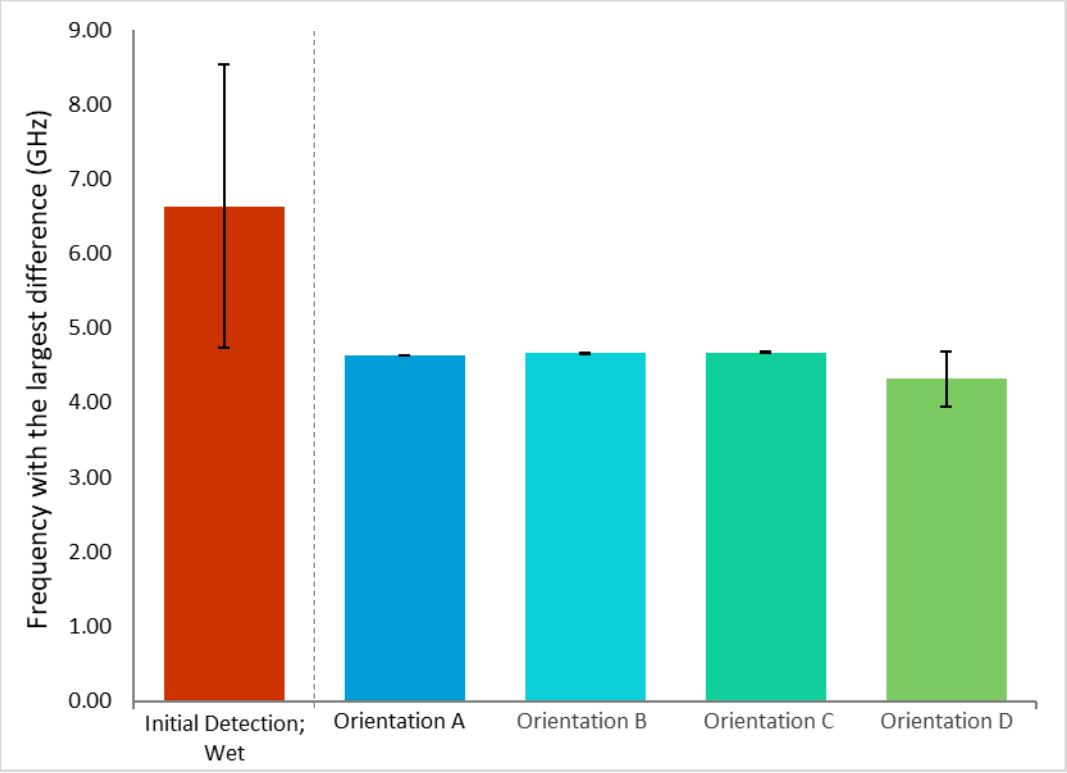

Figure 2.21 – 9pr Au PTFE Sensor; Frequency with the Largest Difference Between the Reflection Coefficient of the Treatment and Control *for the initial detection of M. edulis in the* ***Wet*** *condition and the frequency with the largest difference between the Treatment and Control for the four Orientations -when investigating the impact of Orientation showing a* ***detection frequency range for 9pr Au PTFE Sensor from 4.32 GHz to 6.64 GHz for M. edulis byssal plaque.***

The initial detection of *M. edulis* plaques with the 2 × 3pr Au PTFE sensor showed the biggest difference between the Reflection Coefficient of the Treatment and Control for the **Wet** experiment at 1.61 GHz ± 0.000 GHz. The impact of Orientation showed the biggest difference between the Treatment and Control for Orientation A at 1.58 GHz ± 0.003 GHz; Orientation B at 5.61 GHz ± 3.158 GHz; Orientation C at 1.59 GHz ± 0.003 GHz; and Orientation D at 2.28 GHz ± 0.688 GHz (*figure 2.22*).

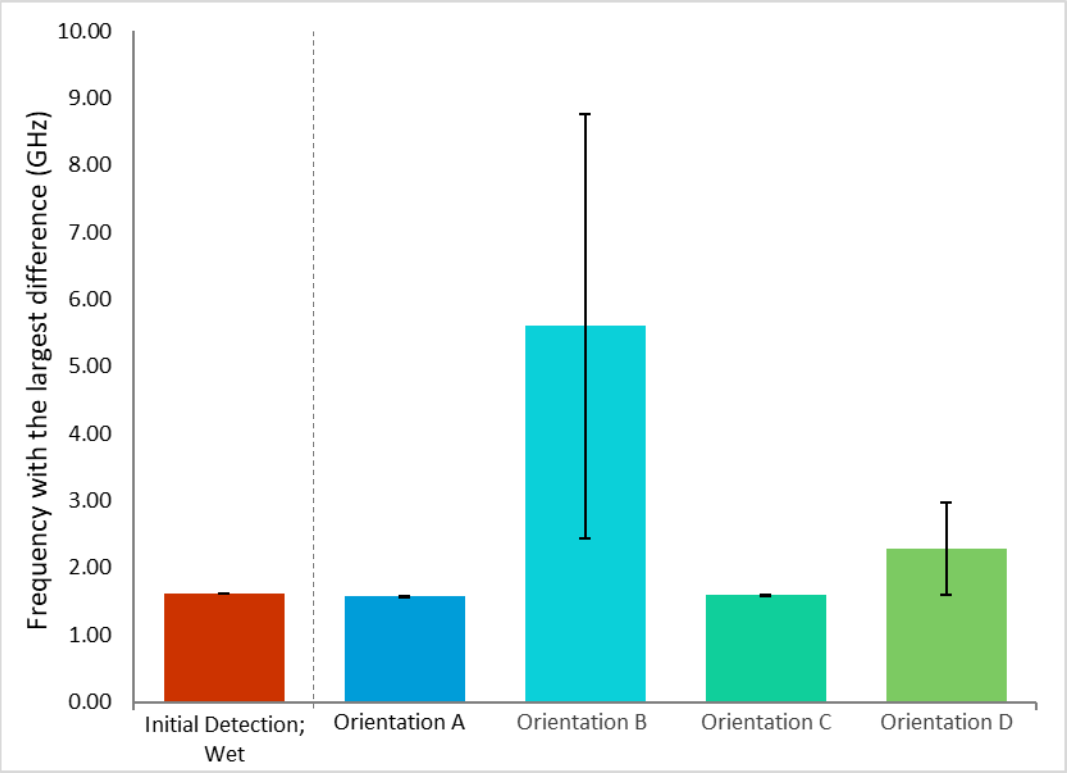

Figure 2.22 – 2 × 3pr Au PTFE Sensor; Frequency with the Largest Difference Between the Reflection Coefficient of the Treatment and Control *for the initial detection of M. edulis in the* ***Wet*** *condition and the frequency with the largest difference between the Treatment and Control for the four Orientations when investigating the impact of Orientation showing a* ***detection frequency range for 2 × 3pr Au PTFE Sensor from 1.58 GHz to 2.28 GHz for M. edulis byssal plaque.***

2.3.2. Efficacy of Varying Sensing Materials for Detecting *M. edulis* Plaque on a Surface with the Selected EMW Sensor

The number of byssal plaques put down by *M. edulis* was significantly different between the four materials (*F = 3.509, df = 3, p = 0.017; figure 2.23).*

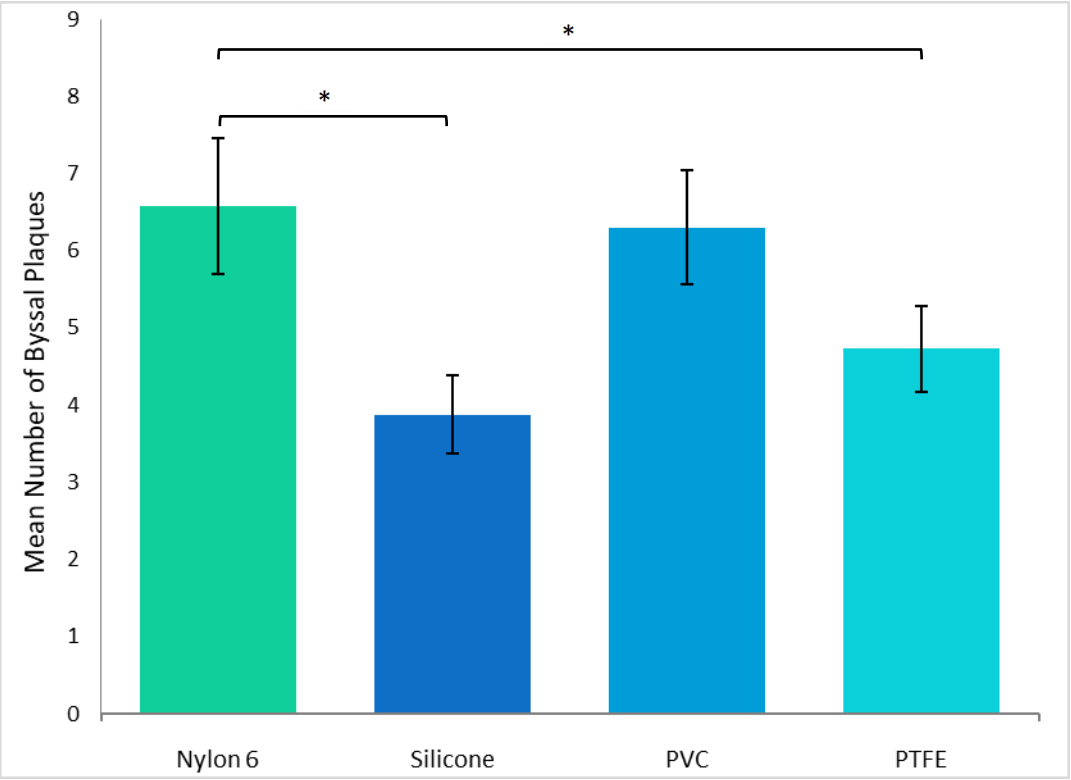

Figure 2.23 – Mean Number of Byssal Plaques per Treatment Panel for all four materials *and the corresponding error bar.*

** indicates statistical significance (p ≤ 0.05).*

Nylon 6 had a significantly higher mean number of byssal plaques (6.575 ± 0.8843) compared to Silicone (3.875 ± 0.5054; *p = 0.031*). There were no significant differences between the other materials (Nylon 6 and PVC: *p = 0.992*; Nylon 6 and PTFE: *p = 0.230*; Silicone and PVC: *p = 0.064;* Silicone and PTFE: *p = 0.818*; and PVC and PTFE: *p = 0.370*).

The mean Reflection Coefficients for the Treatment (n = 40) and Control (n = 40) were plotted together with the standard error (SE) for each Material at each frequency (60,000) between 10 MHz and 15 GHz with the selected senor (9pr Au PTFE) (*figure 2.24)*.

a)

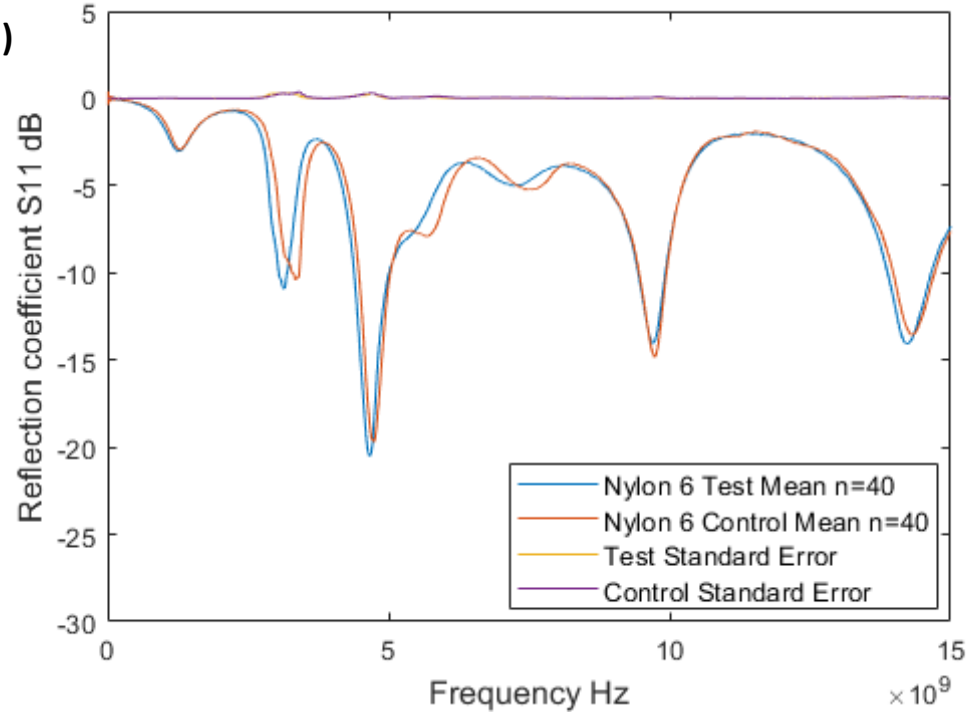

b)

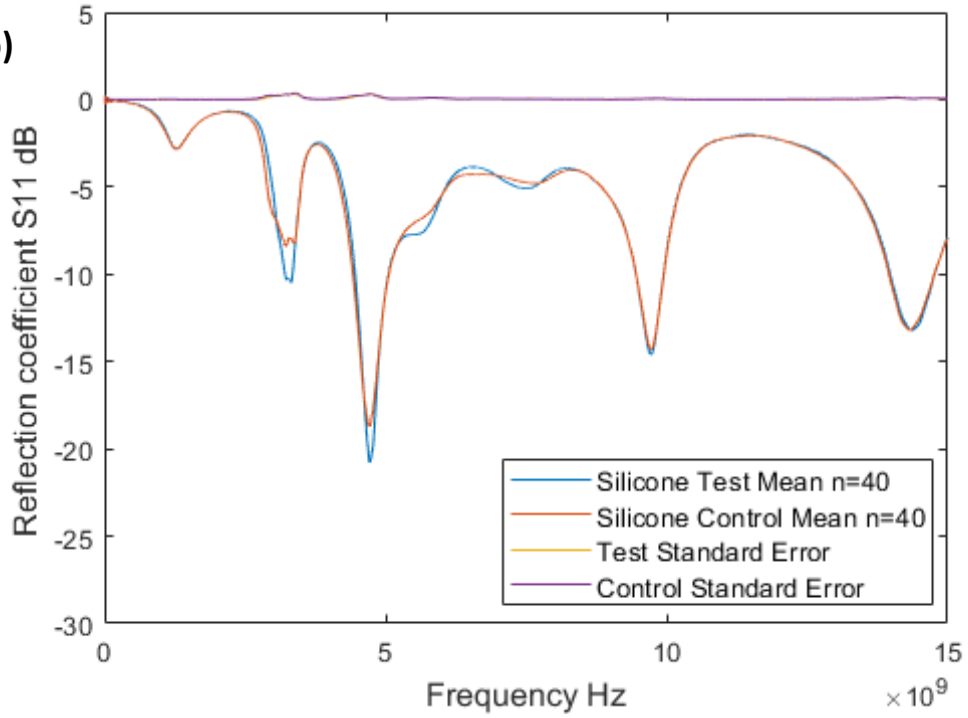

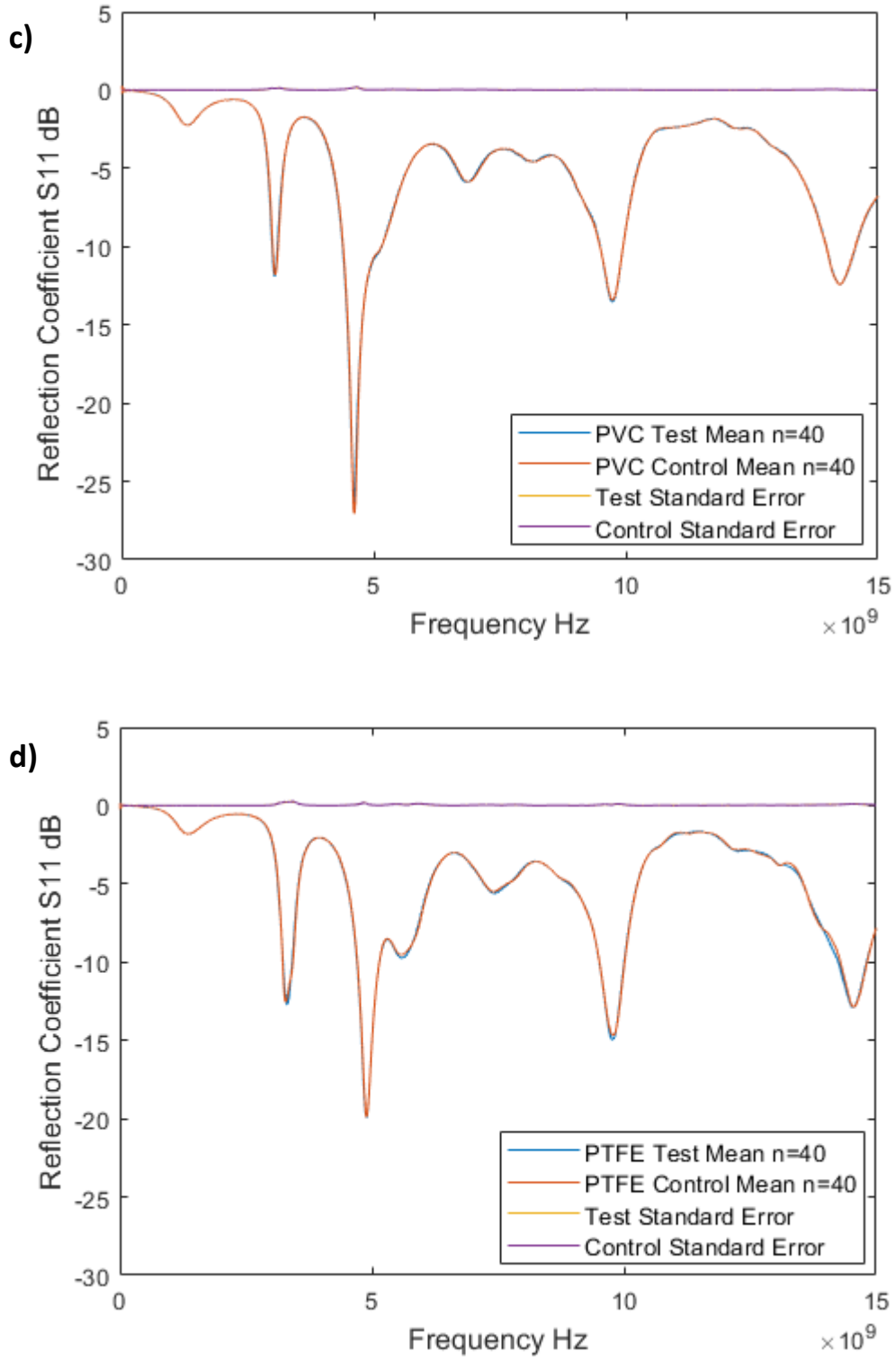

Figure 2.24 – The Mean Reflection Coefficient for the Treatment (n = 40) and Control (n = 40) and Their Respective Standard Error. *These are shown for the four Materials tested, Nylon 6 (**a**), Silicone (**b**), PVC (**c**) and PTFE (**d**).*

There was a significant difference between the Reflection Coefficients at their respective frequencies of the four Materials (*F = 47.042, df = 3, p ≤ 0.001*) as well as a significant difference between the Treatments within each Material (*F = 13.057, df = 4, p ≤ 0.001; figure 2.25*).

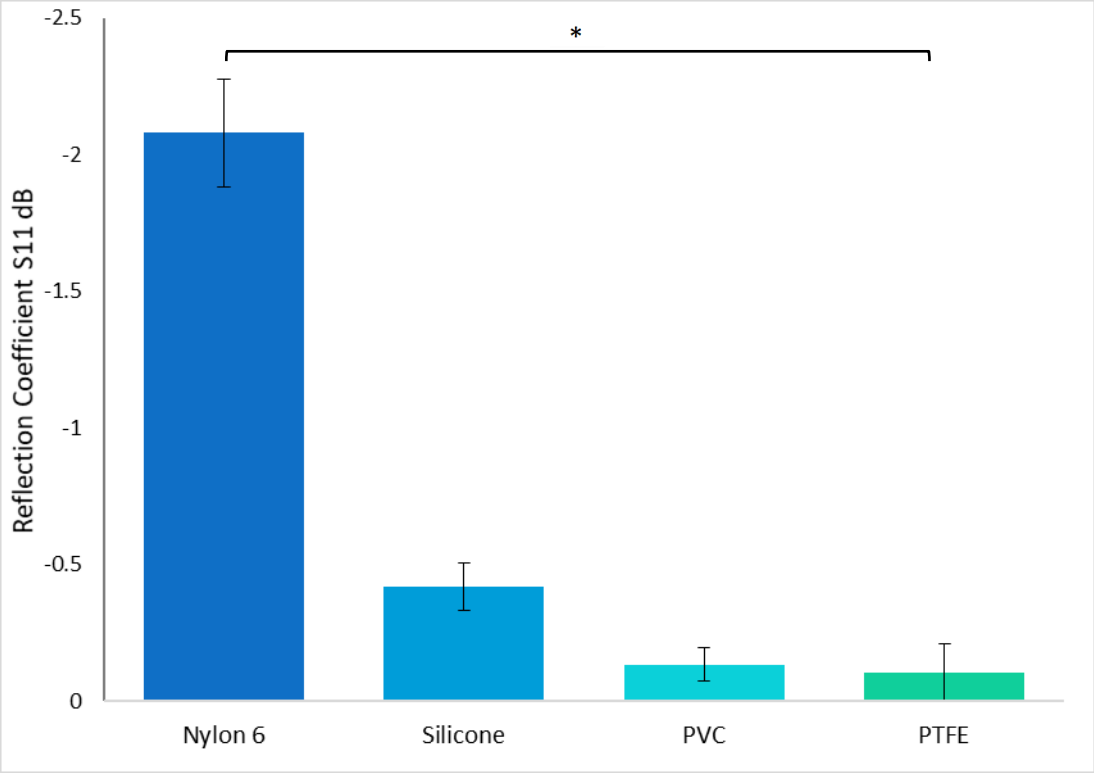

Figure 2.25 – The Biggest Difference Between the Reflection Coefficient of the Treatment and Control for each material *at their respective frequencies and the respective standard error bar.*

** indicates statistical significance (p ≤ 0.05).*

Nylon 6 had a significant difference between the mean Reflection Coefficient of the Treatment and Control of 2.08 (± 0.197) dB at 5.84 GHz (*F = 17.981, df = 1, p ≤ 0.001*) and Silicone had a significant difference of 0.42 (± 0.197) dB at 6.55 GHz (*F = 4.935, df = 1, p = 0.029*). At 7.10 GHz, PVC had a biggest difference of 0.13 (± 0.062) dB, however this was not significant (*F = 2.174, df = 1, p = 0.144*).

PTFE at 7.91 GHz, had a biggest difference of 0.11 (± 0.103) dB which was not significant (*F = 0.175, df = 1, p = 0.677*).

2.3.2.1. Reliability and Replicability of Sensing Materials for Detection of *M. edulis* plaques on a Surface with the Selected EMW Sensor

The mean Reflection Coefficient of the Treatment and Control is shown for each of the four materials as a line graph as well as the largest difference between the mean Reflection Coefficient for each Treatment (n = 40) and Control (n = 40) for each tank as a scatter graph (*figure 2.26*).

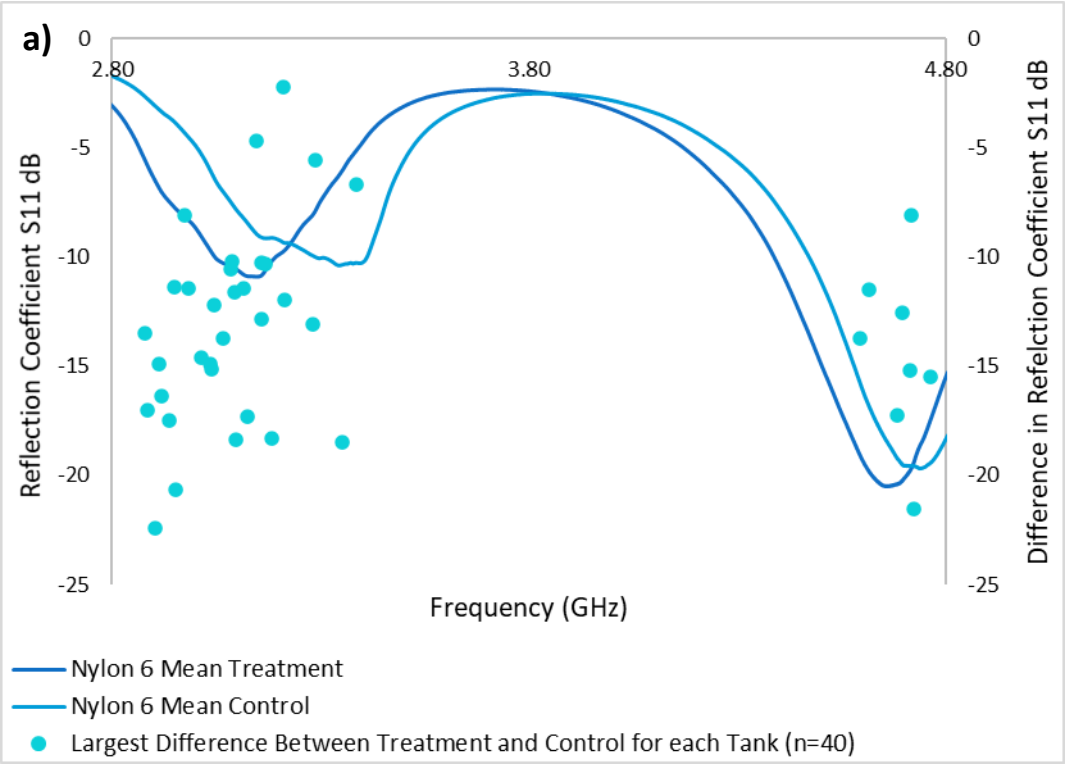

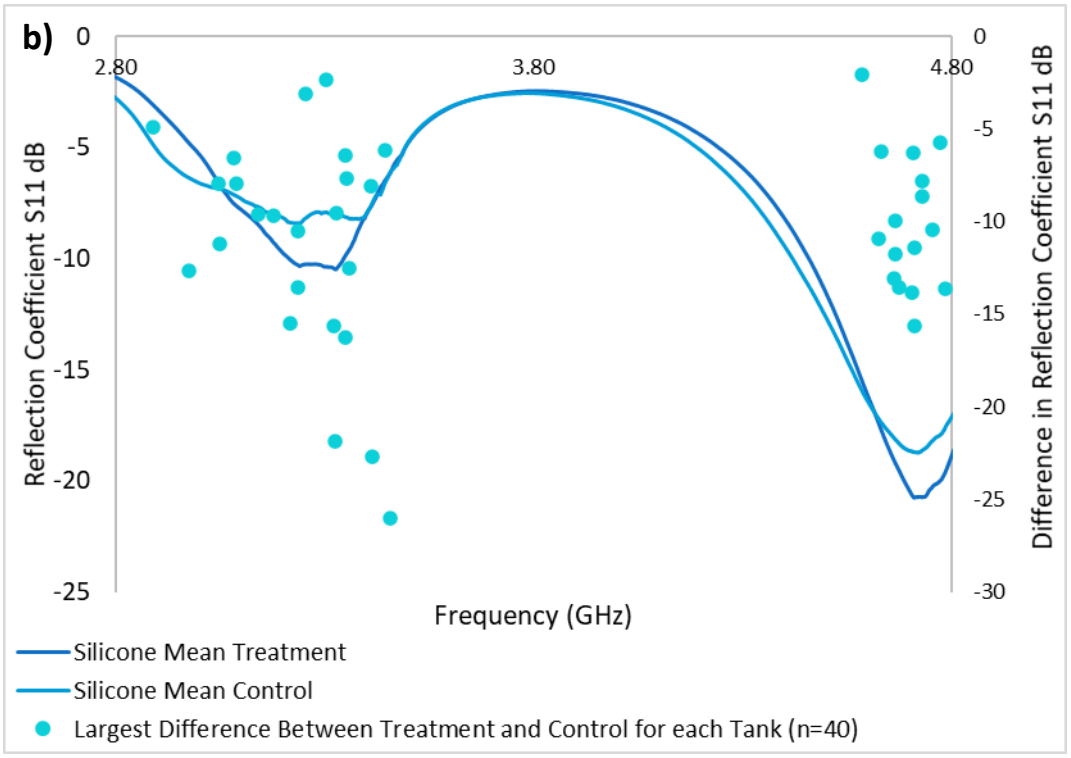
b)
0
2.80
3.80
4.80
-5
-10
-15
-20
-25
0
-5
-10
-15
-20
-25
-30
Reflection Coefficient S11 dB
Difference in Reflection Coefficient S11 dB
Frequency (GHz)
Silicone Mean Treatment
Silicone Mean Control
Largest Difference Between Treatment and Control for each Tank (n=40)

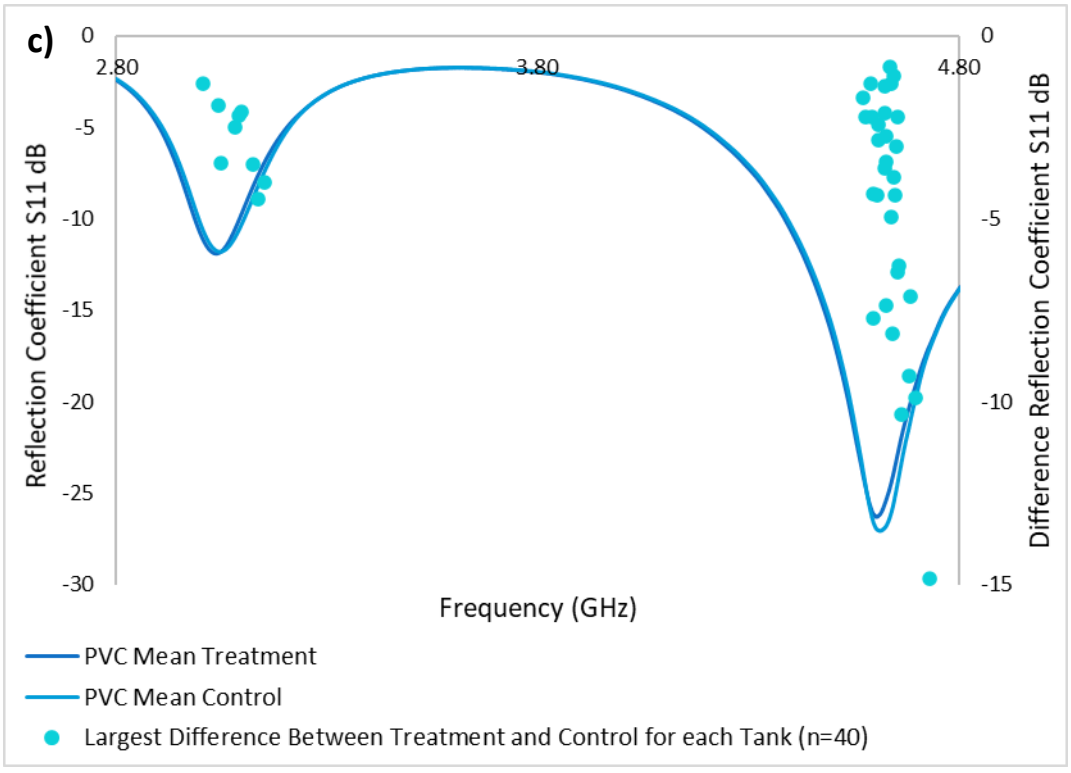
c)
0
2.80
3.80
4.80
-5
-10
-15
-20
-25
-30
0
-5
-10
-15
Reflection Coefficient S11 dB
Difference Reflection Coefficient S11 dB
Frequency (GHz)
PVC Mean Treatment
PVC Mean Control
Largest Difference Between Treatment and Control for each Tank (n=40)

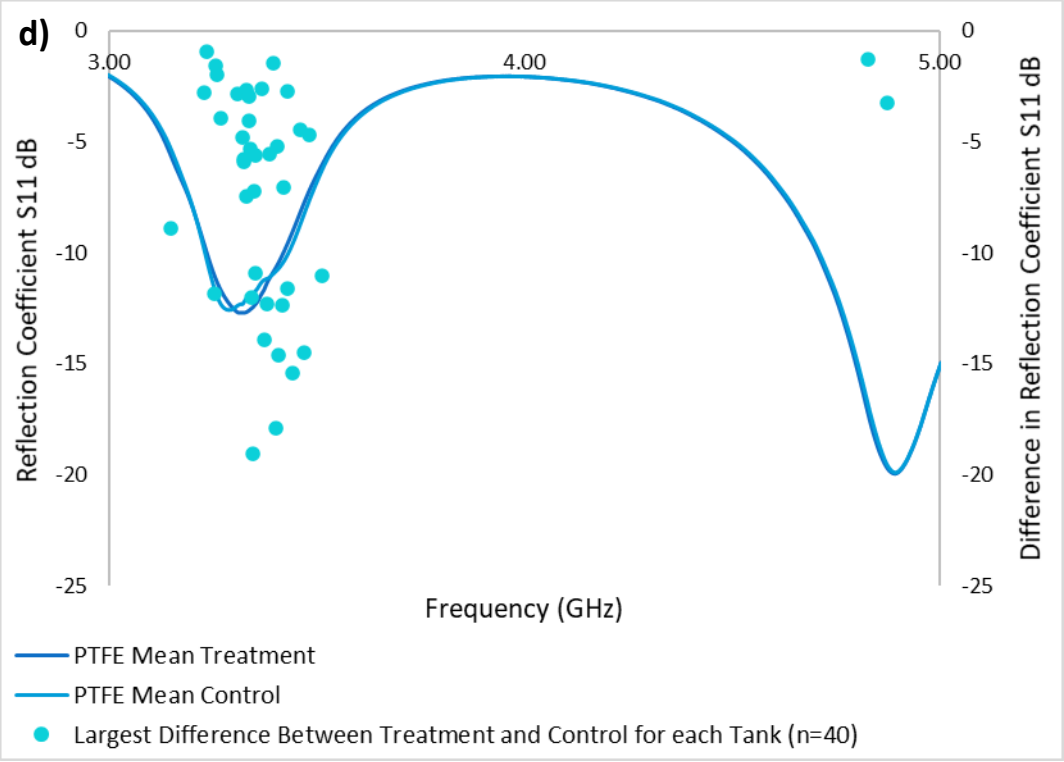

Figure 2.26 – Difference in Reflection Coefficient of the Treatment and Control *for each material; Nylon 6 (**a**), Silicone (**b**), PVC (**c**) and PTFE (**d**); whereby the mean Reflection Coefficient of the Treatment and Control is shown as a line graph (primary y-axis) and the largest difference between the Reflection Coefficient for each Treatment (n = 40) and Control (n = 40) per tank is shown as a scatter graph (secondary y-axis).*

The data show two key regions where the biggest difference between the Reflection Coefficient of the Treatment and Control is consistently at the troughs (*figure 2.27*).

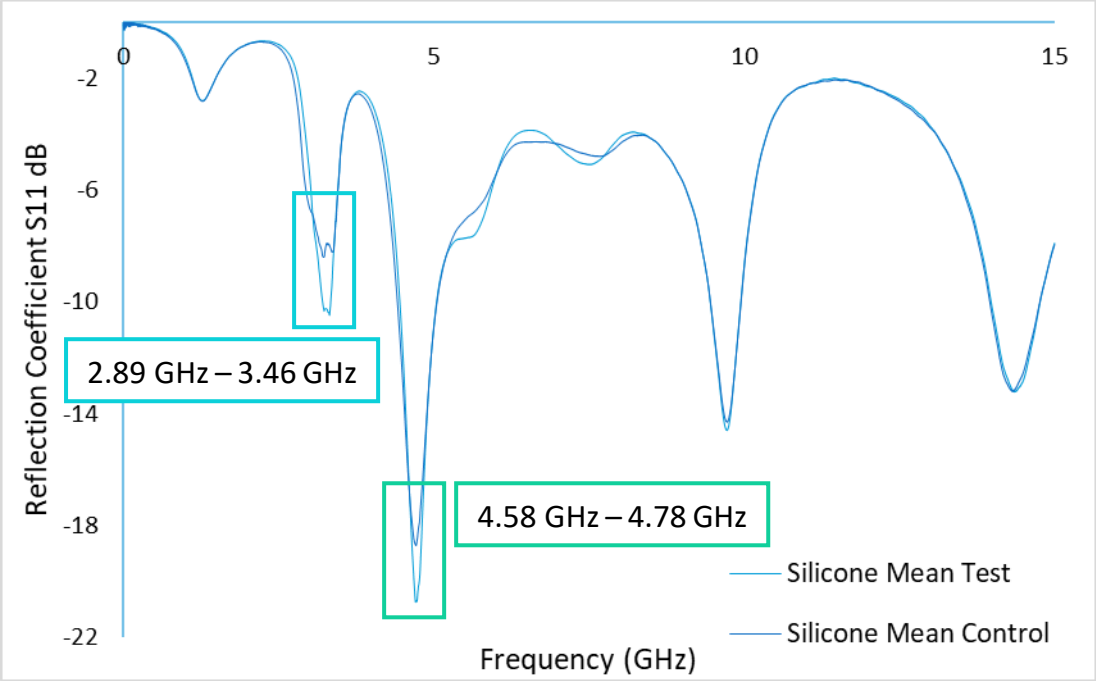

Figure 2.27 – Two Key Frequency Regions with the Biggest Difference for Silicone *between the Reflection Coefficient of the Treatment and Control for all the Panels were identified.*

The overall means were re-evaluated for the biggest difference between the Reflection Coefficient of the Treatment and Control. The new frequency with the biggest difference was found at 3.41 GHz for Nylon 6 with a significant difference between the Reflection Coefficient of the Treatment and Control of 5.56 (± 0.550) dB (*F = 110.091, df = 1, p ≤ 0.001*) and no significant difference between the Orientations (*F = 1.640, df = 6, p = 0.133*). Silicone had a significant difference of the Reflection Coefficient of 2.52 (± 0.656) dB at 3.33 GHz (*F = 18.258, df = 1, p = 0.005*) and no significant difference between the Orientations (*F = 1.615, df = 6, p = 0.140*). PVC had a significant difference between the Reflection Coefficient of the Treatment and Control of 1.67 (± 0.358) dB (*F = 12.080, df = 1, p = 0.013*) at 4.64 GHz, however there was also a significant difference between

the Orientations (*F = 3.630, df = 6, p = 0.001*). At 3.34 GHz, PTFE had a biggest difference of the Reflection Coefficient of 0.66 (± 0.463) dB, however, this was not significant (*F = 3.090, df = 1, p = 0.129*) nor was the effect of Orientation (*F = 1.318, df = 6, p = 0.246*) (*figure 2.28*).

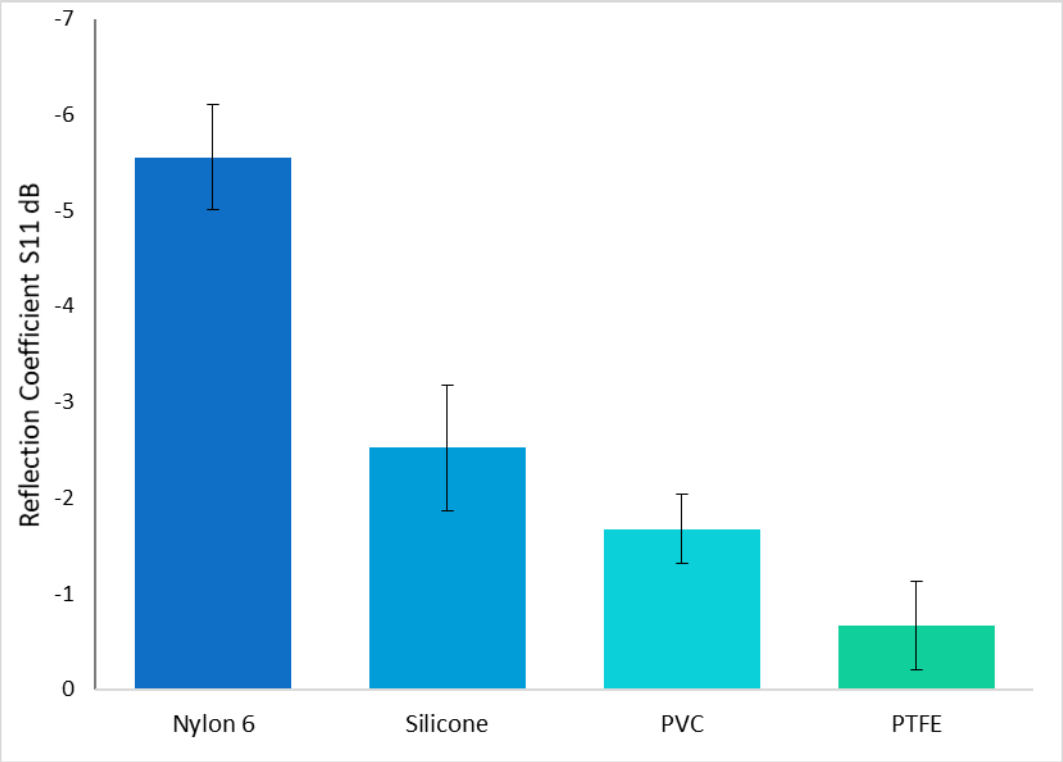

Figure 2.28 – The Biggest Difference Between the Reflection Coefficient of the Treatment and Control *for each material at their respective frequencies and the respective standard error bar.*

There was a significant difference between the Reflection Coefficient at their respective frequencies of the four materials (*F = 999.712, df = 3, p ≤ 0.001; figure 2.28*) as well as a significant difference between the treatments in the materials (*F = 13.057, df = 4, p ≤ 0.001*).

2.4. Discussion

The first aim of the study was to determine the efficacy of the model species, the blue mussel, *M. edulis,* detection depending on the geometry and number of IDEs of the planar EMW sensor, *in vitro*. The study demonstrated that the number and geometry of the IDE of the sensors may impact the detection efficacy in that the sensors were able to detect the presence of artificial seawater on the surface, however, only the 1 line Au PTFE sensor did not show differences with the byssal plaques in the dry condition indicating a lower detection efficacy than that of the 3pr Au PTFE, 9pr Au PTFE and 2 × 3pr Au PTFE sensors.

Furthermore, detection efficacy on a surface may be impacted by the Orientation of the material relative to the sensor array. Therefore, the second aim of the study was to determine if the efficacy of detection was impacted by the Orientation, *in vitro*. There was no effect of Orientation with the 1 line Au PTFE and the 9pr Au PTFE sensors, however, variability with differing Orientations was demonstrated with the 3pr Au PTFE sensor and more distinctly with the 2 × 3pr Au PTFE sensor.

Finally, this led to the consideration of the type of surface to be used for biofouling detection and so, the final aim of the study was to determine the efficacy of *M. edulis* detection on differing materials based on wettability and relative permittivity, *in vitro*. The study demonstrated that the 9pr Au PTFE planar EMW contactless sensor detected the presence of *M. edulis* byssal plaques on Nylon 6 at 5.84 GHz and 3.41 GHz, Silicone at 6.55 GHz and 3.33 GHz, PVC at

4.64 GHz, however it was unable to detect the byssal plaque with the PTFE surface.

2.4.1. Pilot Experiment

Determining the efficacy of the sensors to detect *M. edulis* byssal plaques on a PVC surface demonstrated differences in the Reflection Coefficient output between the Wet and Dry conditions. The 1 line Au PTFE sensor showed differences in the Reflection Coefficient output, particularly at higher frequencies in the Wet condition indicating the sensor's ability to detect the presence of the artificial seawater beyond the PVC panel. However, in the Dry condition the output Reflection Coefficient showed little variance among the different number of byssal plaques on the PVC panels investigated. This may be due to the lack of seawater as well as the position of the plaques relative to the single electrode as they may not be directly over the reduced sensing area resulting in no clear difference between the panels investigated. The presence of a single electrode may result in a lack of a functioning two-electrode system with a redox cycling process for increased sensing capacity as well as a small sensing area (Min and Baeumner, 2004; Alexander *et al.*, 2010; Ibrahim *et al.*, 2013). When examining the effect of Orientation, the 1 line sensor showed little to no disparity in the frequency at which the largest difference was identified nor with the frequency identified in the Wet condition. Again, this may be due to the single electrode with a small and reduced sensing capacity which may be unable to detect the byssal plaque on the PVC surface. By increasing the number of electrodes on the

sensor to 3pr or 9pr, a resultant increase in the sensing area and sensing capacity may be demonstrated with a relatively stable frequency at which detection occurs, a phenomenon widely demonstrated (Alexander *et al.*, 2010; Sun *et al.*, 2018).

The 3pr, 9pr and 2 × 3pr Au PTFE sensors showed differences in the Reflection Coefficient output between the Wet and Dry conditions as well as between the PVC panels investigated. This demonstrated that these sensors may be able to detect not only the presence of the artificial seawater on the surface, but also the byssal plaques. This may be due to the increased number of electrodes that results in an increased sensing area as well as sensing capacity as shown in previous studies (Grover, 1999; Alexander *et al.*, 2010). In the Dry condition, the Control with the 2 × 3pr Au PTFE sensor shows a considerable difference in the Reflection Coefficient at approximately 6 GHz which may be the result of air entrapment, random error of the placement of the panel or fluctuations of the instrument and of the environment. By examining the Reflection Coefficient at "0 GHz" (representative of 10 MHz) the more negative output here at the beginning of the sweep may be indicative of such an error. The 3pr Au PTFE sensor showed larger differences in the Reflection Coefficient between the panels from around 5 GHz in the Wet condition and 7 GHz in the Dry condition, again indicating its ability to detect artificial seawater and byssal plaques on the PVC panel. When examining the effect of Orientation on the detection efficacy, the 2 × 3pr Au PTFE sensor exhibited large variations at which frequency the biggest difference in the Reflection Coefficient between the Treatment and Control

occurred for each Orientation, followed by the 3pr Au PTFE sensor. Although the 2 × 3pr sensor had the same number of electrodes as the 3pr sensor, the large variation in the frequency with the biggest difference in the Reflection Coefficient of the Treatment and Control with the 2 × 3pr sensor may be due to the geometry of the electrodes. The increased gap between the three electrode pairs, compared to the 3pr sensor, may result in a decreased redox cycling efficiency and lower sensitivity (Sun *et al.*, 2018). A previous study demonstrated an overall increase in resistance as the distance between electrodes was increased as the charge carriers had to travel a larger distance between the electrodes (Alexander *et al.*, 2010; Le *et al.*, 2016). Studies experimentally validated the theory that the smaller the IDE gaps, the more sensitive the sensor may be, while decreasing the spacing may result in an increase to the overall effective electrode area (Radke and Alocilja, 2004; Alexander *et al.*, 2010). The same phenomenon may be demonstrated in the present study by reducing the interdigitated gaps from the 2 × 3pr to the 3pr geometry, redox cycling efficiency and sensitivity increase, and therefore a more consistent frequency was identified for the 3pr sensor where the largest difference in the Reflection Coefficient between the Treatment and Control occurred for the Wet experiment and the Orientations.

The 9pr Au PTFE sensor demonstrated differences between the Wet and Dry conditions and between the individual panels, particularly from 5 GHz. The overall frequency spectrum is different between the two conditions which may be indicative of the sensors fundamental resonance at the higher frequencies, which may indicate an increased sensitivity, and that there is less acoustic energy loss

with the presence of seawater (Zhang and Kim, 2005). Additionally, the 9pr Au PTFE sensor demonstrated a consistent frequency among the four Orientations which may be due to increasing the number of IDE's and therefore increasing the signal strength and sensing capacity of the sensor as seen in *equation 2.2*. (Grover, 1999; Alexander *et al.*, 2010). Some studies (Amatore *et al.*, 1988; Min and Baeumner, 2004) showed that increasing the number of electrodes may not affect the signal-to-noise ratio in the way that the electrode width and gaps does; narrower electrodes may result in a higher signal-to-noise ratio and a decrease in gap size results in an increased signal and signal-to-noise ratio. Although the width of the electrodes in the present study remained constant for all the sensors, the increasing number of electrodes may result in an increased signal for the 9pr Au PTFE sensor.

Research using similar IDE sensors work to ascertain a linear relationship with an increasing concentration of an analyte as this will generally show a decrease in the velocity of the wave (Le *et al.*, 2016; Frau *et al.*, 2017; Moejes *et al.*, 2018). Based on this, the initial experimental design in the present study included a single Control, which meant no statistical analysis was possible. By analysing the data as a binary (byssal plaque or no byssal plaque), as has previously been done (Alexander *et al.*, 2010), single frequencies were identified for each material where the sensors were able to successfully detect the presence of the byssal plaques. Furthermore, due to the nature of living organisms, the number of byssi cannot be manipulated, nor can the varying plaque size, placement or

constituents be controlled (Young and Crisp, 1981; Callow and Fletcher, 1994; Vreeland *et al.*, 1998; Warner and Waite, 1999).

The findings highlight the importance of IDE numbers and geometry in the sensing capacity of the sensors as the 9pr Au PTFE demonstrated the ability to detect byssal plaques beyond the PVC surface with no impact of Orientation observed.

2.4.2. Efficacy of Varying Sensing Materials for Detecting *M. edulis* Plaque on a Surface with the Selected EMW Sensor

The four material surfaces investigated demonstrated the highest number of byssal plaques with Nylon 6, followed by PVC, PTFE and Silicone. Despite the widespread use of Nylon 6 in the marine environment (Klust, 1982; Timmers *et al.*, 2005; Andrady, 2011) the findings may highlight the importance of surface energy in mussel adhesion (Callow and Fletcher, 1994). The higher surface energy of Nylon 6 and PVC may result in an increased number of byssal plaques when compared to the lower surface energy of PTFE and Silicone (see table 2.2). The preference of *M. edulis* for high energy surfaces is demonstrated with glass and slate when compared to acetate, paraffin wax and PTFE, as well as with the smaller plaque area and contact area with low energy surfaces (Crisp *et al.*, 1985; Silverman and Roberto, 2007). The impact of surface chemistry and physical properties on *M. edulis* byssal plaque adhesion are suggested to alter the protein expression to appropriately match the surface (Vreeland *et al.*, 1998), however, these studies may not have appropriately considered wettability properties with regards to mussel adhesion. Aldred *et al.,* (2006) suggest an alternative to

equation 1.3 to explain the positive correlation they identified with plaque spreading and increased wettability (*equation 2.4*).

$$W_{sl} - W_{sa} = \gamma_l - \gamma_a + \gamma_{la} - \gamma_{la}\cos\theta_{la}$$

Equation 2.4

Whereby the work of adhesion of the solid/liquid (W_{sl}) and solid/adhesive (W_{sa}) is based on the sum of the surface tension of the liquid (γ_l) minus the surface energy of the adhesive (γ_a) and the interfacial tension between the two (γ_{la}) remains constant, and θ is the external contact angle describing the spreading of the adhesive (Aldred *et al.*, 2006). The equation describes the relationship between an increasing wettability and the increasing W_{sl} resulting in a reduced contact angle and therefore a reduced spreading of the adhesive. The study hypothesised that detection of a high energy surface by the mussel allows for quick byssi deposition, effective spreading of the adhesive allowing for a strong attachment, and therefore only a few byssi are necessary (Aldred *et al.*, 2006). Furthermore, not all biofouling organisms may have the same surface preferences with some demonstrating preference to high energy and hydrophilic surfaces (e.g. *M. edulis, B. balanoides*; Crisp *et al.*, 1985) and others showing a preference for low energy and hydrophobic surfaces (e.g. *B. neritin* ; Mihm *et al.*, 1981; Wiegemann, 2005). The findings in the present study do not agree with the findings of Aldred *et al.,* (2006) as a higher number of byssal plaques were seen with the higher surface energy of Nylon 6, a previously reported phenomenon

(Crisp *et al.*, 1985; Ohkawa *et al.*, 1999), however, this is not always clearly identified (Burkett *et al.*, 2009). Furthermore, the varying constituents of the complex of proteins present in byssal plaques, which may undergo further posttranslational modification, may correspond to the differing surface properties (Papov *et al.*, 1995; Vreeland *et al.*, 1998; Waite and Qin, 2001; Brazee and Carrington, 2006; Silverman and Roberto, 2007; Horsch *et al.*, 2018). Nonetheless, the preference of *M. edulis* in this study, for hydrophilic, high-energy surfaces such as Nylon 6, resulted in a higher number of byssal plaques than the low surface energy materials, such as Silicone and PTFE which may therefore be more suitable in reducing the number of byssal plaques on a surface (Wiegemann, 2005; Aldred *et al.*, 2006; Schumacher *et al.*, 2007).

The differing materials demonstrated an effect on the efficacy of the 9pr Au PTFE sensor to detect the presence of mussel byssal plaques on the surface. By considering the output Reflection Coefficient, standard error and the previous finding that the presence of the mussel plaque may decrease the overall relative permittivity resulting in a less negative reflection coefficient, allowed for an appropriate frequency selection (Alexander *et al.*, 2010; Moejes *et al.*, 2018; Frau *et al.*, 2019). With these factors considered, the biggest difference between the mean Reflection Coefficient of Treatment and Control was the largest for Nylon 6, followed by Silicone, PVC and PTFE. The large difference seen with Nylon 6 may in part be due to the higher average number of byssal plaques on the surface, however, this did not differ from the average number of byssal plaques obtained with PVC and PTFE, both of which demonstrated a smaller difference. Similarly,

there was no difference in the average number of byssal plaques between Silicone, PVC and PTFE, and yet Silicone demonstrated a difference in the Reflection Coefficient over three times greater than that of PVC and PTFE. Furthermore, the larger difference in the Reflection Coefficient for Nylon 6 compared to Silicone may be due to their relative permittivities in addition to the difference in the number of byssal plaques. The higher relative permittivities of Nylon 6 and Silicone may allow for a greater reduction in the wavelength to sufficiently allow for effective detection of *M. edulis* byssal plaques (Sebastian, 2008). Conversely, the lower relative permittivity of PTFE may not reduce the wavelength sufficiently to allow for detection of the byssal plaque on the surface. The implementation of a high relative permittivity (ε_r) is often utilised in circuit miniaturisation as the wavelength within the dielectric (λ_d) is inversely proportional to the square root of the relative permittivity (whereby λ_0 is the wavelength in a vacuum) (*equation 2.5*) (Sebastian, 2008).

$$\lambda_d = \frac{\lambda_0}{\sqrt{\varepsilon_r}}$$

Equation 2.5

It is the permittivity of the material that may reduce the speed of the wave and in turn decrease the wavelength and therefore the lower permittivity of PTFE may result in a higher signal propagation speed that may surpass the presence of the byssal plaques at the frequencies investigated (Sebastian, 2008). Furthermore, it is the degree of polarisation of the dielectric that affects the overall permittivity

as more polarizable materials may result in a higher relative permittivity (Ducharme, 2009; Dang *et al.*, 2013). PVC exhibits relatively strong intermolecular forces with dipole-dipole interactions occurring between the hydrogen and chlorine atoms, whereas the same intermolecular forces in PTFE are weaker, however, the presence of fluorine atoms strongly hold the electrons resulting in the carbon-fluorine bond being considered difficult to polarise (Bureau *et al.*, 2005; Nishi *et al.*, 2012). Nylon 6 and Silicone demonstrate intermolecular hydrogen bonds that may allow for greater polarisation to occur and therefore an increased relative permittivity (De Buyl, 2001; Sheka, 2003; Lukasheva *et al.*, 2017). This same principle may be applied to the various proteins present in the *M. edulis* byssal plaque that may further explain discrepancies between the large differences seen in Nylon 6 when compared to Silicone. This pertains to the mussel's possible posttranslational modifications and varying protein expression according to the surface they are attempting to adhere to (Papov *et al.*, 1995; Vreeland *et al.*, 1998; Waite and Qin, 2001; Brazee and Carrington, 2006; Silverman and Roberto, 2007; Horsch *et al.*, 2018). Furthermore, possible differences in the plaque size as well as the relative permittivity may also contribute to changes in the Reflection Coefficient as was similarly used to detect and evaluate disbanding and delamination events in dielectric layers based on thickness and relative permittivity (Zoughi and Bakhtiari, 1990). Utilisation of differing relative permittivities allowed for the detection of soil moisture based on the difference in the relative permittivity of the moist soil and that of a low-loss slab waveguide which may allow for an effective detection resolution that

may be calibrated based on the moisture content of the soil (Birchak *et al.*, 1974). Another implementation that demonstrated the use of a contactless IDE dielectric sensor was able to identify an appropriate frequency whereby viral binding and detachment was detected (Birnbaumer *et al.*, 2009). Using this method of detection and analysis, the 9pr Au PTFE sensor was able to detect the presence of *M. edulis* plaque on the surface of Nylon 6 and Silicone by successfully distinguishing between the presence of byssal plaque and the lack of. The overall high biological replicate numbers and analysis meant that differences in plaque numbers per sample, their size, composition and placement may be negated (Nettleton, 2006).

2.4.2.1. Reliability and Replicability of Sensing Materials for Detection of *M. edulis* plaques on a Surface with the Selected EMW Sensor

The sensors ability to consistently detect the mussel byssal plaque at similar frequencies demonstrated two distinct frequency regions at the troughs of the mean Reflection Coefficient where there was a higher variability for all four surface types. Utilisation of this analysis method identified possible alternative frequencies whereby the 9pr Au PTFE may detect byssal plaque with Nylon 6, Silicone and PVC. The higher variability at these troughs may in part be due to variation of the byssal plaque constituents as well as the sensor's fundamental resonance (Young and Crisp, 1981; Callow and Fletcher, 1994; Vreeland *et al.*, 1998; Warner and Waite, 1999; Zhang and Kim, 2005). This analysis was no longer based on the presumed notion that the introduction of the test material will result in a less negative Reflection Coefficient as this infers its relative permittivity

allows it to store electrical energy (capacitance) as defined by *Equation 1.2* (A. Mason 2018, personal communication). *M. edulis* byssal plaques are comprised of various specialised adhesive protein types, collagen, polyphenol oxidase and proximal thread matrix protein, which are formed into a porous, foam-like substance (Silverman and Roberto, 2007; Lee *et al.*, 2011; Waite, 2017; Horsch *et al.*, 2018). The porous nature of *M. edulis* plaques may result in an "anomalous" Reflection Coefficient that may be utilised in geophysics for the identification of "soft" oil and gas saturated reservoirs within the "harder" rock (Goloshubin, 2006; Quintal *et al.*, 2011; Onajite, 2014). Implementation of surface acoustic waves in this field demonstrates a frequency dependant reflection from the fluid saturated reservoirs resulting in an increased Reflection Coefficient as an increase in attenuation and the reduction in the speed of the wave indicate a "bright spot" denoting the possible presence of hydrocarbons. Studies demonstrated that the "anomalous" increased Reflection Coefficient with electromagnetic waves may be due to the impact of the pores within a porous material where there is an energy dissipation and resonance loss of the electromagnetic waves, particularly at lower frequencies (Tang *et al.*, 2007). Similarly, the pores within the byssal plaque structure may potentially exhibit this phenomenon whereby the energy attenuation may result in an increased Reflection Coefficient observed at the troughs of the lower frequencies in the present study. An alternative frequency for detection was identified within one of the two key regions and demonstrated a larger difference between the Reflection Coefficient of the Treatment and Control than the first frequency ascertained. The difference in the Reflection

Coefficient for Nylon 6 was over 2.6 times greater, for Silicone it was 6 times greater, for PVC it was 12 times as great and it was 6 times greater for PTFE. The finding may indicate the effect of the porous byssal plaques on the increased Reflection Coefficient with the Treatment and therefore may identify a more appropriate frequency for detection. Moreover, the Orientation of the panels relative to the 9pr Au PTFE sensor did not demonstrate an effect, which may be a result from the sensor IDE numbers and geometry (Grover, 1999; Radke and Alocilja, 2004; Alexander *et al.*, 2010).

The novel use of a contactless, non-specific planar EMW sensor with an IDE array to detect *M. edulis* byssal plaque on various surfaces *in vitro*, may allow for further development of a sensor to detect biofouling that may be compatible with some existing antifouling coatings (such as those that contain silicone; Meyer *et al.*, 2006; Dürr and Watson, 2010; Bressy and Lejars, 2014), materials often used in aquaculture (nylon ropes and netting; Klust, 1982; Timmers *et al.*, 2005; Andrady, 2011) or in scientific research (PVC panels to help study mussel settlement and biofouling; Dürr and Wahl, 2004; Bullard *et al.*, 2010). Detection of a dominant and problematic biofouling species such as *M. edulis*, particularly in temperate regions (Dürr and Wahl, 2004), may facilitate in locating and monitoring biofouling development of the macrofouler. This in turn may allow for effective husbandry with targeted, regular, and gentle hull grooming and removal, particularly in niche areas, resulting in possible longevity and maintenance of the antifouling coating (Holm *et al.*, 2003; Tribou and Swain, 2010). Future development and application of this sensor technology may

therefore facilitate in the reduction of drag and associated damage, costs, fuel penalties and greenhouse gas emissions (Abbott *et al.*, 2000; Hellio and Yebra, 2009; Bixler and Bhushan, 2012).

2.4.3. Conclusion

The study highlights the effect of IDE numbers and geometry on sensing capacity of the planar EMW sensors whereby the 9pr Au PTFE sensor was not impacted by the Orientation of the panels nor the placement of the *M. edulis* byssal plaques. Furthermore, the non-specific surface capacity of the 9pr Au PTFE sensor allowed it to function with the Nylon 6, Silicone and PVC whereby detection of *M. edulis* byssal plaques on the surface was possible and the reduced number of byssal plaques observed with Silicone highlight possible antifouling or foul-release properties of the material.

Chapter 3

Development of a Non-toxic Antifouling and Foul-release Surface

“A ship in harbour is safe, but that

is not what ships are built for.”

- *John A. Shedd*

3.1 Introduction

Biofouling in the maritime industry has caused issues through damage and corrosion of surfaces, introduction of non-native and invasive species as well causing an increase in frictional drag, the latter of which results in increased fuel consumption and greenhouse gas emissions (Abbott *et al.*, 2000; Edyvean, 2010; Lewis and Coutts, 2010). The cost of this is an estimated 486 million tonnes of fuel by 2020 and an estimated increase in greenhouse gas emissions of up to 250% in 2050 (compared to 796 million tonnes of carbon dioxide in 2012) (Hellio and Yebra, 2009; Schultz *et al.*, 2011; International Maritime Organistaion, 2015). The development of antifouling coatings and technology in the maritime industry has helped reduce millions of tonnes of greenhouse gas emissions (384 million and 3.6 million tonnes of carbon dioxide and sulphur dioxide per annum, respectively) as well as save an estimated $60 billion in annual fuel costs (Salta *et al.*, 2010; Bressy and Lejars, 2014). Antifouling technology development continues to progress as research moves from biocide-based coatings, including copper, nanomaterials and even natural based biocides, towards non-toxic alternatives (Rittschof, 2000; Omae, 2003; Khanna, 2008; Dürr and Watson, 2010; Thomas and Brooks, 2010). The development and use of foul-release coatings (FRCs) and systems allowed for a reduction in removal energy of biofouling and so, a reduction in drag (Candries and Anderson, 2001; Townsin and Anderson, 2009; Corbett and Winebrake, 2010). The FRCs advanced with some showing efficacy over a 5 to 10 year period and an efficiency from over just 8 knots (Bressy and Lejars, 2014). Silicone elastomer was included in traditional FRC to create a

hydrophobic, low-surface energy material to reduce adhesion force (Li *et al.*, 2017). Nevertheless, with biofilm persisting up to 30 knots, additive oils were introduced to these foul-release coatings with potential unknown toxicity and environmental impact as well as leaving slow moving or vessels that spend considerable time in port, highly susceptible to biofouling (Nendza, 2007; Bressy and Lejars, 2014). An efficient and effective antifouling technology could save millions of tonnes of potential greenhouse gas emissions and over US$ 150 million annually by 2020 (Hellio and Yebra, 2009). Surface texturing was introduced as a new non-toxic antifouling option that uses the larval behaviour of marine sessile organisms towards their place of final settlement (Salta *et al.*, 2010; Carl *et al.*, 2012). Bioinspired topographies are described as demonstrating a promising reduction in biofouling as high as 98% for the *Balanus improvisus* barnacle cyprids with PVC riblets (Berntsson *et al.*, 2000a). However, the species-specific nature of these topographies are a substantial obstacle for their applicability in a marine environment (Schumacher *et al.*, 2007). Reduction in settlement may be due to the size scale of the topography whereby a topography slightly smaller than the biofouling organism reduces the number of attachment points (Scardino *et al.*, 2006). The wettability of the surface is impacted with the addition of a topography and may enhance the antifouling properties as a two-fold strategy by considering both the physical and chemical properties (Carman *et al.*, 2006). Selection of a material such as Silicone, with an already low-surface energy and surface tension, is described as a crucial factor in its selection as an appropriate antifouling surface.

Fouling organisms such as *Mytilus edulis* are known to demonstrate a preference for hydrophilic, high-energy surfaces to which they may strongly adhere with their byssi (Aldred *et al.*, 2006). It may be this adhesion that allows the mussel to thrive under high hydrodynamic stress environments. The *M. edulis* foot proteins (Mefp) in the byssi plaque are shown to have both a high adhesion and cohesion strength, particularly due to their cross-linking, and their expression may be dependent on the surface type (Warner and Waite, 1999). Topography is however shown to demonstrate an increase in biofouling when the topography scale is larger than the organism as this creates shelter for the fouling organisms (Scardino *et al.*, 2006). With the surface dependant nature of the *M. edulis* plaque the deduction of the protein composition as well as the macromolecular structure of the adhesive plaque pad is made difficult (Silverman and Roberto, 2007; Waite, 2017). With the ability for the mussel to adapt the plaques according to the surface properties, it is important that several topographic scales are assessed.

3.1.1 Plaque Formation and Structure of the *M. edulis* byssus

Production and secretion of various proteins from the exocrine glands of the *M. edulis* foot may allow for the generation of robust and resilient byssi that give the organism the ability to thrive in a hydrodynamically stressful environment (Waite and Tanzer, 1981; Seed and Suchanek, 1992; Silverman and Roberto, 2007). There are two key factors to consider when developing an antifouling foul-release topography for *M. edulis*: 1) process that allows for deposition of the byssi plaques with the foot organ and 2) byssi plaques structure and function.

The foot organ of the blue mussel *M. edulis* is found to be smaller than that of its freshwater mollusc counterparts (e.g. freshwater pearl mussel *Margaritifera margaritifera*) as well as more tongue-like in shape with the ventral groove that allows secretion from the phenol, collagen and accessory glands (Waite, 2017). The necessary collagen, cuticle and adhesive proteins are synthesized and stored by the glands in precise quantities to ensure effective plaque formation and deposition. The thread formation in the ventral groove and plaque formation in the distal depression is described as injection moulding to produce the collagen-rich thread and the porous solid structure of the plaque (*figure 3.1*) (Waite, 2017).

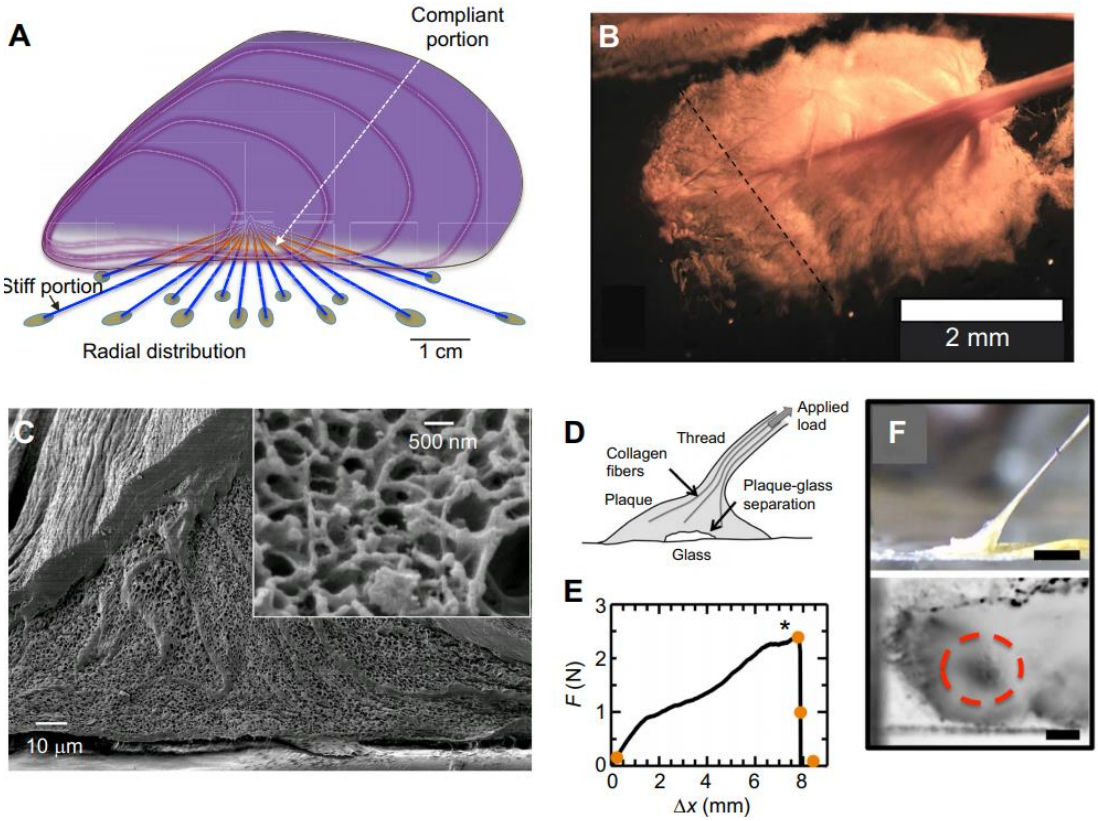

Figure 3.1 – Mussel Plaque Structure. *The mussel byssi are deposited in a radial manner with the stiffer distal section in blue and the more flexible region in orange (**A**). The plaque is then shown (**B**) along with a scanning electron microscopic image of the porous solid nature of the plaque (**C**). An adhesion strength assay of a single plaque on a glass substrate shown schematically (**D**), as a tensile force-deformation plot (**E**) and photographed from the side and bottom (**F**) (source: Waite, 2017).*

The outer cuticle of approximately 5 µm in thickness is shown to protect the porous interior that resembles nickel or aluminium oxide foams with large pores that contain a matrix (Filippidi *et al.*, 2015; Waite, 2017). The overall plaque size is varied from 0.78 mm to 4.8 mm (averaging between 2 to 3 mm) where they try to make a full contact area to create a secure attachment (Tamarin and Keller, 1972). Filippidi *et al.* (2015) found that the sizes of the *Mytilus californianus* plaque structures may be put into two groupings whereby the walls and struts of the plaque are usually between 75 to 130 nm, and the diameter of the large pores are between 1 to 3 µm (*figure 3.2*).

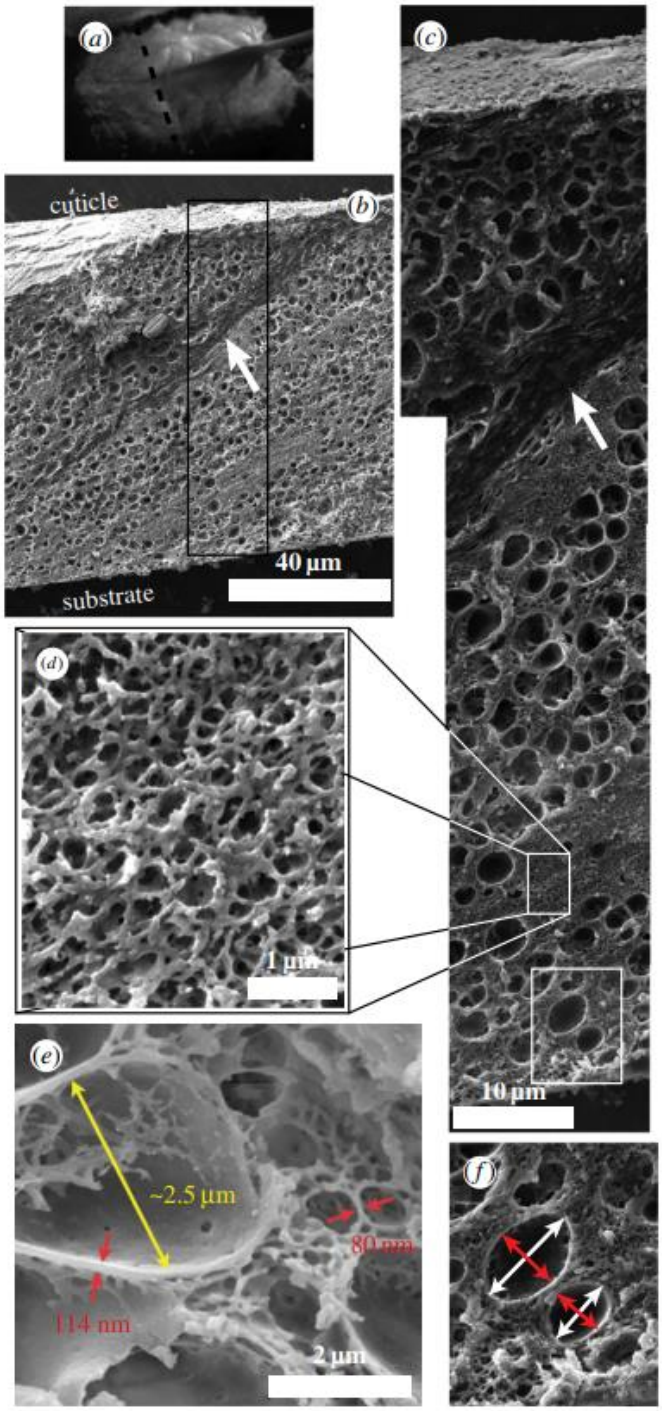

Figure 3.2 – Scanning Electron Micrograph of M. californianus plaque. *The image of a mussel plaque with the site of the cross-section shown (**a**). The cross-section displays the outer cuticle, a collagen thread within the plaque (shown with the arrow) (**b**) and the boxed section is examined closer (**c**). Both the mesh network (d) and the struts within the large pores (**e**) are also observed (the major (white) and minor (red) axes of the pores is also displayed (**f**) (source: Filippidi et al., 2015).*

3.1.2 Laser Machining

The process of laser machining is based on the heating, melting and vaporisation of a surface using a high frequency, amplified light for material removal, light amplification by stimulated emission of radiation (laser) (Williams, 2014). This highly versatile machining technique is applied in cutting, drilling or engraving various materials (Wang *et al.*, 2009; Bogue, 2010; Williams, 2014). Research into laser machining of surfaces to create an antifouling topography are currently being developed with preliminary results showing an antifouling efficacy on stainless steel panels created by laser texturing using Direct Laser Machining (Horner, 2019). This type of laser machining is based on a pulsed laser whereby the substrate is exposed to the laser beam in a series of pulses with a specific amount of energy (a function of the power and pulse duration) (Breitling *et al.*, 2004; Amer *et al.*, 2005; Kim and Na, 2007; Williams, 2014). Changes in power and pulse duration of the laser beam may affect the response of the substrate. The cutting depth (t) is known to be dependant on the power (P) and speed (v) of the laser, but also the size of the spot (d) (*equation 3.1*).

$$t \propto \frac{P}{vd}$$

Equation 3.1

Due to the absorption of the laser energy and its propagation into the material for cutting, there is also the propagation of the thermal wave that can result in undesirable effects including debris and a recast layer (Özisik and Vick, 1984;

Wang and Xu, 2000; Ngoi *et al.*, 2001; Williams, 2014). By reducing the pulse length, the heat transfer rate may be reduced (*figure 3.3*).

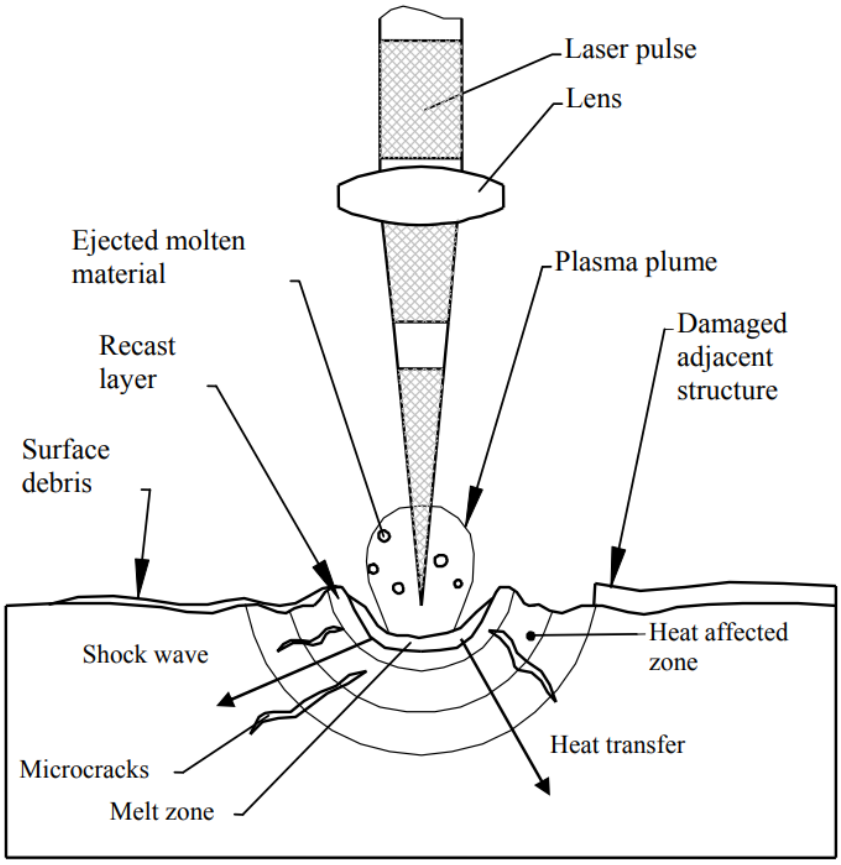

Figure 3.3 – Longer Pulse Laser Ablation *resulting in thermal based damage (source: Petkov, 2011; Williams, 2014).*

The debris is produced from the ablated metal vapour and possible melt expulsion during the machining process (Ngoi *et al.*, 2001). Some of the expelled melt droplets may fall back onto the machined area. If the droplet is still liquid it may "weld" back onto the surface, otherwise it may be a small particle lying on the surface. Ablated metal vapour may also condense and settle, this will be a finer particulate (around 0.5 µm or less) (Williams, 2014).

These undesirable effects of a longer pulse length may actually be beneficial for antifouling applications against *M. edulis* as the unpredictable surface topography may decrease the likelihood for the mussel to adhere. Coupled with the low-surface energy and wettability of the selected material Silicone in the present study, the use of the laser microtextured stainless steel panels as a mould to create an antifouling foul-release topography is examined.

3.1.3 Aims

In order to generate antifouling and foul-release textured Silicone panels, the microtopography needed to be laser etched onto a steel panel that would act as the base for a mould to allow for successful transfer of the microtopography onto Silicone. This meant that the first **aim of the study was to develop a microtopography pattern on stainless steel dependant on the hatch spacing and speed of an SPI nanosecond pulsed fibre laser and transfer of the microtopography to a Silicone surface, *in vitro*** (*Development of Laser Machined Microtextures and Moulds*). Once the method of transferring the microtopography onto the Silicone was successful, the second aim was addressed. The **second aim of the study was to determine the efficacy of the microtopography on Silicone as an antifouling, foul-release surface towards *M. edulis* attachment, *in vitro*** (*Antifouling and Foul-release Efficacy Testing of Laser Textured Silicone Surfaces*).

3.2 Methods

3.2.1 Development of Laser Machined Microtextures and Moulds

The laser used was an SPI G3 20W nanosecond pulsed fibre laser operating at 1.06 µm wavelength with a 1 mW Red diode laser to indicate the centre of the laser processing area. A beam expander (Linos) is used to collimate (make parallel) the beam to enter the Nutfield Galvanometer scanning head fitted with a Linos 160 mm focal length f-theta lens giving a focal spot size of 50 µm. The scanning head allowed the focused beam to be translated across the flat surfaces of the sample coupons at a given speed and in a given pattern.

The laser parameters were standardised with 80% power, 50 µs pulse length and a frequency of 25 kHz. Two speeds and four hatch spacings (distance between the laser path) were investigated in order to account for topographic differences that result from slower or faster speeds and different hatch spacings to identify an appropriate distance to reduce biofouling or allow for foul-release.

The two traverse speeds (V) selected were 20 mm/s and 40 mm/s, and the four hatch spacings (H) used were 50 µm, 100 µm, 150 µm and 200 µm resulting in 8 microtopographies (*figure 3.4*).

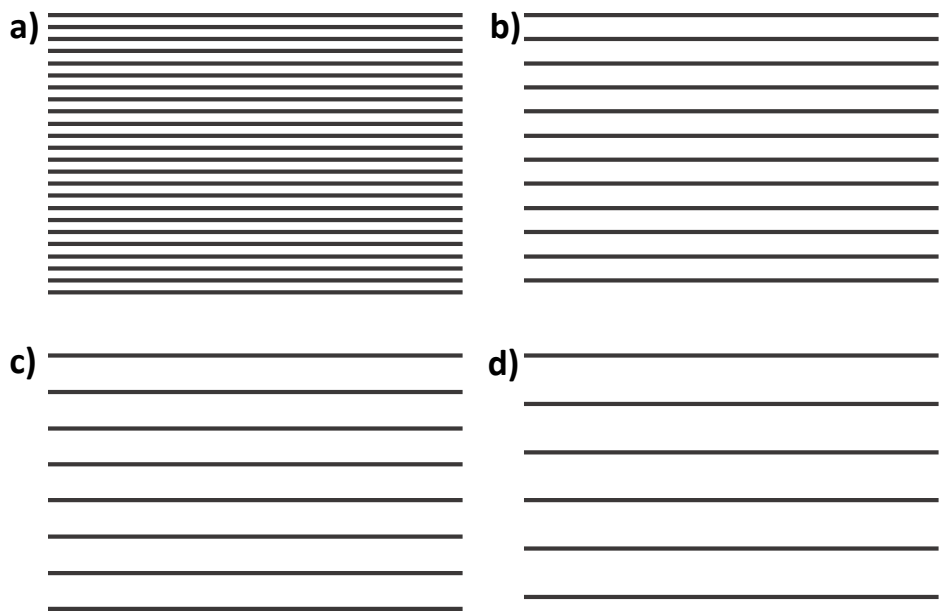

Figure 3.4 – Schematic of the four Hatch Spacings investigated: *50 µm (**a**), 100 µm (**b**), 150 µm (**c**) and 200 µm (**d**).*

Marine grade 316L stainless steel coupons of 50 x 50 x 1 mm were cleaned with acetone and then placed under the laser in order to laser etch the microtopography on to the surface within a central 40 x 40 mm area.

3.2.1.1 Ultrasonic Bath and Ethanol Cleaning Methodologies

Initially, coupons of the 8 microtopographies (n = 2) were generated to investigate two methods of cleaning the etched surface from debris. In order to ensure an accurate transfer of the microtopography, any debris on the surface that may obscure transfer was removed. Loose metallic particles being trapped in the surface of the Silicone cast were prevented with cleaning. Different surface cleaning methods were evaluated before preparation of the samples. The first method was the application of an ultrasonic water bath to dislodge debris. This method is often used in the cleaning of delicate items such as jewellery, electronics and surgical instruments (Mason, 2016). By creating and collapsing

microscopic cavitation bubbles, an ultrasonic bath was able to lift and remove debris from the surface (Awad and Nagarajan, 2010; Yusof *et al.*, 2016). For reliability and consistency, a rack was designed to hold the samples at an angle to allow debris to come off the surface, roll down, and settle at the bottom. The rack was designed using SolidWorks® and printed using the Chemson Ltd. Original Prusa I3 MK2 3D printer (*figure 3.5* (*a*)). Samples were then placed in each rack with the direction of the laser tracks perpendicular to the rack (*figure 3.5* (*b*)) and submerged in deionised water in the ultrasonic bath for 10 minutes and then left to dry (*figure 3.5* (*c*)).

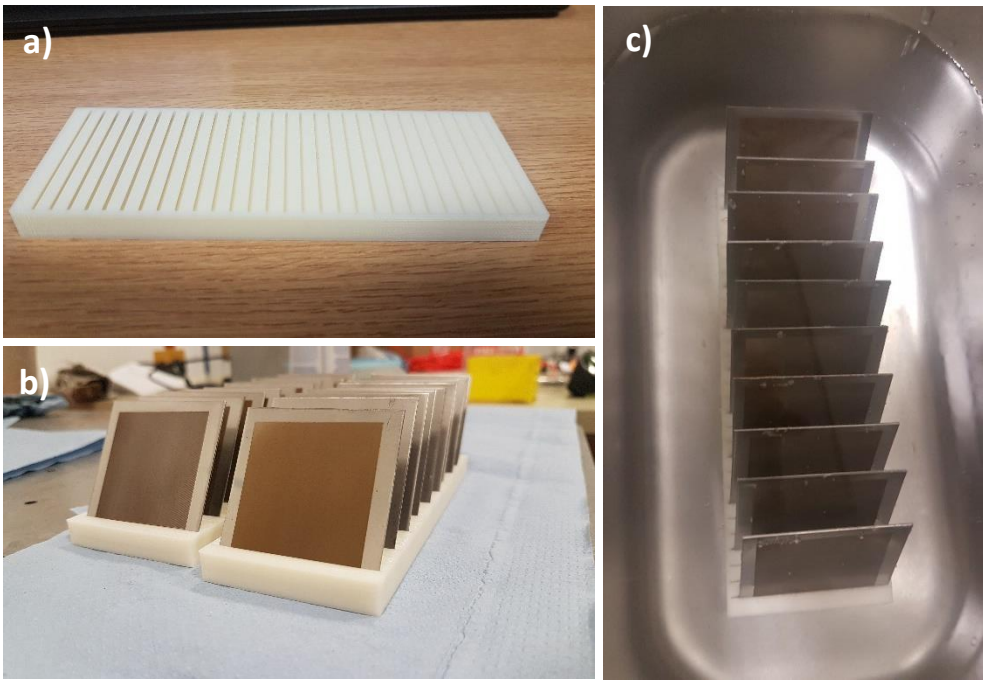

Figure 3.5 – Ultrasonic Bath Cleaning of Laser Textured Surface. *The 3D printed rack (**a**) was used to hold the coupons (evenly distributed) (**b**) and then submerged in deionised water in the ultrasonic bath (**c**) for 20 minutes and left to air dry.*

The second and simplest method investigated was to spray 70% ethanol onto the laser textured coupons with the excess solvent gently wiped and then left. The

coupons were visualised with a Bruker white light interferometric microscope (model Contour GT) before and after the cleaning treatment.

3.2.1.2 Development of a Mould for Microtextured Silicone

In order to transfer the microtopography from the laser textured coupons on to the selected material, Silicone, moulds were made as described in Chapter 2, Section 2.2.3 (*figure 2.7*), with the exception of the base of the mould being the laser textured coupon (*figure 3.6*).

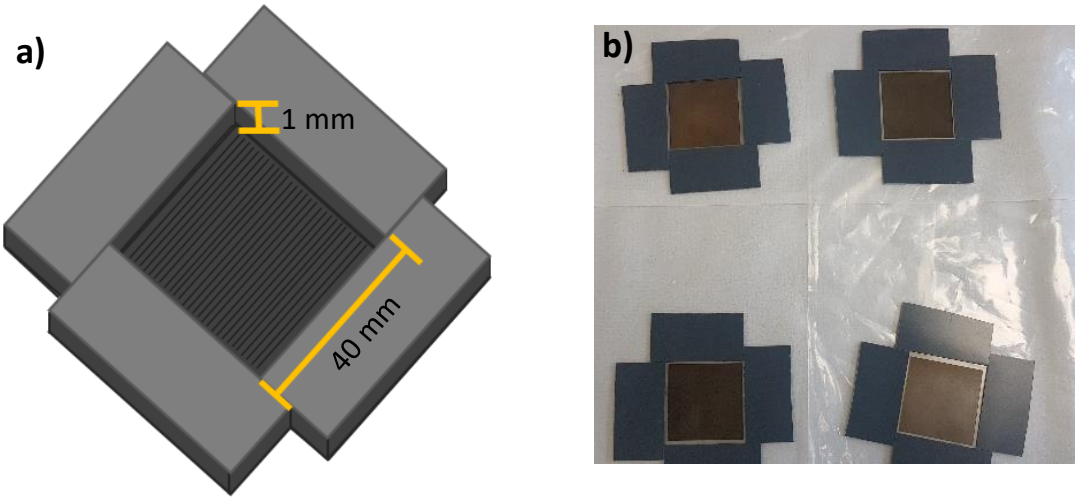

Figure 3.6 – Laser Textured Microtopography Mould*. 1 mm thick PVC panels were secured to the edges of the laser textured surface with precision max Loctite® super glue to create a 1 mm deep mould to pour the Silicone as shown schematically (**a**) and imaged (**b**).*

Silicone was mixed using the standard 10:1 ratio of T30 Silicone base and curing agent (as described in Chapter 2, Section 2.2.3) and poured into the moulds with any excess Silicone scraped off. Once the Silicone had cured for 24 hours, a scalpel was used to cut around the edges and the Silicone sample carefully peeled out to reveal transfer of the microtopography onto the Silicone surface. This was done

for all 8 topographies (n = 2) and examined for any transfer of an unwanted oxide layer from the laser textured coupons onto the Silicone cast. Cleaning time in the ultrasonic bath would then be increased if transfer was visible on the Silicone sample.

3.2.2 Antifouling and Foul-release Efficacy Testing of Laser Textured Silicone Surfaces

Initial Efficacy of the Antifouling and Foul-release Textured Silicone Surfaces

Coupons of the 8 microtopographies (n = 5) were generated (as described in Section 3.2.1) in a random order to account for systematic machining errors over a two-day period (*figure 3.7*).

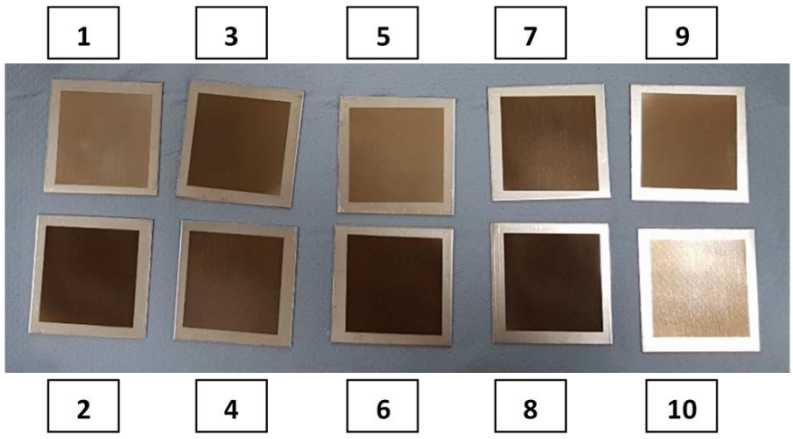

Figure 3.7 – Laser Machined Stainless Steel Panels *with varying tones due to differences in speed and hatch spacing e.g. sample 2 and 8 are Speed (V) 20 and Hatch (H) 50 and sample 1, 5 and 10 are V40 H200.*

A combination of the two cleaning methods (as described in Section 3.2.1.1) was then implemented by first placing the laser textured coupons in deionised water in the ultrasonic bath for 20 minutes followed by cleaning the surface with 70%

ethanol before Silicone pour (increased cleaning time in the ultrasonic bath for further removal of loose debris). In addition to the 8 laser textured coupons (n = 5), Control steel coupons with no microtopography (n = 5) were cleaned and prepared in the same manner (the Control coupons constitute a third speed with no laser).

Silicone was prepared and poured into the moulds as described in Section 3.2.1.2. This was done for all 8 topographies and the Silicone Control (n = 5; **Experiment 1: Topography selection**).

Efficacy of the Top Two Performing Antifouling and Foul-release Textured Silicone Surfaces

From the 8 microtopographies tested, the top two performing antifouling and foul-release topographies were produced as Silicone samples (n = 30) (as described in Section 3.2.1) along with Control Silicone samples (n = 30) (no microtopography). To the standard 10:1 base to curing agent ratio (as described in Chapter 2, Section 2.2.3) a non-toxic royal blue liquid Silicone pigment (Easy Composites) was added to the mix at 3% of the total volume and poured into the moulds as described in Section 3.2.1.2. In addition to the Silicone microtopographies and the Silicone Control, a PVC Control was also introduced (n = 30; **Experiment 2**) as it has widespread use in biofouling research and demonstrates a high energy surface preferred by *M. edulis*, compared to the lower surface energy of Silicone, which may then already result in a reduced

number of *M. edulis* byssal plaque attachment (Crisp *et al.*, 1985; Dürr and Wahl, 2004; Bullard *et al.*, 2010).

For both experiments, the Silicone panels were then secured to a 50 x 50 x 1 mm PVC sheet with precision max Loctite® super glue and the excess PVC trimmed from the edges to fit the 40 x 40 mm area of the microtextured Silicone panel to increase the rigidity of the panel.

3.2.3 Experimental Design

Individual tanks of 8.5 × 15.5 × 10.5 cm were set up with an air tube, air stone and pump in 28 psu artificial seawater at 8 °C for each of the panels. A single *M. edulis* (3 to 5 cm in size) was secured to the Silicone surface of the panel with a rubber band and left for 24 hours to adhere to the surface. The antifouling efficacy of the 8 Silicone microtopographies (n = 5) and the Control (n = 5) (**Experiment 1: Topography Selection**) was setup and conducted just over one 24 hour period, after which the experiment was stopped and samples were assessed in the laboratory for number of byssi, size of plaques and adhesion strength. Samples of **Experiment 2** consisting of the top two performing Silicone Microtopographies (n = 30) with the Silicone Control (n = 30) and the PVC Control (n = 30) were setup and run in the cold room for 24 hours. Samples were assessed in the lab for number of byssi, size of plaques and adhesion strength.

3.2.4 Data Collection

Two aspects were assessed, the laser machining efficacy and the Silicone textured antifouling and foul-release efficacy. Firstly, the quality of the microtopography

on the steel coupons to be used as moulds and the two cleaning methods were examined using a Bruker white light interferometric microscope and by visually assessing any surface transfer from the coupon to the Silicone panels. Secondly, the efficacy of the textured Silicone panels were examined by evaluating the number and size of the byssal plaques as well as their adhesion strength.

3.2.4.1 Imaging the *M. edulis* Byssal Plaque on the Microtextured Silicone

The panels were first removed from the tanks and placed in a petri dish with some artificial seawater, ensuring the surface remained submerged. The rubber band securing the mussel to the surface was carefully cut if possible (some samples had byssi on the rubber band and/or deemed unable to be removed for visualisation under the microscope). The samples including the *M. edulis* specimens were viewed under the Nikon Microscope (model SMZ1270), number of byssi counted and individual plaques photographed for analysis with ImageJ (NIH; version 1.51).

3.2.4.2 Mussel Plaque Adhesion

A loop piece of Korbond® polyester thread (approximately 5 cm) was secured to the dry mussel shell using Loctite® super glue, precision max. A single drop of super glue was placed on the dorsal edge of the shell and the knotted end of the thread pushed into the glue with a graduated Pasteur pipette leaving the loop free. This was left to dry for at least 20 minutes before an extra drop was added. Using a handheld vector force gauge (Imada® model DS2), the looped thread was lifted by the hook of the handheld force gauge and the Silicone held down with two fingers. The force gauge was pulled evenly and consistently vertically, pulling

the mussel off the panel and measuring the total peak force. The force gauge was then used to deduce the force of the mussel by again pulling vertically and measuring the peak force. This was then deducted from the total to give the adhesion force (N).

The Silicone surface was visualised under a light microscope and the number of byssal plaques counted and recorded for comparison to the Nikon microscope data as some plaques were inaccessible due to the presence of the mussel as well as those lifted off by the application of the forge gauge.

3.2.5 Analysis

Initial Efficacy of the Antifouling and Foul-release Textured Silicone Surfaces

Microtopographies with two or less replica panels with mussel byssal plaques were discounted from statistical analysis. The byssal plaque area was analysed using ImageJ (version 1.51) by setting the scale, adjusting the Red Green Blue (RGB), outlining the byssal plaque and measuring the area. Data for the plaque area were tested for the assumptions of normality (Kolmogorov-Smirnov; (Quinn and Keough, 2002)) and homogeneity of variances (Levene's test; (Quinn and Keough, 2002). If assumptions were met a one-way nested ANOVA (factor 1: 5 microtopographies; variable: area of byssal plaques) was used, followed by a Tukey HSD posthoc test to determine differences between microtopographies. The adhesion strength was then analysed using a one-way ANOVA (factor 1: 5 microtopographies; variable: adhesion strength), followed by a Tukey HSD posthoc test to determine differences between microtopographies. Lastly, a two-

way nested ANOVA was carried out to analyse the number of byssal plaques (factor 1: 3 speeds, factor 2: hatch spacing; variable: number of byssal plaque).

Efficacy of the Top Two Performing Antifouling and Foul-release Textured Silicone Surfaces

Data for the number of byssal plaques were tested for the assumptions of normality (Kolmogorov-Smirnov; (Quinn and Keough, 2002)) and homogeneity of variances (Levene's test; (Quinn and Keough, 2002). If assumptions were met, a one-way ANOVA was used (factor 1: 4 microtopographies/materials; variable: number of byssal plaque), followed by a Tukey HSD posthoc test to determine differences between microtopographies. The adhesion strength per byssi was analysed using a one-way ANCOVA (factor 1: 4 microtopographies/material; variable: adhesion strength; covariate: number of byssi).

3.3 Results

3.3.1 Development of Laser Machined Microtextures

The steel textured coupons were cleaned with either 70% ethanol or the ultrasonic bath in deionised water. They were visualised with the Bruker white light interferometric microscope before and after the cleaning treatment (*figure 3.8*).

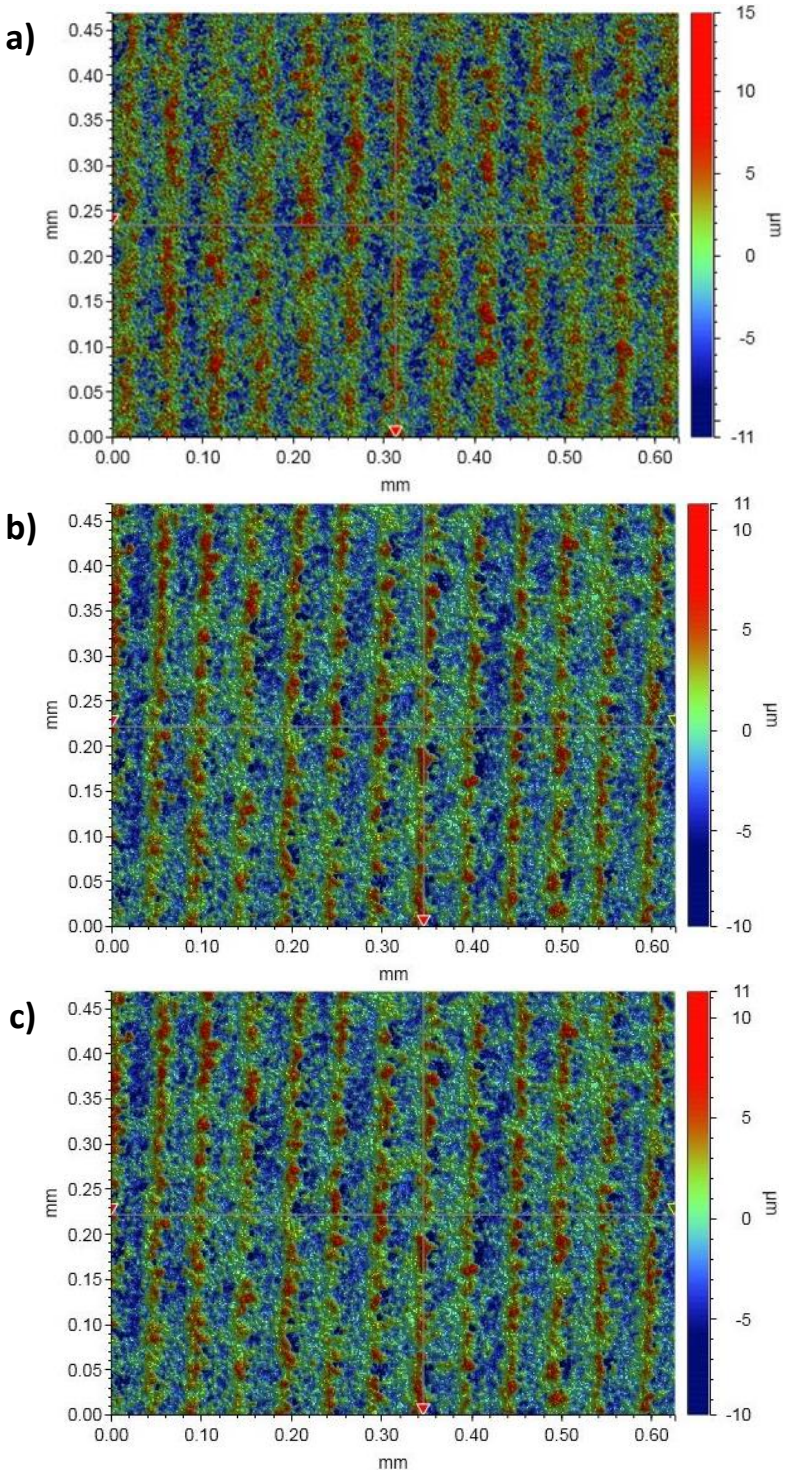
a)
b)
c)
mm
mm
url
0.00
0.05
0.10
0.15
0.20
0.25
0.30
0.35
0.40
0.45
0.00
0.10
0.20
0.30
0.40
0.50
0.60
15
10
5
0
-5
-11
11
10
5
0
-5
-10

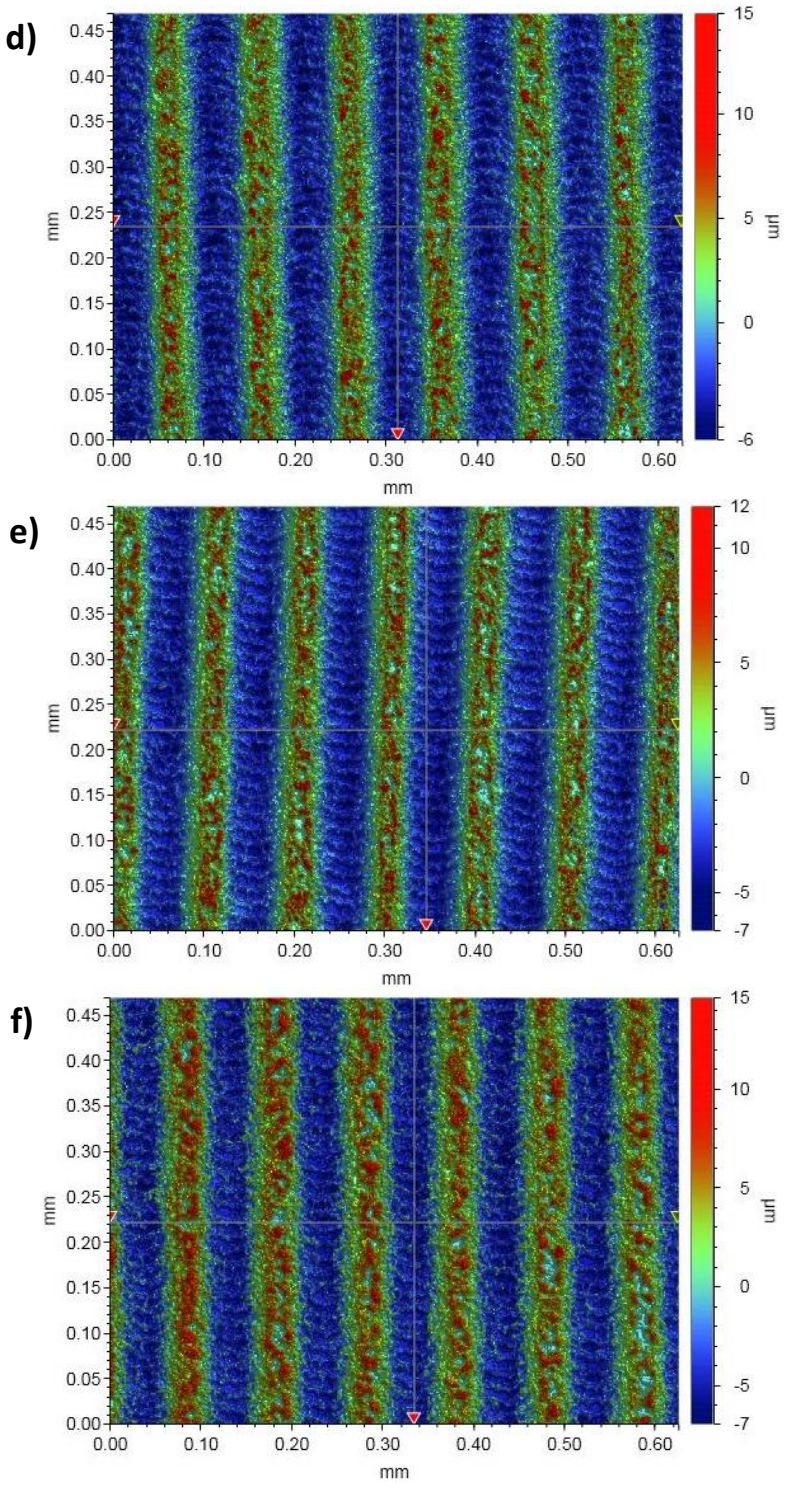

Figure 3.8 – Visualisation of Cleaning Methods for Laser Textured Steel Coupons. *The V20 H50 coupon (**a** – **c**) as seen under the Bruker microscope with no treatment (**a**), cleaned with 70% ethanol only (**b**) and in the ultrasonic bath in deionised water (**c**). Similarly, the V40 H100 (**d** – **f**) is seen with no treatment (**d**), cleaned with 70% ethanol only (**e**) and in the ultrasonic bath in deionised water (**f**).*

Silicone was then poured into the moulds with the coupon bases and left to cure for 24 hours. Once these Silicone panels were removed from the moulds, a brown transfer was visible on the surface, although less so with the ultrasonic bath (*figure 3.9*).

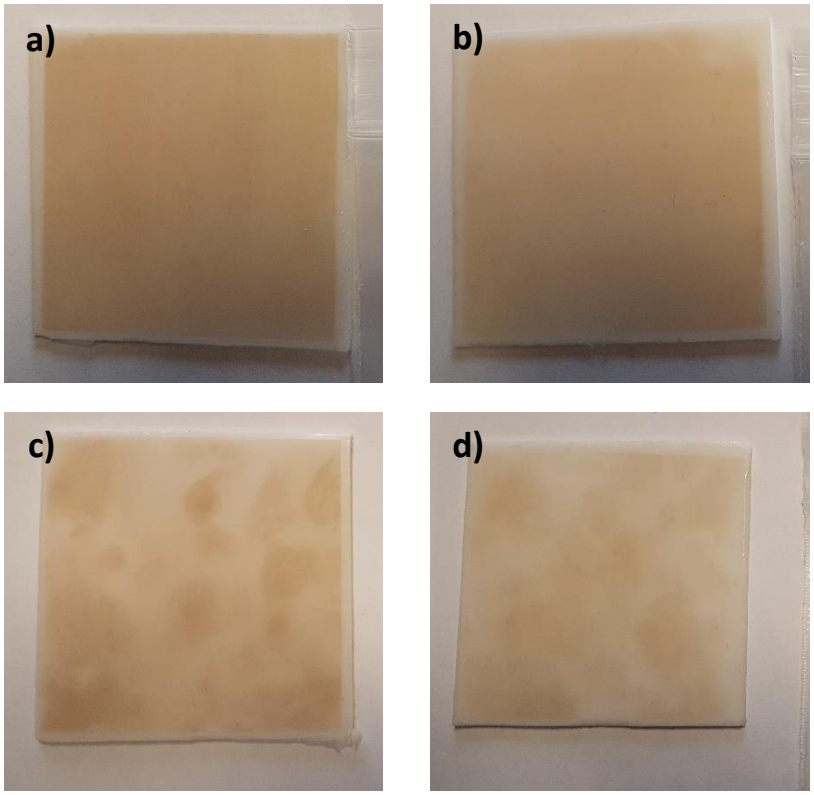

Figure 3.9 – Microtextured Silicone Panels*. Once the cured Silicone was removed from the moulds, it became evident that an oxide layer transferred from the lasered coupons. Particularly for those only cleaned with 70% ethanol (V20 H50 (**a**) and V40 H100 (**b**)), in contrast to those cleaned in the ultrasonic bath in deionised water (V20 H50 (**c**) and V40 H100 (**d**)).*

From the Bruker microscope data, there were no clear visual differences between the two cleaning methods. When considering the results from the Silicone pour, the coupons cleaned in the ultrasonic bath had a lower presence of the oxide layer transfer.

Both cleaning methods would therefore be used; the time in the ultrasonic bath was doubled to 20 minutes to increase removal of the oxide layer and the clean with 70% ethanol was done as preparation before the Silicone was poured.

3.3.2 Initial Efficacy of the Antifouling and Foul-release Textured Silicone Surfaces

Of the 8 microtopographies and the Control tested, only the V20 H100 and V40 H100 had byssal plaques present on all 5 replicates. The Silicone Control panels had plaques present on all but one replicate panel. Conversely, four microtopographies tested had only two replicate panels with plaques present and therefore could not be included in the statistical analysis (V20 H50, V20 H200, V40 H50 and V40 H150). Only panels with three or more replicates were analysed.

Byssal Plaque Area

The plaque area for each individual plaque, per mussel was deduced for each of the microtopographies tested with three or more replicates; V20 H100, V20 H150, V40 H100 and V40 H200. There was a statistically significant difference between the mussels in the byssal plaque area found ($F = 4.092$, $df = 17$, $p \leq 0.001$).

There was a statistically significant difference based on the effect of the microtopographies (*F = 2.593, df = 4, p = 0.041; figure 3.10*) as well as between the plaque area of V40 H100 (0.788 ± 0.0919) and V40 H200 (0.448 ± 0.0484; *p ≤ 0.001*), V40 H100 and the Control (0.552 ± 0.0704; *p = 0.048*) and V40 H200 and V20 H150 (0.676 ± 0.0450; *p = 0.011*).

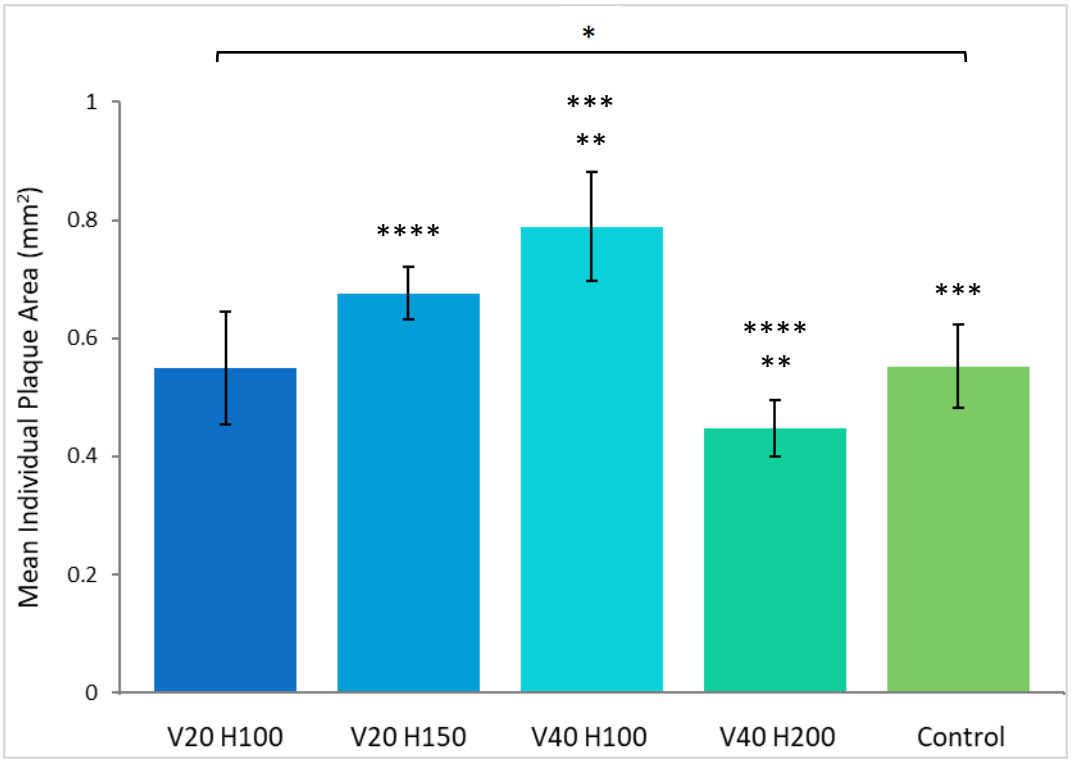

Figure 3.10 – Mean Individual Plaque Area for each Microtopography *with three or more replicates and the corresponding standard error bar.*

; **; *; **** indicates statistical significance (p ≤ 0.05).*

Byssal Plaque Adhesion Strength

Looking at the adhesion strength, there was no statistically significant difference between the microtopographies (*F = 0.168, df = 4, p = 0.951; figure 3.11*).

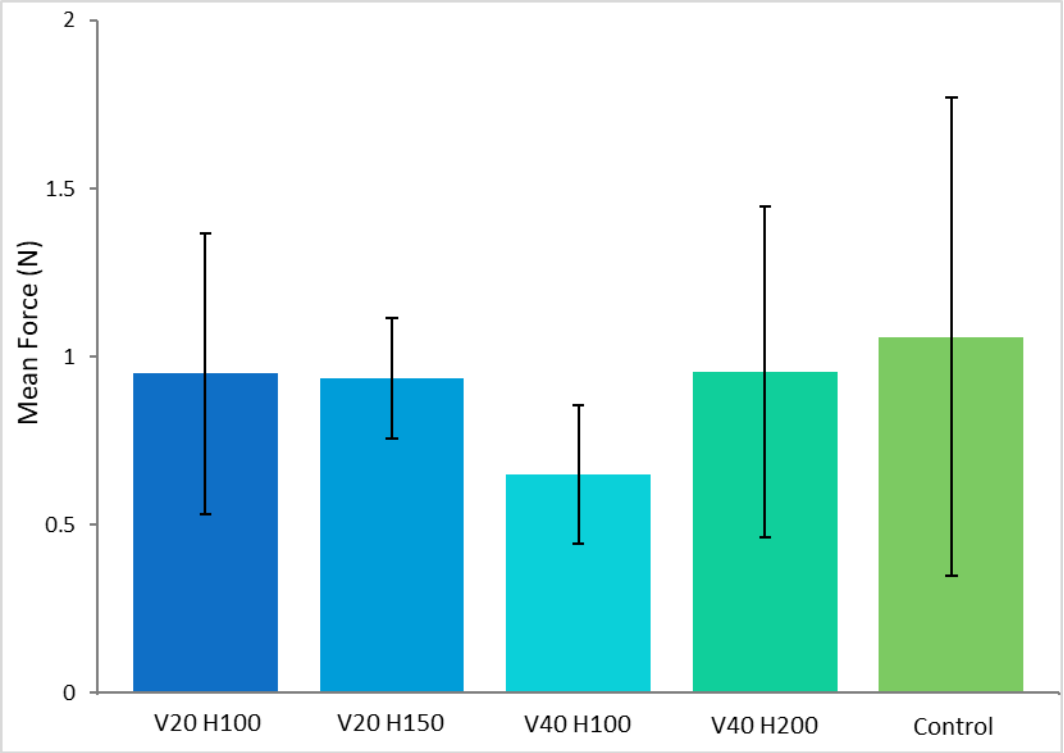

Figure 3.11 – Mean adhesion strength (N) for each Microtopography *with three or more replicates and the corresponding standard error bar (p = n.s.).*

The four microtopographies (V20 H100, V20 H150, V40 H100 and V40 H200) all had a reduced adhesion strength when compared to the Control which had a mean adhesion strength of 1.059 N ± 0.7098. Notably, the two lowest were V20 H150, with a mean adhesion strength of 0.935 N ± 0.1787, and V40 H100, with a mean adhesion strength of 0.650 N ± 0.2074.

Number of Byssal Plaques

The microtopographies were analysed for the number of byssal plaques present on their surfaces and the effect of the speed and/or the hatch dimensions. The additive effect of both the speed and the hatch spacing did not show a statistically significant difference ($F = 1.497,\ df = 3,\ p = 0.232$). However, the Control had a mean number of plaques of 3.4 ± 2.18 and so the microtopographies with a lower mean number of plaques were identified; V20 H100 (3 ± 0.89), V20 H200 (2.6 ± 1.78), V40 H50 (2.0 ± 1.23) and V40 H150 (2.2 ± 1.56). The mean number of byssal plaques for each speed was then found to be 4.1 ± 1.06 and 3.5 ± 0.78 for V20 and V40, respectively. Similarly, the mean number of byssal plaques for the four hatch dimensions were examined to show H100 and H50 had the lowest with 3.8 ± 0.85 and 3 ± 1.34, respectively, other than the Control (*figure 3.12*).

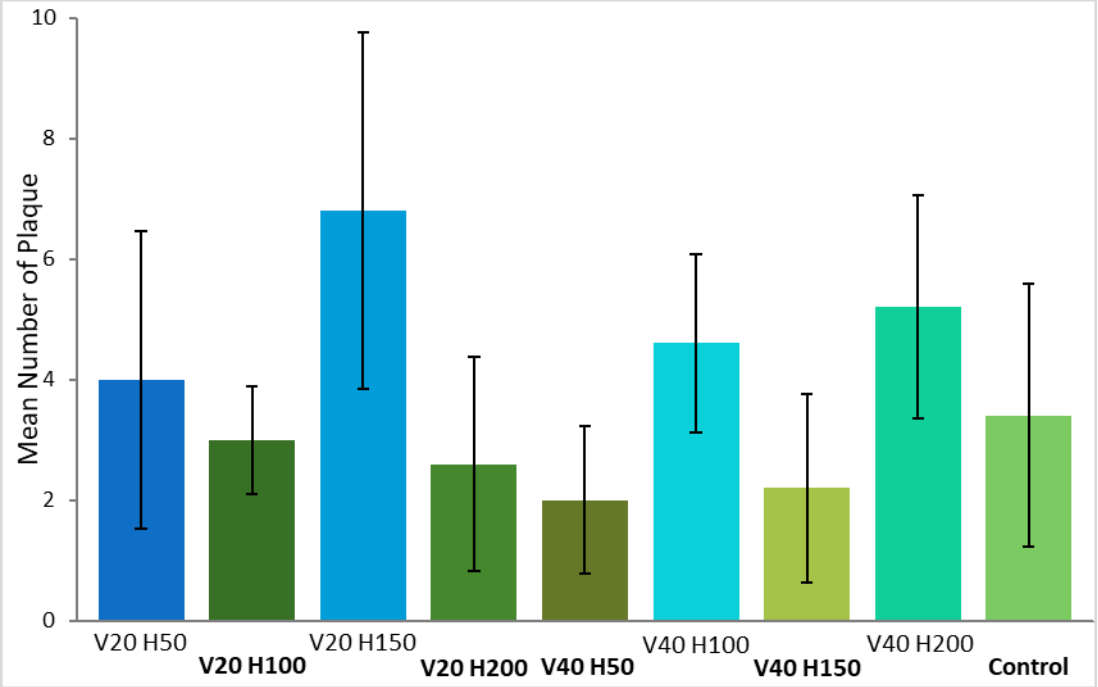

Figure 3.12 – Mean Number of Byssal Plaques for each Microtopography *and the corresponding standard error bar. Microtopographies with a lower number of byssal plaques compared to the Control are in bold (p = n.s.).*

The top performing microtopographies were selected for further testing as they demonstrated the lowest number of byssal plaques: V40 H50 and V40 H150.

3.3.3 Efficacy of the Top Two Performing Antifouling and Foul-release Textured Silicone Surfaces

Two Silicone Microtopographies (V40 H50; n = 30 and V40 H150; n = 30) with the Silicone Control (n = 30) and the PVC Control (n = 30) were exposed to the mussel Treatment, visualised and the number of plaques counted and photographed (*figure 3.13*).

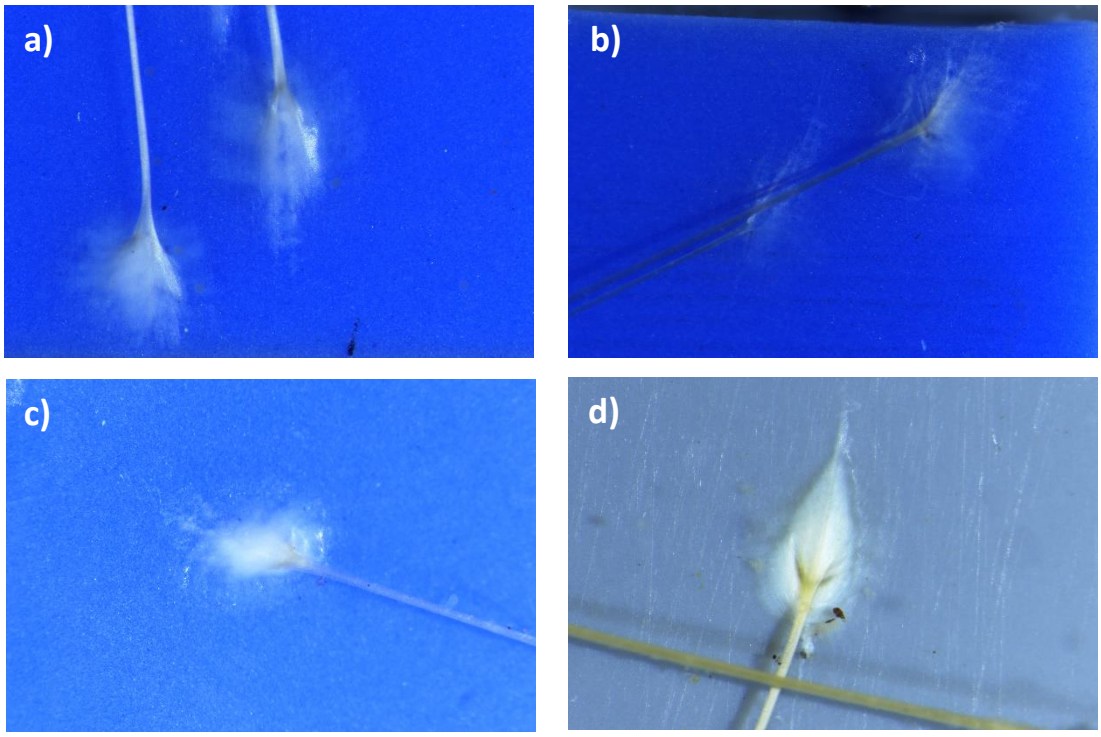

Figure 3.13 – Plaque Deposition on Various Surfaces. *Images from the Nikon SMZ1270 microscope show the plaques on Silicone surfaces with the V40 H50 microtopography (**a**), V40 H150 microtopography (**b**), Silicone Control (**c**) and the PVC panel Control (**d**).*

Number of Byssal Plaques

There was a significant difference between the Microtopography surfaces in number of byssal plaques (*F = 3.003, df = 3, p = 0.033*). Nevertheless, there was no statistically significant difference between the groups (*figure 3.14*).

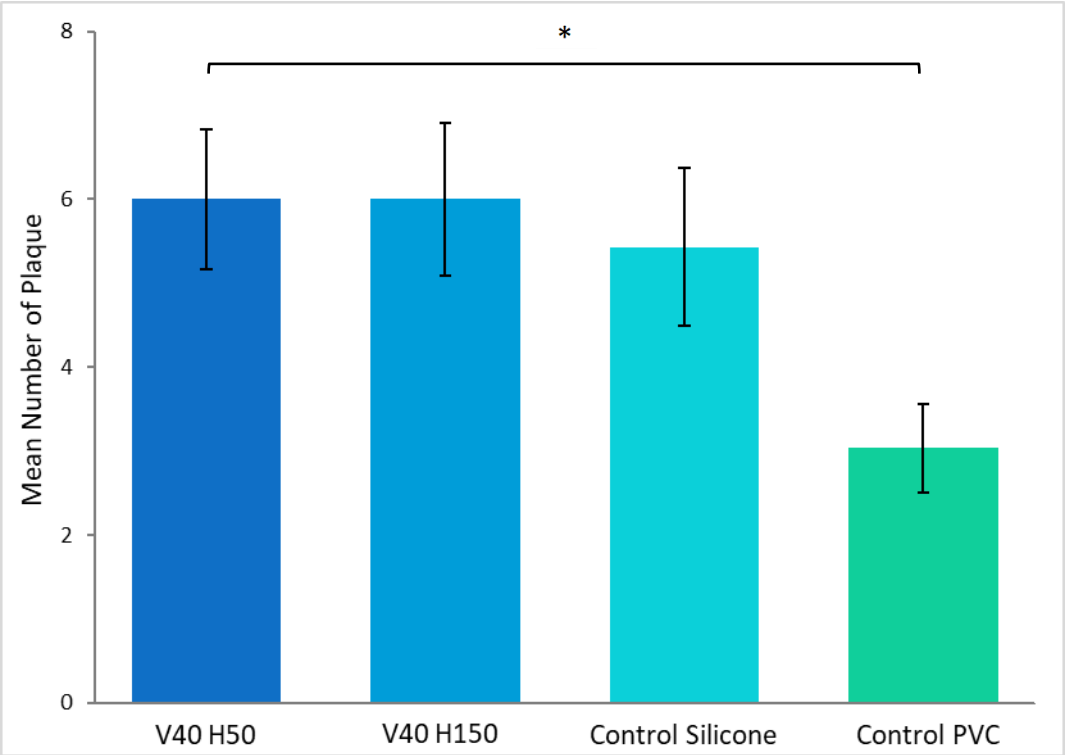

Figure 3.14 – Mean Number of Plaques for each Microtopography *and the corresponding standard error bar.*

** indicates statistical significance (p ≤ 0.05).*

There were non-significant differences between the number of byssal plaques between V40 H50 (6.00 ± 0.829) and PVC (3.03 ± 0.531; *p = 0.055*) and V40 H150 (6.00 ± 0.906) and PVC (*p = 0.055*).

Byssal Plaque Adhesion Strength

The adhesion strength per byssi with the number of byssi as a covariate did not demonstrate a statistically significant difference between the surfaces (*F = 0.593, df = 3, p = 0.622; figure 3.15*). However, the number of byssi as the covariate had a significant effect on the adhesion strength (*F = 8.364, df = 1, p = 0.005*).

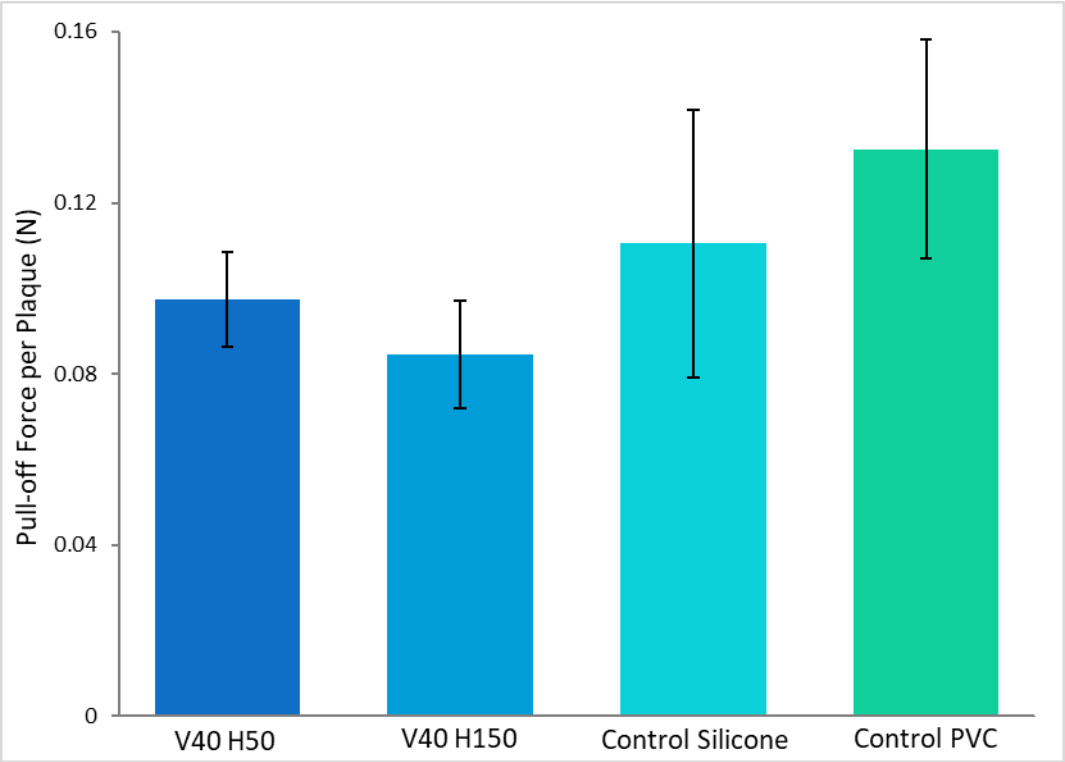

Figure 3.15 – Mean Adhesion Strength per Byssal Plaque for each Microtopography *and the corresponding standard error bar.*

3.4 Discussion

The first aim of the study was to develop a microtopography pattern on stainless steel dependant on the hatch spacing and speed of an SPI nanosecond pulsed fibre laser and transfer of the microtopography to a Silicone surface, *in vitro*. The study demonstrated the production of microtopographies on stainless steel coupons using an SPI nanosecond pulsed fibre laser as visualised with a Bruker microscope. Implementation of two cleaning methods in the study with either deionised water in an ultrasonic bath or with 70% ethanol, did not exhibit a discernible difference under the Bruker microscope. Nonetheless, there was an apparent reduction in the transfer of an oxide layer on to the Silicone panels with deionised water in an ultrasonic bath when compared to 70% ethanol. Implementation of both methods resulted in no visible transfer of an oxide layer and appropriate transfer of the microtopography onto Silicone.

The second aim of the study was to determine the efficacy of the microtopography on Silicone as an antifouling, foul-release surface towards *M. edulis* attachment, *in vitro*. The initial efficacy of the antifouling and foul-release textured Silicone surfaces in this study showed an effect of microtopography on the plaque area. Furthermore, there was no effect of the microtopography on the adhesion strength; however, the microtopographies may show a reduced adhesion strength when compared to the Control. Moreover, there was no effect of microtopography on the number of byssal plaques; however, the V40 H50 and V40 H150 exhibited the lowest number of

byssal plaques. Efficacy of these top two performing antifouling and foul-release textured Silicone surfaces when compared to the Control Silicone and Control PVC demonstrated an effect of the microtopographies on the number of byssal plaques. Additionally, there was no effect of the microtopography on the adhesion strength per byssi plaque; however, the number of byssal plaques did have an effect on the adhesion strength.

3.4.1 Laser Processing

Determining the efficacy of the SPI nanosecond pulsed fibre laser to generate a microtopography on stainless steel coupons was demonstrated with the Bruker white light interferometric microscope whereby the engraved laser track is shown in blue tones denoting their depth in comparison to the spaces between the laser tracks which are shown in green and red tones (*figure 3.8*). The cutting depth and resultant microtopography of the laser may be dependent on the power and speed, as seen in *equation 3.1*, as well as the spacing, all of which may vary the resultant microtopography (Cai *et al.*, 2018). A reduction in the speed and spacing may increase heat transfer and result in more material melting, an increased recast layer and excess overlapping (Özisik and Vick, 1984; Williams, 2014; Cai *et al.*, 2018). Cai *et al.,* (2018) showed that an increase in the spacing may also result in an increased height of the un-treated portion that may be due to expelled melt droplets “welding” here and causing a reciprocal increase in the depth of the laser treated holes. Overlapping of the laser pulses to generate a line may be dependent on the frequency and speed; a higher speed may exhibit a smooth,

wavy path and a Gaussian beam shape groove (Fiorucci *et al.*, 2013). In contrast, a lower speed may produce a deeper groove; however, the debris may remain trapped. The study here showed that at the lower speed of 20 mm/s and smaller spacing of 50 µm, the microtopography might display an increase in recasting and debris, particularly when compared to the increased speed of 40 mm/s and spacing of 100 µm, whereby the laser microtopography is more discernible. Development of a microtopography on stainless steel with the use of a laser may often be shown to be a promising, cost-effective and efficient method for surface texturing (Cai *et al.*, 2018; Li *et al.*, 2018). However, development of such microtopographies with a laser may result in the presence of debris (Williams, 2014) and a superhydrophobic surface (Trdan *et al.*, 2017) that may reduce the ability to transfer effectively the microtopography onto Silicone and so, a cleaning step may be beneficial which was demonstrated in the present study (Schaeffer and Kardos, 2008).

The post-processing cleaning of the laser machined steel coupons in this study demonstrated no discernible difference in the two cleaning methods (ultrasonic bath and 70% ethanol) when examined with the Bruker white light interferometric microscope. Previous studies utilising laser machining may use ultrasonic cleaning with various solutions such as acetone only (Ling *et al.*, 2015) or followed with an additional ultrasonic bath with ethanol (Bizi-Bandoki *et al.*, 2011). Further variations include an acetone ultrasonic bath followed by a deionised water rinse (Razi *et al.*, 2016) or a distilled water ultrasonic bath followed by an ethanol rinse (Trdan *et al.*, 2017). Another study used deionised

water in an ultrasonic bath, followed by an acetone and then ethanol ultrasonic cleaning, and lastly dried in an oven (Cai *et al.*, 2018). Despite the variation in the post-processing cleaning of these studies, there may usually be the presence of an ultrasonic cleaning step as this technique may be shown to generate vast amounts of energy in order to dislodge and remove debris from the surface (Schaeffer and Kardos, 2008). Furthermore, the presence of a solvent, such as the 70% ethanol used in this study, may allow the surfactant to break down the surface tension of the water base. This may be due to the amphiphilic nature of alcohols such as ethanol that have both hydrophobic and hydrophilic properties; as the concentration of ethanol increases, the strength of the hydrophobic interaction decreases (Ballal and Chapman, 2013). The introduction of an alcohol to water causes a drastic decrease in the interfacial tension as well as the contact angle of a water droplet with alcohol on a hydrophobic surface. This may be due to the ability of ethanol's hydrophobic portion to interact and stabilise with the hydrophobic surface while the hydrophilic portion interacts with the water (Ballal and Chapman, 2013). It may therefore be necessary for the inclusion of a surfactant to allow for an efficient transfer of the microtopography from the steel coupon onto the Silicone panel. This notion may be further supported with the possible increased presence of an oxide layer identified on the Silicone panel from the ethanol only cleaned microtopography steel coupon when compared to the Silicone panel from the deionised water ultrasonic bath cleaned coupon. However, there may not be a discernible difference between the coupons cleaned in a deionised water ultrasonic bath and those cleaned with 70% ethanol when

examined with the Bruker microscope. Nonetheless, the apparent reduction in the transfer of an oxide layer with the ultrasonic bath and previous studies demonstrating the use of a solvent for post-processing cleaning, the chosen methodology to implement both techniques may be supported.

The use of interference microscopy for the non-contact evaluation of surface topography may be shown to be highly sensitive with nanometer precision when compared to historical use of contact or near-contact techniques (De Groot, 2015). Microtopographies may generally be assessed using Scanning Electron Microscopy (SEM) (Fiorucci *et al.*, 2013; Ling *et al.*, 2015; Razi *et al.*, 2016; Sun *et al.*, 2016) and/or Atomic Force Microscopy (AFM) (Bizi-Bandoki *et al.*, 2011) to generate a 2D profile (3D profiles may be possible, however this may be time consuming). One study suggested that AFM may show a lateral resolution of 0.2 μm covering an area of 100 μm × 100 μm whereas white light interferometry may generate larger images in seconds (Xu *et al.*, 2013). Implementation of interferometry may be based on light wavelengths that may allow for non-destructive high sensitivity without a dependency on magnification; however, white light interferometry may not function with white Silicone, which may be due to its poor reflectivity (De Groot, 2015) and resulting in no images of the transferred microtopography with interferometric microscopy.

3.4.2 Initial Efficacy of the Antifouling and Foul-release Textured Silicone Surfaces

The microtopographies investigated demonstrated an effect on the byssal plaque area whereby the V40 H100 had a larger average individual plaque area, particularly when compared to the Control. Furthermore, the microtopographies demonstrated a reduced adhesion strength compared to the Control with the V40 H100 exhibiting the weakest adhesion strength of the microtopographies examined. Lastly, four microtopographies (V20 H100, V20 H200, V40 H50 and V40 H150) showed a reduced number of byssal plaques on the surface compared to the Control. The study may highlight a previously identified hypothesis that a smaller byssal plaque area may demonstrate a stronger adhesion force, as was seen with the Control, or vice versa whereby a larger byssal plaque area may demonstrate a weaker adhesion force, as was seen with the V40 H100 microtopography (Allen *et al.*, 1976). Allen *et al.* (1976) also suggested that the byssal plaques are highly variable in size, however, a contrasting study suggests that a larger byssal plaque area resulted in a stronger adhesion strength (Garner and Litvaitis, 2013). These contradictory findings may elude further to the variable nature of byssal plaques as put forth by Allen *et al.* (1976). The larger byssal plaque area with the V40 H100, in comparison to the Control, may be due to the mussels compensating for the textured Silicone surface and thus increasing the overall contact area of the proteins and catechols with the surface to aid adhesion (Hamada *et al.*, 2017). The low surface energy of Silicone may be shown to reduce byssal plaque attachment, while that of a high energy surface may increase

mussel plaque adhesion (Crisp *et al.*, 1985; Callow and Fletcher, 1994; Ohkawa *et al.*, 1999). However, the presence of a microtopography may result in a change in wettability as well, and Carman *et al.* (2006) hypothesised that this may reduce biofouling due to the effect of reduced wettability on the behaviour of biofouling organisms, such as marine green alga *Ulva* and porcine vascular endothelial cells, towards their place of final settlement. Settlement behaviours of biofouling organisms may also be dependent on the height of the microtopographic features as the study by Carman *et al.* (2006) similarly utilised a polydimethylsiloxane elastomer surface whereby variations in the microtopography were predicted to result in either Wenzel wetting, which hypothesises that the water may follow the contours of the increased surface area, or Cassie-Baxter wetting whereby there is a resultant air pocket. The study identified the modified behaviour of the cells investigated as they may try to align within the grooves of the microtopography (similar to Wenzel wetting) or larger cells may bridge across the microtopography (similar to Cassie-Baxter wetting) (Carman *et al.*, 2006). The byssal plaques with the V40 H100 may show a higher number of byssi that are larger and with a weaker adhesion strength when compared to the V20 H100 (same hatch spacing), which may be due to the different laser speeds whereby the lower speed may result in a deeper valley, however, there may be a higher presence of re-melt and debris resulting in a loss of the microtopographic contours in the laser path (*figure 3.16*) (Fiorucci *et al.*, 2013). The microtopography with the higher speed for the V40 H100 may result in bridging

of the byssal plaques and so, a reduced contact area and adhesion strength (Carman *et al.*, 2006).

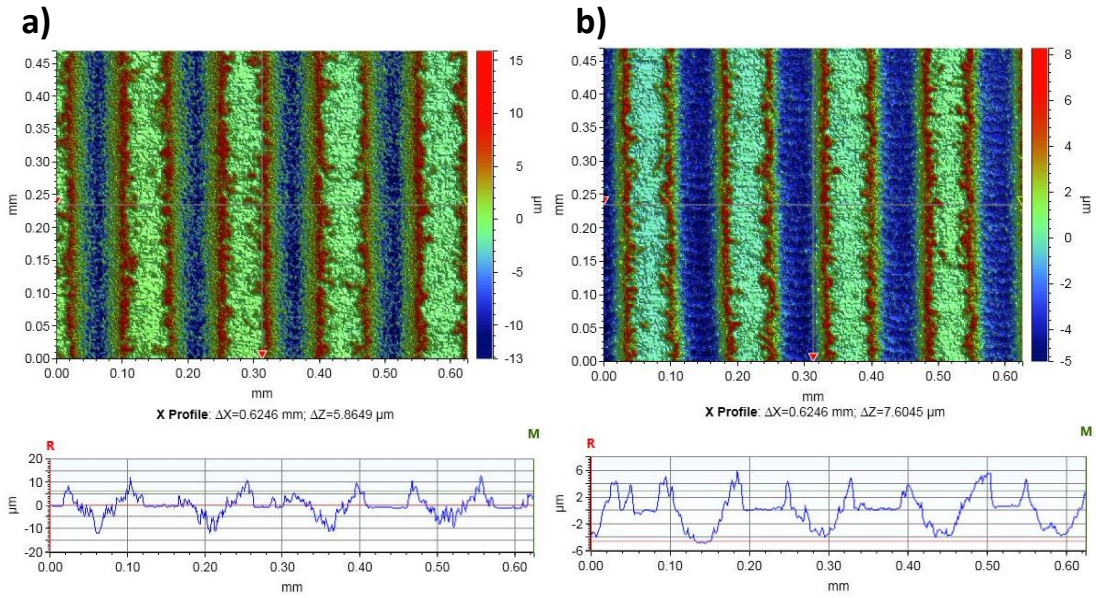

Figure 3.16 – Interferometric Microscopy of V20 H150 (a) and V40 H150 (b) *showing the effect of laser speed on the microtopography. The lower speed of V20 (a) may result in a deeper valley with an increased re-melt layer of trapped debris. A faster speed V40 (b) may show a shallower valley with a Gaussian shape groove.*

Nevertheless, the microtopography may also result in a larger byssal plaque area as the mussel may try to increase the overall contact area with the microtopography features. The occurrence of cavitation by *M. edulis* for byssal plaque adhesion may be disrupted by the microtopography as the mussel may be unable fully to create a negative pressure suction for temporary adhesion and the release of adhesive proteins (Tamarin and Keller, 1972). This may result in a weaker attachment as may be seen with the microtopographies when compared to the Silicone Control. A study investigating the effect of microtopography on barnacle cyprids (*Balanus improvisus*) attachment on a Silicone based

microtopography showed a reduction compared to the smooth surface (Andersson *et al.*, 1999). Similar studies may also demonstrate a decrease in biofouling of microorganisms or larvae due to the presence of a microtopography and/or a low surface energy (Berntsson *et al.*, 2000b; Scardino *et al.*, 2006; Chung *et al.*, 2007; Schumacher *et al.*, 2007; Magin *et al.*, 2010; Cooper *et al.*, 2011). However, the relationship between microtopography, wettability and adhesion may be dynamic and complex, and the possible antifouling properties may be species-specific (Scardino and De Nys, 2004; Carman *et al.*, 2006). This complex nature may be exacerbated by the dynamic nature of the byssal plaques themselves in terms of size (between 0.78 mm to 4.8 mm and averaging around 2-3 mm) and the composition of various proteins that may differ depending on the surface properties (Tamarin and Keller, 1972; Vreeland *et al.*, 1998; Brazee and Carrington, 2006; Silverman and Roberto, 2007; Horsch *et al.*, 2018).

The V40 H100 Silicone microtopography may demonstrate a reduced adhesion strength (compared to the Silicone Control) indicating possible foul-release properties. However, this analysis was only possible due to the fact that the V40 H100 had mussel plaque deposition on all 5 of the replicates and demonstrated a higher number of byssal plaques (compared to the Silicone Control), possibly indicating poor deterrence and antifouling properties. Examination of the descriptive statistics of all 8 microtopographies, and therefore the additive effect of both the speed and hatch dimensions, showed four microtopographies with a reduced number of byssal plaques when compared to the Control (V20 H100, V20 H200, V40 H50 and V40 H150) and may therefore indicate antifouling properties

of these microtopographies. Furthermore, the V40 speed demonstrated a lower number of byssal plaques compared to V20 and the hatch spacings H50 and H100 demonstrated the lowest number of byssal plaques of the four hatch spacings. Due to low replicate numbers, the selection of two microtopographies for further testing was based on the lowest number of byssal plaques; V40 H50 and V40 H150.

3.4.3 Efficacy of the Top Two Performing Antifouling and Foul-release Textured Silicone Surfaces

Investigating the antifouling, foul-release efficacy of two Silicone microtopographies showed a higher number of byssal plaques when compared to the smooth Silicone and smooth PVC Controls. This contradicts the finding in the initial experiment whereby the two microtopographies demonstrated a lower number of byssal plaque. This may be due to the low replicate numbers in the initial experiment. Conversely, a higher number of byssal plaques resulted in a reduced adhesion strength as was identified with the microtopographies. The presence of the microtopography may result in a reduced contact area and adhesion strength, an issue the mussels may try to overcome by increasing the total number byssal plaques (Carman *et al.*, 2006). The presence of the microtopography may be shown to reduce wettability and therefore increase byssal production (Aldred *et al.*, 2006; Carman *et al.*, 2006). Microtopographies have shown their antifoulant efficacy with *Ulva* zoospores (Schumacher *et al.*, 2007; Magin *et al.*, 2010), barnacle cyprids *Balanus amphitrite* (Schumacher *et al.*,

2007), the bacteria *Cobetia marina* (Magin *et al.*, 2010) and *Staphylococcus aureus* bacteria (Chung *et al.*, 2007; Cooper *et al.*, 2011). The Attachment Point Theory (Scardino *et al.*, 2008) may support the results seen in this study, whereby the reduced attachment with the microtopography resulted in a decreased adhesion strength, more so for the V40 H150 than the V40 H50. The V40 H150 hatch dimensions may also be beneficial against other fouling organisms such as barnacle cyprids that showed a 98% reduction in settlement with a 150 – 200 µm microtopography (Berntsson *et al.*, 2000a). This study may demonstrate the possible foul-release properties of the microtopographies with *M. edulis* byssal plaques when compared to the smooth Silicone and smooth PVC Controls.

The introduction of the PVC Control was deemed necessary as Silicone already exhibits hydrophobic, low-surface energy properties and therefore may likely already result in a reduction of *M. edulis* attachment (Crisp *et al.*, 1985). In contrast, PVC has a higher surface energy, which may result in increased plaque deposition. However, this phenomenon is not always decisively identified (Burkett *et al.*, 2009) and the present study may not support this premise as PVC showed the lowest number of byssal plaques. This finding may contradict that identified in Chapter 2 whereby PVC showed a higher number of byssal plaques compared to the Silicone. The contradictory results of this study agree with another previous concept that the *M. edulis* byssal plaque may spread further and with lower tenacity on the low-energy, hydrophobic Silicone surfaces (Aldred *et al.*, 2006). A possible hypothesis for this phenomenon may in part be due to the effect of spawning on byssogenesis (Seed and Suchanek, 1992; Carrington, 2002;

Hennebicq *et al.*, 2013). A number of mussel specimens spawned during the course of the present study and this may result in weakening of the byssal thread due to the high-energy demands of gametogenesis. This may then impact byssal production and adhesive strength, and so, an energy trade-off may result in a reduced number of byssal plaques more strongly attached to the high-energy surface of PVC compared to Silicone (Seed and Suchanek, 1992; Brazee and Carrington, 2006; Hennebicq *et al.*, 2013). Conversely, when gametogenesis is no longer occurring, *M. edulis* may demonstrate a preference for high energy and hydrophilic surfaces (Crisp *et al.*, 1985).

The implementation of laser etching on stainless steel coupons for the development of a foul-release Silicone microtopography (V40 H150) may allow for a non-toxic, foul-release technology to reduce the removal energy of biofouling, particularly the problematic and dominant species *M. edulis* (Dürr and Wahl, 2004). This may help to address the 86% powering penalty associated with heavy calcareous biofouling and therefore may reduce the associated drag, greenhouse gas emissions and introduction of invasive species, without the need of toxic substances currently used in the maritime industry (Abbott *et al.*, 2000; Rittschof, 2000; Schultz, 2007; Hellio and Yebra, 2009; Dürr and Watson, 2010; Lewis and Coutts, 2010; Thomas and Brooks, 2010).

3.4.4 Conclusion

The presence of a microtopography on Silicone may demonstrate a reduction in *M. edulis* byssal plaque adhesion strength in comparison to a smooth Silicone and smooth PVC Controls. This reduction may be due to a decrease in points of attachment as well as the decrease in wettability with the microtopography, which may indicate a possible foul-release efficacy.

Chapter 4

Efficacy Testing of the Antifouling and Foul-Release Sensory Surface in situ and under real-time conditions

“To reach a port we must set sail –

Sail, not tie at anchor

Sail, not Drift.”

- *Franklin D. Roosevelt*

4.1. Introduction

The longstanding relationship between the maritime industry and biofouling resulted in billions of dollars in expenses per annum (Abbott *et al.*, 2000; Hellio and Yebra, 2009; Schultz *et al.*, 2011; Seatrade Maritime News, 2018). The costs are incurred due to hull cleaning or grooming, application of antifouling coatings, inspections, corrosion damage, excess fuel consumption and dry-docking (Salta *et al.*, 2009). The subsequent problems are caused by the release of millions of tons of carbon dioxide and the transportation of non-native species and pathogens. The mounting economic and environmental pressures for the shipping industry to address biofouling and to streamline its management are intersected with the need for an efficient detection system (Schultz, 2007; Hellio and Yebra, 2009; Lewis and Coutts, 2010; Schultz *et al.*, 2011). Both are addressed as mutually exclusive issues with focus on the development of antifouling systems that have a long-term efficacy of 5 to 10 years often dictating the timeline of biofouling management (Salta *et al.*, 2009). However, the increasing demand by countries for vessels to quantify and carefully manage biofouling on ships entering their waters is conducted by visual inspection by divers and remote operated vehicles (ROVs) (Tribou and Swain, 2010, 2015; Floerl and Coutts, 2013; Hearin *et al.*, 2015).

Antifouling coatings are developed under controlled laboratory conditions (Xue *et al.*, 2014; Al-Naamani *et al.*, 2017; Liu *et al.*, 2017) as well as *in situ* (Briand *et al.*, 2012; Yong *et al.*, 2015; Silva *et al.*, 2019). There are well known setbacks of

laboratory-based research, particularly with the lack of a community of marine organisms as well as seawater quality. Laboratory based testing is generally carried out with artificial seawater that has some distinct differences to *in situ* seawater such as temperature fluctuations, dissolved inorganic matter concentrations and pH fluctuations (Berges *et al.*, 2001; Little *et al.*, 2014). More importantly, particularly for biofouling research, is the presence of other biofouling organisms. Biofouling is often described as a chronological process beginning with the near-immediate development of a conditioning film, followed by a biofilm (microfouling) (Railkin, 2003; Dobretsov *et al.*, 2006). It is often thought that the development of the biofilm may be the precursor for macrofouling settlement, however some contradictory findings demonstrate that some settlement may in fact be inhibited by the biofilm (Maki *et al.*, 1988; Olivier *et al.*, 2000). Although the presence of a biofilm is not required for all macrofouling to settle, the subtidal biofouling communities in temperate regions remain highly dynamic and diverse with some central fouling organisms to consider such as algae, sea squirts, barnacles, bryozoans, hydroids, serpulids and mussels (Zobell and Allen, 1935; Callow and Callow, 2002; Ralston and Swain, 2009; Salta *et al.*, 2009) (*figure 4.1*).

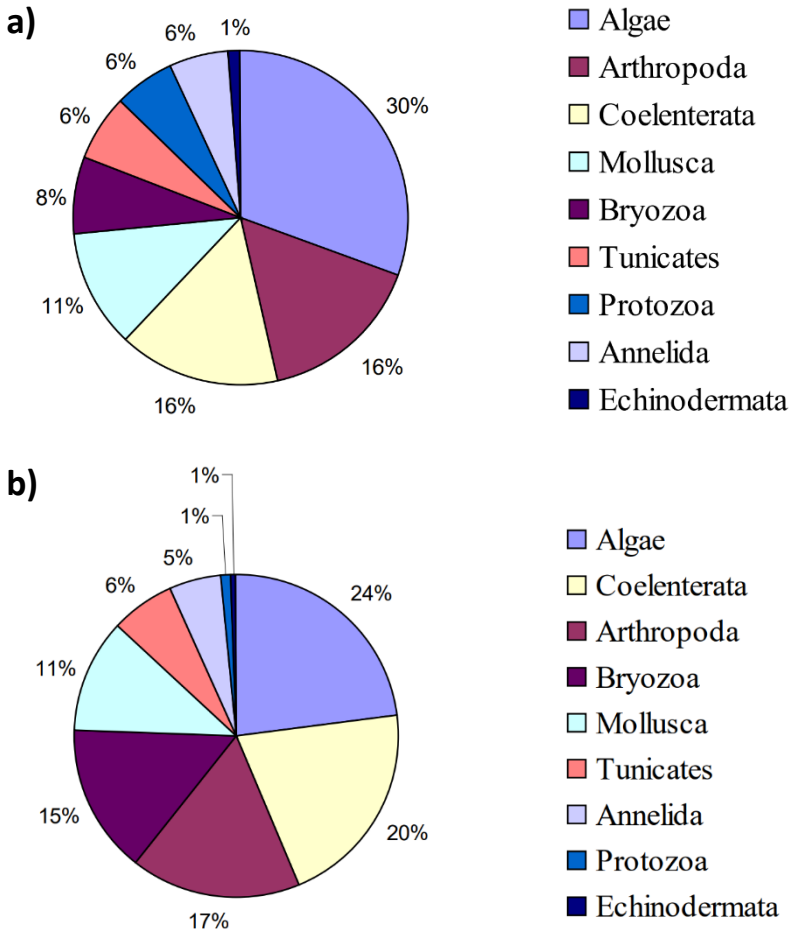

Figure 4.1 – Biofouling Community Composition *on artificial materials including pipes, buoys, submarine cables, wrecks, pontoon floats and ships (**a**) and on ships only (yachts, skiffs, barges and vessels) (**b**) in American waters. The five most abundant groups in both cases are algae, Arthropoda (e.g. barnacles), Coelenterata (e.g. hydroids), Mollusca (e.g. mussels) and Bryozoa. (source: Woods Hole Oceanographic Institute, 1953; Salta et al., 2009).*

The biofouling community composition has remained consistent over time, with the same key groups being identified globally, including the group Mollusca, such as the blue mussel, *Mytilus edulis* (Salta *et al.*, 2009).

Although *M. edulis* is known to be a dominant biofouling species with the ability to monopolise substrata, the presence of other dominant biofouling organisms

such as diatoms may interfere with antifouling efficacy as well as detection efficacy (Lewin, 1984; Dürr and Wahl, 2004; Cao *et al.*, 2011). Moreover, the interaction between an electromagnetic wave (EMW) sensor and a living organism may display behavioural changes in itself due to EMW sensitivity; this is most notable in EMW sensitive species such as sharks and skates where at lower frequencies and intensities they may search for the source, but at higher frequencies and intensities, they may display an avoidance behaviour (Fisher and Slater, 2010). The use of high-frequency waves may be able to interfere with barnacle larvae settlement due to cell damage and retraction of their antennae (Leya *et al.*, 1999). Conversely, the same principle did not prevent algal settlement at a constant voltage, as the smaller spores experience a weaker electric field. When *M. edulis* was exposed to magnetic fields, hydration and amine nitrogen was decreased by 20% and 15%, respectively (Fisher and Slater, 2010).

A sensory antifouling surface in the maritime industry may be able to address both needs, 1) the reduction of macrofouling, here the model species *M. edulis* and 2) the detection of biofouling accumulation in real-time.

4.1.1. Aims

Ascertaining the efficacy of a sensory surface to deter and detect biofouling meant that the two components of the research were brought together; Chapter 2, the sensor to detect *M. edulis* biofouling, and Chapter 3, the antifouling microtopography. The *in situ,* real-time efficacy of the planar EMW sensor and the antifouling microtopography surface was then tested in order to

address **the aim which was to determine the efficacy of the sensory antifouling surface towards *M. edulis* attachment and detection under real-time conditions, *in situ*** (*Efficacy of 8 Pair Interdigitated Electrode Sensor of PVDF in vitro* and *Efficacy of the antifouling Sensory Surface in situ and in Real-Time*).

4.2. Methods

4.2.1. Study Site

Queens Dock situated in Liverpool, UK was designed by Henry Berry and opened in 1795 as part of the Port of Liverpool (Harris, 1937; Allison, 1953). The dock was named in honour of Queen Charlotte, consort of King George III and was part of a revolutionary interconnected dock system, some of which now hold a World Heritage Site title (*figure 4.2*) (UNESCO, 2004).

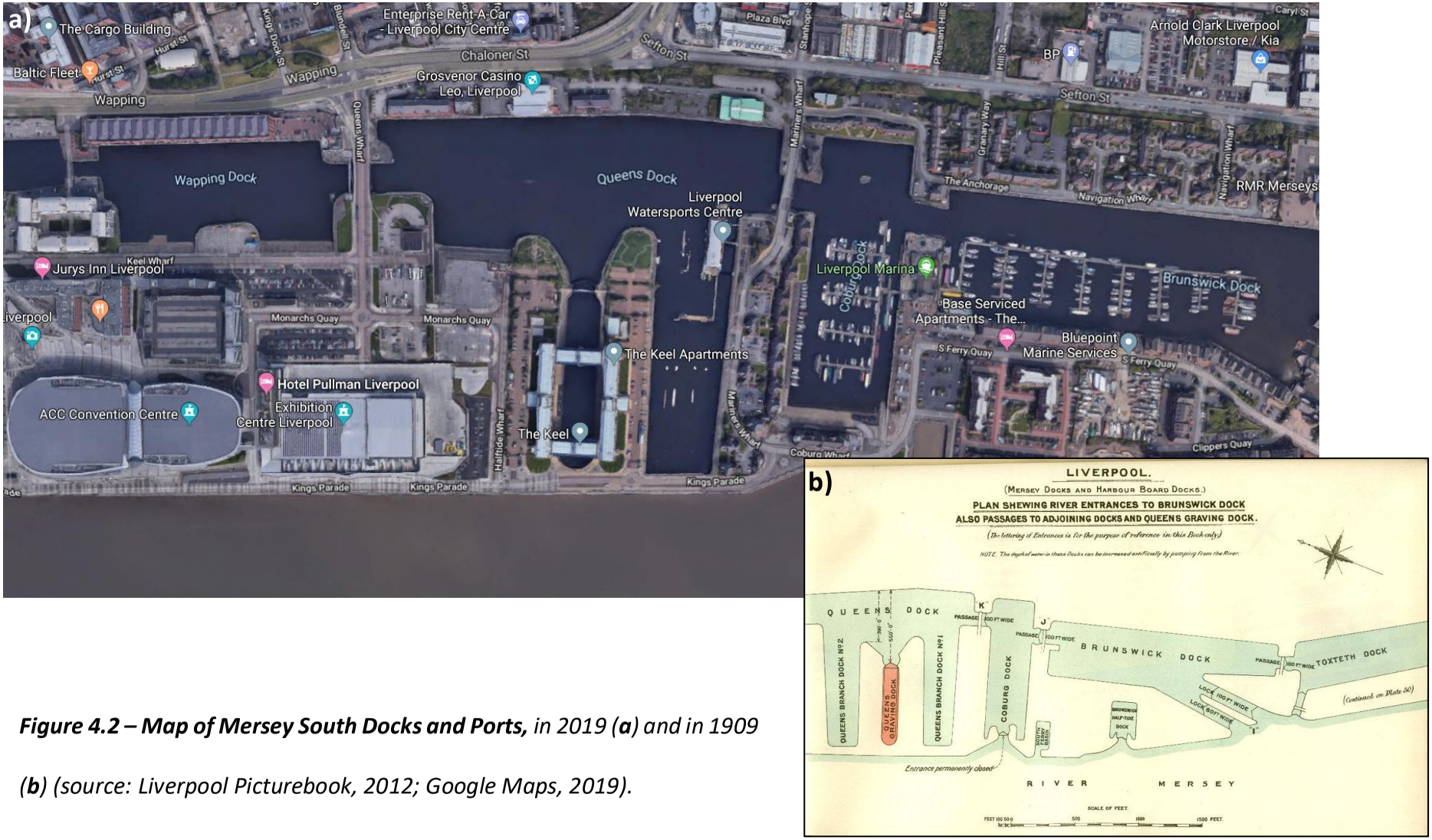

Figure 4.2 – Map of Mersey South Docks and Ports, *in 2019 (**a**) and in 1909 (**b**) (source: Liverpool Picturebook, 2012; Google Maps, 2019).*

Over the years, many of the docks began to close, in particular the smaller South Docks in 1971, including the Kings Dock, and the Queens Dock Branch Number 2 and the graving dock (Merseyside Maritime Museum, 2019). In 1972, the Brunswick Dock gates were opened and allowed for movement of the River Mersey into the South Docks resulting in it becoming clogged with contaminated, sewage-polluted silt (Whomersley *et al.*, 2007; Merseyside Maritime Museum, 2017). It was not until the 1980's that re-development of the docks began, including filling in some of the closed Docks to create land for buildings as well as dredging of polluted silt (Merseyside Maritime Museum, 2019).

Rectifying the damage caused by the opening of the Brunswick Dock gates was underlined with the removal of the polluted silt and replacement of the gates (Wilkinson *et al.*, 1996). This led to the development of a dynamic benthic community of tunicates, amphipods, polychaetes, bryozoans, barnacles and dominated by *M. edulis*. Originally owned by British Waterways, these docks were transferred to the Canal & River Trust in 2012 (BBC News, 2012). In 1994, the Liverpool Watersports Centre moved from the Leeds Liverpool Canal to Queen's Dock where it stands today (Liverpool Watersports Centre, 2019).

The field study was conducted at Liverpool Watersports Centre (53°23'33.9"N 2°59'07.6"W) in Liverpool, UK, on 15th July 2019. The selected site was situated on a slipway located to the east of the Watersports Centre (*figure 4.3*). The biofouling community underneath the Liverpool Watersports centre pontoons was where the *M. edulis* specimens were collected for all testing over the course

of the present study and were therefore from the same habitat that the sensory surface was tested.

Figure 4.3 – Satellite Image of the Study Site at Liverpool Watersports Centre at Liverpool Queen Dock *(source: Google Maps, 2019)*.

4.2.2. Experimental Design

4.2.2.1. Efficacy of the 8 Pair Gold Interdigitated Electrode Sensor of PVDF

In the present study (Chapter 2) experiments were based on a 9pr Au PTFE sensor, however, due to a shortage of available manufactured sensors, two 8pr Au PVDF (polyvinylidene difluoride) sensors were used (*figure 4.4*).

Figure 4.4 – The 8pr Au PVDF Sensors *with a RF coaxial SMA connector soldered.*

In order to ensure that the 8pr Au PVDF sensor was able to perform in a similar manner to the 9pr Au PTFE sensor, a small-scale laboratory test was conducted with both a Silicone Microtopography and a Smooth Silicone panel. V40 H150 Antifouling Microtopography was selected from Chapter 3 due to its foul-release properties with a reduced adhesion strength per byssal plaque of *M. edulis*. The V40 H150 Silicone Antifouling Microtopography was generated along with a Smooth Silicone Panel (no texture), as described in Chapter 3.

Experimental Setup

As with the experimental setup described in Chapter 2, an individual *M. edulis* was secured to a V40 H150 Antifouling Microtopography Silicone panel (Treatment) (n = 1) and placed in a 30 x 19.3 x 20.6 cm tank together with a V40 H150 Antifouling Microtopography Silicone panel without a mussel (Control) (n = 1). Another 30 x 19.3 x 20.6 cm tank was also setup with an individual *M. edulis* secured to a Smooth Silicone (no texture) panel (Treatment) (n = 1) together with another Smooth Silicone (no texture) panel without a mussel

(Control) (n = 1). After 24 hours, they were removed and prepared with the FR4 with side stick to create the 25 x 25 mm well. These were then to be tested in the temperature controlled (21°C) sensor laboratory with the 8pr Au PVDF sensor, along with the coaxial cable to be used at the field site and the 9pr Au PTFE sensor.

4.2.2.2. Efficacy of the Antifouling Sensory Surface *in situ* and in real-time

Antifouling Sensory Surface Production for in situ use

To produce the antifouling sensory surface for the field, the 8pr Au PVDF sensor and Silicone surface (with the V40 H150 Antifouling Microtopography and the Smooth Silicone) were combined and waterproofed. The sensors were fully enclosed in Thomtastic 30 (T30) Silicone mix (Thomson Brothers Ltd.) with a 10:1 (w/w) base to curing agent ratio. In order to obtain a sensory surface with an exact 1 mm Silicone thickness over the electrodes with either the Microtopography surface or the Smooth surface, a novel and unique mould was developed using SolidWorks® (Solid Solutions). The mould was then printed using the Chemson Ltd. Original Prusa I3 MK2 3D printer. The mould allowed for the 8pr Au PVDF sensor, the RF coaxial SMA connector and the V40 H150 laser textured or non-textured marine grade stainless steel coupons (50 x 50 mm; see Chapter 3) to fit together for the Silicone pour (*figure 4.5*).

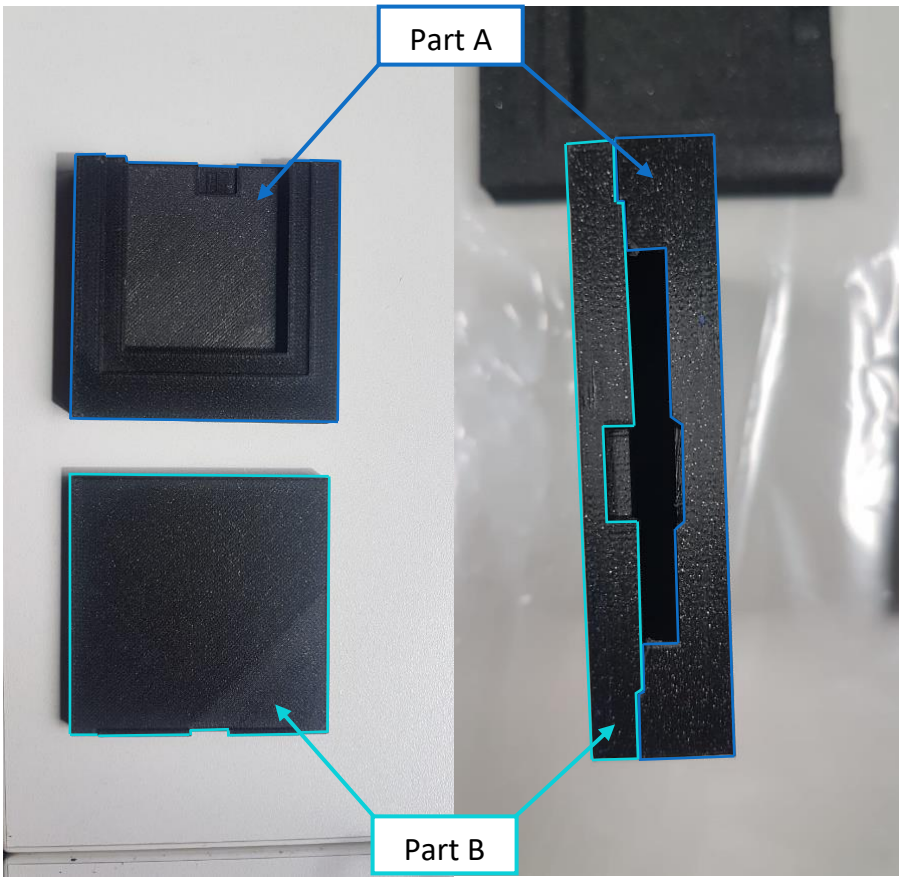

Figure 4.5 – Bespoke 3D Printed Mould for the Development of a Sensory Surface *made of two parts, A and B, whereby silicone was first poured into part A and the stainless steel coupon placed over it. Part B was then placed over to close the mould and the sensor inserted. Extra silicone was then poured into the mould.*

Silicone mix (see Chapter 2) was poured into part A of the mould. Part B and the stainless steel coupon were then placed onto Part A and carefully placed upright (a laser textured coupon for the V40 H150 Microtopography and Smooth Surface steel coupons with no microtopography). The 8pr Au PVDF sensor was then pushed into the mould into the correct position with the connector sat at the top. Rubber bands were used to hold the two halves of the mould together, with extra silicone poured at the top to ensure full coverage and left to cure for 48 hours (*figure 4.6*).

Figure 4.6 – Poured Silicone in Moulds with 8pr Au PVDF Sensor.

After 48 hours the sensory surfaces were carefully removed from the moulds; one Sensory Surface with the V40 H150 Antifouling Microtopography and the other with a Smooth Surface. The connection between a RG316 1.5 metre coaxial cable and the soldered female SMA, straight jack connector was lastly waterproofed using self-amalgamating tape. In order to ensure the electrical components were sufficiently waterproofed, the self-amalgamating tape was wrapped around the base of the sensor as well, ensuring it did not cover the electrodes (*figure 4.7*).

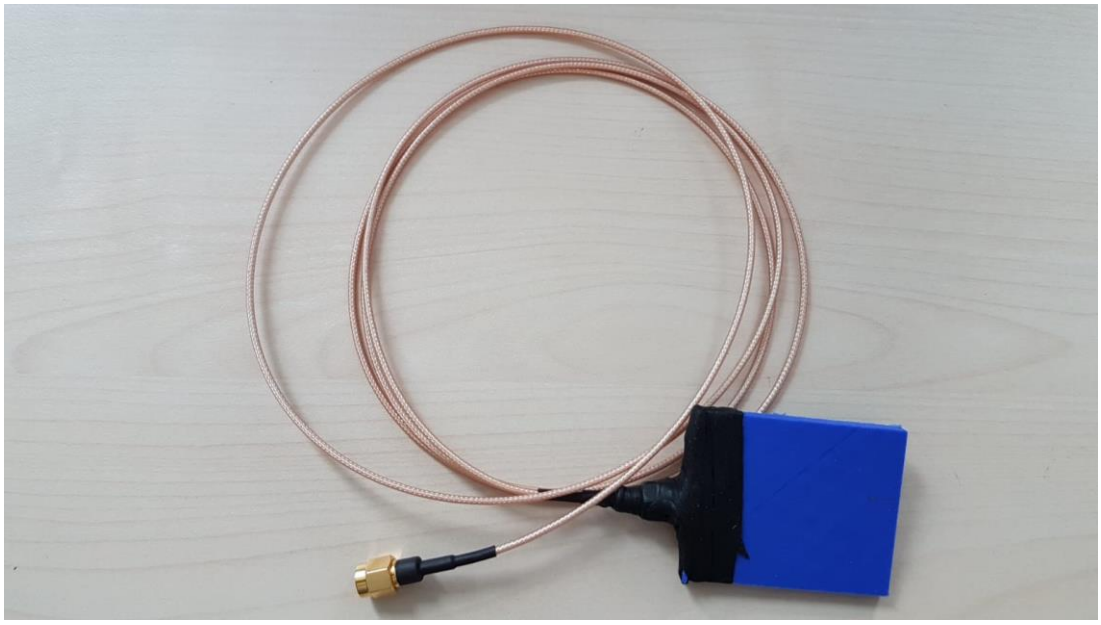

Figure 4.7 – Sensory Surface with the Coaxial Cable Secured with Self-amalgamating Tape.

Experimental Setup

The field site was located on a slipway east of the main Watersports Centre where measurements and observations of the behaviour of the *M. edulis* specimen where recorded. The site slipway allowed for easy access to the water as well as access to an electric socket for the Vector Network Analyser (VNA) (Rohde & Schwarz ZVL). The VNA was able to run from 9 kHz to 13 GHz, however, the frequencies of interest were from 3 GHz to 5 GHz (see Chapter 2).

The experimental rig was made up of PVC piping, a blue 20 x 20 cm PVC panel secured to the piping with cable ties, blue rope to secure the rig to shore and the sensory surface placed on the PVC panel. The sensory surface was then connected via a radio frequency (RF) coaxial, SubMiniture version A (SMA), straight jack (50 ohm) connector to a 1.5 metre RF coaxial cable which in turn was connected to another 3 metre RF coaxial cable with a female to female adaptor. *M. edulis*

specimens were collected from the pontoon at the Watersports Centre (4.8 to 5.9 cm in length) and loosely secured to the sensory surface with a cable tie (*figure 4.8* and *4.9*).

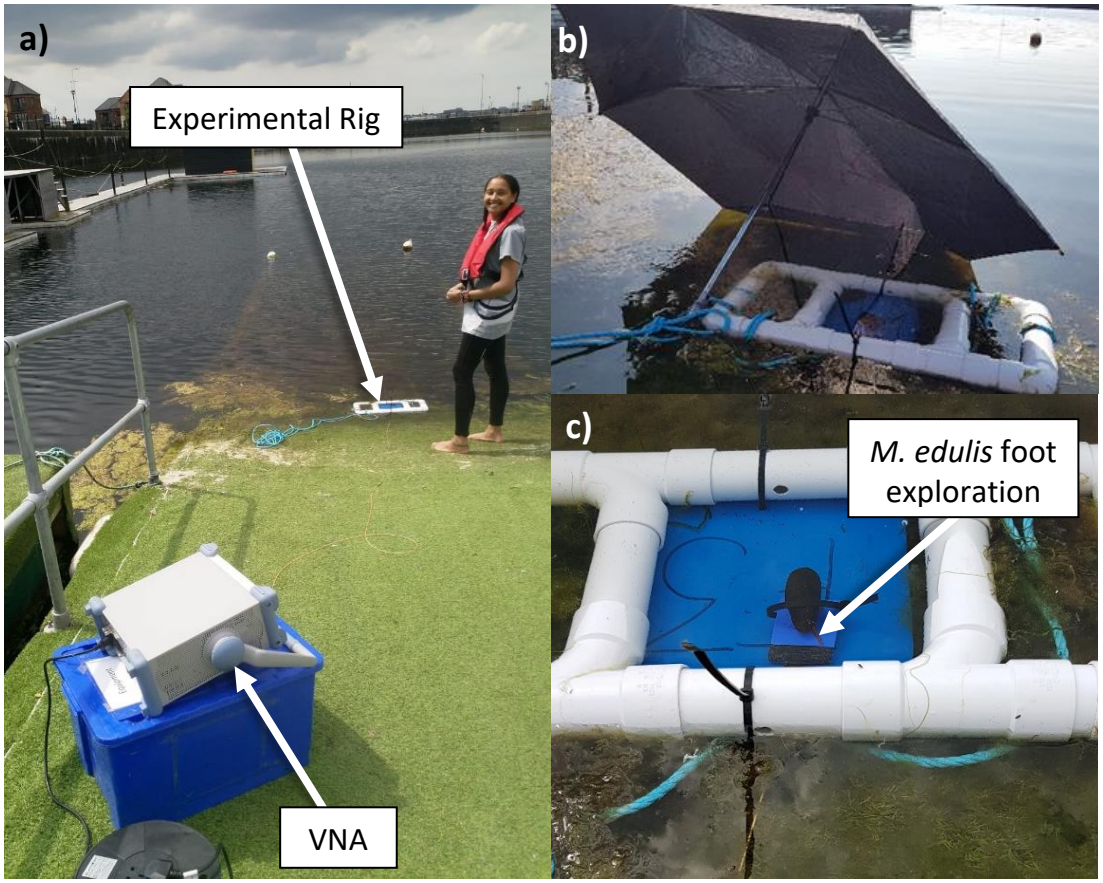

Figure 4.8 – The Experimental Setup *whereby the rig was placed in the docks on the slipway and was connected to the VNA via a coaxial cable (**a**). An umbrella to shade the model specimen (**b**) and the model specimen secured to the sensory surface (foot is exploring surface indicated) (**c**).*

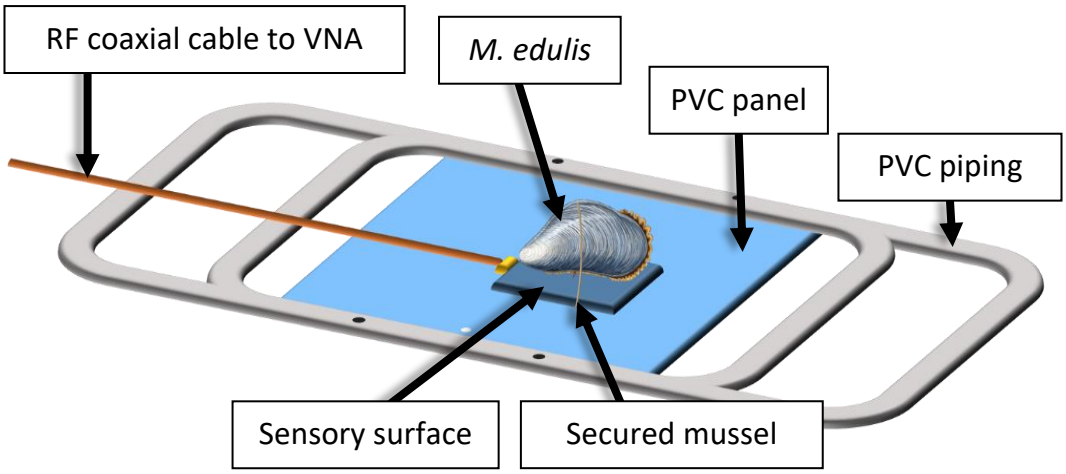

Figure 4.9 – Schematic of the Experimental Setup *with the mussel secured directly to the sensory surface.*

Each sensory surface, V40 H150 Sensory Surface and the Smooth Sensory Surface, was exposed to a different individual *M. edulis* (n =1) for 45 minutes and 30 minutes, respectively.

4.2.3. Data Collection

4.2.3.1. Efficacy of 8 Pair Gold Interdigitated Electrode Sensor of PVDF

Laboratory panels were visually examined and the number of byssal plaques on the surface recorded. Measurements were recorded on a VNA (Rohde & Schwarz ZVA24) calibrated from 10 MHz to 15 GHz with 60,000 points as S_{11} scattering parameter (S parameter) of the reflected signal in a temperature controlled (21°C) sensor laboratory. The data collected included the air spectrum of the VNA, the additional coaxial cable, the 9pr Au PTFE sensor and the 8pr Au PVDF sensor (all plotted using MATLAB (version R2019b). Samples were measured with 400 µl of 28 psu artificial seawater added to the FR4 well and 3 repeat measurements

taken of each of the four orientations with the 8pr AU PVDF sensor (See Chapter 2).

4.2.3.2. Efficacy of the Antifouling Sensory Surface *in situ* and in real-time

For the field study, the VNA was firstly calibrated from 3 GHz to 5 GHz and a 4000 data points sweep run (10 measurements at 3 GHz and 5 GHz, and 20 measurements at each frequency in between at 10 MHz increments) and recorded as real and imaginary numbers with a time stamp. The *M. edulis* specimen was placed on the sensory surface, the behaviour observed and recorded. Multiple repeat measurements were taken of the Sensory Surface in the docks alone, with the mussel and then with the byssi only (between 1 and 21).

4.2.4. Analysis

4.2.4.1. Efficacy of 8 Pair Gold Interdigitated Electrode Sensor of PVDF

The mean Reflection Coefficient S_{11} dB was calculated per panel (all 4 orientations) and graphically represented. The largest difference in the mean (multiple measurements of the same surface) Reflection Coefficient of the Treatments (with byssi) and the Control (no byssi) allowed a single frequency to be deduced where detection was occurring. This was done with both the V40 H150 Silicone Antifouling Microtopography and the Smooth Silicone Panel.

No statistical analysis was carried out due to there being only one sample with multiple measurements, which would act as a pseudoreplication.

4.2.4.2. Efficacy of the Antifouling Sensory Surface *in situ* and in real-time

For the field study, data were converted from real (re) and imaginary (im) components by firstly calculating the magnitude ($|z|$) (*equation 4.1*).

$$|z| = \sqrt{re^2 + im^2}$$

Equation 4.1

The decibels (dB) represented power, but the S parameters (magnitude) were squared when power was calculated, so $10\log(S^2) = 10\log(S) + 10\log(S) = 20\log(S)$.

Data were separated into the Sensory Surface only, the Sensory Surface with the mussel and the Sensory Surface with byssi only (all taken with the Sensory Surface in the docks). For each of the 3 phases during the experiment, the average at each of the 4000 data points between 3 GHz and 5 GHz was deduced. As there were 20 measurements at each frequency in 10 MHz increments (10 measurements at 3 GHz and 5 GHz) the average for each frequency was calculated. Finally, the biggest difference between the Sensory Surface only and the Sensory Surface with the mussel, and the Sensory Surface only and the Sensory Surface with byssi only, was determined and the corresponding frequency identified.

No statistical analysis was carried out due to the lack of replication of samples while the repeat measurements at each data point would result in pseudoreplication.

4.3. Results

4.3.1. Efficacy of 8 Pair Gold Interdigitated Electrode Sensor of PVDF *in vitro*

The air spectrums were visualised for the effect of the additional coaxial cable compared to the VNA alone (*figure 4.10*) as well as for the difference in the air spectrum with the 8pr Au PVDF sensor and the 9pr Au PTFE sensor (*figure 4.11*).

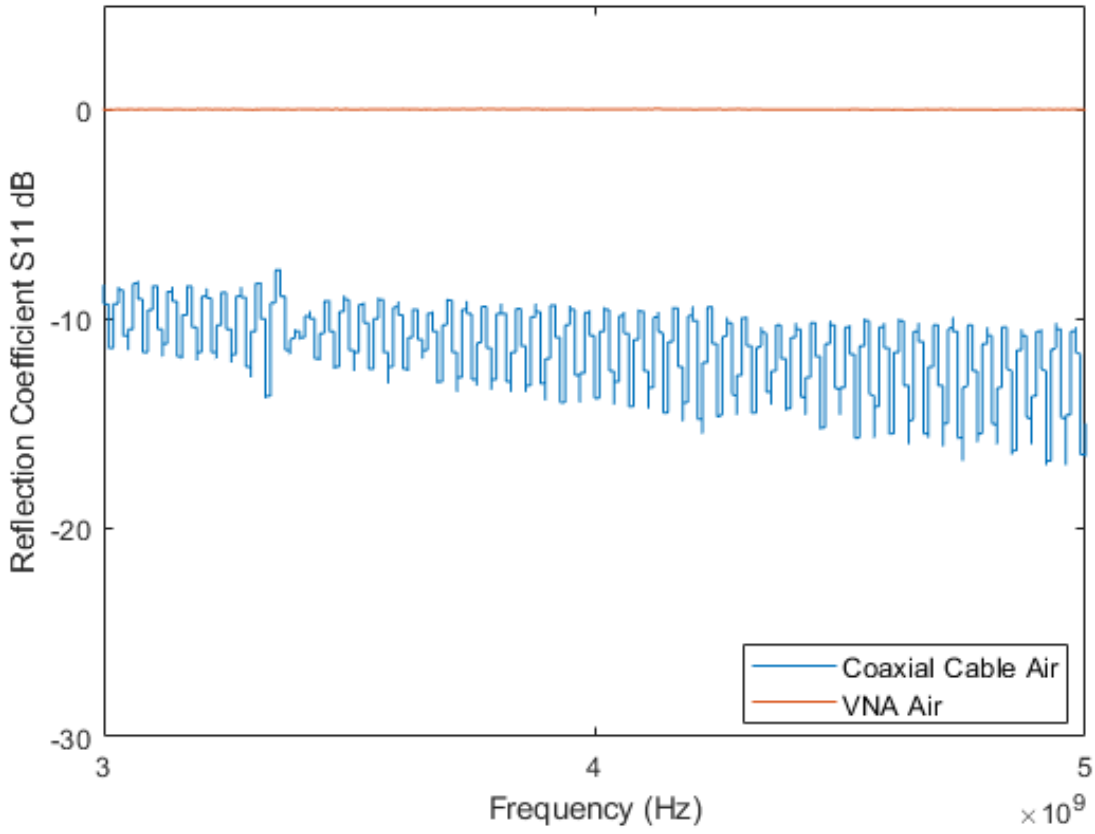

Figure 4.10 – Air spectrum of the VNA and the Additional Coaxial Cable

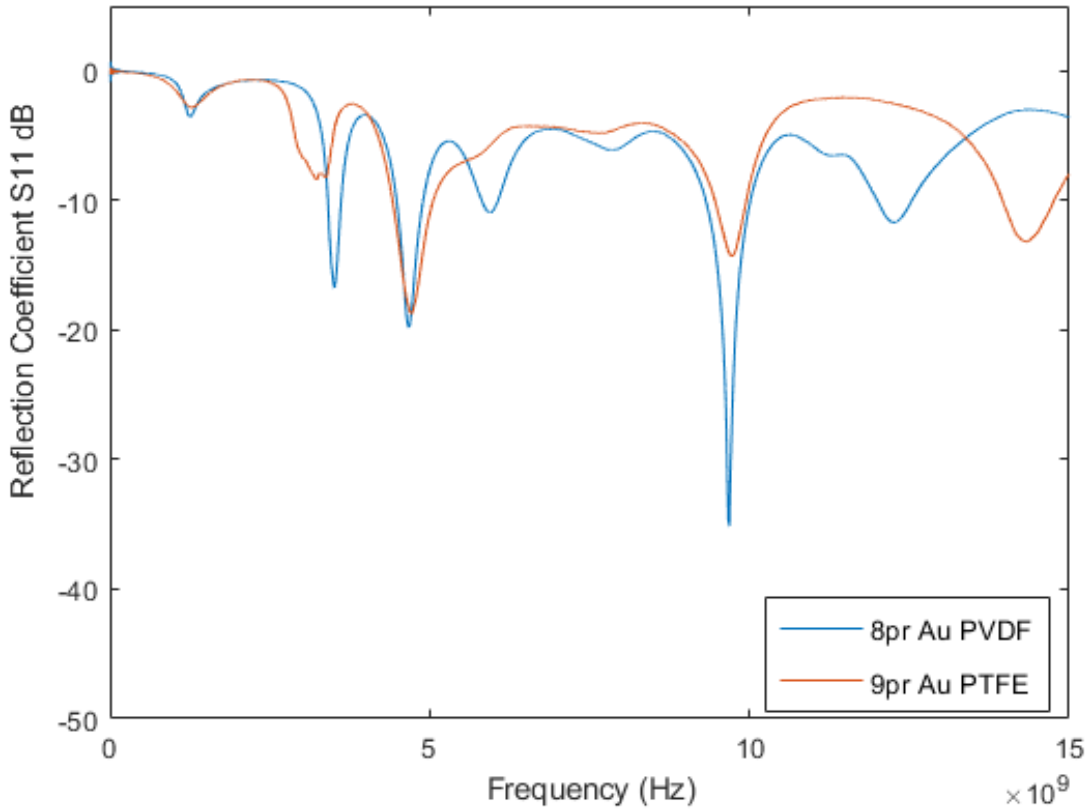

Figure 4.11 – Reflection Coefficient of the 8pr Au PVDF and 9pr Au PTFE Sensor with Air

The V40 H150 Antifouling Microtopography Treatment panel was found to have 1 byssus present on the surface while the Smooth Sensory Surface Treatment did not have any byssi present and could therefore not be analysed towards presence of byssi, nevertheless this was graphically represented (*figure 4.12*).

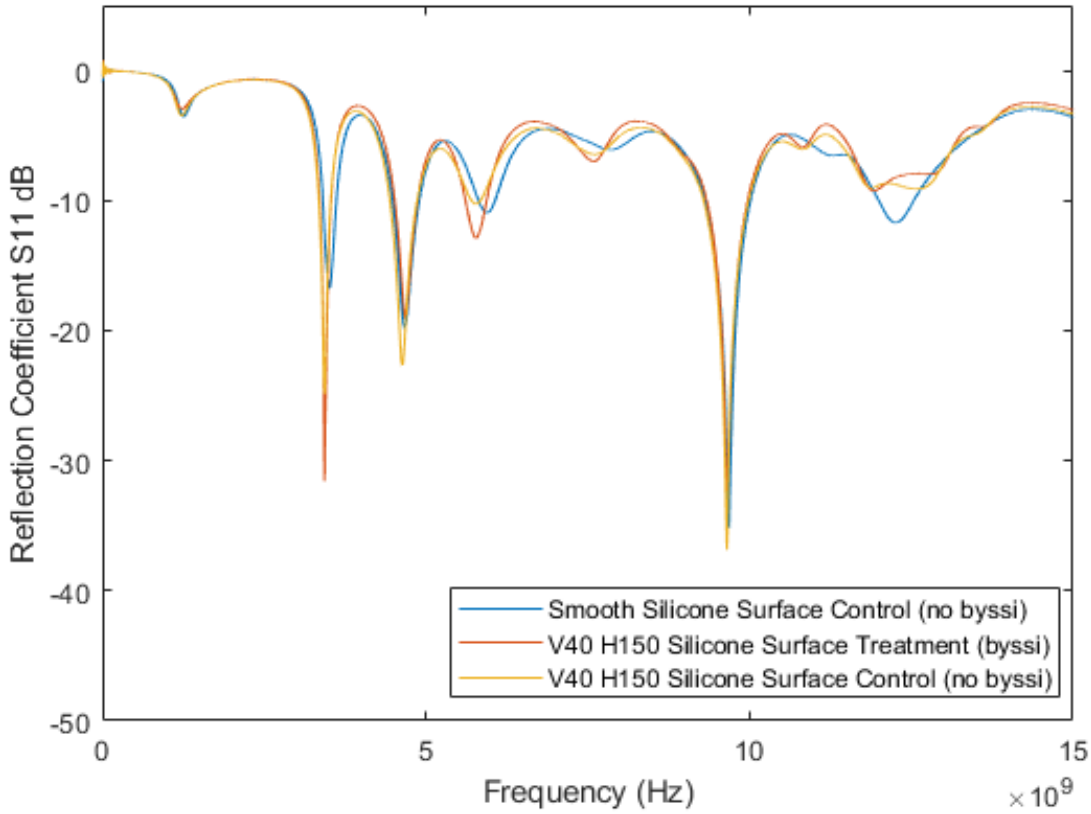

Figure 4.12 - The Reflection Coefficient for the V40 H150 Antifouling Microtopography *Treatment (with byssi) (n = 1) and Control (without byssi) (n = 1), and the Average Reflection Coefficient for the Smooth Sensory Surface Control (without byssi) (n = 1).*

The biggest difference between the Treatment (byssi present) and Control (byssi absent) of the V40 H150 Antifouling Microtopography surface was at 3.43 GHz, with a difference of 6.87 dB and was graphically represented (*figure 4.13*).

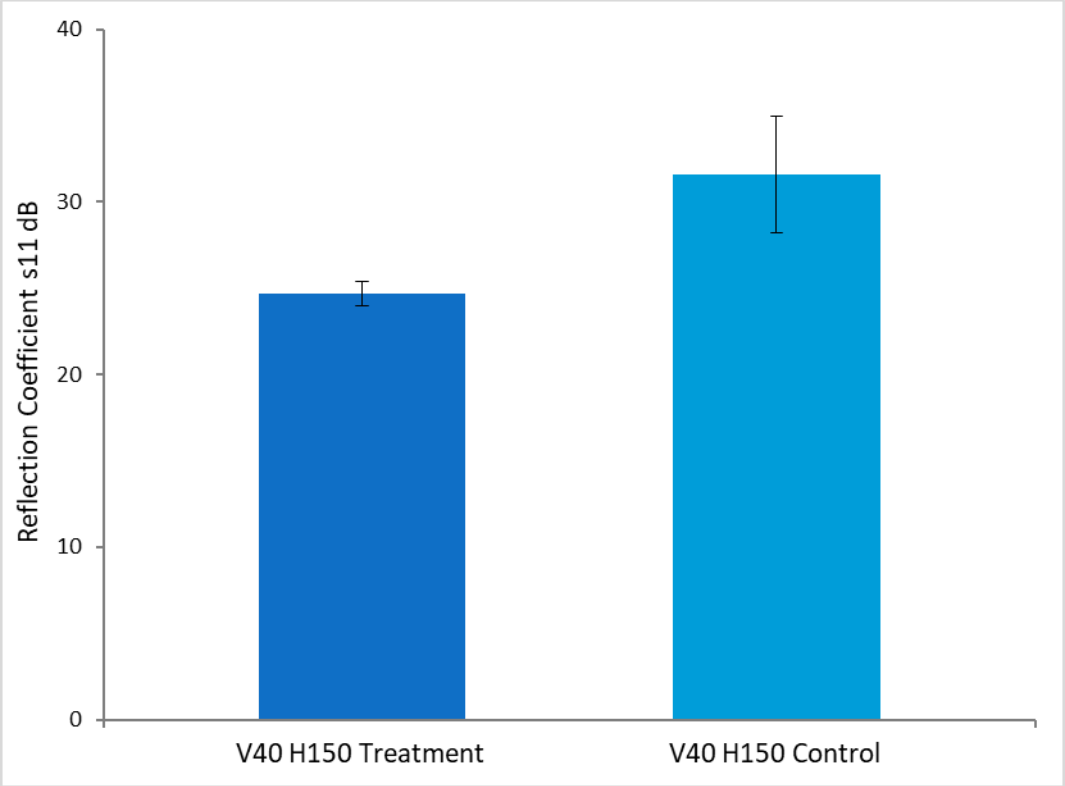

Figure 4.13 – The Average Reflection Coefficient for the V40 H150 Microtopography *Treatment (byssi; n = 1) and Control (no byssi; n = 1) at 3.43 GHz with the standard error of the average of the repeat measurements.*

4.3.2. Efficacy of the Antifouling Sensory Surface *in situ* and in real-time

The average of each frequency of the Smooth Sensory Surface was visualised with the full spectrum from 3 GHz to 5 GHz of the Sensory Surface alone, Sensory Surface with the *M. edulis* specimen and Sensory Surface with the byssi only (1 byssal plaque was placed on the surface) (*figure 4.14*).

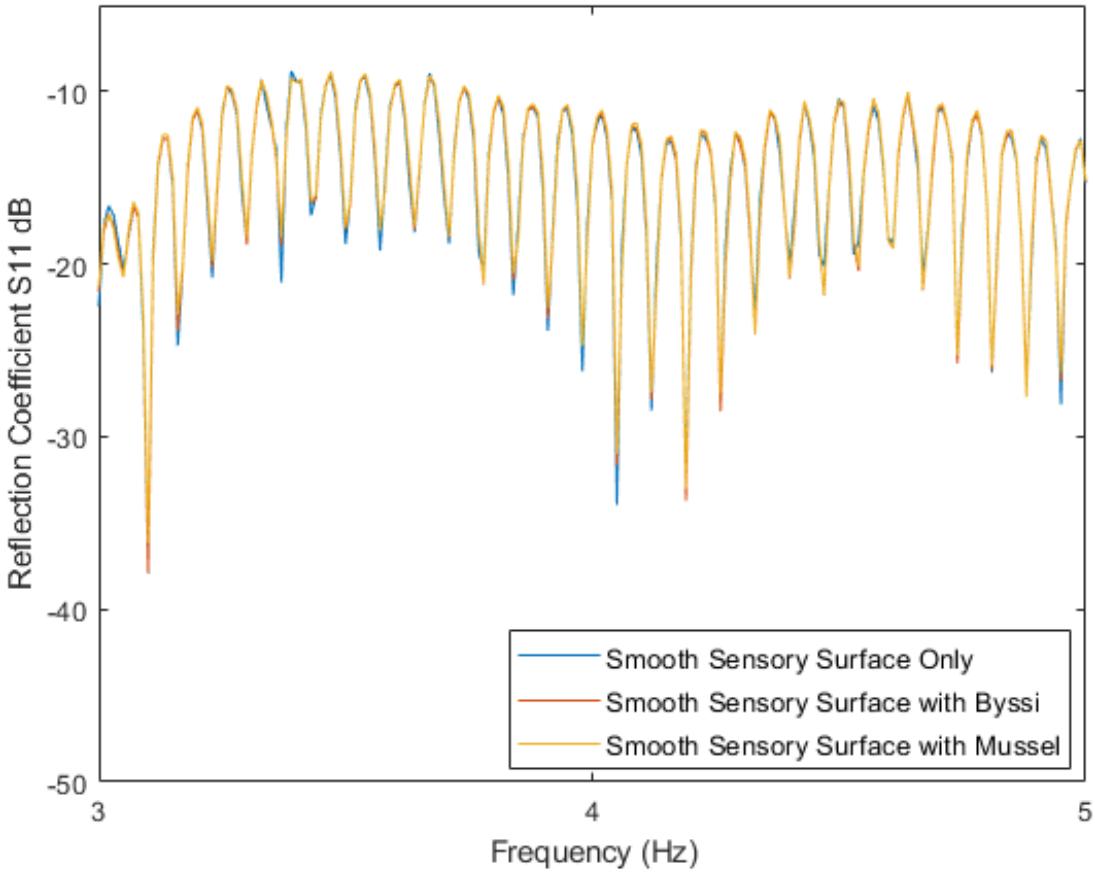

Figure 4.14 - The Mean Reflection Coefficient for the Smooth Sensory Surface *(1 repeat measurement), Smooth Sensory Surface with the byssi (1 repeat measurement) and Smooth Sensory Surface with the M. edulis Specimen (8 repeat measurements).*

The biggest difference between the Smooth Sensory Surface only and the Smooth Sensory Surface with the mussel was 0.2 dB at 4.05 GHz. The biggest difference between the Smooth Sensory Surface only and the Smooth Sensory Surface with byssi only was 0.3 dB also at 4.05 GHz (*figure 4.15*).

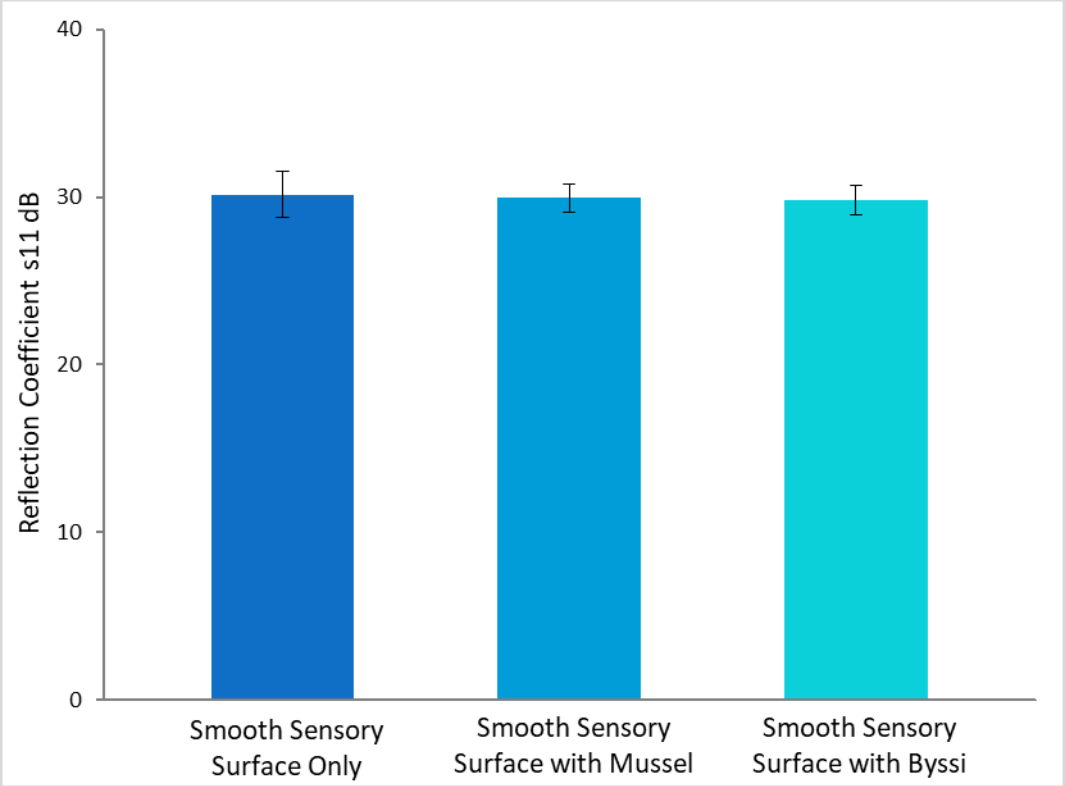

Figure 4.15 - The Reflection Coefficient for the Smooth Sensory Surface only, Sensory Surface with M. edulis specimen and Sensory Surface with the byssi at 4.05 GHz *with the standard error of the average of the repeat measurements.*

The average at each frequency of the V40 H150 Antifouling Microtopography Sensory Surface was visualised with the full spectrum from 3 GHz to 5 GHz; the V40 H150 Antifouling Microtopography Sensory Surface alone, the V40 H150 Antifouling Microtopography Sensory Surface with the byssi only and the V40 H150 Antifouling Microtopography Sensory Surface with the mussel (*figure 4.16*).

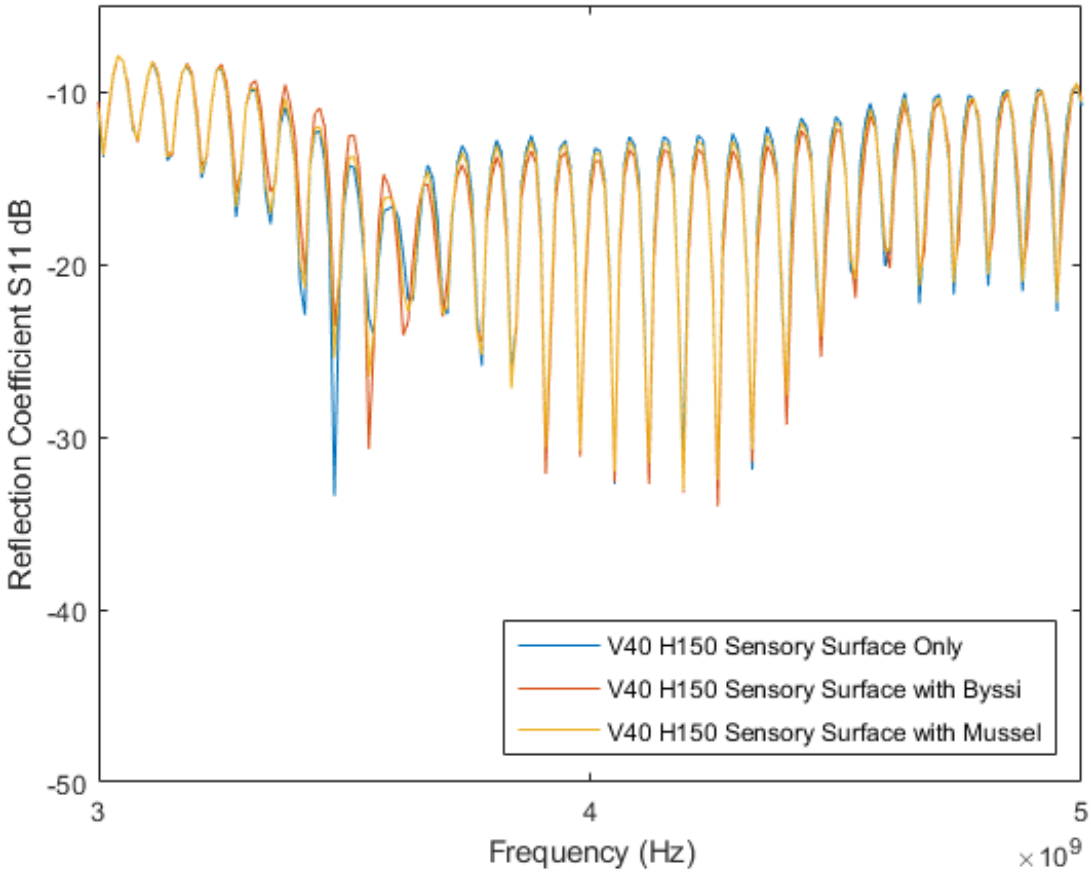

Figure 4.16 – The Reflection Coefficient for the V40 H150 Antifouling Microtopography Sensory Surface *only (1 repeat measurement), Sensory Surface with the byssi (5 repeat measurement) and Sensory Surface with the mussel (21 repeat measurements).*

The biggest difference between the V40 H150 Sensory Surface only and the V40 H150 Sensory Surface with the mussel was 8 dB, at 3.48 GHz. The biggest difference between the V40 H150 Sensory Surface only and the V40 H150 Sensory Surface with byssi only was 9.9 dB, at 3.48 GHz (*figure 4.17*).

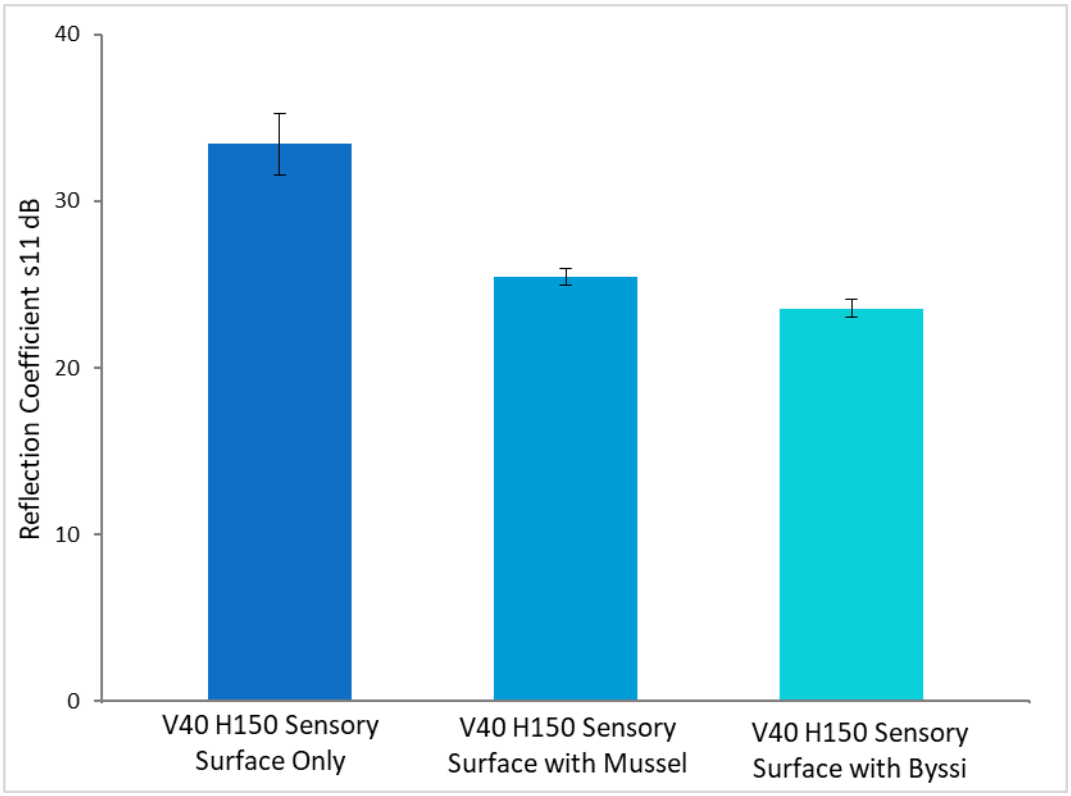

Figure 4.17 - The Average Reflection Coefficient for the V40 H150 Antifouling Microtopography Sensory Surface only, V40 H150 Sensory Surface with the M. edulis Specimen and V40 H150 Sensory Surface with the byssi at 3.48 GHz *with the standard error of the average of the repeat measurements.*

4.4. Discussion

The aim of the study was to determine the efficacy of a sensory antifouling surface towards *M. edulis* attachment and detection under real-time conditions, *in situ*. The laboratory-based study demonstrated an effect of the additional coaxial cable on the Reflection Coefficient output as well as the differing spectrum with the 8pr Au PVDF and 9pr Au PTFE sensors. Furthermore, a V40 H150 Antifouling Microtopography panel with the 8pr Au PVDF sensor showed detection of *M. edulis* byssal plaque on the surface at 3.43 GHz with a difference of 6.87 dB.

The *in situ* field study demonstrated the ability of the Smooth Sensory Surface to detect the presence of *M. edulis* or the byssal plaque on the surface at 4.05 GHz with a difference of 0.2 dB and 0.3 dB, respectively. Moreover, the V40 H150 Antifouling Microtopography Sensory Surface detected the presence of *M. edulis* and the byssal plaque at 3.48 GHz with a difference of 8 dB and 9.9 dB, respectively.

4.4.1. Efficacy of 8 Pair Gold Interdigitated Electrode Sensor of PVDF

The additional coaxial cable demonstrated an effect on the Reflection Coefficient output. This phenomenon may be due to the characteristic oscillating waves at a given radio frequency from the VNA and reflected back within the waveguide cable (Boswell, 1984). Although the coaxial cable connected to the VNA was calibrated, the additional RG316 coaxial cable remained uncalibrated and therefore did not account for independent error sources of finite directivity, generator mismatch and cable transfer function (Caspers and Kowina, 2013). This

may result in a loss of power reaching the sensor and a reduced sensing capacity, however, the VNA carries out an internal error calibration for frequency-dependent losses and phase-transfer functions of the cable allowing the cable to remain functional, but with a reduced measurement quality (Caspers and Kowina, 2013).

The 8pr Au PVDF had an effect on the Reflection Coefficient with air when compared to the 9pr Au PTFE sensor. The air spectrum of the two sensors demonstrated similar outputs, particularly at lower frequencies ($f \leq 5$ GHz) whereby the second peak, approximately between 3 GHz and 4 GHz, showed an increased Reflection Coefficient for the 8pr Au PVDF sensor. The electrodes of the two sensor types was gold and both PTFE and PVDF are fluoropolymers that are widely used as a substrate for various sensor types (Bott and Jones, 1984; Wienecke *et al.*, 2003; Shirinov and Schomburg, 2008; Xia *et al.*, 2018). However, the differences in the output between the two sensors may be due to differences in the number of electrodes present resulting in the 8pr Au PVDF having a slightly decreased sensing capacity (Grover, 1999; Alexander *et al.*, 2010; Sun *et al.*, 2018). Nonetheless, with a difference of only 1 pair of electrodes, this discrepancy was considered negligible and the similar output frequency allowed for the presumption that the 8pr Au PVDF may detect the presence *M. edulis* byssal plaque on a surface as effectively as the 9pr Au PTFE sensor (see Chapter 2).

There was an effect on the Reflection Coefficient output by the V40 H150 Silicone Microtopography with 1 byssus (Treatment) and with no byssi (Control) whereby

the biggest difference was at 3.43 GHz of 6.87 dB. Furthermore, the large difference of 6.87 dB in the Reflection Coefficient with the Silicone microtopography differed from the 2.52 dB at 3.33 GHz found in Chapter 2. This may be due to the single replicate in this study yielding a large difference in comparison to the 40 replicates investigated in Chapter 2. However, the presence of the microtopography may not affect the Reflection Coefficient at lower frequencies ($f \leq 5$ GHz) as the Smooth Silicone Surface with no byssi shows a similar output, *in vitro*. Nevertheless, at frequencies between 5 GHz and 10 GHz, there may be an effect of the microtopography on the Reflection Coefficient for both Treatment and Control, whereby there may be a slight phase shift to the left compared to the Smooth Silicone. This may be due to the microtopography allowing the presence of artificial seawater or air within the troughs of the Silicone surface (depending on the wetting type) (Carman *et al.*, 2006) and therefore resulting in an effect of the Reflection Coefficient due to the various relative permittivities of Silicone and artificial seawater and/or air occurring at different depths (Sebastian, 2008).

4.4.2. Efficacy of the Antifouling Sensory Surface *in situ* and in real-time

The Smooth Sensory Surface *in situ* may demonstrate an effect of the mussel specimen and the byssal plaque on detection at 4.05 GHz. In addition, the V40 H150 Antifouling Microtopography may demonstrate an effect of the *M. edulis* specimen and the byssal plaque on detection at 3.48 GHz. In both conditions, the study demonstrated a consistent frequency whereby detection may occur.

However, examining the difference in Reflection Coefficient between the Sensory Surface only and the Sensory Surface with the *M. edulis* specimen, and the difference between the Sensory Surface only and the Sensory Surface with byssal plaque was 0.2 dB and 0.3 dB respectively, for the Smooth Sensory Surface, and 8 dB and 9.9 dB respectively, for the V40 H150 Sensory Surface.

The Smooth Sensory Surface demonstrated a smaller difference in Reflection Coefficient that may be due to the lack of replicates for analysis as well as reduced power and measurement quality with the uncalibrated coaxial cable (Caspers and Kowina, 2013). Nevertheless, the V40 H150 Antifouling Microtopography demonstrated a large difference in the Reflection Coefficient between the Sensory Surface only and the Sensory Surface with the *M. edulis* specimen, and the Sensory Surface with byssal plaque, utilising the same equipment and with a single replicate. Similarly, the Reflection Coefficient of the V40 H150 Sensory Surface only was greater than the Smooth Sensory Surface only. The effect of the microtopography on the propagation of the electromagnetic wave may be due to the troughs which may allow for the presence of air (Carman *et al.*, 2006) that may result in attenuation of the wave and an increase in the Reflection Coefficient to allow for a more sensitive detection capacity (Tang *et al.*, 2007). The possible effect on enhanced detection with the microtopography may allow for the reduced Reflection Coefficient for the V40 H150 Sensory Surface with the presence of the mussel specimen or byssal plaques to be better identified and may be due to their respective relative permittivities as expressed by *equation 1.1* (Korostynska *et al.*, 2013). Furthermore, *M. edulis* may be between 5 and 10 cm

in length and the byssal plaques may range from 0.78 to 4.8 mm (Tamarin and Keller, 1972; Tyler-Walters, 2008) and although their relative permittivities are unknown, the large size of the mussel compared to the byssal plaques may be shown to result in a reduced Reflection Coefficient (Korostynska *et al.*, 2013), however, the present study does not support this. Both Sensory Surfaces demonstrated a larger difference in the Reflection Coefficient with the byssal plaque only than with the mussel. This may be due to measurements with the mussel including periods with no byssi put down on the surface. Nevertheless, the lower Reflection Coefficient with the byssal plaque only, in both conditions, may demonstrate the near-field and surface sensing capacity of the Sensory Surfaces without interference of matter in the water column of the marine environment.

The novel development of a sensory surface for *M. edulis* biofouling may allow for the development of a non-toxic foul-release technology with the capacity to detect the presence of *M. edulis* byssal plaque on the surface only. This may allow for the maritime industry to implement this type of technology in order to assist in monitoring biofouling development in real-time for effective husbandry and compliance with regulations as well as offer an alternative to toxic antifouling strategies (Abbott *et al.*, 2000; Rittschof, 2000; Thomas and Brooks, 2010; International maritime organistaion, 2016; Zabin *et al.*, 2018). With the further development of an effective sensory surface as an antifouling strategy, the intention would be to reduce the problems of drag increase and therefore the associated increase in costs, fuel consumption, greenhouse gas emissions and transport of invasive species (Hellio and Yebra, 2009; Lewis and Coutts, 2010;

International maritime organistaion, 2011, 2016; Schultz *et al.*, 2011; Bixler and Bhushan, 2012; Bressy and Lejars, 2014).

4.4.3. Conclusion

The Silicone Sensory Surfaces examined in the present study showed the ability for the detection of *M. edulis* byssal plaque, *in situ* and in real-time. Furthermore, the presence of a microtopography on the V40 H150 Sensory Surface may demonstrate an increased sensitivity towards detection of *M. edulis* byssal plaque, *in situ* and in real-time.

Chapter 5

General Discussion

“The cure for anything is saltwater –

sweat, tears, or the sea.”

- *Isak Dinesen*

5.1. Overview

The universal and ancient issue of marine biofouling is known to cause both financial and environmental costs with the occurrence of fuel penalties, damage to vessels, greenhouse gas emissions, introduction of non-native species and spread of disease (Mee *et al.*, 1986; McCarthy and Khambaty, 1994; Ruiz *et al.*, 2000; Davidson *et al.*, 2008; Brooks and Waldock, 2009; Edyvean, 2010; Lewis and Coutts, 2010; Ribeiro *et al.*, 2012). Research, development and investment into managing and tackling these issues is focused on a few main strategies such as antifouling measures, cleaning and removal methods, implementation of regulations, and visual inspections (Schultz *et al.*, 1999; Kiil *et al.*, 2001; Holm *et al.*, 2004; Howell and Behrends, 2006; International maritime organistaion, 2011, 2016; Floerl and Coutts, 2013; Bressy and Lejars, 2014; Tribou and Swain, 2015; Zabin *et al.*, 2018). Antifouling preventative measures are based on toxic biocides, poor long-term durability as well as costly, time consuming and speed dependant efficacy (Abbott *et al.*, 2000; Schultz, 2007; Hellio and Yebra, 2009). Furthermore, a decreased efficacy of the antifouling paint are known to occur due to damage of the surfaces caused by docking, cleaning and removal strategies (Holm *et al.*, 2003; Oliveira and Granhag, 2016). The ship's Biofouling Management Plan and record book, as well as the history and certificates of the vessel, are used to enforce biofouling regulations (Irving and McCarthy, 2018).

Nevertheless, the maritime industries long-term aim is focused towards a more environmentally conscious future with the implementation of the 2018

mandatory measures to reduce emissions by 50% by 2050 (compared to 2008) as well as moving away from biocide based antifouling technologies and towards non-toxic methods (Khanna, 2008; AMBIO, 2010; Thomas and Brooks, 2010; European Union, 2012; Bressy and Lejars, 2014; European chemicals agency, 2015; International Maritime Organistaion, 2018). Non-toxic, foul-release coatings (FRCs) and microtopographies are shown to reduce settlement and attachment efficacy of biofouling organisms such as barnacle cyprids, *Ulva* zoospores and bacteria (Berntsson *et al.*, 2000; Candries and Anderson, 2001; Chung *et al.*, 2007; Schumacher *et al.*, 2007; Scardino *et al.*, 2008; Townsin and Anderson, 2009; Corbett and Winebrake, 2010; Magin *et al.*, 2010; Salta *et al.*, 2010). Nevertheless, the industry lacks a method for real-time, *in situ* detection that may allow for more effective biofouling management, particularly with the possibility of some biofouling development over time with a non-toxic antifouling FRC and the species-specific nature of microtopographies (Callow *et al.*, 2002; Prendergast, 2010; Carl *et al.*, 2012; Bressy and Lejars, 2014).

The implementation of a Sensory Antifouling Surface to deter and detect the presence of biofouling *in situ* and in real-time may facilitate the industry and its biofouling management strategy to be more efficient and proactive in its approach to the issue. The overall aim of the present study was to **develop a bespoke sensory surface to monitor *in situ* biofouling in real-time and demonstrate its use synergistically with a novel non-toxic antifouling technology, laser microtexturing.** The first aim was to **determine the efficacy of *M. edulis* detection depending on the geometry and number of IDEs of the**

planar EMW sensor, determining if the efficacy of the sensor was impacted by the orientation and **determining the efficacy of the sensor when detecting *M. edulis* byssal plaques on differing materials based on wettability and relative permittivity, *in vitro*** (Chapter 2). Secondly, the present study aimed to **develop a microtopography pattern on stainless steel dependant on the hatch spacing and speed of an SPI nanosecond pulsed fibre laser and transfer of the microtopography to a silicone surface** and **to determine the efficacy of the developed microtopography on silicone as an antifouling, foul-release surface towards *M. edulis* attachment, *in vitro*** (Chapter 3). Lastly, the present study aimed to **determine the efficacy of the sensory antifouling surface towards *M. edulis* attachment and detection under real-time conditions, *in situ*** (Chapter 4).

5.1.1. Summary of Findings

Chapter 2 – Detection of the Blue Mussel, Mytilus edulis, on a Surface with a Planar IDE Sensor

The IDE number and geometry of the sensors demonstrated an effect on the detection efficacy of artificial seawater and *M. edulis* byssal plaques on the surface. The 1 line Au PTFE sensor did not demonstrate a difference with the presence of byssal plaques in the dry condition indicating a lower detection efficacy than that of the 3pr Au PTFE, 9pr Au PTFE and 2 × 3pr Au PTFE sensors. The orientation of the panels' showed no effect with the 1 line Au PTFE and the 9pr Au PTFE sensors, however, variability with differing orientations was

demonstrated with the 3pr Au PTFE sensor and more distinctly with the 2 × 3pr Au PTFE sensor.

The 9pr Au PTFE sensor selected as the best sensor type for detection was further developed by evaluating the detection efficacy and the attachment for four materials; Nylon 6, Silicone, PVC and PTFE. The number of byssal plaques that the *M. edulis* specimens deposited on the four materials was lower with the low surface energy and hydrophobic materials, particularly Silicone. Conversely, the highest number of byssal plaques occurred with hydrophilic Nylon 6. The 9pr Au PTFE planar EMW contactless sensor detected the presence of *M. edulis* byssal plaques on Nylon 6 at 5.84 GHz and 3.41 GHz, Silicone at 6.55 GHz and 3.33 GHz, PVC at 4.64 GHz; however, it was unable to detect the byssal plaque with the PTFE surface.

This study demonstrated the ability of the 9pr Au PTFE sensor to detect *M. edulis* byssal plaques on different surface materials at a selected frequency. Silicone demonstrated the lowest number of byssal plaques as well as compatibility as a sensing surface with the selected sensor for detection of *M. edulis* byssal plaque at 3.33 GHz and was therefore selected for further development as an antifouling, foul-release microtopography.

Chapter 3 – Development of a Non-toxic Antifouling and Foul-release Surface

The production of microtopographies on stainless steel coupons using an SPI nanosecond pulsed fibre laser were visualised with a Bruker microscope and implementation of both deionised water ultrasonic clean and 70% ethanol

demonstrated no visible transfer of an oxide layer and an appropriate transfer of the microtopography onto Silicone.

The effect of a microtopography demonstrated an increased plaque area with the V40 H100 microtopography compared to the smooth surface, however, the adhesion force of the byssal plaques was weakest with the V40 H100 microtopography and strongest with the smooth surface. Overall, the microtopographies did not demonstrate an effect on the number of byssal plaques; however, the V40 H50 and V40 H150 exhibited the lowest number of byssal plaques and were then further examined.

The V40 H50 and V40 H150 microtopographies showed an effect on the number of byssal plaques with an increased amount when compared to the smooth silicone surface and smooth PVC control. Furthermore, the microtopography did demonstrate an effect on the adhesion strength per byssi, whereby the V40 H150 microtopography showed the weakest adhesion strength, followed by the V40 H50 microtopography, smooth silicone control and then the smooth PVC control.

The study demonstrated a reduced *M. edulis* byssal plaque adhesion strength with the presence of a microtopography on silicone, particularly with the V40 H150 microtopography when compared to a smooth silicone surface and a smooth PVC surface. Due to the foul-release effect of the V40 H150 microtopography, the silicone microtopography was therefore selected for the development of a waterproof Sensory Surface to detect and reduce *M. edulis* biofouling *in situ* and in real-time.

Initial laboratory-based testing of the additional coaxial cable and the 8pr Au PVDF sensor demonstrated a characteristic oscillating output and a similar Reflection Coefficient to the 9pr Au PTFE sensor, respectively. The 8pr Au PVDF sensor showed detection of the byssal plaque at 3.43 GHz with the V40 H150 silicone panel.

The Smooth Sensory Surface and the Antifouling Microtopography Sensory Surface showed the detection of a *M. edulis* specimen and the byssal plaques at 4.05 GHz and 3.48 GHz, respectively.

The study demonstrated the ability for the V40 H150 microtopography Sensory Surface to detect the presence of a *M. edulis* specimen as well as the byssal plaque on the surface *in situ* and in real-time.

5.2. Microtopography Sensory Surface with IDE Planar Sensor for *in situ* and Real-time Biofouling Detection

Upon writing this thesis, there are currently no methods for real-time and *in situ* detection of biofouling in the maritime industry. The study presented here demonstrated the ability of the 8pr Au PVDF and 9pr Au PTFE sensor to detect *M. edulis* (a dominant biofouling organism; Dürr and Wahl, 2004) byssal plaques on silicone at selected frequencies, *in vitro*. Furthermore, the 9pr Au PTFE sensor also demonstrated detection of the byssal plaque with other materials due to the

contactless and non-specific nature of the sensor (Mason *et al.*, 2013), which may allow for widespread use with varying surfaces including available antifouling coatings and common materials in the maritime industries. Moreover, there are multiple cost-effective processes for the development of such sensor types including print screening, ink-jet printing and photolithography (Brischwein *et al.*, 2006; Crowley *et al.*, 2010). These methods are compatible with various substrates such as paper and plastic, as well as electrode materials such as silver, platinum and aluminium (Tsouti *et al.*, 2011; Molina-Lopez *et al.*, 2012; Chou and Lee, 2014; Motha *et al.*, 2015; Yang *et al.*, 2015; Gaspar *et al.*, 2017). The use of gold electrodes in this study was based on availability of manufactured sensors as well as its inert nature and good electrical conductivity (Summerlot *et al.*, 2011). However, such a sensor may be developed using conductive paints based on carbon/graphene that may be used in biosensors, and the detection of gases and heavy metals (Shao *et al.*, 2010; Yavari and Koratkar, 2012; Varghese *et al.*, 2015; Justino *et al.*, 2017).

Similar IDE planar sensors, as those used in the present study, found widespread use in part due to their localised electromagnetic field with a high sensitivity likely attributable to altering the size, space and number of electrodes (Grover, 1999; Mukhopadhyay, 2005). Testing of an additional V40 H150 Antifouling Microtopography Sensory Surface *in situ*, did not yield any byssal plaque deposition, however, the behaviour of *M. edulis* on the Sensory Surface was of interest. The initial mussel was placed on the Sensory Surface for 10 minutes and did not put any byssi down, but foot exploration occurred away from the sensing

area of the Sensory Surface. Subsequent mussels (4 additional mussels) behaved similarly when exposed to the Sensory Surface for between 5 and 22 minutes. This observation may elude to some EMW sensitivity of *M. edulis* similar to that of barnacle larvae (Leya *et al.*, 1999), particularly as it was shown that exposure to a magnetic field impacted the hydration and amine nitrogen of the mussel (Fisher and Slater, 2010).

The presence of the microtopography may impede the mussel's ability to undergo effective cavitation in order to release adhesive proteins for the formation of the byssal plaque (Tamarin and Keller, 1972) as was visualised *in vitro*. Differences in the byssal plaque with differing microtopographies in the present study may elude to the poor formation of the byssal plaques and the resultant reduced adhesion strength (*figure 5.1*).

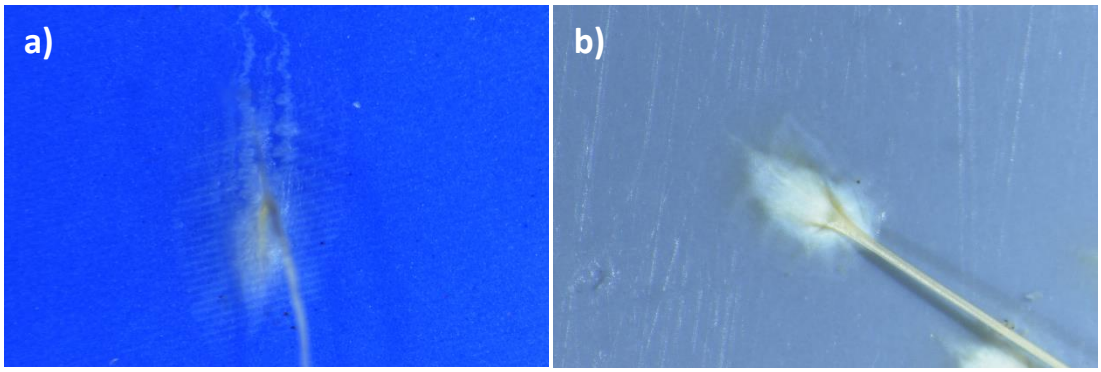

Figure 5.1 – M. edulis Byssal Plaque on V40 H50 Microtopography (a) and on PVC (b), in vitro *showing unusual formation of the plaque on the microtopography*

In the present study, the IDE geometry with relatively small dimensions and an increased number of electrodes demonstrated a localised electromagnetic field with high sensitivity (Grover, 1999; Mukhopadhyay, 2005; Mason *et al.*, 2013). Moreover, the non-destructive, contactless and non-specific sensor showed

compatibility with various sensing materials, such as silicone, whose higher relative permittivity may be appropriate to allow for a sufficient reduction in the wavelength for detection of *M. edulis* byssal plaques (Korostynska *et al.*, 2013; Rumpf, 2017). In addition, the lower surface energy of silicone may exhibit antifouling properties due to the general preference of *M. edulis* towards high energy surfaces such as nylon 6 (Crisp *et al.*, 1985; Aldred *et al.*, 2006). The presence of a microtopography on silicone may reduce wettability and experience Cassie-Baxter wetting, which may result in bridging of the byssal plaques between the microtopography features and resulting in a decreased adhesion strength of *M. edulis* byssal plaque for foul-release (Carman *et al.*, 2006). With the occurrence of Cassie-Baxter wetting, the presence of air in the valleys of the microtopography may result in attenuation of the EMW and increase the detection capacity of the sensor (Tang *et al.*, 2007). Nevertheless, the presence of the electromagnetic field of the IDE planar sensor may deter *M. edulis* biofouling as the organism may show sensitivity towards EMW.

5.2.1. Application for Industry

The 2.5 × 2.5 mm sensing area of the gold electrodes of the sensors used in the present study may be unsuitable for applications in the maritime industry due to the currently small sensing area as well as the high cost of gold. However, utilising alternative electrode materials (such as a conductive paint) and fabrication processes (such as screen-printing) may allow for a more cost-effective application. Upscaling of IDE planar sensors is dependent on the geometry of the

electrodes whereby the efficiency is defined in *equation 2.3* and an increase in the width and/or number of electrodes may increase the signal (Grover, 1999). IDE sensors may exhibit high sensitivity in the near-field, however, an increased penetration height of the electromagnetic field may cause the non-specific acoustic sensor to detect beyond the surface, which may result in an unreliable measurement due to the dynamic nature of the marine environment (Van Gerwen *et al.*, 1998). It is therefore an important feature of the sensor to maintain near-field detection, which may only occur with maintaining a small IDE gap (Shim *et al.*, 2013). A sensor array network may overcome this limitation as well as the use of different sensor geometries including circular or hexagonal arrays (*figure 5.2*; Grover, 1999).

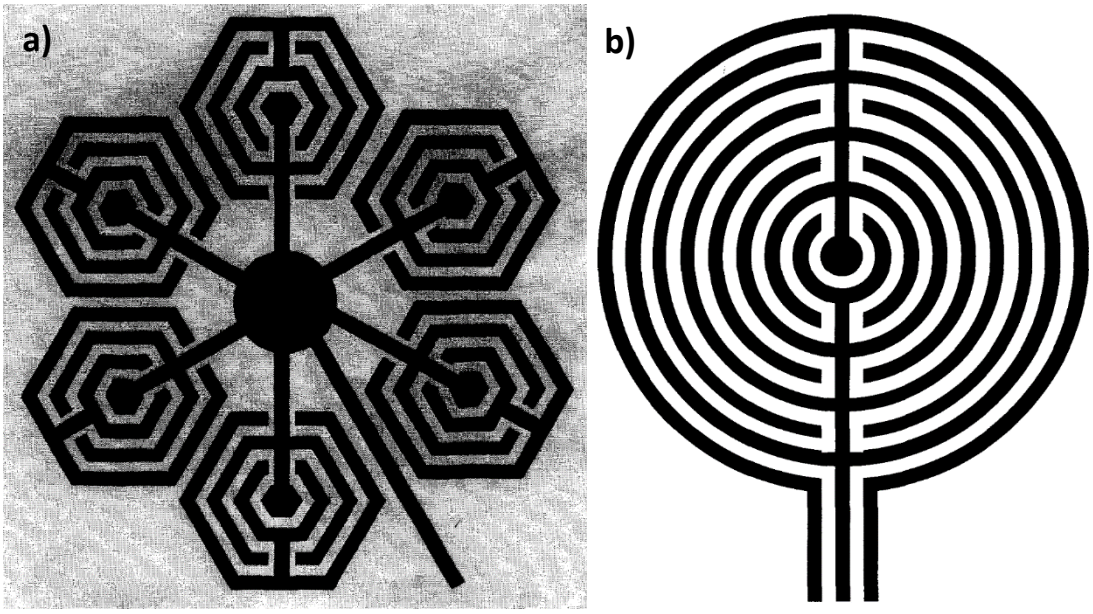

Figure 5.2 – IDE in a hexagonal network (a) and in a circular geometry (b) *(source:* Grover, 1999*)*

An array network of individual sensing elements may additionally allow each to sense a different analyte and therefore detect a complex mixture (Grover, 1999) as is found in biofouling communities (Lewis and Coutts, 2010). Additionally, the use of gold electrodes may not be feasible on a larger scale and therefore, the use of conductive paints may allow for the IDE to be directly screen printed to the surface, particularly in niche areas (Brischwein *et al.*, 2006; Crowley *et al.*, 2010). Similarly, industry application of the microtopography and the fabrication process used in the present study may be adjusted for suitable large-scale application. This may involve the use of a moulded thin film of the microtopography for application within niche areas (Berntsson *et al.*, 2000). In the shipping industry, niche areas refer to areas such as the rudder, propeller, grates, stabilisers, bilge keels, dock block areas, stern tubes, stern thrusters, sea chests and ballast water tanks and pipes (Davidson *et al.*, 2013; Moser *et al.*, 2017). Moser *et al.* (2017)

identified that the proportion of niche area relative to the total wetted surface area was higher for passenger vessels at 27% and lower for bulk carriers and tankers at 7-8%. Furthermore, the thruster tunnel was identified as representing over half of the total niche areas, recognising it as a 'super-hot spot' for biofouling (Moser *et al.*, 2017). Such niche areas may often be overlooked during hull inspections, which may pose a biosecurity risk, as they tend to be highly biofouled hotspots (Davidson *et al.*, 2016). Further development and testing of a planar IDE acoustic wave sensor operating at microwave frequencies for the detection of biofouling organisms, such as *M. edulis,* may be used within niche biofouling hotspots. This may allow for a reduction in biosecurity risks imposed by invasive species and allow for biofouling quantification in order for governments and international bodies to enforce regulations (International maritime organistaion, 2016; Irving and McCarthy, 2018; Zabin *et al.*, 2018).

5.3. Future Recommendations

EMW sensor development may be dependent on the sensing material to allow for precise detection based on a unique interaction of the material and the analyte (Radke and Alocilja, 2004; Blakey and Morales-Partera, 2016; Frau *et al.*, 2017, 2019). Some key proteins found in *M. edulis* byssal plaque include various *Mytilus edulis* foot proteins (Mefp's) that may be targeted for detection; however, this may limit the sensor's ability to detect other biofouling organisms. Implementation of algorithms to detect various analytes independent of their concentration may stimulate the sensor to generate a unique signal response that may be further analysed to determine the amount and presence of a broad range of biofouling organisms (Carmel *et al.*, 2003). By generating data based on the unique signal response to major biofouling organisms, such an algorithm may be used to provide a quantitative output of the biofouling community present on the ship as well as their location. This may allow for appropriate decisions for the ship's biofouling management in order to reduce drag, the use of excess fuel, greenhouse gas emissions and damage to the vessel (Townsin, 2003; Schultz, 2007; Edyvean, 2010; Schultz *et al.*, 2011; Zabin *et al.*, 2018). Additionally, these data may be instrumental for governments and international bodies to make decisions on the movement and maintenance of ships, and thus reducing the risks involved with the introduction of invasive species (Davidson *et al.*, 2009; Lewis and Coutts, 2010; Zabin *et al.*, 2018)

Further development of the microtopography may depend on characterisation of contact angle measurements (Magin *et al.*, 2010), visualisation with an alternative method such as SEM (Fiorucci *et al.*, 2013; Ling *et al.*, 2015; Razi *et al.*, 2016; Sun *et al.*, 2016) and further replicate studies. This may include a longitudinal study of the microtopography sensory surface *in situ* in order to assess the possible long-term antifouling performance (surface erosion) and real-time detection with the sensor. Furthermore, assessment of multiscale microtopography may allow for broad spectrum antifouling towards smaller biofoulers, such as diatoms and bacteria, that may adhere to the larger microtopography of V40 H150 where they may benefit from a high number of attachment points (Scardino *et al.*, 2006). Additional comparison research of the microtopography in both static and dynamic conditions may highlight the foul-release properties.

Lastly, analysis of the effect of the sensor and microtopography on *M. edulis* may be necessary. This may include behavioural analysis and preference assay with exposure to the EMW of the sensor and sensory surface. Furthermore, potential bioassays of various protein expression levels and structural characterisation of the byssal plaque may highlight their response to the microtopography sensory surface. Data on the mussel response may be informative towards further development of the microtopography sensory surface.

5.4. Conclusions

Current strategies to address the problems of biofouling are based on regulations from international bodies and governments, visual quantification and use of antifouling coatings that may be dependent on biocides for antifouling efficacy. Research on antifouling coatings and strategies, including non-toxic coatings and microtopographies, is vast and always developing. However, to date there are no studies utilising antifouling microtopographies for adult *M. edulis*, nor methods and technologies to detect biofouling *in situ* and in real-time.

The present study demonstrated the application of a planar electromagnetic wave sensor for the detection of *M. edulis* biofouling on nylon 6, silicone and PVC surfaces, *in vitro*. Development of a microtopography with silicone indicated a reduced adhesion strength of *M. edulis* byssal plaque with the microtopography, *in vitro*. Furthermore, the present study indicates the application of the planar EMW sensor with the silicone microtopography for a non-destructive and non-toxic sensory surface for the detection of *M. edulis* biofouling, *in situ*. The study may allow for the application of a microtopography sensory surface within the maritime industry, such as in aquaculture whereby biofouling of infrastructure (e.g. cages, ropes, nets, buoys) causes physical damage as well as impacts productivity as biofouling organisms compete for resources. Furthermore, application on offshore oil rigs and offshore wind turbines may address the physical damage and structural load issues that occur with biofouling. Lastly, the sensory surface may allow for application within niche biofouling areas of ships,

particularly in grates and pipes where biofouling may be overlooked, but implications of blockages may be considerable.

References

Aalsalem, M. Y., Khan, W. Z., Gharibi, W. and Armi, N. (2018) An intelligent oil and gas well monitoring system based on Internet of Things. *Proceeding - 2017 International Conference on Radar, Antenna, Microwave, Electronics, and Telecommunications, ICRAMET 2017*, 2018–Janua, pp. 124–127.

Abbott, A., Abel, P. D., Arnold, D. W. and Milne, A. (2000) Cost-benefit analysis of the use of TBT: The case for a treatment approach. *Science of the Total Environment*, 258(1–2), pp. 5–19.

Adland, R., Cariou, P., Jia, H. and Wolff, F. C. (2018) The energy efficiency effects of periodic ship hull cleaning. *Journal of Cleaner Production*. Elsevier Ltd, 178, pp. 1–13.

Aldred, N., Ista, L. K., Callow, M. E., Callow, J. A., Lopez, G. P. and Clare, A. S. (2006) Mussel (Mytilus edulis) byssus deposition in response to variations in surface wettability. *Journal of the Royal Society Interface*, 3(6), pp. 37–43.

Alexander, F., Price, D. T. and Bhansali, S. (2010) Optimization of interdigitated electrode (IDE) arrays for impedance based evaluation of Hs 578T cancer cells. *Journal of Physics: Conference Series*, 224(1).

References

Allen, J. A., Cook, M., Jackson, D. J., Preston, S. and Worth, E. M. (1976) Observations on the rate of production and mechanical properties of the byssus threads of Mytilus edulis L. *Journal of Molluscan Studies*, 42(2), pp. 279–289.

Allison, J. E. (1953) The Development of Merseyside and the Port of Liverpool. *Town Planning Review*, 24(1), p. 52.

Al-Naamani, L., Dobretsov, S., Dutta, J. and Burgess, J. G. (2017) Chitosan-zinc oxide nanocomposite coatings for the prevention of marine biofouling. *Chemosphere*. Elsevier Ltd, 168, pp. 408–417.

Amatore, C., Fosset, B., Bartelt, J., Deakin, M. R. and Wightman, R. M. (1988) Electrochemical kinetics at microelectrodes. Part V. Migrational effects on steady or quasi-steady-state voltammograms. *Journal of Electroanalytical Chemistry*, 256(2), pp. 255–268.

AMBIO (2010) *Advanced nanostructured surfaces for the control of biofouling*. Birmingham.

Amer, M. S., El-Ashry, M. A., Dosser, L. R., Hix, K. E., Maguire, J. F. and Irwin, B. (2005) Femtosecond versus nanosecond laser machining: Comparison of induced stresses and structural changes in silicon wafers. *Applied Surface Science*, 242(1–2), pp. 162–167.

References

Andersson, M., Berntsson, K., Jonsson, P. and Gatenholm, P. (1999) Microtextured surfaces: Towards macrofouling resistant coatings. *Biofouling*, 14(2), pp. 167–178.

Andrady, A. L. (2011) Microplastics in the marine environment. *Marine Pollution Bulletin*. Elsevier Ltd, 62(8), pp. 1596–1605.

Awad, S. B. and Nagarajan, R. (2010) Ultrasonic Cleaning. *Developments in Surface Contamination and Cleaning: Particle Deposition, Control and Removal*. Elsevier Inc., pp. 225–280.

Baker-Jarvis, J. and Kim, S. (2012) The interaction of radio-frequency fields with dielectric materials at macroscopic to mesoscopic scales. *Journal of Research of the National Institute of Standards and Technology*, 117(1), pp. 1–60.

Ballal, D. and Chapman, W. G. (2013) Hydrophobic and hydrophilic interactions in aqueous mixtures of alcohols at a hydrophobic surface. *Journal of Chemical Physics*, 139(11).

Bax, N., Williamson, A., Aguero, M., Gonzalez, E. and Geeves, W. (2003) Marine invasive alien species : a threat to global biodiversity. *Marine Policy*, 27, pp. 313–323.

BBC News (2012) *Canal and River Trust takes over from British Waterways*. *BBC News*.

Bechert, D. W. and Bartenwerfer, M. (1989) The viscous flow on surfaces with longitudinal ribs. *Journal of Fluid Mechanics*, 206, pp. 105–129.

References

Bechert, D. W., Bruse, M., Hage, W., Van Der Hoeven, J. G. T. and Hoppe, G. (1997) Experiments on drag-reducing surfaces and their optimization with an adjustable geometry. *Journal of Fluid Mechanics*, 338, pp. 59–87.

Beigl, M., Krohn, A., Zimmer, T. and Decker, C. (2004) Typical sensors needed in ubiquitous and pervasive computing. *Proceesdings of INSS*, (1).

Berges, J. a., Franklin, D. J. and Harrison, P. J. (2001) Evolution of an Artificial Seawater Medium: Improvements in Enriched Seawater, Artificial Water Over the Last Two Decades. *Journal of Phycology*, 37(6), pp. 1138–1145.

Berntsson, Andreasson, H., Jonsson, P. R., Larsson, L., Ring, K., Petronis, S. and Gatenholm, P. (2000a) Reduction of barnacle recruitment on micro-textured surfaces: Analysis of effective topographic characteristics and evaluation of skin friction. *Biofouling*, 16(2–4), pp. 245–261.

Berntsson, K. M., Jonsson, P. R., Lejhall, M. and Gatenholm, P. (2000b) Analysis of behavioural rejection of micro-textured surfaces and implications for recruitment by the barnacle Balanus improvisus. *Journal of Experimental Marine Biology and Ecology*, 251(1), pp. 59–83.

Bers, A. V. and Wahl, M. (2004) The influence of natural surface microtopographies on fouling. *Biofouling*, 20(1), pp. 43–51.

References

Bers, A. V., D'Souza, F., Klijnstra, J. W., Willemsen, P. R. and Wahl, M. (2006) Chemical defence in mussels: Antifouling effect of crude extracts of the periostracum of the blue mussel Mytilus edulis. *Biofouling*, 22(4), pp. 251–259.

Birchak, J. R., Gardner, C. G., Hipp, J. E. and Victor, J. M. (1974) High Dielectric Constant Microwave Probes for Sensing Soil Moisture. *Proceedings of the IEEE*, 62(1), pp. 93–98.

Birnbaumer, G. M., Lieberzeit, P. A., Richter, L., Schirhagl, R., Milnera, M., Dickert, F. L., Bailey, A. and Ertl, P. (2009) Detection of viruses with molecularly imprinted polymers integrated on a microfluidic biochip using contact-less dielectric microsensors. *Lab on a Chip*, 9(24), pp. 3549–3556.

Bixler, G. D. and Bhushan, B. (2012) Review article: Biofouling: Lessons from nature. *Philosophical Transactions of the Royal Society A: Mathematical, Physical and Engineering Sciences*, 370(1967), pp. 2381–2417.

Bizi-Bandoki, P., Benayoun, S., Valette, S., Beaugiraud, B. and Audouard, E. (2011) Modifications of roughness and wettability properties of metals induced by femtosecond laser treatment. *Applied Surface Science*. Elsevier B.V., 257(12), pp. 5213–5218.

Blakey, R. T. and Morales-Partera, A. M. (2016) Microwave dielectric spectroscopy – A versatile methodology for online, non-destructive food analysis, monitoring and process control. *Engineering in Agriculture, Environment and Food*, 9(3), pp. 264–273.

References

Bogue, R. (2010) Fifty years of the laser: Its role in material processing. *Assembly Automation*, 30(4), pp. 317–322.

Boswell, R. W. (1984) Very efficient plasma generation by whistler waves near the lower hybrid frequency. *Plasma Physics and Controlled Fusion*, 26(10), pp. 1147–1162.

Bott, B. and Jones, T. A. (1984) A highly sensitive NO2 sensor based on electrical conductivity changes in phthalocyanine films. *Sensors and Actuators*, 5(1), pp. 43–53.

Brazee, S. L. and Carrington, E. (2006) Interspecific Comparison of the Mechanical Properties of Mussel Byssus. *Biological Bulletin*, 211(3), pp. 263–274.

Breitling, D., Ruf, A. and Dausinger, F. (2004) Fundamental aspects in machining of metals with short and ultrashort laser pulses. *Photon Processing in Microelectronics and Photonics III*, 5339, p. 49.

Bressy, C. and Lejars, M. (2014) Marine fouling : An overview marine fouling. *Journal of Ocean Technology*, 9(4), pp. 19–28.

Bressy, C. and Lejars, M. (2014) Marine fouling : An overview marine fouling. *Journal of Ocean Technology*, 9(4), pp. 19–28.

Bressy, C., Margaillan, A., Faÿ, F., Linossier, I. and Réhel, K. (2009) *Tin-free self-polishing marine antifouling coatings*. *Advances in Marine Antifouling Coatings and Technologies*. Woodhead Publishing Limited.

References

Briand, J. F., Djeridi, I., Jamet, D., Coupé, S., Bressy, C., Molmeret, M., Le Berre, B., Rimet, F., Bouchez, A. and Blache, Y. (2012) Pioneer marine biofilms on artificial surfaces including antifouling coatings immersed in two contrasting French Mediterranean coast sites. *Biofouling*, 28(5), pp. 453–463.

Brischwein, M., Herrmann, S., Vonau, W., Berthold, F., Grothe, H., Motrescu, E. R. and Wolf, B. (2006) Electric cell-substrate impedance sensing with screen printed electrode structures. *Lab on a Chip*, 6(6), pp. 819–822.

Brooks, S. and Waldock, M. (2009) The use of copper as a biocide in marine antifouling paints. in Hellio, C. and Yebra, D. (eds) *Advances in Marine Antifouling Coatings and Technologies*. Cambridge: Woodhead Publishing Limited, pp. 492–521.

Bullard, S. G., Shumway, S. E. and Davis, C. V. (2010) The use of aeration as a simple and environmentally sound means to prevent biofouling. *Biofouling*, 26(5), pp. 587–593.

Bureau, E., Cabot, C., Marais, S. and Saiter, J. M. (2005) Study of the α-relaxation of PVC, EVA and 50/50 EVA70/PVC blend. *European Polymer Journal*, 41(5), pp. 1152–1158.

Burkett, J. R., Wojtas, J. L., Cloud, J. L. and Wilker, J. J. (2009) A method for measuring the adhesion strength of marine mussels. *Journal of Adhesion*, 85(9), pp. 601–615.

References

Byrne, M., Morrice, M. G. and Wolf, B. (1997) Introduction of the northern Pacific asteroid Asterias amurensis to Tasmania: Reproduction and current distribution. *Marine Biology*, 127(4), pp. 673–685.

Cai, Y., Chang, W., Luo, X., Sousa, A. M. L., Lau, K. H. A. and Qin, Y. (2018) Superhydrophobic structures on 316L stainless steel surfaces machined by nanosecond pulsed laser. *Precision Engineering*. Elsevier, 52(January), pp. 266–275.

Callow, M. and Callow, J. (2002) Marine biofouling: a sticky problem. *Biologist*, 49(1), pp. 10–14.

Callow, M. E. and Fletcher, R. L. (1994) The influence of low surface energy materials on bioadhesion - a review. *International Biodeterioration and Biodegradation*, 34(3–4), pp. 333–348.

Callow, M. E., Jennings, A. R., Brennan, A. B., Seegert, C. E., Gibson, A., Wilson, L., Feinberg, A., Baney, R. and Callow, J. A. (2002) Microtopgraphic Cues for Settlement of Zoospores of the Green Fouling Alga Enteromorpha. *Biofouling*, 18(3), pp. 229–236.

Candries, M. and Anderson, C. D. (2001) Foul Release systems and drag. *Consolidation of Technical Advances in the Protective and Marine Coatings Industry*, Proceeding, pp. 273–286.

Cao, S., Wang, J. D., Chen, H. S. and Chen, D. R. (2011) Progress of marine biofouling

and antifouling technologies. *Chinese Science Bulletin*, 56(7), pp. 598–612.

Carl, C., Poole, A. J., Sexton, B. A., Glenn, F. L., Vucko, M. J., Williams, M. R., Whalan, S. and de Nys, R. (2012) Enhancing the settlement and attachment strength of pediveligers of Mytilus galloprovincialis bychanging surface wettability and microtopography. *Biofouling*, 28(2), pp. 175–186.

Carman, M. L., Estes, T. G., Feinberg, A. W., Schumacher, J. F., Wilkerson, W., Wilson, L. H., Callow, M. E., Callow, J. A. and Brennan, A. B. (2006) Engineered antifouling microtopographies - Correlating wettability with cell attachment. *Biofouling*, 22(1), pp. 11–21.

Carmel, L., Sever, N., Lancet, D. and Harel, D. (2003) An eNose algorithm for identifying chemicals and determining their concentration. *Sensors and Actuators, B: Chemical*, 93(1–3), pp. 77–83.

Carrington, E. (2002) Seasonal variation in the attachment strength of blue mussels: Causes and consequences. *Limnology and Oceanography*, 47(6), pp. 1723–1733.

Caspers, F. and Kowina, P. (2013) RF measurement concepts. *Proceedings of the CAS-CERN Accelerator School: Advanced Accelerator Physics*, 009(August 2013), pp. 101–156.

Chen, D., Liu, Y., Chen, H. and Zhang, D. (2018) Bio-inspired drag reduction surface from sharkskin. *Biosurface and Biotribology*, 4(2), pp. 39–45.

References

Chen, Y., Lee, G. M., Shu, L. and Crespi, N. (2016) Industrial internet of things-based collaborative sensing intelligence: Framework and research challenges. *Sensors (Switzerland)*, 16(2), pp. 1–19.

Chipperfield, P. N. J. (1953) Observations on the breeding and settlement of mytilus edulis (L.) in British waters. *Journal of the Marine Biological Association of the United Kingdom*. Liverpool John Moores University, 32(2), pp. 449–476.

Choi, W. Y., Park, H. J., Ahn, D. J., Lee, J. and Lee, C. Y. (2002) Wettability of chitosan coating solution on 'Fuji' apple skin. *Journal of Food Science*, 67(7), pp. 2668–2672.

Chou, K. Sen and Lee, C. H. (2014) Fabrication of silver interdigitated electrode by a stamp method. *Advances in Materials Science and Engineering*, 2014.

Chung, K. K., Schumacher, J. F., Sampson, E. M., Burne, R. A., Antonelli, P. J. and Brennan, A. B. (2007) Impact of engineered surface microtopography on biofilm formation of Staphylococcus aureus . *Biointerphases*, 2(2), pp. 89–94.

Civerchia, F., Bocchino, S., Salvadori, C., Rossi, E., Maggiani, L. and Petracca, M. (2017) Industrial Internet of Things monitoring solution for advanced predictive maintenance applications. *Journal of Industrial Information Integration*. Elsevier Inc., 7, pp. 4–12.

Commercial Diving (2013) *Ship Hull Inspection Services*. *Commercial Diving Services Pty Ltd*.

References

Cooper, S. P., Finlay, J. A., Cone, G., Callow, M. E., Callow, J. A. and Brennan, A. B. (2011) Engineered antifouling microtopographies: Kinetic analysis of the attachment of zoospores of the green alga Ulva to silicone elastomers. *Biofouling*, 27(8), pp. 881–892.

Corbett, J. J. and Winebrake, J. J. (2010) Energy and GHG Emissions Savings Analysis of Fluoropolymer Foul Release Hull Coating. *Energy and …*, (May 2016).

Crisp, D. J., Walker, G., Young, G. A. and Yule, A. B. (1985) Adhesion and substrate choice in mussels and barnacles. *Journal of Colloid And Interface Science*, 104(1), pp. 40–50.

Crisp, D. J., Walker, G., Young, G. A. and Yule, A. B. (1985) Adhesion and substrate choice in mussels and barnacles. *Journal of Colloid And Interface Science*, 104(1), pp. 40–50.

Crowley, K., Morrin, A., Shepherd, R. L., In Het Panhuis, M., Wallace, G. G., Smyth, M. R. and Killard, A. J. (2010) Fabrication of polyaniline-based gas sensors using piezoelectric inkjet and screen printing for the detection of hydrogen sulfide. *IEEE Sensors Journal*, 10(9), pp. 1419–1426.

Dang, Z. M., Yuan, J. K., Yao, S. H. and Liao, R. J. (2013) Flexible nanodielectric materials with high permittivity for power energy storage. *Advanced Materials*, 25(44), pp. 6334–6365.

References

Dare, P. J. and Edwards, D. B. (1975) Seasonal Changes in Flesh Weight and Biochemical Composition of Mussel (Mytilus edulis L.) in the Conwy Estuary, North Wales. *Journal of Experimental Marine Biology and Ecology*, 18, pp. 89–97.

Davidson, I. C., Brown, C. W., Sytsma, M. D. and Ruiz, G. M. (2009) The role of containerships as transfer mechanisms of marine biofouling species. *Biofouling*, 25(7), pp. 645–655.

Davidson, I. C., McCann, L. D., Sytsma, M. D. and Ruiz, G. M. (2008) Interrupting a multi-species bioinvasion vector: The efficacy of in-water cleaning for removing biofouling on obsolete vessels. *Marine Pollution Bulletin*, 56(9), pp. 1538–1544.

Davidson, I., Ashton, G., Ruiz, G., Scianni, C., Brown, C., Pagenkopp-Lohan, K. and Fleischer, R. (2013) *Richness, extent, condition, reproductive status, and parasitism of fouling communities on commercial vessels. Report to the California State Lands Commission, Marine Invasive Species Program*. Sacramento, California.

Davidson, I., Scianni, C., Hewitt, C., Everett, R., Holm, E., Tamburri, M. and Ruiz, G. (2016) Mini-review: Assessing the drivers of ship biofouling management – aligning industry and biosecurity goals. *Biofouling*. Taylor & Francis, 32(4), pp. 411–428.

References

Davies, G. (1974) A method for monitoring the spatfall of mussels (Mytilus edulis L.). *ICES Journal of Marine Science*, 36(1), pp. 27–34.

De Buyl, F. (2001) Silicone sealants and structural adhesives. *International Journal of Adhesion and Adhesives*, 21(5), pp. 411–422.

De Groot, P. (2015) the Talbot Effect: Recent Advances in Classical Optics. *Advances in Optics and Photonics*, 7, pp. 1–65.

Dobretsov, S., Dahms, H. and Qian, P. (2006) Inhibition of biofouling by marine microorganisms and their metabolites. *Biofouling*, 22(1), pp. 43–54.

Dobretsov, S., Teplitski, M. and Paul, V. (2009) Mini-Review: quorum sensing in the marine environment and its relationship to biofouling. *Biofouling*, 25(5), pp. 413–427.

Drake, L. A., Meyer, A. E., Forsberg, R. L., Baier, R. E., Doblin, M. A., Heinemann, S., Johnson, W. P., Koch, M., Rublee, P. A. and Dobbs, F. C. (2005) Potential invasion of microorganisms and pathogens via 'interior hull fouling': Biofilms inside ballast water tanks. *Biological Invasions*, 7(6), pp. 969–982.

Dring, M. J., Wagner, A., Boeskov, J., Lüning, K. and Boeskov, J. (1996) Sensitivity of intertidal and subtidal red algae to uva and uvb radiation, as monitored by chlorophyll fluorescence measurements: Influence of collection depth and season, and length of irradiation. *European Journal of Phycology*, 31(4), pp. 293–302.

References

Ducharme, S. (2009) An inside-out approach to storing electrostatic energy. *ACS Nano*, 3(9), pp. 2447–2450.

Dürr, S. and Wahl, M. (2004) Isolated and combined impacts of blue mussels (Mytilus edulis) and barnacles (Balanus improvisus) on structure and diversity of a fouling community, 306, pp. 181–195.

Dürr, S. and Watson, D. I. (2010) Biofouling and antifouling in aquaculture. in Dürr, S. and Thomason, J. C. (eds) *Biofouling*. Oxford: Wiley-Blackwell, pp. 267–287.

Edgar, G. J., Stuart-Smith, R. D., Cooper, A., Jacques, M. and Valentine, J. (2017) New opportunities for conservation of handfishes (Family Brachionichthyidae) and other inconspicuous and threatened marine species through citizen science. *Biological Conservation*. Elsevier Ltd, 208, pp. 174–182.

Edyvean, R. (2010) Consequences of Fouling on Shipping. in Dürr, S. and Thomason, J. (eds) *Biofouling*. Oxford: Wiley-Blackwell, pp. 217–225.

Enderlein, P. (2000) *Direkte und indirekte Wechselwirkungen zwischen Konsumenten, Beute und deren Aufwuchs in Mytilus Gemeinschaften der westlichen Ostee*. University of Kiel.

Enderlein, P., Moorthi, S., Röhrscheidt, H. and Wahl, M. (2003) Optimal foraging versus shared doom effects: Interactive influence of mussel size and epibiosis on predator preference. *Journal of Experimental Marine Biology and Ecology*, 292(2), pp. 231–242.

References

European chemicals agency (2015) *Update of the workplan on nanomaterials*. Luxembourg.

European Union (2012) Regulation (EU) No 528/2012 of the European Parliament and of the Council of 22 May 2012 concerning the making available on the market and use of biocidal products. *Official Journal of the European Union*, pp. 1–123.

Evans, S. M., Birchenough, a C. and Brancato, M. S. (2000) The Tbt Ban: Out of the Prying Pan Into the Fire? *Marine Pollution Bulletin*, 40(3), pp. 204–211.

Feng, D., Wang, F. and Chen, Z. (2009) Electrochemical glucose sensor based on one-step construction of gold nanoparticle-chitosan composite film. *Sensors and Actuators, B: Chemical*, 138(2), pp. 539–544.

Filgueira, R., Brown, M. S., Comeau, L. A. and Grant, J. (2014) Predicting the timing of the pediveliger stage of Mytilus edulis based on ocean temperature. *Journal of Molluscan Studies*, 81(2), pp. 269–273.

Filippidi, E., DeMartini, D. G., De Molina, P. M., Danner, E. W., Kim, J., Helgeson, M. E., Waite, J. H. and Valentine, M. T. (2015) The microscopic network structure of mussel (Mytilus) adhesive plaques. *Journal of the Royal Society Interface*, 12(113).

References

Fiorucci, M. P., López, A. J. and Ramil, A. (2013) Influence of irradiation parameters in nanosecond Nd:YVO 4 laser micro-machining of stainless steel for biomedical applications . *8th Iberoamerican Optics Meeting and 11th Latin American Meeting on Optics, Lasers, and Applications*, 8785(November 2013), p. 87854B.

Fischer, M., Wahl, M. and Friedrichs, G. (2012) Design and field application of a UV-LED based optical fiber biofilm sensor. *Biosensors and Bioelectronics*. Elsevier B.V., 33(1), pp. 172–178.

Fisher, C. and Slater, M. (2010) Effects of electromagnetic fields on marine species.

Flemming, H., Neu, T. R., Wozniak, D. J., Carolina, N., Decho, A., Kreft, J., Neu, T., Nielsen, P., Ro, U., Schooling, S., Szewzyk, U. and Wolfaardt, G. (2007) The EPS Matrix : The ' House of Biofilm Cells '. *Journal of bacteriology*, 189(22), pp. 7945–7947.

Fletcher, M. (1977) The effects of culture concentration and age, time, and temperature to polystyrene. *Canadian Journal of Microbiology*, 23, pp. 1–6.

Floerl, O. and Coutts, A. (2013) *Feasibility of using remote- operated vehicles (ROVs) for vessel biofouling inspections*. Department of Fisheries, Government of Western Australia.

References

Foteinos, M. I., Tzanos, E. I. and Kyrtatos, N. P. (2017) Ship Hull Fouling Estimation Using Shipboard Measurements, Models for Resistance Components, and Shaft Torque Calculation Using Engine Model. *Journal of Ship Research*, 61(2), pp. 64–74.

Frau, I., Byrne, P. and Mason, A. (2017) Continous Monitorin of Zn in water with Bismuth Oxide Thick-film using Microwave and Electric Techniques. *Eleventh International Conference on Sensing Technology*, pp. 4–9.

Frau, I., Korostynska, O., Mason, A. and Byrne, P. (2018) Comparison of Electromagnetic Wave Sensors with Optical and Low-frequency Spectroscopy Methods for Real-time Monitoring of Lead Concentrations in Mine Water. *Mine Water and the Environment*. Springer Berlin Heidelberg, 37(3), pp. 617–624.

Frau, I., Korostynska, O., Mason, A. and Byrne, P. (2018) Comparison of Electromagnetic Wave Sensors with Optical and Low-frequency Spectroscopy Methods for Real-time Monitoring of Lead Concentrations in Mine Water. *Mine Water and the Environment*. Springer Berlin Heidelberg, 37(3), pp. 617–624.

Frau, I., Wylie, S., Byrne, P., Cullen, J., Korostynska, O. and Mason, A. (2019) Detection of Zn in water using novel functionalised planar microwave sensors. *Materials Science and Engineering B: Solid-State Materials for Advanced Technology*, 247(May).

References

Garner, Y. L. and Litvaitis, M. K. (2013) Effects of injured conspecifics and predators on byssogenesis, attachment strength and movement in the blue mussel, Mytilus edulis. *Journal of Experimental Marine Biology and Ecology*. Elsevier B.V., 448, pp. 136–140.

Gaspar, C., Olkkonen, J., Passoja, S. and Smolander, M. (2017) Paper as active layer in inkjet-printed capacitive humidity sensors. *Sensors (Switzerland)*, 17(7).

Geophysics (2015) *Electromagnetic Radiation*. *WDC for Geophysics, Beijing*.

Goloshubin, G. (2006) Coordinated by Bill Dragoset Reservoir imaging using low frequencies of seismic reflections. *Geology*, (January 2006), pp. 527–531.

Gong, S., Schwalb, W., Wang, Y., Chen, Y., Tang, Y., Si, J., Shirinzadeh, B. and Cheng, W. (2014) A wearable and highly sensitive pressure sensor with ultrathin gold nanowires. *Nature Communications*. Nature Publishing Group, 5, pp. 1–8.

Goodfellow (2019) *Polyamide - Nylon 6 (PA 6)*. *Goodfellow*.

Google Maps (2019) *Google Maps Liverpool Docks*. *Google*.

Grover, W. H. (1999) Interdigitated Array Electrode Sensors : Their Design , Efficiency , and Applications. *Honors thesis , University of Tennessee*, 3, pp. 1–62.

Haemers, S., Van Der Leeden, M. C. and Frens, G. (2005) Coil dimensions of the mussel adhesive protein Mefp-1. *Biomaterials*, 26(11), pp. 1231–1236.

Hallegraeff, G. M. (2010) Ocean climate change, phytoplankton community responses, and harmful algal blooms: A formidable predictive challenge. *Journal of Phycology*. Blackwell Publishing Ltd, 46(2), pp. 220–235.

Hamada, N., Roman, V., Howell, S. and Wilker, J. (2017) Examining Potential Active Tempering of Adhesive Curing by Marine Mussels. *Biomimetics*, 2(4), p. 16.

Han, S., Yang, R., Li, C. and Yang, L. (2019) The wettability and numerical model of different silicon microstructural surfaces. *Applied Sciences (Switzerland)*, 9(3).

Hao, J. H. and Wang, Z. J. (2016) Modeling Cassie–Baxter State on Superhydrophobic Surfaces. *Journal of Dispersion Science and Technology*. Taylor & Francis, 37(8), pp. 1208–1213.

Harris, S. A. (1937) Henry Berry (1720 - 1812): Liverpool's Second Dock Engineer. *The Historic Society of Lancashire and Cheshire*, pp. 91–109.

Hearin, J., Hunsucker, K. Z., Swain, G., Stephens, A., Gardner, H., Lieberman, K. and Harper, M. (2015) Analysis of long-term mechanical grooming on large-scale test panels coated with an antifouling and a fouling-release coating. *Biofouling*. Taylor & Francis, 31(8), pp. 625–638.

Hebbar, R. S., Isloor, A. M. and Ismail, A. F. (2017) Contact Angle Measurements. in Hilal, N., Ismail, Ahmad Fauzi, Matsuura, T., and Oatley-Radcliffe, D. (eds) *Membrane Characterization*. Elsevier B.V., pp. 219–255.

Hellio, C. and Yebra, D. (2009) Advances in marine antifouling coatings and technologies. in Hellio, C. and Yebra, D. (eds) *Woodhead Publishing Limited*. Cambridge: Woodhead Publishing Limited, pp. 1–15.

Hennebicq, R., Fabra, G., Pellerin, C., Marcotte, I., Myrand, B. and Tremblay, R. (2013) The effect of spawning of cultured mussels (Mytilus edulis) on mechanical properties, chemical and biochemical composition of byssal threads. *Aquaculture*. Elsevier B.V., 410–411, pp. 11–17.

Henniker Plasma (2017) *Improved Adhesion/Bonding due to Plasma Treatment of PDMS*. *AZO Materials*.

Holm, E. R., Haslbeck, E. G. and Horinek, A. A. (2003) Evaluation of Brushes for Removal of Fouling from Fouling-release Surfaces, Using a Hydraulic Cleaning Device. *Biofouling*, 19(5), pp. 297–305.

Holm, E. R., Schultz, M. P., Haslbeck, E. G., Talbott, W. J. and Field, A. J. (2004) Evaluation of hydrodynamic drag on experimental fouling-release surfaces, using rotating disks. *Biofouling*, 20(4–5), pp. 219–226.

Homola, J., Yee, S. S. and Gauglitz, G. (2014) Surface plasmon resonance: review. *Surface Plasmon Resonance*, 54, pp. 1–112.

Hopkins, G. A. and Forrest, B. M. (2008) Management options for vessel hull fouling: An overview of risks posed by in-water cleaning. *ICES Journal of Marine Science*, 65(5), pp. 811–815.

References

Horner, R. (2019) *(Unpublished) Laser surface texturing to create biomimetic surface topography for marine antifouling efficacy testing*. Liverpool John Moores University.

Horsch, J., Wilke, P., Pretzler, M., Seuss, M., Melnyk, I., Remmler, D., Fery, A., Rompel, A. and Börner, H. G. (2018) Polymerizing Like Mussels Do: Toward Synthetic Mussel Foot Proteins and Resistant Glues. *Angewandte Chemie - International Edition*, 57(48), pp. 15728–15732.

Hossain, M. S. and Muhammad, G. (2016) Cloud-assisted Industrial Internet of Things (IIoT) - Enabled framework for health monitoring. *Computer Networks*. Elsevier B.V., 101, pp. 192–202.

Howell, D. and Behrends, B. (2006) A methodology for evaluating biocide release rate, surface roughness and leach layer formation in a TBT-free, self-polishing antifouling coating. *Biofouling*, 22(5), pp. 303–315.

Hwang, I. H., Kim, D. W., Kim, S. J., Min, B. S., Lee, S. H., Son, J. K., Kim, C. H., Chang, H. W. and Na, M. K. (2011) Asterosaponins isolated from the starfish asterias amurensis. *Chemical and Pharmaceutical Bulletin*, 59(1), pp. 78–83.

Ibrahim, M., Claudel, J., Kourtiche, D. and Nadi, M. (2013) Geometric parameters optimization of planar interdigitated electrodes for bioimpedance spectroscopy. *Journal of Electrical Bioimpedance*, 4(1), pp. 13–22.

References

International Energy Agency (2017) *CO2 Emissions from Fuel Combustion - Highlights*. *International Energy Agency*.

International maritime organistaion (2011) MEPC.207(62) Add.1 Guidelines for the control and management of ships' biofouling to minimize the transfer of invasive aquatic specie, pp. 1–25.

International Maritime Organistaion (2015) *Third IMO GHG Study 2014*. *International Maritime Organization (IMO)*. London.

International maritime organistaion (2016) *Anti-fouling systems*. *International Maritime Organization (IMO)*.

International Maritime Organistaion (2018) *Note by the International Maritime Organization to the UNFCCC Talanoa Dialogue*.

International Maritime Organistaion (2019) *Ballast water management - the control of harmful invasive species*.

Irving, A. and McCarthy, M. (2018) New Zealand - Biofouling - Craft Risk Management Standard, pp. 1–5.

Johnson, L. and Padilla, D. (1996) Geographic spread of exotic species: ecological lessons and oppurtunities from the invasion of the zebra mussel Dreissena polymorpha. *Biological Conservation*, 78, pp. 23–33.

References

Joshi, K. H., Mason, A., Korostynska, O. and Al-Shamma'a, A. (2017) Milk Quality Monitoring Using Electromagnetic Wave Sensors. in Mukhopadhyay, S. C., Postolache, O. A., Jayasundera, K. P., and Swain, A. K. (eds) *Sensors for Everyday Life: Environmental and Food Engineering*. Cham: Springer International Publishing, pp. 205–227.

Justino, C. I. L., Gomes, A. R., Freitas, A. C., Duarte, A. C. and Rocha-Santos, T. A. P. (2017) Graphene based sensors and biosensors. *TrAC - Trends in Analytical Chemistry*. Elsevier Ltd, 91, pp. 53–66.

Khan, W. Z., Aalsalem, M. Y., Khan, M. K., Hossain, M. S. and Atiquzzaman, M. (2017) A reliable Internet of Things based architecture for oil and gas industry. *International Conference on Advanced Communication Technology, ICACT*. Global IT Research Institute - GiRI, pp. 705–710.

Khanna, a S. (2008) Nanotechnology in High Performance Paint Coatings. *Asian Journal of Experimental Science*, 21(2), pp. 25–32.

Kiil, S., Weinell, C. E., Pedersen, M. S. and Dam-Johansen, K. (2001) Analysis of self-polishing antifouling paints using rotary experiments and mathematical modeling. *Industrial and Engineering Chemistry Research*, 40(18), pp. 3906–3920.

Kim, J. and Na, S. (2007) Metal thin film ablation with femtosecond pulsed laser. *Optics and Laser Technology*, 39(7), pp. 1443–1448.

Klust, G. (1982) Netting Materials for fishing gear. *New Books for FAO*.

Korostynska, O., Mason, A. and Al-Shammaa, A. I. (2013) Flexible microwave sensors for real-time analysis of water contaminants. *Journal of Electromagnetic Waves and Applications*, 27(16), pp. 2075–2089.

Korostynska, O., Ortoneda-Pedrola, M., Mason, A. and Al-Shamma'a, A. I. (2014) Flexible electromagnetic wave sensor operating at GHz frequencies for instantaneous concentration measurements of NaCl, KCl, MnCl 2 and CuCl solutions. *Measurement Science and Technology*, 25(6), p. 65105.

Kosowska-Stamirowska, Z., Ducruet, C. and Rai, N. (2016) Evolving structure of the maritime trade network: evidence from the Lloyd's Shipping Index (1890–2000). *Journal of Shipping and Trade*. Journal of Shipping and Trade, 1(1), pp. 1–17.

Kuoni, A., Holzherr, R., Boillat, M. and De Rooij, N. F. (2003) Polyimide membrane with ZnO piezoelectric thin film pressure transducers as a differential pressure liquid flow sensor. *Journal of Micromechanics and Microengineering*, 13(4).

Laihonen, P. and Furman, E. R. (1986) Oecologia. *Oecologia*, 71, pp. 38–40.

Lawrence, E. L. and Turner, I. G. (2005) Materials for urinary catheters: A review of their history and development in the UK. *Medical Engineering and Physics*, 27(6), pp. 443–453.

Le, D. D., Nguyen, T. N. N., Doan, D. C. T., Dang, T. M. D. and Dang, M. C. (2016) Fabrication of interdigitated electrodes by inkjet printing technology for apllication in ammonia sensing. *Advances in Natural Sciences: Nanoscience and Nanotechnology*. IOP Publishing, 7(2).

Lee, B. P., Messersmith, P. B., Israelachvili, J. N. and Waite, J. H. (2011) Mussel-Inspired Adhesives and Coatings. *Annual Review of Materials Research*, 41(1), pp. 99–132.

Lee, C., Lee, G. W., Choi, W., Yoo, C. H., Chun, B., Lee, J. S., Lee, J. H. and Jung, H. W. (2020) Pattern flow dynamics over rectangular Sharklet patterned membrane surfaces. *Applied Surface Science*. Elsevier, 514(September 2019), p. 145961.

Lee, I. and Lee, K. (2015) The Internet of Things (IoT): Applications, investments, and challenges for enterprises. *Business Horizons*. Kelley School of Business, Indiana University, 58(4), pp. 431–440.

Lehaitre, M. and Compère, C. (2008) BIOFOULING and UNDERWATER MEASUREMENTS. *Real-Time Coastal Observing Systems for Marine Ecosystem Dynamics and Harmful Algal Blooms: Theory, instrumentation and modelling*, pp. 463–493.

Lekakou, C., Cook, S., Deng, Y., Ang, T. W. and Reed, G. T. (2006) Optical fibre sensor for monitoring flow and resin curing in composites manufacturing. *Composites Part A: Applied Science and Manufacturing*, 37(6 SPEC. ISS.), pp. 934–938.

Leung, A., Rijal, K., Shankar, P. M. and Mutharasan, R. (2006) Effects of geometry on transmission and sensing potential of tapered fiber sensors. *Biosensors and Bioelectronics*, 21(12), pp. 2202–2209.

Lewin, R. (1984) Microbial Adhesion Is a Sticky Problem. *Science*, 224(4647), pp. 375–377.

Lewis, J. A. and Coutts, A. (2010) Biofouling Invasions. in Dürr, S. and Thomason, J. C. (eds) *Biofouling*. Oxford: Wiley-Blackwell, pp. 348–365.

Lewis, J. A. and Coutts, A. (2010) Biofouling Invasions. in Dürr, S. and Thomason, J. C. (eds) *Biofouling*. Oxford: Wiley-Blackwell, pp. 348–365.

Lewthwaite, J. C., Molland, A. F. and Thomas, K. W. (1985) An investigation into the variation of ship skin frictional resistance with fouling. *Transactions of the Royal Instituition of Naval Architects*, 127, pp. 269–284.

Leya, T., Rother, A., Torsten, M., Fuhr, G., Gropius, M. and Watermann, B. (1999) 10th International Congress on Marine Corrosion and Fouling, University of Melbourne, February 1999. *DSTO Aeronautical and Maritime Research Laboratory*, (February), pp. 98–110.

References

Li, J., Xie, Z., Wang, G., Ding, C., Jiang, H. and Wang, P. (2017) Preparation and evaluation of amphiphilic polymer as fouling-release coating in marine environment. *Journal of Coatings Technology and Research*. Springer US, 14(6), pp. 1237–1245.

Li, J., Xie, Z., Wang, G., Ding, C., Jiang, H. and Wang, P. (2017) Preparation and evaluation of amphiphilic polymer as fouling-release coating in marine environment. *Journal of Coatings Technology and Research*. Springer US, 14(6), pp. 1237–1245.

Li, N., Mou, L., Li, Z., Kang, M. and Wang, X. (2018) Evolution of surface topography of 304L stainless steel irradiated by long pulse laser. *AIP Advances*, 8(7).

Ling, E. J. Y., Saïd, J., Brodusch, N., Gauvin, R., Servio, P. and Kietzig, A. M. (2015) Investigating and understanding the effects of multiple femtosecond laser scans on the surface topography of stainless steel 304 and titanium. *Applied Surface Science*. Elsevier B.V., 353, pp. 512–521.

Little, B. J., Lee, J. S. and Ray, R. I. (2008) *The influence of marine microfouling on the corrosion behaviour of passive materials and copper alloys*. *Defense technical information center*.

Liu, C., Ma, C., Xie, Q. and Zhang, G. (2017) Self-repairing silicone coatings for marine anti-biofouling. *Journal of Materials Chemistry A*. Royal Society of Chemistry, 5(30), pp. 15855–15861.

References

Liverpool Picturebook (2012) *Liverpool Docks - A History*. *Liverpool Picturebook*.

Liverpool Watersports Centre (2019) *Liverpool Watersports Centre About Us*. *Liverpool Watersports Centre*.

Logan, K. (2012) Using a Ship's Propeller for Hull Condition Monitoring. *Naval Engineers Journal*, 124(1), pp. 71–87.

Lowe, D. and Rezkallah, K. S. (1999) A capacitance sensor for the characterization of microgravity two-phase liquid-gas flows. *Measurement Science and Technology*, 10(10), pp. 965–975.

Lowe, S., Browne, M., Boudjelas, S. and De Poorter, M. (2000) *100 of The World's Worst Invasive Alien Species*. The Invasive Species Specialist Group.

Lukasheva, N. V., Tolmachev, D. A., Nazarychev, V. M., Kenny, J. M. and Lyulin, S. V. (2017) Influence of specific intermolecular interactions on the thermal and dielectric properties of bulk polymers: atomistic molecular dynamics simulations of Nylon 6. *Soft Matter*. Royal Society of Chemistry, 13(2), pp. 474–485.

Mace, M. (2016) *AkzoNobel launches bio-renewable coating following anti-fouling accusations*. *edie newsroom*.

Magin, C. M., Long, C. J., Cooper, S. P., Ista, L. K., López, G. P. and Brennan, A. B. (2010) Engineered antifouling microtopographies: the role of Reynolds number in a model that predicts attachment of zoospores of Ulva and cells of Cobetia marina. *Biofouling*, 26(6), pp. 719–727.

Maki, J. S., Rittschof, D., Costlow, J. D. and Mitchell, R. (1988) Inhibition of attachment of larval barnacles, Balanus amphitrite, by bacterial surface films. *Marine Biology*, 97(2), pp. 199–206.

Marine Stewardship Council (2019) *Schleswig-Holstein blue shell mussel*. *Marine Stewardship Council*.

Mason, A., Goh, J. H., Korostynska, O., Al-Shamma'a, A. I., Field, M. and Browning, P. (2013) Real-Time Monitoring of Bodily Fluids Using a Novel Electromagnetic Wave Sensor. *Public Health Frontier*, 2, pp. 201–206.

Mason, A., Korostynska, O., Ortoneda-Pedrola, M., Shaw, A. and Al-Shamma'A, A. (2013) A resonant co-planar sensor at microwave frequencies for biomedical applications. *Sensors and Actuators, A: Physical*. Elsevier B.V., 202, pp. 170–175.

Mason, T. J. (2016) Ultrasonic cleaning: An historical perspective. *Ultrasonics Sonochemistry*. Elsevier B.V., 29, pp. 519–523.

McCarthy, S. A. and Khambaty, F. M. (1994) International dissemination of epidemic Vibrio cholerae by cargo ship ballast and other nonpotable waters. *Applied and Environmental Microbiology*. 1994/07/01, 60(7), pp. 2597–2601.

McDowell, L. M., Burzio, L. A., Waite, J. H. and Schaefer, J. (1999) Rotational echo double resonance detection of cross-links formed in mussel byssus under high-flow stress. *Journal of Biological Chemistry*, 274(29), pp. 20293–20295.

McQuade, D. T., Pullen, A. E. and Swager, T. M. (2000) Conjugated polymer-based chemical sensors. *Chemical Reviews*, 100(7), pp. 2537–2574.

Mee, L. D., Espinosa, M. and Diaz, G. (1986) Paralytic shellfish poisoning with a Gymnodinium catenatum red tide on the Pacific Coast of Mexico. *Mar Environ Res*, 19(1), pp. 77–92.

Merseyside Maritime Museum (2017) Albert Dock Lecture Series. InterPro 175 Lecture Series.

Merseyside Maritime Museum (2019) *Construction, heyday and decline of the Albert Dock*. *National Museums Liverpool*.

Meyer, A., Baier, R., Wood, C. D., Stein, J., Truby, K., Holm, E., Montemarano, J., Kavanagh, C., Nedved, B., Smith, C., Swain, G. and Wiebe, D. (2006) Contact angle anomalies indicate that surface-active eluates from silicone coatings inhibit the adhesive mechanisms of fouling organisms. *Biofouling*, 22(6), pp. 411–423.

Mihm, J. W., Banta, W. C. and Loeb, G. I. (1981) Effects of adsorbed organic and primary fouling films on bryozoan settlement. *Journal of Experimental Marine Biology and Ecology*, 54(2), pp. 167–179.

Mills, E. L., Leach, J. H., Carlton, J. T. and Secor, C. L. (1993) Exotic Species in the Great Lakes: A History of Biotic Crises and Anthropogenic Introductions. *Journal of Great Lakes Research*. Elsevier, 19(1), pp. 1–54.

Min, J. and Baeumner, A. J. (2004) Characterization and optimization of interdigitated ultramicroelectrode arrays as electrochemical biosensor transducers. *Electroanalysis*, 16(9), pp. 724–729.

Moejes, K., Sherif, R., Dürr, S., Conlan, S., Mason, A. and Korostynska, O. (2018) Real-Time Monitoring of Tetraselmis suecica in A Saline Environment as Means of Early Water Pollution Detection. *Toxics*, 6(4), p. 57.

Molina-Lopez, F., Briand, D. and De Rooij, N. F. (2012) All additive inkjet printed humidity sensors on plastic substrate. *Sensors and Actuators, B: Chemical*. Elsevier B.V., 166–167, pp. 212–222.

Morrisey, D. and Woods, C. (2015) *In-water cleaning technologies: review of information*. *Ministry for Primary Industries*.

Moser, C. S., Wier, T. P., First, M. R., Grant, J. F., Riley, S. C., Robbins-Wamsley, S. H., Tamburri, M. N., Ruiz, G. M., Miller, A. W. and Drake, L. A. (2017) Quantifying the extent of niche areas in the global fleet of commercial ships: the potential for 'super-hot spots' of biofouling. *Biological Invasions*. Springer International Publishing, 19(6), pp. 1745–1759.

Motha, L., Kim, J. and Kim, W. S. (2015) Instrumented rubber insole for plantar pressure sensing. *Organic Electronics: physics, materials, applications*. Elsevier B.V., 23, pp. 82–86.

Mukhopadhyay, S. C. (2005) Novel planar electromagnetic sensors: Modeling and performance evaluation. *Sensors*, 5(12), pp. 546–579.

Negahdaripour, S. and Firoozfam, P. (2006) An ROV stereovision system for ship-hull inspection. *IEEE Journal of Oceanic Engineering*, 31(3), pp. 551–564.

Nendza, M. (2007) Hazard assessment of silicone oils (polydimethylsiloxanes, PDMS) used in antifouling-/foul-release-products in the marine environment. *Marine Pollution Bulletin*, 54(8), pp. 1190–1196.

Nettleton, D. (2006) A discussion of statistical methods for design and analysis of microarray experiments for plant scientists. *Plant Cell*, 18(9), pp. 2112–2121.

Ngoi, B. K. A., Venkatakrishnan, K., Lim, E. N. L., Tan, B. and Koh, L. H. K. (2001) Effect of energy above laser-induced damage thresholds in the micromachining of silicon by femtosecond pulse laser. *Optics and Lasers in Engineering*, 35(6), pp. 361–369.

Nishi, Y., Uyama, M., Kawazu, H., Takei, H., Iwata, K., Kudoh, H. and Mitsubayashi, K. (2012) Effects of electron beam irradiation on adhesive force of laminated sheet of high strength polytetrafluoroethylene (PTFE) and bio-adaptable polydimethylsiloxane (PDMS). *Materials Transactions*, 53(9), pp. 1657–1664.

Nomura, T., Saitoh, A. and Horikoshi, Y. (2001) Measurement of acoustic properties of liquid using liquid flow SH-SAW sensor system. *Sensors and Actuators, B: Chemical*, 76(1–3), pp. 69–73.

Nosonovsky, M. and Bhushan, B. (2016) Why re-entrant surface topography is needed for robust oleophobicity. *Philosophical Transactions of the Royal Society A: Mathematical, Physical and Engineering Sciences*, 374(2073).

Ohkawa, K., Nishida, A., Honma, R., Matsui, Y., Nagaya, K., Yuasa, A. and Yamamoto, H. (1999) Studies on fouling by the freshwater mussel Limnoperna fortunei and the antifouling effects of low energy surfaces. *Biofouling*, 13(4), pp. 337–350.

Oliveira, D. and Granhag, L. (2016) Matching forces applied in underwater hull cleaning with adhesion strength of marine organisms. *Journal of Marine Science and Engineering*, 4(4).

Olivier, F., Tremblay, R., Bourget, E. and Rittschof, D. (2000) Barnacle settlement: Field experiments on the influence of larval supply, tidal level, biofilm quality and age on Balanus amphitrite cyprids. *Marine Ecology Progress Series*, 199, pp. 185–204.

Olmer, N., Comer, B., Roy, B., Mao, X. and Rutherford, D. (2017) *Greenhouse Gas Emissions From Global Shipping, 2013–2015*. *The International Council on Clean Transportation*.

Omae, I. (2003) Organotin antifouling paints and their alternatives. *Applied Organometallic Chemistry*, 17(2), pp. 81–105.

Onajite, E. (2014) Understanding Reflection Coefficient. *Seismic Data Analysis Techniques in Hydrocarbon Exploration*, pp. 213–228.

Özisik, M. N. and Vick, B. (1984) Propagation and reflection of thermal waves in a finite medium due to axisymmetric surface sources. *International Journal of Heat and Mass Transfer*, 27(10), pp. 897–912.

Papov, V. V, Diamond, T. V, Biemann, K. and Waite, J. H. (1995) Hydroxyargenine Containing Phenolic Proteins in the Adhesive Plaques of Mytilus Eduilis. *The Journal of Biological Chemistry*, 270(35), pp. 20183–20192.

Pathak, M., Lintern, K., Chopda, V., Bracewell, D. G. and Rathore, A. S. (2017) Fluorescence based real time monitoring of fouling in process chromatography. *Scientific Reports*. Nature Publishing Group, 7(March), pp. 1–8.

Pechenik, J. A., Eyster, L. S., Widdows, J. and Bayne, B. L. (1990) The influence of food concentration and temperature on growth and morphological differentiation of blue mussel Mytilus edulis L. larvae. *Journal of Experimental Marine Biology and Ecology*, 136(1), pp. 47–64.

Petkov, P. (2011) Laser Milling: Surface Integrity, Removal Strategies and Process Accuracy, p. 254.

Polymer Properties Database (2015) *DIELECTRIC STRENGTH OF POLYMERS*. *Polymer Properties Database*.

Potyrailo, R. A. (2016) Multivariable Sensors for Ubiquitous Monitoring of Gases in the Era of Internet of Things and Industrial Internet. *Chemical Reviews*, 116(19), pp. 11877–11923.

Prendergast, G. S. (2010) Settlement and Behaviour of Marine Fouling Organisms. in Durr, S. and Thomason, J. (eds) *Biofouling*. Oxford: Wiley-Blackwell, pp. 30–59.

Pu, X., Li, G. and Huang, H. (2016) Preparation, anti-biofouling and drag-reduction properties of a biomimetic shark skin surface. *Biology Open*, 5(4), pp. 389–396.

Quinn, G. P. and Keough, M. J. (2002) *Experimental Design and Data Analysis for Biologists*.

Quintal, B., Schmalholz, S. M. and Podladchikov, Y. Y. (2011) Impact of fluid saturation on the reflection coefficient of a poroelastic layer. *Geophysics*, 76(2).

Radke, S. M. and Alocilja, E. C. (2004) Design and fabrication of a microimpedance biosensor for bacterial detection. *IEEE Sensors Journal*, 4(4), pp. 434–440.

Railkin, A. I. (2003) *Marine Biofouling: Colonization Processes and Defenses*. Boca Raton: CRC Press LLC.

Ralston, E. and Swain, G. (2009) Bioinspiration—the solution for biofouling control? *Bioinspiration & Biomimetics*, 4(4), pp. 15007–9.

Razi, S., Madanipour, K. and Mollabashi, M. (2016) Laser surface texturing of 316L stainless steel in air and water: A method for increasing hydrophilicity via direct creation of microstructures. *Optics and Laser Technology*. Elsevier, 80, pp. 237–246.

Ribeiro, S., Amorim, A., Andersen, T. J. T. J., Abrantes, F. F., Ellegaard, M. and Ellengaard, M. (2012) Reconstructing the history of an invasion : the toxic phytoplankton species Gymnodinium catenatum in the Northeast Atlantic. *Biological Invasions*, 14(5), pp. 969–985.

Rittschof, D. (2000) Natural product antifoulants: One perspective on the challenges related to coatings development. *Biofouling*, 15(1–3), pp. 119–127.

Roberts, D., Rittschof, D., Holm, E. and Schmidt, A. R. (1991) Factors influencing initial larval settlement: temporal, spatial and surface molecular components. *Journal of Experimental Marine Biology and Ecology*, 150(2), pp. 203–221.

Ross, D. J., Johnson, C. R. and Hewitt, C. L. (2002) Impact of introduced seastars Asterias amurensis on survivorship of juvenile commercial bivalves Fulvia tenuicostata. *Marine Ecology Progress Series*, 241, pp. 99–112.

Ruiz, G. M., Rawlings, T. K., Dobbs, F. C., Drake, L. A., Mullady, T., Huq, A. and Colwell, R. R. (2000) Global spread of microorganisms by ships. *Nature*, 408(November), pp. 49–50.

Rumpf, R. C. (2017) Electromagnetic Waves & Polarization. *EMPossible*.

Salazar-Alvarez, M., Korostynska, O., Mason, A., Al-Shamma'a, A., Cooney, J. C., Magner, E. and Tofail, S. a M. (2014) Label free detection of specific protein binding using a microwave sensor. *The Analyst*. Royal Society of Chemistry, 139(21), pp. 5335–8.

Salta, M., Chambers, L., Wharton, J., Wood, R., Briand, F., Blache, Y., Stokes, K., Toulon-var, U. S. and Garde, L. (2009) Marine fouling organisms and their use in antifouling bioassays. *Eurocorr 2009*, (May 2014), pp. 1–26.

Salta, M., Wharton, J. A., Stoodley, P., Dennington, S. P., Goodes, L. R., Werwinski, S., Mart, U., Wood, R. J. K. and Stokes, K. R. (2010) Designing biomimetic antifouling surfaces. *Philosophical Transactions of the Royal Society A: Mathematical, Physical and Engineering Sciences*, 368(1929), pp. 4729–4754.

Salters, B. and Piola, R. (2017) UVC Light for Antifouling. *Marine Technology Society Journal*, 51(2), pp. 59–70.

Scardino, A. J. and De Nys, R. (2004) Fouling deterrence on the bivalve shell Mytilus galloprovincialis: A physical phenomenon? *Biofouling*, 20(4–5), pp. 249–257.

Scardino, A. J. and de Nys, R. (2011) Mini review: Biomimetic models and bioinspired surfaces for fouling control. *Biofouling*, 27(1), pp. 73–86.

Scardino, A. J., Guenther, J. and de Nys, R. (2008) Attachment point theory revisited: the fouling response to a microtextured matrix. *Biofouling*, 24(1), pp. 45–53.

Scardino, A. J., Harvey, E. and De Nys, R. (2006) Testing attachment point theory: Diatom attachment on microtextured polyimide biomimics. *Biofouling*, 22(1), pp. 55–60.

Scardino, A., De Nys, R., Ison, O., O'Connor, W. and Steinberg, P. (2003) Microtopography and antifouling properties of the shell surface of the bivalve molluscs Mytilus galloprovincialis and Pinctada imbricata. *Biofouling*, 19(SUPPL.), pp. 221–230.

Schaeffer, R. D. and Kardos, G. (2008) *Post-Laser processing Cleaning Techniques*. *Industial Laser Solutions For Manufcaturing*.

Schultz, M. P. (2007) Effects of coating roughness and biofouling on ship resistance and powering. *Biofouling*, 23(5–6), pp. 331–41.

Schultz, M. P., Bendick, J. a, Holm, E. R. and Hertel, W. M. (2011) Economic impact of biofouling on a naval surface ship. *Biofouling*, 27(1), pp. 87–98.

Schultz, M. P., Kavanagh, C. J. and Swain, G. W. (1999) Hydrodynamic forces on barnacles: Implications on detachment from fouling-release surfaces. *Biofouling*, 13(4), pp. 323–335.

Schumacher, J. F., Aldred, N., Callow, M. E., Finlay, J. A., Callow, J. A., Clare, A. S. and Brennan, A. B. (2007) Species-specific engineered antifouling topographies: Correlations between the settlement of algal zoospores and barnacle cyprids. *Biofouling*, 23(5), pp. 307–317.

Scianni, C. and Georgiades, E. (2019) Vessel In-Water Cleaning or Treatment: Identification of Environmental Risks and Science Needs for Evidence-Based Decision Making. *Frontiers in Marine Science*, 6(July), pp. 1–12.

Seatrade Maritime News (2018) *New solution for biofouling inspired by pitcher plants*. *Seatrade Maritime News*.

Sebastian, M. T. (2008) Chapter Two - Measurement of microwave dielectric properties and factors affecting them. in *Dielectric Materials for Wireless Communication*. Elsevier Ltd, pp. 11–47.

Sebastian, M. T. (2008) Measurement of Microwave Dielectric Properties and Factors Affecting Them. in *Dielectric Materials for Wireless Communication*, pp. 11–47.

Seed, R. and Suchanek, T. H. (1992) Population and Community Ecology of Mytilus. *Developments in Aquaculture and Fisheries Science*, 25, pp. 87–169.

Seed, R. and Suchanek, T. H. (1992) Population and Community Ecology of Mytilus. *Developments in Aquaculture and Fisheries Science*, 25, pp. 87–169.

Senger, H. (1995) *Ecophysiology of photosynthesis*. *Journal of Photochemistry and Photobiology B: Biology*.

Shao, Y., Wang, J., Wu, H., Liu, J., Aksay, I. A. and Lin, Y. (2010) Graphene based electrochemical sensors and biosensors: A review. *Electroanalysis*, 22(10), pp. 1027–1036.

Sheka, E. F. (2003) Intermolecular interaction and vibrational spectra at fumed silica particles/silicone polymer interface. *Journal of Nanoparticle Research*, 5(5–6), pp. 419–437.

Shim, J. S., Rust, M. J. and Ahn, C. H. (2013) A large area nano-gap interdigitated electrode array on a polymer substrate as a disposable nano-biosensor. *Journal of Micromechanics and Microengineering*, 23(3).

Shirinov, A. V. and Schomburg, W. K. (2008) Pressure sensor from a PVDF film. *Sensors and Actuators, A: Physical*, 142(1), pp. 48–55.

Silva, E. R., Ferreira, O., Ramalho, P. A., Azevedo, N. F., Bayón, R., Igartua, A., Bordado, J. C. and Calhorda, M. J. (2019) Eco-friendly non-biocide-release coatings for marine biofouling prevention. *Science of the Total Environment*. Elsevier B.V., 650, pp. 2499–2511.

Silverman, H. G. and Roberto, F. F. (2007) Understanding marine mussel adhesion. *Marine Biotechnology*, 9(6), pp. 661–681.

Sullivan, T., McGuinness, K., O'Connor, N. E. and Regan, F. (2014) Characterization and anti-settlement aspects of surface micro-structures from Cancer pagurus. *Bioinspiration and Biomimetics*. IOP Publishing, 9(4).

Sumetsky, M., Windeler, R. S., Dulashko, Y. and Fan, X. (2007) Optical liquid ring resonator sensor. *Optics Express*, 15(22), p. 14376.

Summerlot, D., Kumar, A., Das, S., Lee, G., Seal, S., Diaz, D. and Cho, H. J. (2011) Nanoporous gold electrode for electrochemical sensors in biological environment. *Procedia Engineering*. Elsevier B.V., 25, pp. 1457–1460.

Sun, A. C., Alvarez-Fontecilla, E., Venkatesh, A. G., Aronoff-Spencer, E. and Hall, D. A. (2018) High-Density Redox Amplified Coulostatic Discharge-Based Biosensor Array. *Solid-State Circuits*, 53(7), pp. 2054–2064.

Sun, C., Vaccaro, E. and Waite, J. H. (2001) Oxidative stress and the mechanical properties of naturally occurring chimeric collagen-containing fibers. *Biophysical Journal*. Elsevier, 81(6), pp. 3590–3595.

Sun, Z., Tan, X., Tor, S. B. and Yeong, W. Y. (2016) Selective laser melting of stainless steel 316L with low porosity and high build rates. *Materials and Design*. Elsevier Ltd, 104, pp. 197–204.

Tamarin, A. and Keller, P. J. (1972) An ultrastructutal Study of the Byssal Thread Forming System in Mytilus. *Journal of Ultrastructure Research*, 416, pp. 401–416.

Tang, X., Tian, Q., Zhao, B. and Hu, K. (2007) The microwave electromagnetic and absorption properties of some porous iron powders. *Materials Science and Engineering A*, 445–446, pp. 135–140.

Teng, M. F., Hariz, A., Hsu, H. Y. and Omari, T. (2007) Flexible pressure sensor on polymeric materials. *Microelectronics: Design, Technology, and Packaging III*, 6798(December 2007), p. 67981D.

Thomas, K. V. and Brooks, S. (2010) The environmental fate and effects of antifouling paint biocides. *Biofouling*, 26(1), pp. 73–88.

Timmers, M. A., Kistner, C. A. and Donohue, M. . (2005) Marine Debris of the Northwestern Hawaiian Islands: Ghost Net Identification. *US Department of Commerce, National Oceanic and Atmospheric Administration, National Sea Grant College Program*.

Townsin, R. L. (2003) The ship hull fouling penalty. *Biofouling*, 19(March), pp. 9–15.

Townsin, R. L. and Anderson, C. D. (2009) *Fouling control coatings using low surface energy, foul release technology*. *Advances in Marine Antifouling Coatings and Technologies*. Woodhead Publishing Limited.

Trdan, U., Hočevar, M. and Gregorčič, P. (2017) Transition from superhydrophilic to superhydrophobic state of laser textured stainless steel surface and its effect on corrosion resistance. *Corrosion Science*, 123(January), pp. 21–26.

Trepte, A. (2019) *Blue Mussel*. *Encyclopaedia Britannica*.

Tribou, M. and Swain, G. (2010) The use of proactive in-water grooming to improve the performance of ship hull antifouling coatings. *Biofouling*, 26(1), pp. 47–56.

Tribou, M. and Swain, G. (2015) Grooming using rotating brushes as a proactive method to control ship hull fouling. *Biofouling*. Taylor & Francis, 31(4), pp. 309–319.

Tsouti, V., Boutopoulos, C., Zergioti, I. and Chatzandroulis, S. (2011) Capacitive microsystems for biological sensing. *Biosensors and Bioelectronics*. Elsevier B.V., 27(1), pp. 1–11.

Tyler-Walters, H. (2008) *Mytilus edulis Common mussel*. *In Tyler-Walters H. and Hiscock K. (eds) Marine Life Information Network: Biology and Sensitivity Key Information Reviews, [on-line]. Plymouth: Marine Biological Association of the United Kingdom. [cited 09-09-2019]*.

Tylkowski, B. and Tsibranska, I. (2015) Overview of main techniques used for membrane characterization. *Journal of Chemical Technology and Metallurgy*, 50(1), pp. 3–12.

Underwood, A. J. (1996) *Experiments in Ecology*.

UNESCO (2004) *Liverpool - Maritime Mercantile City*. *UNESCO*.

Vaganay, J., Elkins, M., Esposito, D., O'Halloran, W., Hover, F. and Kokko, M. (2006) Ship hull inspection with the HAUV: US Navy and NATO demonstrations results. *Oceans 2006*, (1), pp. 1–6.

Valavanis, K. P., Gracanin, D., Matijasevic, M., Kolluru, R. and Demetriou, G. A. (1997) Control architecture for autonomous underwater vehicles. *IEEE Control Systems Magazine*, 17(6), pp. 233–246.

Van Gerwen, P., Laureyn, W., Laureys, W., Huyberechts, G., Op De Beeck, M., Baert, K., Suls, J., Sansen, W., Jacobs, P., Hermans, L. and Mertens, R. (1998) Nanoscaled interdigitated electrode arrays for biochemical sensors. *Sensors and Actuators, B: Chemical*, 49(1–2), pp. 73–80.

Varghese, S. S., Lonkar, S., Singh, K. K., Swaminathan, S. and Abdala, A. (2015) Recent advances in graphene based gas sensors. *Sensors and Actuators, B: Chemical*. Elsevier B.V., 218, pp. 160–183.

Venugopalan, H. (2016) *Photonic Frontiers: LEDs - UVC LEDs reduce marine biofouling*. *Laser Focus World*.

Vreeland, V., Waite, J. H. and Epstein, L. (1998) Polyphenols and oxidases in substratum adhesion by marine algae and mussels. *Journal of Phycology*, 34(1), pp. 1–8.

Wahl, M. (1989) Marine epibiosis. I. Fouling and antifouling:some basic aspects. *Marine Ecology Progress Series*, 58(December 1989), pp. 175–189.

Wahl, M., Hay, M. E. and Enderlein, P. (1997) Effects of epibiosis on consumer-prey interactions. *Hydrobiologia*, 355(1–3), pp. 49–59.

Waite, J. H. (2017) Mussel adhesion - Essential footwork. *Journal of Experimental Biology*, 220(4), pp. 517–530.

Waite, J. H. and Qin, X. (2001) Polyphosphoprotein from the adhesive pads of Mytilus edulis. *Biochemistry*, 40(9), pp. 2887–2893.

Waite, J. H. and Tanzer, M. L. (1981) Polyphenolic substance of mytilus edulis: novel adhesive containing L-dopa and hydroxyproline. *Science*, 212(4498), pp. 1038–1040.

Wan, J., Tang, S., Shu, Z., Li, D., Wang, S., Imran, M. and Vasilakos, A. V. (2016) Software-Defined Industrial Internet of Things in the Context of Industry 4.0. *IEEE Sensors Journal*, 16(20), pp. 7373–7380.

Wang, W. and Widdows, J. (1991) Physiological responses of mussel larvae Mytilus edulis to environmental hypoxia and anoxia. *Marine Ecology Progress Series*, 70(1989), pp. 223–236.

Wang, W. H., Chen, X. Q., Marburg, A., Chase, J. G. and Hann, C. E. (2008) A Low-Cost unmanned underwater vehicle prototype for shallow water tasks. *2008 IEEE/ASME International Conference on Mechatronics and Embedded Systems and Applications, MESA 2008*, (1), pp. 204–209.

Wang, X. and Xu, X. (2000) Thermoelastic wave induced by pulsed laser heating. *American Society of Mechanical Engineers, Heat Transfer Division, (Publication) HTD*, 366, pp. 201–210.

Wang, X. D., Michalowski, A., Walter, D., Sommer, S., Kraus, M., Liu, J. S. and Dausinger, F. (2009) Laser drilling of stainless steel with nanosecond double-pulse. *Optics and Laser Technology*, 41(2), pp. 148–153.

Warner, S. C. and Waite, J. H. (1999) Expression of multiple forms of an adhesive plaque protein in an individual mussel, Mytilus edulis. *Marine Biology*, 134(4), pp. 729–734.

Wemli, R. L. (2002) AUVs - A technology whose time has come. *Underwater Technology*, 2002–Janua, pp. 309–314.

Whomersley, P., Schratzberger, M., Huxham, M., Bates, H. and Rees, H. (2007) The use of time-series data in the assessment of macrobenthic community change after the cessation of sewage-sludge disposal in Liverpool Bay (UK). *Marine Pollution Bulletin*, 54(1), pp. 32–41.

Widdows, J. (1991) Physiological ecology of mussel larvae. *Aquaculture*, 94(2–3), pp. 147–163.

Wiegemann, M. (2005) Adhesion in blue mussels (Mytilus edulis) and barnacles (genus Balanus): Mechanisms and technical applications. *Aquatic Sciences*, 67(2), pp. 166–176.

Wienecke, M., Bunescu, M. C., Pietrzak, M., Deistung, K. and Fedtke, P. (2003) PTFE membrane electrodes with increased sensitivity for gas sensor applications. *Synthetic Metals*, 138(1–2), pp. 165–171.

Wilkens, S. L., Stanley, J. A. and Jeffs, A. G. (2012) Induction of settlement in mussel (*Perna canaliculus*) larvae by vessel noise. *Biofouling*, 28(1), pp. 65–72.

Wilkinson, S. B., Zheng, W., Allen, J. R., Fielding, N. J., Wanstall, V. C., Russell, G. and Hawkins, S. J. (1996) Water quality improvements in Liverpool docks: The role of filter feeders in algal and nutrient dynamics. *Marine Ecology*, 17(1–3), pp. 197–211.

Williams, E. (2014) *Experimental and Theoretical Investigations of Nanosecond Fibre Laser Micromachining*. Cardiff University.

Woods Hole Oceanographic Institute (1953) *Marine Fouling and Its Prevention.*

Wrange, A. L., Charrier, G., Thonig, A., Rosenblad, M. A., Blomberg, A., Havenhand, J. N., Jonsson, P. R. and André, C. (2016) The story of a hitchhiker: Population genetic patterns in the invasive barnacle balanus (amphibalanus) improvisus Darwin 1854. *PLoS ONE*, 11(1), pp. 1–28.

Xia, K., Zhu, Z., Zhang, H. and Xu, Z. (2018) A triboelectric nanogenerator as self-powered temperature sensor based on PVDF and PTFE. *Applied Physics A: Materials Science and Processing*. Springer Berlin Heidelberg, 124(8), pp. 1–7.

Xu, C., Reece, C. and Kelley, M. (2013) Characterization of Nb SRF cavity materials by white light interferometry and replica techniques. *Applied Surface Science*. Elsevier B.V., 274, pp. 15–21.

Xue, L., Lu, X., Wei, H., Long, P., Xu, J. and Zheng, Y. (2014) Bio-inspired self-cleaning PAAS hydrogel released coating for marine antifouling. *Journal of Colloid and Interface Science*. Elsevier Inc., 421, pp. 178–183.

Yang, D., Tian, H. and Ji, Y. (2011) Nanoscale photonic crystal sensor arrays on monolithic substrates using side-coupled resonant cavity arrays. *Optics Express*, 19(21), p. 20023.

Yang, T., Yu, Y. Z., Zhu, L. S., Wu, X., Wang, X. H. and Zhang, J. (2015) Fabrication of silver interdigitated electrodes on polyimide films via surface modification and ion-exchange technique and its flexible humidity sensor application. *Sensors and Actuators, B: Chemical*, 208, pp. 327–333.

Yavari, F. and Koratkar, N. (2012) Graphene-based chemical sensors. *Journal of Physical Chemistry Letters*, 3(13), pp. 1746–1753.

Yong, H. E., Krishnamoorthy, K., Hyun, K. T. and Kim, S. J. (2015) Preparation of ZnO nanopaint for marine antifouling applications. *Journal of Industrial and Engineering Chemistry*. The Korean Society of Industrial and Engineering Chemistry, 29, pp. 39–42.

Young, G. A. and Crisp, D. J. (1981) Marine animals and adhesion. *Applied Science Publishers Ltd*, pp. 19–39.

Yu, J., Wei, W., Danner, E., Ashley, R. K., Israelachvili, J. N. and Waite, J. H. (2012) Mussel protein adhesion depends on thiol-mediated redox modulation. *Nature Chemical Biology*, 7(9), pp. 588–590.

Yusof, N. S. M., Babgi, B., Alghamdi, Y., Aksu, M., Madhavan, J. and Ashokkumar, M. (2016) Physical and chemical effects of acoustic cavitation in selected ultrasonic cleaning applications. *Ultrasonics Sonochemistry*. Elsevier B.V., 29, pp. 568–576.

Zabin, C. J., Davidson, I. C., Holzer, K. K., Smith, G., Ashton, G. V., Tamburri, M. N. and Ruiz, G. M. (2018) How will vessels be inspected to meet emerging biofouling regulations for the prevention of marine invasions? *Management of Biological Invasions*, 9(3), pp. 195–208.

Zhang, B. X., Wang, S. L. and Wang, X. D. (2019) Wetting Transition from the Cassie-Baxter State to the Wenzel State on Regularly Nanostructured Surfaces Induced by an Electric Field. *Langmuir*, 35(3), pp. 662–670.

Zhang, H. and Kim, E. S. (2005) Micromachined acoustic resonant mass sensor. *Journal of Microelectromechanical Systems*, 14(4), pp. 699–706.

Zhang, Q., Zhu, C., Yang, L. T., Chen, Z., Zhao, L. and Li, P. (2017) An Incremental CFS Algorithm for Clustering Large Data in Industrial Internet of Things. *IEEE Transactions on Industrial Informatics*. IEEE, 13(3), pp. 1193–1201.

Zhang, X., Monroe, M. E., Chen, B., Chin, M. H., Heibeck, T. H., Schepmoes, A. A., Yang, F., Petritis, B. O., Camp, D. G., Pounds, J. G., Jacobs, J. M., Smith, D. J., Bigelow, D. J., Smith, R. D. and Qian, W. J. (2010) Endogenous 3,4-dihydroxyphenylalanine and dopaquinone modifications on protein tyrosine: Links to mitochondrially derived oxidative stress via hydroxyl radical. *Molecular and Cellular Proteomics*, 9(6), pp. 1199–1208.

Zhao, Q., Lee, D. W., Ahn, B. K., Seo, S., Kaufman, Y., Israelachvili, J. N. and Waite, J. H. (2016) Underwater contact adhesion and microarchitecture in polyelectrolyte complexes actuated by solvent exchange. *Nature Materials*, 15(4), pp. 407–412.

Zobell, C. E. and Allen, E. C. (1935) The significance of marine bacteria in the fouling of submerged surfaces. *Journal of bacteriology*, 3(Mar), pp. 239–251.

Zoughi, R. and Bakhtiari, S. (1990) Microwave Nondestructive Detection and Evaluation of Disbonding and Delamination in Layered-Dielectric-Slabs. *IEEE Transactions on Instrumentation and Measurement*, 39(6), pp. 1059–1063.